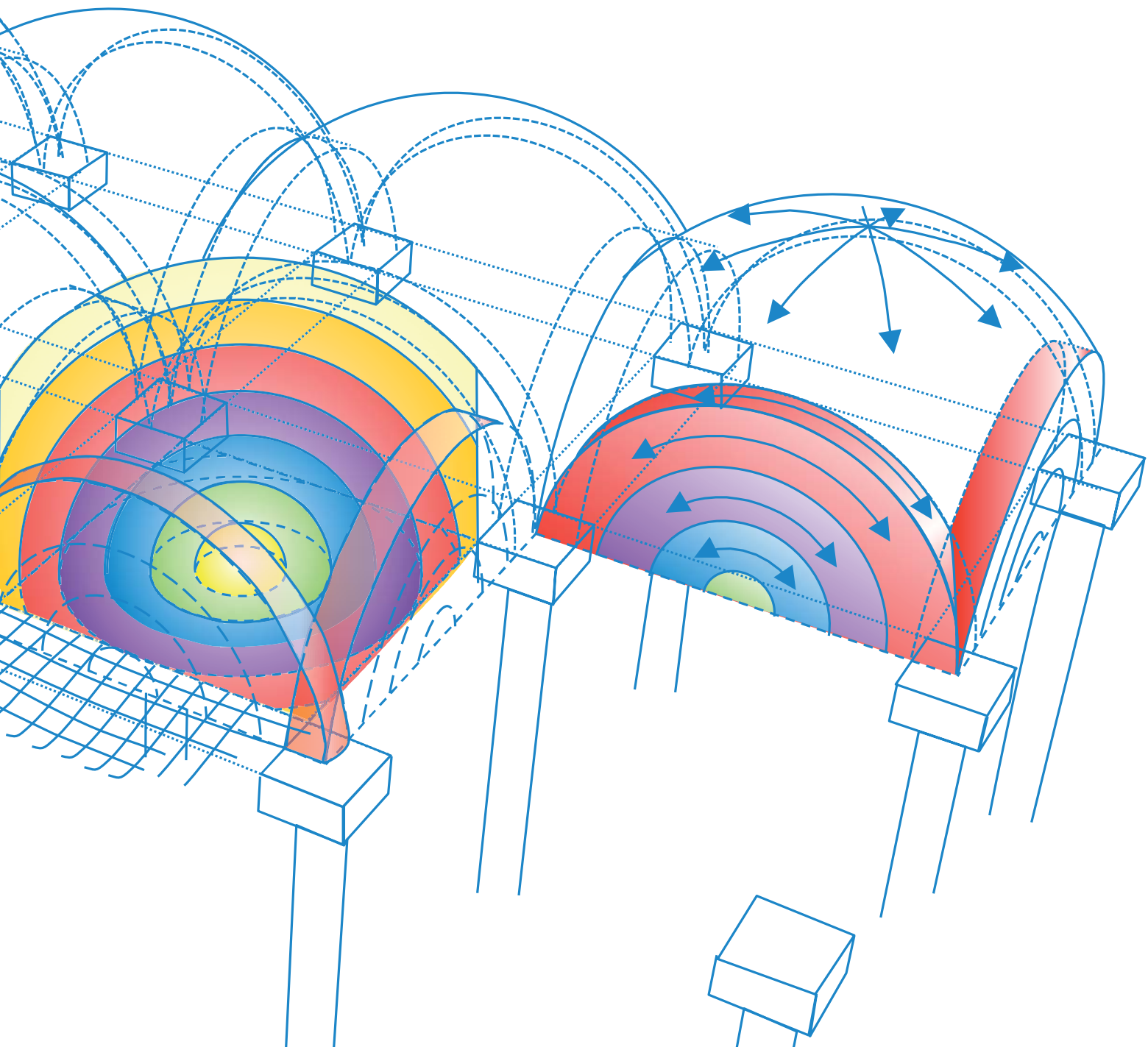# Suzanne J. M. van Eekelen

Basal Reinforced Piled Embankments

Experiments, field studies and the development and validation of a new analytical design model

Basal Reinforced Piled Embankments

Experiments, field studies and the development and validation
of a new analytical design model

Basal Reinforced Piled Embankments
Experiments, field studies and the development and validation
of a new analytical design model

Proefschrift

ter verkrijging van de graad van doctor
aan de Technische Universiteit Delft,
op gezag van de Rector Magnificus, prof.ir. K.C.A.M. Luyben,
voorzitter van het College voor Promoties,
in het openbaar te verdedigen op
woensdag 1 juli 2015 om 15:00 uur

door Suzanne Julie Marie VAN EEKELEN

civiel-technisch ingenieur
geboren te Nottingham, Groot-Brittannië

This dissertation has been approved by the promotors:
Prof. ir. A.F. van Tol
Prof. dr. ir. A. Bezuijen

Composition of the doctoral committee:

Rector Magnificus	TU Delft, chair
Prof. ir. A.F. van Tol	TU Delft, promotor
Prof. dr. ir. A. Bezuijen	University of Ghent, Belgium, promotor

Independent members:

Prof. dr. C. Jommi	Civil Engineering, TU Delft
C.R. Lawson	TenCate, Malaysia
Prof. dr. J. Han	University of Kansas, USA
Prof. dr. D. Dias	l'Université Grenoble-Alpes, France
Prof. dr.-ing. C. Moorman	Universität Stuttgart, Germany
Prof. dr. M.A. Hicks	Civil Engineering, TU Delft, substitute member

Acknowledgements

I thought I would never start on a doctorate. The prospect of the combination with family life was not an appealing one. However, Professor Frits van Tol unexpectedly asked me to take the plunge. I hesitated for two months before deciding to take up the challenge. And I have never regretted my decision. On the contrary, I have immensely enjoyed everything: cooperating closely with my supervisors, colleagues and many others, and the time I had to concentrate on one subject, analysing data and writing papers. I also liked the travel and giving the presentations, reviewing engineering designs and research papers, being involved in numerous discussions with all kinds of people or groups, and working in the CUR committee on a design guideline for piled embankments. And so I am grateful to Frits van Tol for his encouragement, and not least because I enjoyed working with him so much, particularly during the past year, as we started working together more closely.

The end result would never have been the same without the day-to-day supervision from my colleague Adam Bezuijen, who is also a Professor at the University of Ghent. He made a substantial contribution to the research, and to my development. I enjoyed working with him immensely: he is a kind person, a visionary coach and a master in data interpretation. He invested a great deal of time in my doctorate. I am also very grateful to my employer, Deltares, for giving me the opportunity to write this thesis and I thank them for their trust and support.

Luck was on my side: I was able to conduct experiments in the Deltares laboratory. My colleagues there are highly professional, and I could trust them completely to carry out correctly the measurements I asked for, including the detailed design, the construction of the test set-up and the correct calibration of transducers. I would therefore like to express my gratitude to Jack van der Vegt, Willem van Pernis, Rob Zwaan, Ruud van den Berg and Paul Schaminee, also for their collegiality and the creative approach to solving any problems that arose. The high quality of their work was undoubtedly one reason why the resulting paper – Chapter 2 – was honoured with the 2012 Best Paper Award by the journal Geotextiles and Geomembranes. Delft Cluster and Deltares financed the development and the mobilisation of the test set-up for the experiment series, for which I am grateful. The granular material was delivered free of charge by Eerland Bouwstoffen Management.

Another piece of luck was the involvement of several manufacturers. I am grateful for the financial support of manufacturers Huesker, Naue and TenCate for my entire study of piled embankments. Their willingness to engage in fruitful debate

the new calculation rule for subsoil support and received the IGS Student Award for the Netherlands in 2012 for his Master's work. Theresa Liere - den Boogert (Den Boogert, 2011) simulated the experiments with Plaxis 3D tunnel and validated the analytical model for the load-deflection behaviour (step 2). She also carried out large-scale triaxial tests in the laboratory of Delft University of Technology on the fill of the crushed recycled construction material used in the model experiments. Finally, Tara van der Peet (2014) validated the new analytical model for calculation step 1, the Concentric Arches model with Plaxis 3D. She wrote a paper on the basis of her Master's thesis that was awarded the best paper prize at the Young Member Session at the 10th IGS conference in Berlin in 2014 (Van der Peet and Van Eekelen, 2014). It was a pleasure to work with Herman-Jaap, Theresa and Tara.

I very much appreciated the corrections, suggestions and discussions with the linguist Pete Thomas. It was a joy to work with him. I am also grateful to my father, Hans van Eekelen, and Arjan Venmans for going through the manuscript, making suggestions, dotting the i's and crossing the t's.

Combining this study with a family life turned out to be straightforward on a practical level. I was actually at home more often to write and so I was able to listen to my children's stories when they got home from school. I am enormously grateful to my parents, my husband Maarten and my children Gerrit, Roel and Ida for their support over the years.

Summary

A basal reinforced piled embankment consists of a reinforced embankment on a pile foundation. The reinforcement consists of one or more horizontal layers of geosynthetic reinforcement (GR) installed at the base of the embankment. The design of the GR is the subject of this thesis.

A basal reinforced piled embankment can be used for the construction of a road or a railway when a traditional construction method would require too much construction time, affect vulnerable objects nearby or give too much residual settlement, making frequent maintenance necessary.

The GR strain needs to be calculated to design the GR. Multiplying this GR strain by the GR stiffness gives the tensile force, which needs to be smaller than the long-term GR tensile strength. The GR strain is calculated in two steps. Calculation step 1 divides the load – the weight of the embankment fill, road construction and traffic load – into two load parts. One part (load part A) is transferred to the piles directly. This part is relatively large because a load tends to be transferred to the stiffer parts of a construction. This mechanism is known as 'arching'. The second, residual load part ($B+C$) rests on the GR (B) and the underlying subsoil (C).

Calculation step 2 determines the GR strain on the basis of the result of step 1. Only the GR strips between each pair of adjacent piles are considered: they are loaded by $B+C$ and may or may not be supported by the subsoil. The GR strain can be calculated if the distribution of load part $B+C$ on the GR strip, the amount of subsoil support and the GR stiffness are known. An implicit result of this calculation step is the further division of load part $B+C$ into parts B and C.

Several methods for the GR design are available, all with their own models for calculation steps 1 and 2. The methods give results that differ immensely. The Dutch CUR226 (2010) and the German EBGEO (2010) adopted Zaeske's method (2001). However, measurements that were published later (Van Duijnen et al., 2010; Van Eekelen et al., 2015a) showed that this method could be calculating much higher GR strains than those measured in practice, leading to heavier and more expensive designs than necessary.

The objective of the present study was to establish a clearer picture of load distribution in a basal reinforced piled embankment and, on that basis, to develop and validate an analytical design model for the geosynthetic reinforcement in a piled embankment. The results were described in five papers published in the international scientific journal 'Geotextiles and Geomembranes'. Those journal

papers can be found in Chapters 2, 3, 4, 5 and Appendix A of this thesis (Van Eekelen et al., 2012a, 2012b, 2013, 2015a and 2011 respectively).

Chapter 2 presents a series of twelve 3D experiments that were carried out at the Deltares laboratory. The scaled model tests were carried out under high surcharge loads to achieve stress situations comparable with those in practice. A unique feature of these tests was that load parts *A, B* and *C* could be measured separately, making it possible to compare the measurements with calculation steps 1 and 2 separately.

In these tests (static load, laboratory scale), smooth relationships were obtained between the net load on the fill (surcharge load minus subsoil support) and several measured parameters such as load distribution and deformation. Consolidation of the subsoil resulted in an increase in arching (more *A*) and more tensile force in the GR (more *B* and more GR strain). The measured response to consolidation depends on the fill's friction angle. A higher friction angle results in more arching during consolidation.

One of the major conclusions based on the test series was that the load on a GR strip is approximately distributed as an inverse triangle, with the lowest pressure in the centre and higher pressure close to the piles. This conclusion was the basis for the remainder of this doctorate study and the development of the new calculation model.

Chapter 3 considers calculation step 2. This chapter starts by comparing the measurements in the experiments with the calculation results of step 2 of the Zaeske (2001) model, which uses a triangular load distribution on the GR strip and considers the support of the subsoil underneath the GR strip only. It was found that Zaeske's model calculates GR strains that are larger than the measured GR strains (approximately a factor of two for GR strains larger than 1%).

Chapter 3 continues with the suggestion of two modifications to Zaeske's step 2. Firstly, the load distribution is changed from a triangular to an inverse triangular load distribution. Secondly, the subsoil support is extended from the support by the subsoil underneath the GR strip to the subsoil underneath the entire GR between the piles. The new step 2 model with these modifications produces a much better fit with field measurements than Zaeske's model.

Chapter 4 considers calculation step 1, the arching. Additional tests were conducted for this purpose, varying factors such as the fill height. This chapter gives an overview of the existing arching models and introduces a new model. This Concentric Arches model (CA model) is an adaptation and extension of the models

of Hewlett and Randolph (1988), and Zaeske (2001), which have been adopted in several European design guidelines.

Some countries use piled embankments without GR. Introducing GR changes the load distribution considerably. A major part of the load is then exerted on the piles and the residual load is mainly exerted on the GR strips between the piles, with the load being distributed approximately as an inverse triangle.

Chapter 4 explains the development of the load distribution as a result of continuing GR deflection; new small arches grow within the older larger ones. Smaller arches exert less load on their subsurface. This idea is related to the concentric arches of the new model, which gives an almost perfect description of the observed load distribution in the limit state situation. Furthermore, the new model describes the influence of the fill strength and embankment height correctly.

Chapter 5 compares the existing, and the newly introduced, design models with measurements from seven full-scale projects and four series of scaled model experiments. Two of these seven field projects were conducted in the Netherlands and they were carried out in part for this doctorate research. One of the four experimental series – the one presented in Chapters 2 and 4 – was conducted specifically for the present research. The other measurements were reported earlier in the literature.

The calculations were carried out using mean, best-guess values for the material properties. The calculation results from the CA model match the measurements much better than the results of the arching models of Hewlett and Randolph (1988), and of Zaeske (2001). The results of the CA model are also the closest match with the results of the 3D numerical calculations, as described in Van der Peet and Van Eekelen (2014). These authors also show that the new CA model responds better to changes in the fill friction angle than any of the other models considered.

When there is no subsoil support, or almost no subsoil support, the inverse triangular load distribution on the GR strips between adjacent piles gives the best match with the measurements. When there is significant subsoil support, the load distribution is approximately uniform. This difference between the situation with or without subsoil support is understandable when one considers that most load is attracted to the construction parts that move least. In the cases with limited subsoil support, the load distribution that gives the minimum GR strain should be used to find the best match with the measurements.

The GR strain calculated with Zaeske's model is on average 2.46 times the measured GR strain. The GR strain calculated with the new model is on average 1.06 times the measured GR strain. The calculated GR strain is therefore almost a perfect match with the measured GR strain. The new Dutch CUR226 (2015) has therefore adopted the model proposed in this thesis.

Samenvatting

Paalmatrassen gewapend met geokunststof
Experimenten, monitoring in praktijkprojecten en de ontwikkeling en validatie van een nieuw analytisch ontwerpmodel

Een paalmatras bestaat uit een fundering van palen met daarop paaldeksels en daarboven een gewapende aardebaan. De wapening van de aardebaan wordt onderin de aardebaan aangebracht en bestaat uit een of meer horizontale lagen geokunststof (GR, een afkorting van 'geosynthetic reinforcement'). Het ontwerp van de geokunststof is het onderwerp van dit proefschrift.

Een paalmatras kan worden toegepast bij de aanleg van een weg of een spoorweg op slappe grond als een traditionele oplossing te veel bouwtijd vraagt, of kwetsbare objecten in de omgeving zal beschadigen door verticale of horizontale grondvervormingen, of als er teveel restzetting wordt verwacht die frequent onderhoud noodzakelijk maakt.

Voor het ontwerpen van de GR moet de te verwachten GR rek worden berekend. Dit gebeurt in twee rekenstappen. Rekenstap 1 splitst de belasting, die bestaat uit het gewicht van de aardebaan, de wegconstructie en het verkeer, in twee delen. Het ene deel (deel *A*) gaat rechtstreeks naar de palen. Dit deel is relatief groot. Dat komt doordat objecten die relatief stijf zijn, relatief veel belasting naar zich toe trekken. Dit verschijnsel heet boogwerking. De resterende belasting (*B+C*) rust op de GR (*B*) en de onderliggende grond (*C*).

Rekenstap 2 beschouwt alleen de GR strip tussen twee belendende palen. Het belastingsdeel *B+C* wordt verondersteld in zijn geheel op deze strip te rusten. De strip wordt vaak ook ondersteund door de grond onder de strip. De GR rek kan worden berekend als een drietal zaken bekend zijn: hoe het belastingsdeel *B+C* is verdeeld over de strip, de mate waarin de ondergrond de GR ondersteunt en de GR-stijfheid. Een impliciet resultaat van deze berekening is dat het belastingsdeel *B+C* verder wordt opgesplitst in de delen *B* en *C*.

Er zijn verschillende ontwerpmethoden beschikbaar voor het ontwerp van de GR. Deze hebben ieder hun eigen modellen voor rekenstappen 1 en 2. De diverse methoden geven flink verschillende resultaten. De Nederlandse ontwerprichtlijn CUR226 (2010) gebruikte het model van Zaeske (2001). Dit was overgenomen van de Duitse EBGEO (2010). Er waren echter aanwijzingen dat dit model in bepaalde gevallen een veel hogere GR rek geeft dan in de praktijk werd gemeten. Dit kan leiden tot zwaardere en dus duurdere ontwerpen dan nodig.

Het doel van dit onderzoek was om meer inzicht te krijgen in de belastingsverdeling in een met geokunststof gewapend paalmatras en op basis daarvan een analytisch ontwerpmodel te ontwikkelen en valideren voor de geokunststof wapening. De resultaten van dit onderzoek zijn beschreven in een vijftal artikelen in het internationale wetenschappelijke tijdschrift 'Geotextiles and Geomembranes'. Deze artikelen zijn in dit proefschrift opgenomen in achtereenvolgens hoofdstukken 2, 3, 4, 5 en appendix A (respectievelijk Van Eekelen et al., 2012a, 2012b, 2013, 2015a en 2011).

Hoofdstuk 2 presenteert een serie van twaalf 3D proeven die zijn uitgevoerd in het Deltares laboratorium. De schaalproeven werden uitgevoerd met hoge bovenbelastingen, zodat de spanningen in de aardebaan vergelijkbaar zijn met die in de praktijk. Het unieke van deze proeven is dat de belastingsdelen *A, B* en *C* apart konden worden gemeten. Daardoor is het mogelijk om rekenstappen 1 en 2 ieder apart te vergelijken met de meetresultaten.

De proeven lieten een duidelijke relatie zien tussen de netto belasting op de aardebaan (bovenbelasting minus ondersteuning) en verschillende parameters, zoals de belastingsverdeling en de vervorming. Zo werd aangetoond dat consolidatie van de ondergrond een verhoging geeft van de boogwerking (meer *A*) en de trekkracht in de GR (meer *B*, meer GR rek). De respons op consolidatie is afhankelijk van de sterkte-eigenschappen van de aardebaan; een hogere wrijvingshoek geeft meer boogwerkingstoename bij consolidatie van de ondergrond.

De belasting op de GR strippen tussen belendende palen is duidelijk hoger dan op de GR tussen de strippen in. Een van de belangrijkste conclusies van de proevenserie is dat de verdeling van de belasting op die GR strippen bij benadering de vorm heeft van een omgekeerde driehoek; de laagste druk in het midden, een hogere druk bij de palen. Deze conclusie vormde de basis voor de rest van het onderzoek en de ontwikkeling van het nieuw rekenmodel.

Hoofdstuk 3 gaat in op rekenstap 2. Het hoofdstuk vergelijkt de meetresultaten van de proeven met de resultaten van rekenstap 2 van het model van Zaeske (2001). Hierin is de belastingsverdeling driehoekig: de hoogste druk in het midden, een lagere druk bij de palen. Bovendien wordt alleen gerekend met de ondersteuning van de ondergrond onder de GR strip. Het blijkt dat als de gemeten GR rek groter is dan 1%, dan is de berekende rek nog eens ongeveer twee maal zo groot.
Twee aanpassingen van het oude stap 2 - rekenmodel worden voorgesteld. Ten eerste een omgekeerde driehoekige belastingsverdeling en ten tweede het uitbreiden van de ondergrondondersteuning; niet alleen de ondergrond onder de

GR strip, maar alle ondergrond onder de GR wordt meegerekend. De resultaten van dit nieuwe rekenmodel voor stap 2 komen aanzienlijk beter overeen met de metingen.

Hoofdstuk 4 gaat in op rekenstap 1, de boogwerking. Voor dit deel van het onderzoek zijn speciaal nog zes extra laboratorium proeven uitgevoerd, waarbij ondermeer de aardebaandikte werd gevarieerd. Dit hoofdstuk geeft een overzicht van beschikbare boogwerkingsmodellen en introduceert vervolgens een nieuw model. Dit model, het Concentric Arches model (CA model), is een aanpassing en een uitbreiding van de modellen van Hewlett en Randolph (1988) en Zaeske (2001), die zijn opgenomen in diverse Europese ontwerprichtlijnen.

Aardebanen op palen worden in sommige landen ook wel toegepast zonder GR, dit proefschrift gaat echter alleen over aardebanen op palen met GR: paalmatrassen. De toevoeging van een GR verandert de belastingsverdeling ingrijpend. De meeste belasting gaat dan rechtstreeks naar de palen, het resterende deel gaat grotendeels naar de GR strippen tussen belendende palen. De belastingsverdeling op die strippen heeft bij benadering de vorm van een omgekeerde driehoek. Hoofdstuk 4 geeft een verklaring voor het ontstaan van deze belastingsverdeling; tijdens het steeds verder doorhangen van de GR vormen zich binnen de bestaande bogen steeds nieuwe, kleinere boogjes. Een kleinere boog levert minder belasting af op zijn ondergrond. Dit is gerelateerd aan de concentrische bogen in het nieuwe model, dat een bijna perfecte beschrijving geeft van de geobserveerde belastingsverdeling voor de eindsituatie waar de ondergrond is weggezakt. Het nieuwe model beschrijft bovendien de invloed van de sterkte van het aardebaanmateriaal en de hoogte van de aardebaan op correcte wijze.

Hoofdstuk 5 vergelijkt de oude en nieuwe ontwerpmodellen met metingen in zeven praktijkprojecten en een viertal proevenseries. Twee van deze zeven praktijkprojecten zijn Nederlands en mede uitgevoerd in het kader van dit promotie-onderzoek. Eén van de vier proevenseries is uitgevoerd voor dit promotie-onderzoek en beschreven in hoofdstukken 2 en 4. De andere metingen komen uit de literatuur.

De vergelijkende berekeningen zijn uitgevoerd met verwachtingswaarden voor de materiaalparameters. De rekenresultaten van het CA model blijken beter overeen te komen met de metingen dan de resultaten van de modellen van Hewlett en Randolph (1988) en Zaeske (2001). De resultaten van het CA model komen ook beter overeen met 3D numerieke berekeningen beschreven in Van der Peet en Van Eekelen (2014), waarbij bovendien wordt aangetoond dat het nieuwe model beter reageert op veranderingen in de wrijvingshoek van de aardebaan dan de oude modellen.

Als er geen of heel weinig ondergrondondersteuning is, geeft de omgekeerde driehoekige belastingsverdeling de beste overeenkomst met de metingen. Als er echter wel een aanzienlijke ondersteuning is van de ondergrond, dan is de belastingsverdeling bij benadering uniform. Dit onderscheid tussen de situatie met of zonder ondergrond is begrijpelijk vanuit de filosofie dat de constructiedelen die het minst verplaatsen de meeste belasting naar zich toe trekken. Als er heel weinig ondersteuning van de ondergrond is, dan kan het beste worden gerekend met de belastingsverdeling die de minste GR rek geeft: de uniforme of de omgekeerde driehoek.

De GR rek die wordt berekend met het oude model van Zaeske (2001), dat is opgenomen in EBGEO (2010) en CUR226 (2010) is gemiddeld 2.46 keer zo groot als de gemeten rek. De GR rek berekend met het nieuwe model is gemiddeld 1.06 keer de gemeten rek. De berekende en de gemeten rek komen dus vrijwel overeen. De nieuwe CUR226 (2015) bevat daarom het model dat wordt voorgesteld in dit proefschrift.

Table of Contents

Nomenclature

A	kN/pile	Load part transferred directly to the pile ('arching *A*' in this thesis) expressed as kN/pile = kN/unit cell
A%	%	Arching *A* presented as a percentage of the total load, *A%* is the same as the pile efficacy ("*E*") as used by several authors:

$$A\% = E = 1 - \frac{B+C}{A+B+C} \text{ or}$$

$$A\% = E = \frac{A}{A+B+C} = \frac{A}{(\gamma H + p) \cdot s_x \cdot s_y}$$

A_{fill}	m^2	Area of the fill in the test box in (A_{fill} = 1.1 · 1.1 m^2)
A_{foam}	m^2	Area of the foam cushion (modelling the subsoil) in the test box = $(1.1)^2 - 4 \cdot \frac{1}{4}\pi(0.1)^2$
A_i	m^2	Area of influence of one pile grid ($A_s = s_x \cdot s_y$)
A_{Lx}, A_{Ly}	m^2	GR area belonging to a GR strip in *x*- or *y*-directions respectively, assuming circular pile caps, see equation (5.8), Figure 3.8 and Figure 6.6
A_{rx}, A_{ry}	m^2	GR area belonging to a GR strip in *x*- or *y*-directions respectively, assuming square pile caps, see equation (A.37) and Figure A.7
A_p	m^2	Area of a pile cap ($A_p = a \cdot a$ for a square pile cap)
A_r	m^2	Area of the reinforcement ($A_r = A_i - A_p$)
A_s	m^2	Area of one GR strip between two piles ($A_{sx} = (s_x - B_{ers}) \cdot B_{ers}$)
a	m	Width of square pile cap
a_{eq}	m	Equivalent width of circular pile cap. $a_{eq} = B_{ers}$
all		Support of subsoil underneath *all* GR between the pile caps (subscript)
B	kN/pile	Load part that passes through the geosynthetic reinforcement (GR) to the pile expressed as kN/pile = kN/unit cell
B_{ers}	m	Equivalent width of circular pile cap, $B_{ers} = \frac{1}{2} \cdot d \cdot \sqrt{\pi}$ or the width of a square pile cap
B_{ps}	kN/pile	Load part that is transferred through the geosynthetic reinforcement to the pile, assuming a plane strain geometry (diaphragm walls instead of piles, see appendix A)
bl	subscript	Bottom grid layer (subscript)
C	kN/pile	Load part that is carried by the soft soil between the piles (this soft soil foundation is called 'subsoil' in this thesis) expressed as kN/pile = kN/unit cell
C	-	A constant to be calculated with boundary conditions (equations (4.29)-(4.34) and (4.47)-(4.50) in appendix 4.A)
CA	-	Concentric Arches model (Van Eekelen et al, 2013, Chapter 4 of this thesis)
C_c	-	Arching coefficient adapted by Jones et al. (1990) for the piled embankment
c	kPa	cohesion
d	m	Diameter circular pile (cap)

d_{eq}	m	Equivalent diameter of square pile cap.
DEM		Discrete Element Method
E or E_p	- (kN/kN)	Pile efficacy or pile efficiency, the same as $A\%$,

$$A\% = E = 1 - \frac{B+C}{w_{tot}}, \text{ in BS8006 } C = 0 \text{ kN/pile, thus } E = 1 - \frac{B}{w_{tot}}$$

E	kPa	Young's modulus
F	kN	Force
F_1, F_2	-	Calculation factors (see equations (3.7) for EBGEO and (3.11) for 'modified subsoil[1]')
f	m	Maximum deflection of the reinforcement in the centre between two pile caps
FDM		Finite Difference Method
FEM		Finite Element Method
GR	-	Geosynthetic reinforcement
h or H	m	Height of the fill above bottom layer of GR, or height of fill above a pipe (Figure 4.12)
h_g	m	Arch height of Zaeske's model (2001), $h_g = s/2$ for $h \geq s/2$ or $h_g = h$ for h , $s/2$
H_{g2D}	m	Height of the largest of the 2D arches of the new Concentric Arches model, see equations (4.2) and (4.13), Figure 4.10 and Figure 4.12. H_{xg2D} refers to the height of a 2D arch that is oriented along the x-axis, as indicated in Figure 4.12. H_{yg2D} refers to the height of a 2D arch that is oriented along the y-axis.
H_{g3D}	m	Height of the largest 3D hemisphere of the new Concentric Arches model, see equation (4.4) and Figure 4.10
h_g	m	Arch height in EBGEO, $h_g = s_d/2$ for $h \geq s_d/2$ or $h_g = h$ for $h < s_d/2$
HR		Model of Hewlett & Randolph (1988)
inv		Inverse triangular load distribution (see Figure 5.3c) (subscript)
J_x, J_y	kN/m	Tensile stiffness of the GR parallel to the x-axis or parallel to the y-axis.
$J_{2\%}$	kN/m	Tensile stiffness of the GR at a GR strain of 2%
K	kN/m³	Calculation value for subgrade reaction (see equation (3.10)) used to account for 'all subsoil' (Chapter 5.4.1) which is referred to as 'modified subsoil' in Chapter 3.
K_{crit}	-	Critical principal stress ratio $K_{crit} = \tan^2\left(45^o + \frac{\varphi'}{2}\right)$
k or k_s	kN/m³	Subgrade reaction
K_p	-	Passive or critical earth pressure coefficient
K_v	m/s	Vertical permeability
L, L_x, L_y	m	The clear distance between adjacent pile caps ($L_x = s_x - a_{eq}$ and $L_y = s_y - a_{eq}$)

---

[1] Chapter 3 uses the term "modified subsoil", which is referred to as "all subsoil" in Chapter 5.

L_{x2D}	m	Part of the GR strip that is oriented along the *x*-axis and on which the 2D arches exert a force, see Figure 4.23 and equation (4.12).
L_{y2D}	m	Part of the GR strip that is oriented along the *y*-axis and on which the 2D arches exert a force, see Figure 4.23 and equation (4.12).
L_{x3D}	m	Width of square on which the 3D hemispheres exert a load, see Figure 4.22 and equation (4.8). Note that L_{y3D} is not in use ($L_{x3D} = L_{y3D}$).
l_d	m	Length of the deformed reinforcement strip between two adjacent pile caps
MD		Machine direction of a GR (the long direction)
P_{2D}	kPa/m^{Kp-1}	Calculation parameter given by equation (4.1). P_{x2D} refers to a 2D arch that is oriented parallel to the *x*-axis, as indicated in Figure 4.12 and equation (4.14). P_{y2D} refers to a 2D arch that is oriented parallel to the *y*-axis.
P_{3D}	kPa/m^{2Kp-2}	Calculation parameter given by equation (4.7)
PET		Polyester
PP		Polypropylene
PVA		Polyvinyl Alcohol
p	kPa	Uniformly distributed surcharge on top of the fill (top load) $p = w_s$
p'_c	kPa	Vertical stress on pile cap (stress part on pile cap that is transferred directly to the pile). $p'_c = A/A_p$ with A (kN) is the load part directly on the pile as shown in Figure A.1 and A_p (m^2) is the area of the pile cap; $A_p = a^2$
p'_r	kPa	Average vertical stress on geosynthetic reinforcement
p'_{rt}	kPa	Average vertical stress on geosynthetic reinforcement, temporary calculation value
Q_{2D}	kN/m^3	Calculation parameter given by equation (4.1)
Q_{3D}	kN/m^3	Calculation parameter given by equation (4.7)
Q^2	kPa	Extreme of inverse tensile load (Figure 3.17), $Q = (B+C)/A_s$
$q(x)$	kPa	Load on GR strip
q_{av}	kPa	Average load on GR strips, see equation (5.9)
r	m	Radius of a 2D arch
$r(x)$	kPa	Subsoil support working as an 'upward' load on the GR
R	m	Radius of a hemisphere (Chapter 4, in this thesis a hemisphere is a 3D arch)
R or R_b	kN/pile	Total friction between fill / box walls and foam cushion / box walls and piles, see Van Eekelen et al., 2012a (Chapter 2.3.4) and 2012b (Chapter 3).
s or s_d	m	The diagonal centre-to-centre distance between piles $s_d = \sqrt{s_x^2 + s_y^2}$. In the BS8006 (see appendix A of this thesis), s is the same as s_x, s_y
str		*Str*ip: support of subsoil underneath the GR *str*ips between adjacent pile caps only (subscript)

---

[2] See equation (3.13) and the accompanying footnote.

s_x, s_y	m	Centre-to-centre pile distance parallel to the *x*-axis or parallel to the *y*- axis.
T or T_{rp}	kN/m	Tensile force in GR strip
T	kN	Tensile force in GR strip, width of load strip is zero (used in appendix A (BS8006))
T_H	kN/m	Horizontal component of T
T_H	kN	Horizontal component of the tensile force T in the GR strip, width of load strip is zero (used in appendix A (BS8006))
T_V	kN	Vertical component of T
t	m	Thickness of a soft soil layer underneath the embankment
tl	subscript	Top grid layer (subscript)
total	subscript	Entire reinforcement layer (i.e. two grid layers plus the granular layer between the grid layers) (subscript)
tri		*Tri*angular load distribution (see Figure 5.3a) (subscript)
uni		*Uni*form load distribution (see Figure 5.3b) (subscript)
W	%	Water content
W_n	kN/pile	Net load ($= W_s - C - R_b$)
W_s	kN/pile	Total surcharge load on a unit area $W_s = p \cdot s_x \cdot s_y$
w_s or p	kPa	Uniformly distributed surcharge on top of the fill (top load) $w_s = p$
W_T	kN/m	Equally-distributed vertical (line) load acting on the reinforcement strip between adjacent pile caps, BS8006 property (appendix A)
w_{tot}	kN/pile	Total load of traffic and soil weight in one $s \cdot s$ area, $s^2(\gamma H + p)$, BS8006 property (appendix A, where $s = s_y = s_y$)
X	-	Grouped variable (see equation (A.11))
XMD		Direction perpendicular to the machine direction of a GR
Z		Multi-scale arching model of Zaeske (2001)
z	m	Distance along the vertical axis as indicated in, for example, Figure 4.3.
z or $z(x)$	m	GR vertical deflection
ε *(or eps)*	-	GR strain (Chapter 2: if the GR strain was measured rather than calculated, it was measured with strain cables as described in Chapter 2.3.2)
$s\varepsilon$ *(or s eps)*		(In Chapter 2: GR strain measured with a traditional strain gauge as described in Chapter 2.3.2)
φ	deg	Internal friction angle
γ	kN/m^3	Fill unit weight
λ_1, λ_2, λ_3	-	Constants used by Zaeske (2001), see equation (3.2)
σ_r	kPa	Radial stress in a 2D arch
σ_R	kPa	Radial stress in a 3D hemisphere
σ'_v	kPa	Average vertical stress at the level of the bottom GR layer
$\sigma_{v;p}$	kPa	Vertical stress on pile (cap), see equation (3.1)
$\sigma_{v;r}$	kPa	Vertical stress on the GR between the pile caps
σ_θ	kPa	Tangential stress in 2D arch or 3D hemisphere
χ	-	Constant used by EBGEO, see equation (3.2)
ψ	deg	Dilation angle

| 600/50 | kN/m and kN/m | Indicates the strength of geosynthetic reinforcement layer. The first value (600 kN/m in this case) gives the characteristic short-term tensile strength in machine direction (MD) and the second value (50 kN/m in this case) gives the characteristic short-term tensile strength in the direction perpendicular to the machine direction (XMD). |

1 Introduction

Deltares experiments

1.1 Basal reinforced piled embankments: foundations for roads or railways on soft soil

A piled embankment consists of an embankment on a pile foundation. In a basal reinforced piled embankment, the embankment is reinforced at its base with a geosynthetic reinforcement (GR).

Figure 1.1 shows the components of the basal reinforced piled embankment. Before the installation of the piles, it is often necessary to install a working platform, for example a layer of sand. This layer is left below the GR and can cause settlement of the soft soil. The piles can be of any type and, in most cases, pile caps are installed on top of them to reduce the GR span.
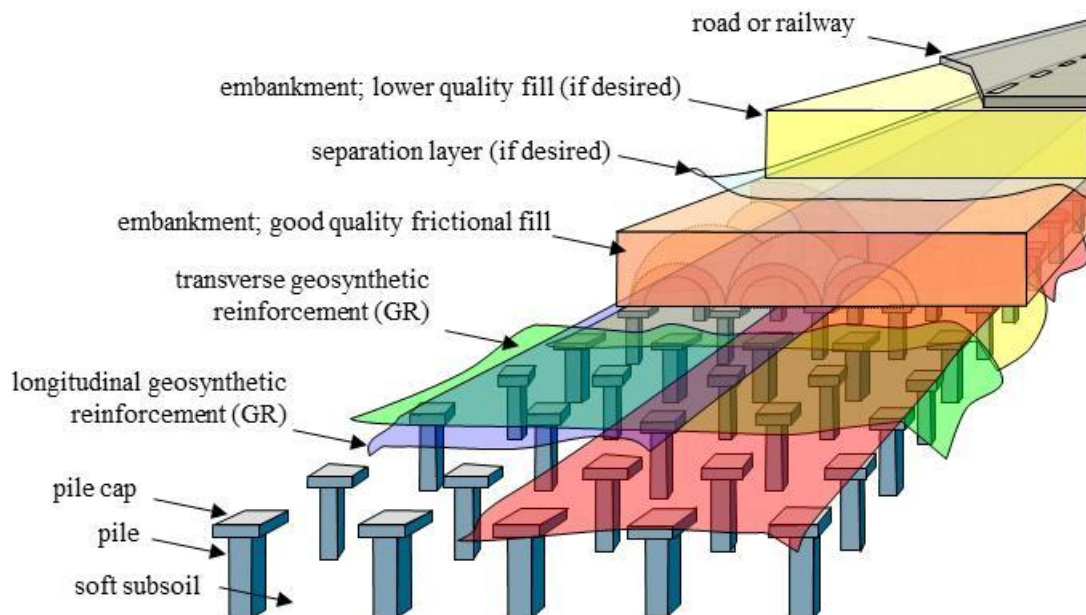
Figure 1.1 A basal reinforced piled embankment.

The GR is installed in one or more layers at the base of the fill. In many cases, uniaxial material is installed in both the transverse and the longitudinal directions. The overlap between two neighbouring layers should, in each case, be located above the pile caps. The lower part of the embankment (the 'mattress') must consist of a frictional material like angular sand or crushed aggregate (crushed rock or crushed recycled construction material). In many cases, the mattress consists of crushed aggregate, and the rest of the embankment consists of a lower-quality fill such as sand.

A geosynthetic separation layer can be applied between these two fill layers if desired. Figure 1.2 shows some examples of piled embankments under construction.

Figure 1.2 Basal reinforced piled embankments under construction. (*a*) Krimpenerwaard N210 (Ballast Nedam, Huesker, Fugro, Movares), (*b*) A-15 MAVA project, source: Royal TenCate, contractor: A-Lanes (*c*) Piled embankment for an abutment necessary for the widening of the A2 near Beesd, the Netherlands (Voorbij Funderingstechniek, Heijmans, CRUX Engineering, Huesker and Deltares), (*d*) Houten railway (Movares, de Bataafse Alliantie, (ProRail, Mobilis, CFE en KWS Infra), Huesker, Voorbij Funderingstechniek, CRUX Engineering and Deltares), (*e*) Krimpenerwaard N210 (Ballast Nedam, Huesker, Fugro, Movares), (*f*) Hamburg (Naue).

As can be seen in Figure 1.1, arching occurs in the embankment. This arching is the mechanism by which stiffer construction elements attract a large proportion of the load and this is the basis for the GR design. A major part of the load is transferred to the pile caps directly due to this arching. Another part of the load is transferred to the pile caps via tensile forces in the GR. The piles and their pile caps further transfer the load to the firm substratum, and there is therefore little or no load on the soft subsoil between the piles. Some settlement of the subsoil and deformation of the GR is necessary to develop the arching in the embankment.

Piled embankments are built for roads, railways, parking areas or industrial storage areas, usually in locations with soft soil. Building such constructions in soft soil areas is often problematic. Traditionally, a granular fill is placed directly on the soft subsoil, which needs a lot of time to consolidate and compact, and large residual or differential settlement or instabilities are a risk. Four types of solutions are in use to reduce construction time, settlement and risks:

- Acceleration of consolidation with the installation of vertical drainage, frequently in combination with a temporary surcharge load to reduce post-construction settlement.
- Replacement of the soft layers, which is only feasible when the soft soil layer is relatively thin.
- Using lightweight construction material such as expanded polystyrene foam.
- Leading the load directly to the firm substratum by using a pile foundation. A concrete slab, or an embankment with or without a basal reinforcement, can be positioned on top of the piles. An embankment is usually cheaper than a concrete slab, but a slab needs less height.

These techniques all have their own advantages and they are in widespread use. Traditionally, the first option has been used most widely. A piled embankment can be a useful option when this traditional construction method leads to problems, such as too much residual settlement given the available construction time and/or given the subsoil. The traditional approach would then require more frequent maintenance and it may be preferable or cheaper to avoid this.

Another potential reason to opt for a piled embankment is the presence of objects that are sensitive to horizontal ground movement such as sensitive foundations, existing roads, railways, tubes or pipes. Finally, piled embankments can be useful if the available construction time is limited: piled embankments can be built quickly because it is not necessary to wait for the consolidation of the soft subsoil.

In delta areas, the subsoil often consists of a thick layer of soft clay or peat. The undrained shear strength in these areas is typically 10 – 25 kPa or even less.

In many cases, the settlement of the subsoil due to the weight of the working platform below the GR will exceed the deformation of the GR. This leaves a gap between the mattress and the subsoil between the piles. This does not constitute a problem as long as it is taken into consideration in the design.

Piled embankments can be applied with or without GR. GR increases the arching mechanism, and helps to transfer part of the load to the piles. The presence of soft clay and peat layers indicates that GR is needed in the base of the embankment. This is, for example, the case in the Netherlands. In some other countries like France, by contrast, piled embankments are frequently built without GR. In these cases, the soil between the piles is usually sand, which is stiff enough to carry a major part of the load. Even then it may still be worth considering GR: it may reduce costs since the pile spacing can be increased.

Load distributions in piled embankments with or without basal reinforcement differ, as will be seen in this thesis. The design method should therefore be different as well. This thesis looks only at basal reinforced piled embankments, in other words piled embankments with GR in the base.

1.2 Design of a piled embankment

Several countries have issued design guidelines for basal reinforced piled embankments. Researchers (listed in Chapters 3 and 4) are still working on improvements to analytical design methods. Europe alone already has six different guidelines: the Dutch CUR 226 (2010, updated in 2015), the German EBGEO (2010), the British Standard BS8006 (1995, updated in 2010), the Finnish Liikennevirasto (2012), the Nordic Guidelines of Reinforced Soils and Fills (2004) and the French ASIRI (2012).

These guidelines usually state geometry requirements such as the minimum embankment height or the minimum pile cap size in relation to the pile spacing and they also give requirements for the fill properties. The pile diameter, pile length and the size and reinforcement of the pile caps have to be designed in accordance with local geotechnical standards and these design regulations are not given in the guidelines listed above.

The design code and guidelines mentioned relate mostly to the GR design, which needs to be done analytically. Numerical methods are used widely to determine deformations and pile bending moments but they are generally not allowed in GR design since these methods tend to underpredict the GR strain, as shown by for example Farag (2008). This seems to be specifically the case for situations with

subsoil support of the kind discussed by Van der Peet and Van Eekelen (2014). The design guidelines and this thesis therefore focus on analytical GR design models.

All analytical design models calculate the tensile strain in the GR. Multiplying this strain by the GR stiffness gives the GR tensile force (kN/m). The long-term tensile strength of the GR needs to be higher than this tensile force. The calculation of the GR strain includes two calculation steps, as illustrated in Figure 1.3.
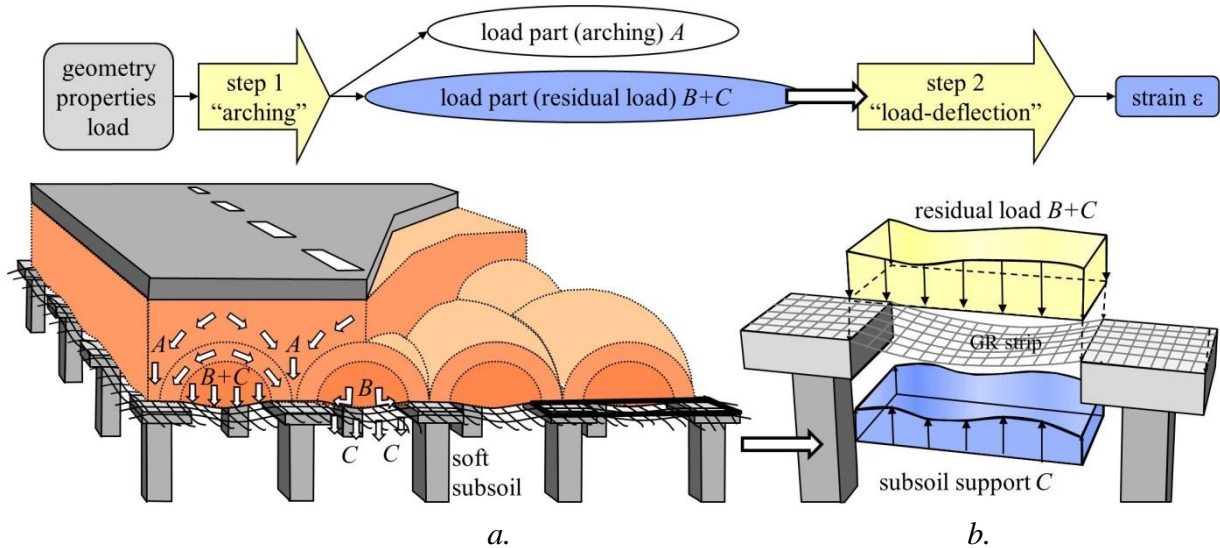
Figure 1.3 Calculating the geosynthetic reinforcement (GR) strain comprises two calculation steps.

Calculation step 1 divides the total vertical load into two parts: load part *A* and the 'residual load' (*B+C* in Figure 1.3*a*). Load part *A*, which is also referred to as 'arching *A*' in this thesis, is the part of the load that is transferred to the piles directly. The value of *A* is dependent on the arching behaviour in the fill. Chapter 4 considers the arching behaviour and the existing analytical arching models for step 1 and proposes a new analytical arching model: the Concentric Arches model.

Calculation step 2 calculates the GR strain from the residual load *B+C*, which was calculated in step 1. This calculation step considers the load-deflection behaviour of the GR strips between each pair of adjacent piles. These GR strips are loaded by *B+C* and may or may not be supported by springs that simulate subsoil support (Figure 1.3*b*). Analysis leads to differential equations which can be solved to calculate the GR strain.

The purpose of step 2 is to calculate the GR strain, but the second calculation step also results in a further division of the vertical load into load part *B*, that passes through the GR to the piles, and load part *C,* which is the subsoil support, as indicated in Figure 1.3*a*. Considering *B* and *C* separately is useful for the

validation of design models but, for design purposes, only the calculated GR strain is of importance.

Chapter 3 of this thesis considers calculation step 2 and proposes a new distribution for the residual load $B+C$ on the GR strip. Chapter 5 extends the step 2 model proposed in Chapter 3 to make it more generally applicable.

To validate calculation steps 1 and 2 separately, arching A needs to be measured. This had, somewhat surprisingly, never been done before and the decision to conduct these measurements in the course of this research therefore represented a major step forward.

Most analytical calculation methods account for the traffic load by introducing a vertical, uniformly distributed surcharge load. CUR (2015) gives a guideline for determining this design load on the basis of standard truck passages. This conversion from truck axle load to uniformly distributed surcharge load, as well as the influence of cyclic loading and lateral loading, are outside the scope of this thesis.

Several methods for the GR design are available, all with their own models for calculation steps 1 and 2. The methods give results that differ immensely. The Dutch CUR226 (2010) and the German EBGEO (2010) adopted Zaeske's method (2001). Measurements that were published later in, for example, Van Duijnen et al. (2010), Van Eekelen et al. (2015a), showed that this method, as well as other methods adopted in the European guidelines mentioned, could be calculating much higher GR strains than those measured in practice, leading to heavier and more expensive designs than necessary. The research presented in this thesis began in response to this shortcoming.

1.3   Scope, objective and research question of this thesis

The research focused on the two calculation steps that analytically determine the GR strain that results from the dead embankment weight and traffic weight in a basal reinforced piled embankment.

The objective was to further our understanding of the load distribution in a basal reinforced piled embankment and, on that basis, to develop and validate an analytical design model for geosynthetic reinforcement in a piled embankment. However, a radical departure from existing European design models was felt to be undesirable.

The main research question for this research was: how can we predict the GR strains in a basal reinforced piled embankment? The research questions are:
- How is the vertical load distributed on the basal reinforcement of a piled embankment?
- How can this load distribution be explained and how can it be described with an analytical arching model?
- Which design method fits best with observations and measured arching *A* and GR strains in field monitoring projects and experiments?

1.4   Activities undertaken

Two series of a total of nineteen 3D scaled model experiments were conducted in the Deltares laboratory (Chapter 2 and Chapter 4.2). These experiments guided the thinking that led to the new analytical design model (Chapters 3, 4 and 5.5).

The theory was implemented in three field studies in the Netherlands: the trial "Kyoto Road" project in Giessenburg, (presented in Appendix A), a railway in Houten (Chapters 4.5, 5.3.4 and 5.4.4) and a motorway exit in Woerden (Chapters 4.5, 5.3.3 and 5.4.3). The existing and newly proposed analytical design models were validated with measurements in eleven field studies and model test series (Chapter 5).

Two Master's students numerically validated the newly proposed analytical model, using the finite element method (FEM), which was reported in Den Boogert (2011), Den Boogert et al. (2012a and b), Van der Peet (2014) and Van der Peet and Van Eekelen (2014).

1.5   Thesis outline

Chapter 2 (Van Eekelen et al., 2012a) describes the first series of model experiments undertaken in the Deltares laboratory. The experiments show how arching depends on several features and how the GR deforms. The net load distribution on the GR can be derived from the results of these experiments. On the basis of the experiments, it is concluded that the load on the GR is concentrated on the strips between each pair of adjacent piles and that the load is larger at locations closer to the pile caps. The net load distribution on these GR strips is an approximate inverse triangle.

Chapter 3 (Van Eekelen et al., 2012b) considers calculation step 2. The chapter analyses the results of the experiments and introduces an analytical model for step 2, the load-deflection behaviour. The newly presented model includes the inverse-triangular load distribution and a new subsoil support model.

Chapter 4 (Van Eekelen et al., 2013) focuses on calculation step 1. The chapter presents the second series of model experiments, discusses the results from these experiments and from other research projects presented in the literature, looks at existing analytical arching models and introduces a new model for arching: the Concentric Arches model. This model provides an explanation for the findings in Chapters 2 and 3.

Chapter 5 (Van Eekelen et al., 2015a) presents GR strains measured in seven field monitoring projects and four series of experiments. Eight of these eleven projects were taken from the literature. The chapter shows that the newly presented analytical models give GR strains that match the measured GR strains much better than the values resulting from the existing models.

Chapter 6 discusses the results and Chapter 7 presents conclusions and recommendations.

Finally, Appendix A (Van Eekelen et al., 2011a) describes the basics of piled embankment design. The appendix analyses the design model adopted in BS8006 (2010) and proposes an improvement to that model. A field study, the Kyoto Road, was undertaken and the measurements were compared with both versions of the BS8006 model.

Chapters 2, 3, 4, 5 and appendix A have been published previously in the international journal *Geotextiles and Geomembranes* and so these chapters can be read separately. Accordingly, some explanations appear more than once. Minor changes were made in the text to correct small mistakes in the equations or language. Some footnotes have been added to clarify differences in notation and the relationship between the papers.

Chapter 4.4.5 gives the equations for the new step 1 model and Appendix 5.A gives the equations for step 2. Appendix 4.B gives calculation examples for both calculation steps.

2 Model Experiments on Piled Embankments

Deltares experiments

Abstract

A series of twelve 3D laboratory model tests was performed on piled embankments. In this first part of a two-part study, the measured load distribution, deformation, and strains are presented and analysed. In the second part (Chapter 3), the measurements are compared with calculations using EBGEO (2010), and suggestions are given for improvements to the calculation model.

In the test series, the vertical load parts on the piles, on the geosynthetic reinforcement (GR), and on the subsoil could be measured separately. This makes it possible to compare the test results with the separate parts of the analytical models. For the test conditions (static load, laboratory scale), smooth relationships were obtained between the net load on the fill (top load on fill minus subsoil support) and several measured parameters, such as load distribution and deformation. Consolidation of the subsoil resulted in an increase of the load transferred through the GR, and also an increase of arching. The measured response to consolidation depends on the fill's friction angle. A higher friction angle gives more arching during consolidation.

Loading on the geosynthetic reinforcement is concentrated on the strips lying above and between adjacent piles (the "GR strips"). The line load on a GR strip has the distribution of an inverse triangle, although the load may be even more concentrated around the pile caps than this indicates. This follows from the measured shape of the deformed GR.

A geogrid gives negligible differences in comparison with a geotextile. No difference is found between the use of a single biaxial grid layer and two uniaxial grid layers positioned directly on top of each other. Only limited differences were found between a situation with one grid layer, and one where two grid layers were used with a granular material in between.

2.1 Introduction

In 2010, new or updated design guidelines for piled embankments were published in the Netherlands, Germany, and the United Kingdom (respectively CUR226 (2010, in Dutch), described in English in Van Eekelen et al., (2010b); EBGEO (2010); and BS8006-1 (2010)). In the Netherlands, this was the first result of an ongoing research and development programme, which includes laboratory and field tests aimed at improving understanding of the arching mechanism, investigating the factors of influence, and further optimisation of the Dutch CUR Design Guideline.

This paper presents and analyses the results of a series of laboratory model tests. Several researchers have carried out experimental research on piled embankments in the past. As with most of the earlier research, this paper focuses on a situation with a vertical load only i.e. without a slope that results in horizontal loads.

The majority of researchers used a fill of dry or moist sand, except for Horgan and Sarsby (2002) who applied an additional 10 mm gravel in their 'trap door' tests. Jenck et al. (2009) used a mix of steel rods measuring 3, 4 and 5 mm in diameter and 60 mm in length. The model is therefore two-dimensional. However, a granular fill must be used to model the three-dimensional interaction between a geogrid and granular material.

Several researchers simply took away subsoil support during the test, either via a 'trap door' (Horgan and Sarsby, 2002) or by removal (Le Hello, 2007). Most others forced compression of the subsoil by applying peat (Zaeske, 2001; Heitz, 2006; and later Farag, 2008), rubber foam (the 2D tests of Jenck et al., 2009, Low et al, 1994 and Van Eekelen et al., 2003), or rubber foam chips (Hewlett and Randolph, 1988). Ellis and Aslam (2009a and 2009b) varied the stiffness of the subsoil by applying two grades of EPS in their centrifuge tests. Chen et al. (2008) modelled the consolidation of the subsoil in their 2D tests by permitting water to flow out gradually from water bags. No researchers chose to control and measure the subsoil support, and only a few (such as Zaeske, 2001, Heitz, 2006, Le Hello, 2007 and Chen et al., 2008) included geosynthetic reinforcement (GR).

Many researchers observed arching through a glass wall (such as Hewlett and Randolph, 1988; Low et al., 1994; Chen et al, 2008, Jenck et al., 2009; and Ellis and Aslam, 2009a and 2009b), and some measured vertical deflection. The strains of the geosynthetic reinforcement were usually not measured, with the exception of Zaeske (2001) and Heitz (2006). The forces on or below the piles were often measured (Low et al., 1994; Zaeske, 2001; Heitz, 2006; Farag, 2008; Chen et al., 2008a and Ellis and Aslam, 2009a and 2009b), and sometimes the pressures within the fill (Zaeske, 2001; and Heitz, 2006). All researchers found arching. Some proved that the arch was virtually resistant to some cyclic load if sufficient reinforcement was used (for example Hewlett & Randolph, 1988, and Heitz, 2006).

The distribution of the load over the subsoil, the reinforcement, and the piles was not measured separately in the tests mentioned above. In the test series described in this paper, these load parts could be measured separately. This made it possible to compare the measurement results with the separate parts of the analytical models, as presented in the second part of this study (Van Eekelen et al., 2012b, see Chapter 3 of this thesis). The two main questions are: (1) how is the load

distribution influenced by an increase in top load, and by subsoil support and subsoil consolidation? (2) how do certain factors, such as fill material or reinforcement type, influence this load distribution? To answer these questions, it must be possible to control the subsoil support and to use realistic granular material in combination with several types of geosynthetics.

This paper describes a series of 12 model tests that were performed on piled embankments. The tests are similar to those reported by Zaeske (2001) and Heitz (2006), which form the basis of the German standard, EBGEO. This set-up was chosen because the size of Zaeske's 3D test set-up was suitable for carrying out several tests.

The measured load distribution, deformation, and GR strains were presented and analysed in this first part of a two-part study. The results are used to discuss several influencing factors, such as the properties or specifications of the fill, subsoil, or reinforcement.

The second paper in this study compares these measurements with analytical calculations using EBGEO (2010). Possible improvements to the analytical model are also suggested. The results are used to discuss several influencing factors.

2.2   Definition of load distribution

The vertical load (traffic weight, road and fill weight) is distributed into three load parts *A*, *B* and *C* (shown in Figure 2.1). These are defined as follows: part *A* ('arching' or 'arching load part') is transferred directly to the piles, part *B* goes through the GR to the piles, and part *C* ('subsoil') is carried by the soft subsoil. This paper gives load parts *A*, *B* and *C* in kN/pile. Note that *A*, *B* and *C* are vertical loads.
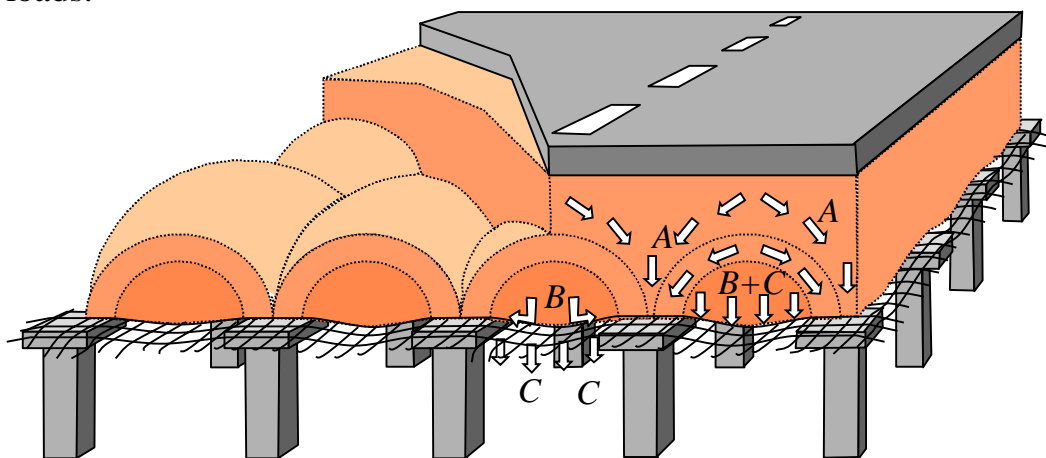
Figure 2.1 Load distribution in piled embankments. Distribution of the vertical load is in three parts: *A* (arching) directly to the piles; *B* via the GR to the piles; *C* (subsoil) to the soft subsoil between the piles.

2.3 Test set-up and testing programme

2.3.1 Test set-up

The tests were conducted using the test set-up shown in Figure 2.2. A steel plate supports a cushion that models the soft soil (hereafter called 'subsoil') around the piles. This cushion is a watertight, soaked foam rubber cushion (hereafter called 'foam cushion'). A tap allows drainage of the cushion during the test, which models the consolidation process of the soft soil.
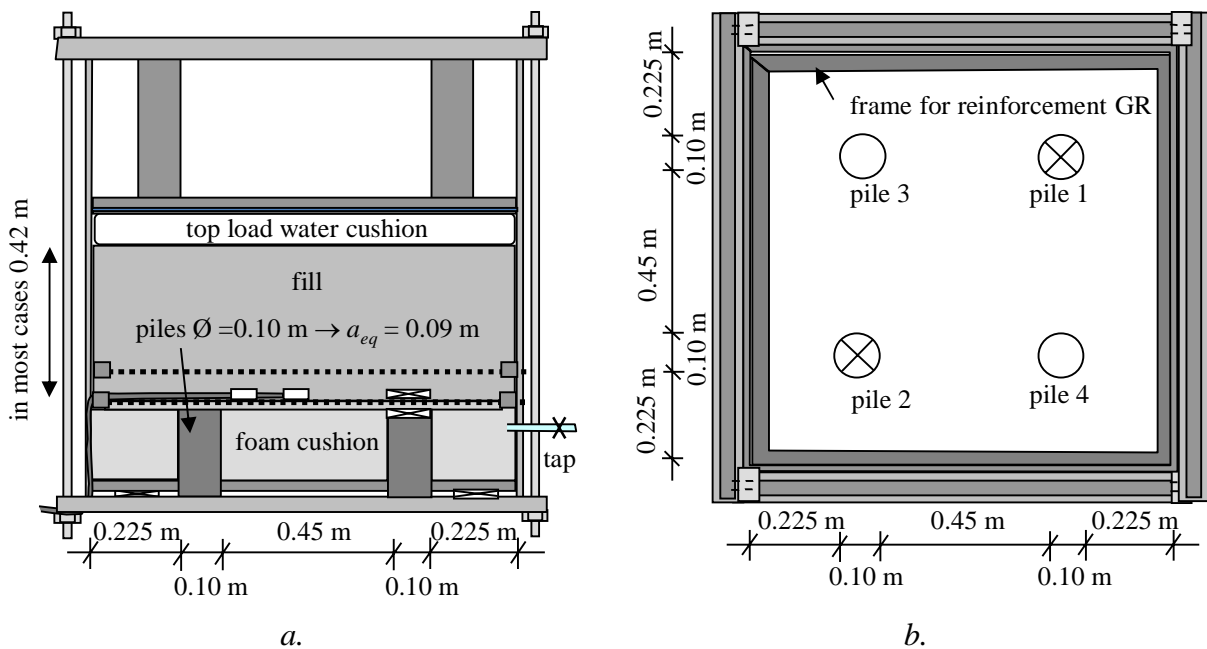
Figure 2.2 Side view and top view of test set-up.

The four 'piles' extend through the steel plate and rest on the bottom of the box. A sand layer measuring between 0.015 and 0.02 m is placed on top of the foam cushion and the piles. One or two stiff steel frames are placed on top of this, to which the geosynthetic reinforcement (GR) is attached. If two steel frames with GR are used, 0.05 or 0.10 m of granular material is placed in between. The embankment is a 0.42-m-layer of sand or granular fill. The top load is applied by means of a water cushion. This provides an equally-distributed top load, even when the ground level deforms. The applied top load represents both the traffic load and the weight of the top layer of the embankment. A rubber sheet combined with Vaseline or Shell Retinax A minimises the friction between the fill, the box walls, the foam cushion and the piles.

The tests reported in this paper are similar to those of the Kempfert group, as reported by Zaeske (2001) and Heitz (2006) for example. In the test series reported

here, however, the fill was granular material instead of sand, the subsoil support was controlled by means of the foam cushion, and the load distribution was measured differently. This allowed the influence of subsoil loading on the load parameters A and B to be tested. Another difference was that load parts A, B and C could be measured separately.

2.3.2   Measurements

The general measurement set-up is presented in Figure 2.3, although the number of transducers and their exact location differ for each test. In addition to what is shown in Figure 2.3, the pressure in both cushions, and the amount of water drained from the foam cushion are also measured.

Load parts A and B were measured using total pressure cells with a diameter equal to the pile diameter of 0.1 m. In all tests, two total pressure cells measured $A + B$. They were located below the reinforcement, on top of the piles.
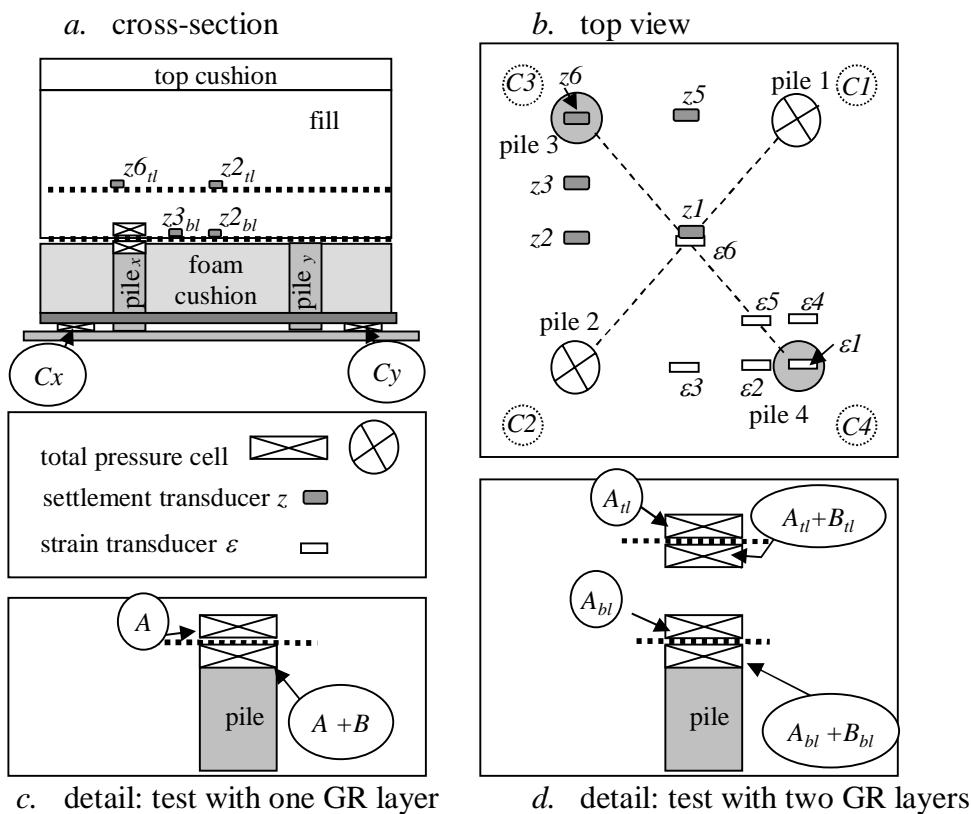
Figure 2.3 Nomenclature of measurements: '*tl*' indicates 'top grid layer', and '*bl*' indicates 'bottom grid layer'.

For measuring load part *B*, two types of tests are distinguished: tests with only one reinforcement layer in one frame (hereafter called 'single-layered tests'), and tests with two reinforcement layers in two frames (hereafter called 'double-layered tests').

In the single-layered tests (see Figure 2.3c), load part *A* was measured by total pressure cells positioned above a pile and on top of the GR. Load part *B* was found by subtraction i.e. $B = (A+B) - A$. Where loads were measured at two locations, the average is given in the results.

In the double-layered tests (see Figure 2.3d), two total pressure cells below the bottom GR layer measured load parts A_{bl} and B_{bl} together. The locations of some additional pressure cells varied between the positions given in Figure 2.3. Three types of 'load part *B*' were distinguished: $B_{total} = (A_{bl}+B_{bl}) - A_{tl}$, $B_{bl} = (A_{bl}+B_{bl}) - A_{bl}$ and $B_{tl} = (A_{tl}+B_{tl}) - A_{tl}$. Load part *C* was determined by measuring the pressure in the foam cushion.
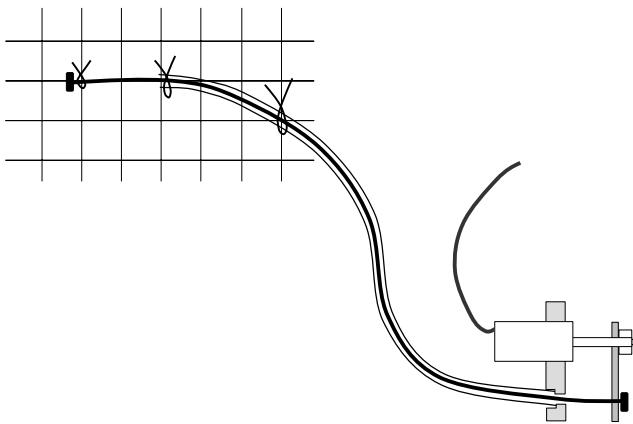
Figure 2.4 Gear cable to measure GR strains.

Vertical deflection of the reinforcement was measured using a liquid levelling system.

One type of grid (used in tests N1, N2 and N3) was suitable for the adherence of traditional strain gauges due to its flat and monolithic bars. They gave convincing results up to approximately 4% GR strain. By applying the strain gauges on the bottom as well as on top of the bars, bending normalised total medium strain could be measured. In the other tests, strains within the geosynthetic were measured using bicycle gear cables, hereafter called 'strain cables' (shown in Figure 2.4).

In most tests, six strain cables were attached to the reinforcement with tie-ribs. Displacement transducers registered the difference between displacement of the inner cable and the outer tube.

Table 2.1 Specification of the twelve tests.

Test		Geosynthetic reinforcement (GR)				Fill			Load
sequence of tests	test code	GR	height fill between 2 GR layers	material GR	stiffness GR $J_{2\%}$ [a,b] (direction 1 / direction 2)	fill 0.42 m	fill unit weight	internal friction angle (φ_{peak})	increasing top load (kPa). After each top load increase, drainage of the foam cushion follows in one or more steps of usually 6 litres
			m		kN/m		kN/m³	deg	kPa and kN/pile
1	N1	2 laid grids biaxial	0.05	PET	2090	granular	15.74	49	0-10-25-50 kPa (0-3.1-7.7-15.1 kN/pile)
2	N2	1 laid grid biaxial		PET	1045	granular	17.24	49	0-10-25-50-75 kPa (0-3.1-7.7-15.1-22.7 kN/pile)
12	N3	2 laid grids biaxial	0.087	PET	2090	granular	16.16	49	0-25-50-75-100 kPa (0-7.6-15.1-22.7-30.1 kN/pile)
3	T1	1 woven geotextile		PP	670	sand	16.24	40.33	0-10-25-50 kPa (0-3.1-7.7-15.1 kN/pile)
5	T2	1 woven geotextile		PP	970/1810[c]	sand	16.55	40.90	0-25-50-75 kPa (0-7.6-15.1-22.7 kN/pile)
7	T3	1 woven geotextile		PP	970/1810[c]	granular	16.70	49	0-25-50-75 kPa (0-7.6-15.1-22.7kN/pile)
9	T4	1 knitted grid biaxial		PET	1715/1742	granular	15.19	49	0-25-50-75-100 kPa (0-7.6-15.1-22.7-30.2 kN/pile)
4	K1	1 woven grid biaxial		PVA	2399/2904	granular	16.70	49	0-25-50-75-100 kPa (0-7.6-15.1-22.7-30.2 kN/pile)
6	K2	2 woven grids uniaxial[d]	0.00	PVA	2269	granular	16.59	49	0-25-50-75-100 kPa (0-7.6-15.1-22.7-30.2 kN/pile)
10	K3	2 woven grids uniaxial	0.05	PVA	2269	granular	16.60	49	0-25-50-75-100 kPa (0-7.6-15.1-22.7-30.2 kN/pile)
8	S1	2 extruded grids	0.10	PP	757	granular	16.75	49	0-25-50-75-100 kPa (0-7.6-15.1-22.7-30.2 kN/pile)
11	S2	2 extruded grids	0.10	PP	757	granular	16.15	49	0-25-50-75-100 kPa (0-7.6-15.1-22.7-30.2 kN/pile)

[a] The total stiffness of the reinforcement is given. If more layers of reinforcement are applied, the stiffness values are summed.

[b] The stiffness of geosynthetic reinforcement is dependent on the GR strain and the duration of loading, as well as other factors. The $J_{2\%}$ given in this table is for a GR strain of 2%, and is determined in accordance with CEN ISO 10319. These ISO tests are much faster than the piled embankment model tests. This means that the GR in the model tests is loaded longer and will behave differently (less stiff) from the behaviour suggested by this $J_{2\%}$.

[c] This material is completely biaxial for larger strains.

[d] Two uniaxial geogrids are placed directly upon each other on one frame. The strength direction of one geogrid is perpendicular to the other. There is no distance between these two geogrids, and they are therefore considered as a single GR layer that is completely biaxial.

Results appeared to depend on fixation of the outer gear cable over the whole of the GR and pre-stress in the cable. The results from the strain cables were consistent, but were too high in the first tests. In addition, GR strains measured locally were strongly dependent on the exact location of the strain cable or strain gauge. For both these reasons, the results of the strain cables were only considered qualitatively throughout the tests. Most 'measured GR strains' presented in this paper were calculated using the measured deflection of the GR, as described in Chapter 2.4.3.

2.3.3 Testing programme and materials

Table 2.1 lists the tests that were conducted and specifies the GR used in each test. This paper focuses on the results from some of these tests. Two tests, namely T1 and T2, were carried out with a fill of Itterbeck sand (125-250 µm). The peak friction angle is determined using a triaxial test. For the densities in T1 and T2, the peak friction angle φ_{peak} is respectively 40.3° and 40.9°.

The other tests were carried out using a well-graded granular material (crushed recycled construction material, 0 – 16.5 mm). The average unit weight is 16.38 kN/m^3 (see Table 2.1). Den Boogert (2011) carried out displacement-controlled (2 mm/min) triaxial tests on three 300 mm · 600 mm samples (diameter · height). The unit weight of the samples was respectively 16.48, 16.47 and 16.36 kN/m^3, which is in the same range as the unit weight of models in the piled embankment tests. A vacuum pressure of respectively 16 kPa, 55 kPa and 90 kPa was applied as the confining pressure. Radial and axial displacements were measured at 1/3 and 2/3 of the sample height. Den Boogert determined the stiffness and strength parameters from the triaxial test results in accordance with BS1377 (1990). A peak friction angle φ_{peak} of 49.0° and a dilation angle of 9.0° were found. The friction angle of the granular fill is approximately 8.5 degrees higher than the friction angle of the sand.

2.3.4 Test procedure, definition of net load

After the fill was in place, the following steps were carried out in each test: (1) drainage of the foam cushion (modelling subsoil consolidation); (2) the first increase in top load, see Table 2.1; (3) one or more subsequent drainage steps; (4) second top load increase; (5) one or more drainage steps; (6) third top load increase; (7) one or more drainage steps; continuing until the maximum top load had been reached and the subsequent drainage steps were completed.

In some tests, vacuum pressure was then applied to the foam cushion below the GR to suck it away from the GR, until the resulting load part *C* had been reduced to zero. The test procedure represents a stepwise increase in load, and subsequent consolidation of the subsoil underneath the piled embankment. After each drainage step or top load increase, the system was allowed to stabilise for several hours or sometimes throughout the night, until the measurements became stable. This was necessary so that the foam cushion had time to consolidate.

Many results will be presented as a function of the net load W_n. Net load is defined as follows:

$$W_n = W_s - C - R \tag{2.1}$$

where W_n is the net load in kN/pile, W_s is the surcharge on top of the fill (top load) in kN/pile, *C* is the subsoil support (kN/pile), and *R* is the total friction between fill and box walls, and between foam cushion and box walls and piles. *R* is measured as follows:

$$R = 0.25 A_{fill} \left(\gamma H + w_s \right) - \left(A + B + C \right) \tag{2.2}$$

where A_{fill} is the area of the fill = $(1.1)^2$ m^2, γ is the fill unit weight in kN/m^3, *H* is the height of the fill above the bottom layer of the GR in m, w_s is the surcharge on top of the fill in kPa, and *A*, *B* and *C* in kN/pile are explained in Chapter 2.2. The embankment pressure is the only factor that drives drainage of the foam cushion, except in the last vacuum step. Six litres were drained from the foam cushion during most of the drainage steps.

2.3.5 Limitations

The research programme has the following limitations:
(1) The test set-up aims to investigate the distribution of vertical loads within a reinforced embankment supported by stiff elements. Horizontal loads, for example spreading forces, are outside the scope of this research. (2) Dynamic effects fall beyond the scope of this research. (3) Each test is carried out within a time-frame of one week. The consolidation process is accelerated in the test series. Other time-dependent effects, such as creep, differ from those seen in the field. These effects are not taken into account in this study. (4) The results and conclusions of this test series are therefore only applicable for this type of geometry and a relatively thin embankment.

The stresses in the model tests presented are not scaled, but are the same as in the prototype. Consequently, the shear modulus of the fill in the model is the same as in the prototype. This approach was chosen to avoid complications due to stress-dependent behaviour of the fill. This is possible because the weight of the fill is negligible in comparison with the applied surcharge load. This means that length (m), stiffness (kN/m) and tensile strength (kN/m) are scaled down by $1 : x$, and area (m^2) and force (kN) are scaled down by $1 : x^2$. When compared to Dutch piled embankments, the model tests are on a scale between 1:1.6 and 1:4.5. However, it should be noted that it is not necessary to use these scaling rules when comparing the results of the model tests with the results of calculations. If the calculation model is correct, it is expected to work for both prototype and model dimensions.

2.4   Typical results

This chapter presents typical results of the test series, mainly illustrated using the results from a representative test with a single reinforcement layer, namely test K2. Following on from the general conclusions given in this chapter, Chapter 2.5 discusses several factors that influence the behaviour of the reinforced piled embankment using results from the other tests.

2.4.1   Arching

Figure 2.5 shows the measured load distribution of test K2. Figure 2.6 shows the corresponding measured vertical deflection of the GR. It appears that the measured load parts *A* and *B*, both in kN/pile as well as GR vertical deflection, follow a smoothly ascending curve when plotted against net load W_n.

Le Hello (2007) constructed a relatively thin fill before completely removing the subsoil, then increasing the fill height by 50%. The central graph in Figure 2.6 is based on Figure 3.6 in his thesis. It shows a comparable 'smooth' increase of vertical deflection, confirming the findings in Figure 2.5 and Figure 2.6.
An important finding is that measurements plotted against the net load W_n give meaningful results. This means that the surcharge load on the fill (for the stresses used) is not important, but that it is the net load on the fill and the GR that determines its behaviour. This is different from results obtained using calculation models, as will be discussed in Van Eekelen et al., 2012b, see Chapter 3 of this thesis.
Figure 2.5 also shows the parameters *A* and *B* as a percentage of the total measured load (*A*% and *B*%). The two types of loading can now easily be distinguished: (1) top load increase and (2) consolidation of the subsoil.
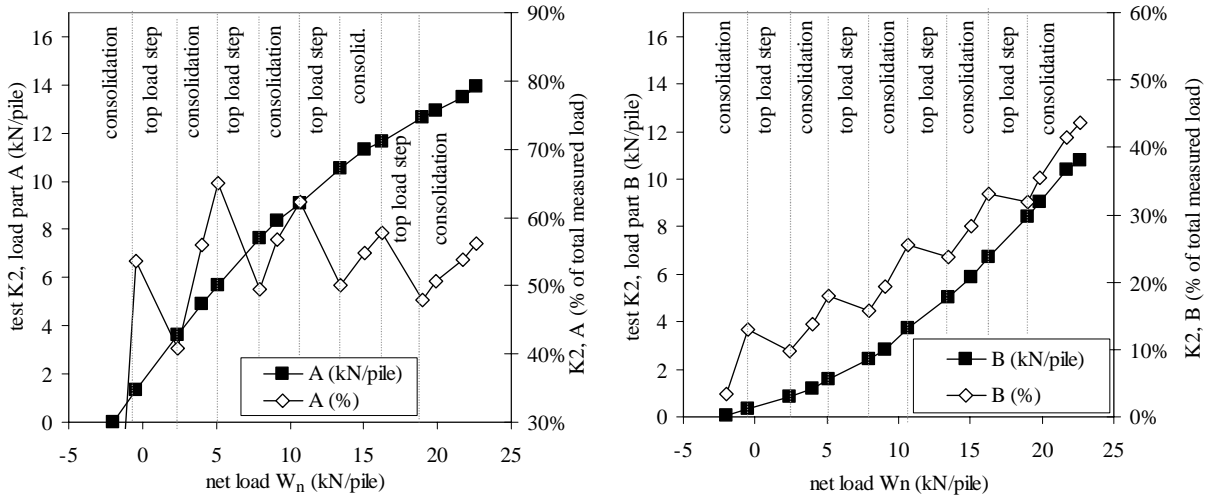
Figure 2.5 Measured load distribution in a representative test (K2), both in kN/pile and as % of total measured load *A+B+C*.
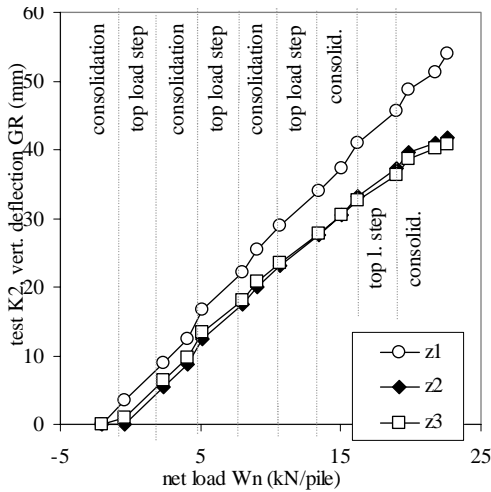
a.
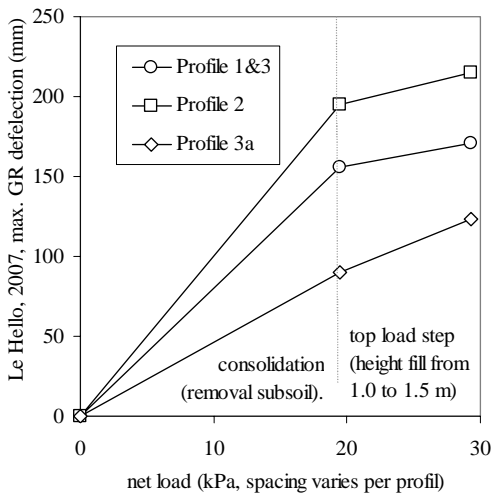
b.
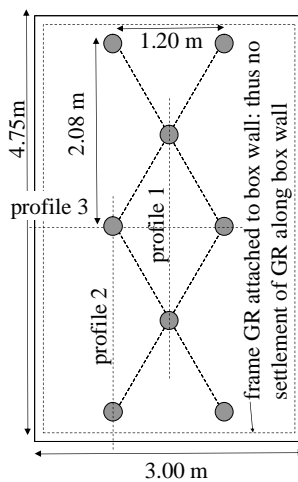
c.

Figure 2.6 (*a*) Measured GR vertical deflection (*z1, z2, z3* see Figure 2.3), representative test (K2). (*b*) and (*c*) measurements of Le Hello (2007).

Each top load increase results in an increase in the *A* and *B* (and *C*) parameters in kN/pile. However, load part *A*% decreases when considered as a percentage of the total load. Load part *B*% also decreases as a result of a top load increase, but this decrease is very limited.

The consolidation steps result in an increasing *B*%, as well as an increase in *A*%. The arch thus improves as a result of consolidation, although this improvement is lower for higher top loads. This means that the decrease of load part *C* (subsoil) during consolidation is divided between load parts *A* and *B* (the division is equal in this test). This is not in agreement with EBGEO (2010), but in agreement with – for example – the results of the model of Deb (2010).
Each consolidation period results in an *A*% that is lower than the value at the end of the previous consolidation period. As the top load increases, the *A*% therefore decreases for consolidated subsoil conditions. The values of the *A*% measured immediately after and just before a consolidation period become closer. It is possible that these two extremes will eventually become nearly identical for higher top loads. The *B*%, measured as the top load increases, rises for consolidated subsoil conditions.

Each test starts with one consolidation step. The top load remains zero during this step, so the only loading is the weight of the granular fill. Even during this first consolidation step, arching is found immediately, as shown by the relatively high initial *A* value of 53.5% seen in Figure 2.5.

2.4.2   *Localisation of GR strain*

Figure 2.7 and Figure 2.8 show the GR strains measured in tests K2 and N2 respectively. The GR strains are measured along the longest side of each strain gauge as shown in the figures. The GR strains shown by the strain cables in the K2 test in Figure 2.7 are too high, as described in Chapter 2.3.2. The measured strain pattern in both tests is consistent, and is similar throughout all tests.

Both figures show that the GR strains localise in the tensile strips between and above the piles. The highest GR strains occur on top of the piles ($\varepsilon 1$ and $s\varepsilon 1$).
Zaeske (2001) measured similar localisation of GR strains in the tensile strips. Jones et al. (2010) and Halvordson et al (2010) found the same with their 3D calculations. Zaeske (2001) also found that the maximum strains were on top of the piles. Den Boogert (2011) came to the same conclusion, based on the finite element simulations using Plaxis 3D Tunnel in the test series presented in this paper. However, measurements from the regional road N210 (Haring et al., 2008) and HafenCity Hamburg (Weihrauch et al, 2010) show smaller GR strains above the pile caps than in the surrounding tensile strips. One difference is that smooth

piles with a relatively small diameter were used in the model tests presented here, as well as in the model tests of Zaeske. Along the N210, however, square prefab concrete pile caps were used measuring $0.75 \cdot 0.75$ m^2 and in Hamburg, cast-in-place concrete caps were used measuring 0.6 m in diameter. As a result, the size of the pile caps and friction between GR and the pile cap causes the GR to be clamped in place, so that smaller GR strains occur above the centre of the pile cap. Jones et al. (2010) and Halvordson et al (2010) found a spike in GR strain at the pile-cap edge with their 3D calculations. The GR strains on top of their piles were not much larger than the GR strains in the rest of the GR strips. It is possible that the GR is clamped in place in their calculations.
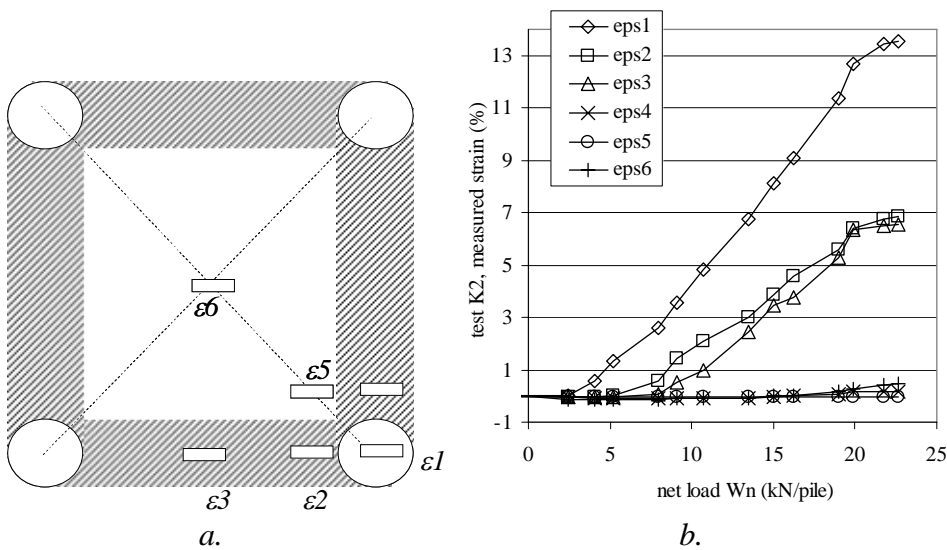
Figure 2.7 (*a*) strain cables ε (gear cables) in K2, the arched areas are parts of the GR that act as tensile strips, (*b*) measured GR strains in K2.
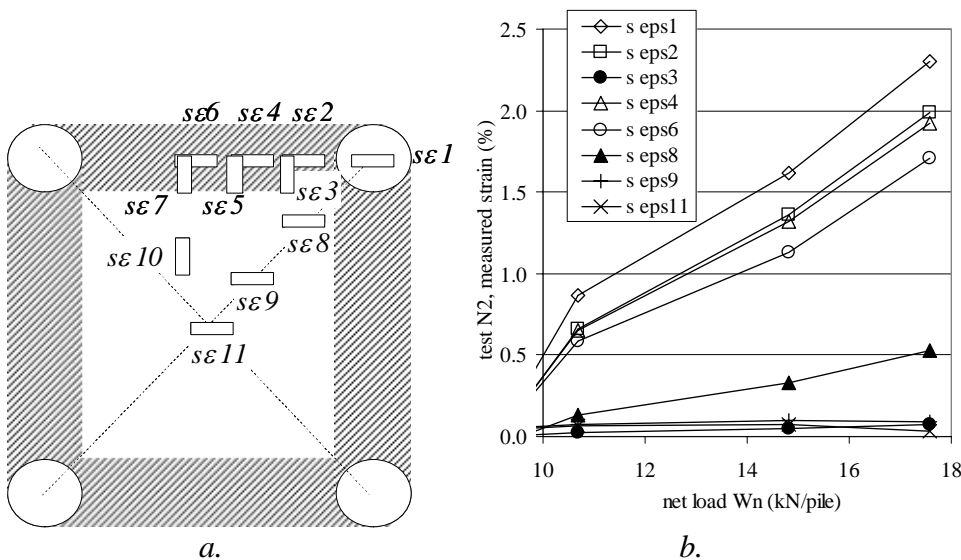
Figure 2.8 (*a*) strain gauges $s\varepsilon$ in N2, (*b*) measured GR strains in N2

2.4.3   Distribution of the vertical line load on the GR tensile strips

A relationship can be found between the deformation pattern of the GR tensile strip and the distribution of the load on that strip. This is considered in Figure 2.9. Three load distributions are compared: (Δ) the triangular load, which is used in EBGEO; (□) the equally-distributed load, which is used in BS8006-1, as described in Van Eekelen et al. (2011a); and (x) the inverse triangular load. The diagram shows that an equally-distributed load gives a parabolic deformation pattern (ax^2). The inverse triangular load gives a third order power law function (ax^3). Both follow analytically from solving the cable equation:

$$\frac{d^2w}{dx^2} = -\frac{q(x)}{T_H}$$
(2.3)

where z is vertical deflection of the GR in m, q is the vertical load on the GR, and T_H is the horizontal component of the tensile force in the GR. This is presented in more detail in Van Eekelen et al., 2012b, adopted in Chapter 3 of this thesis.

a.   *b.*
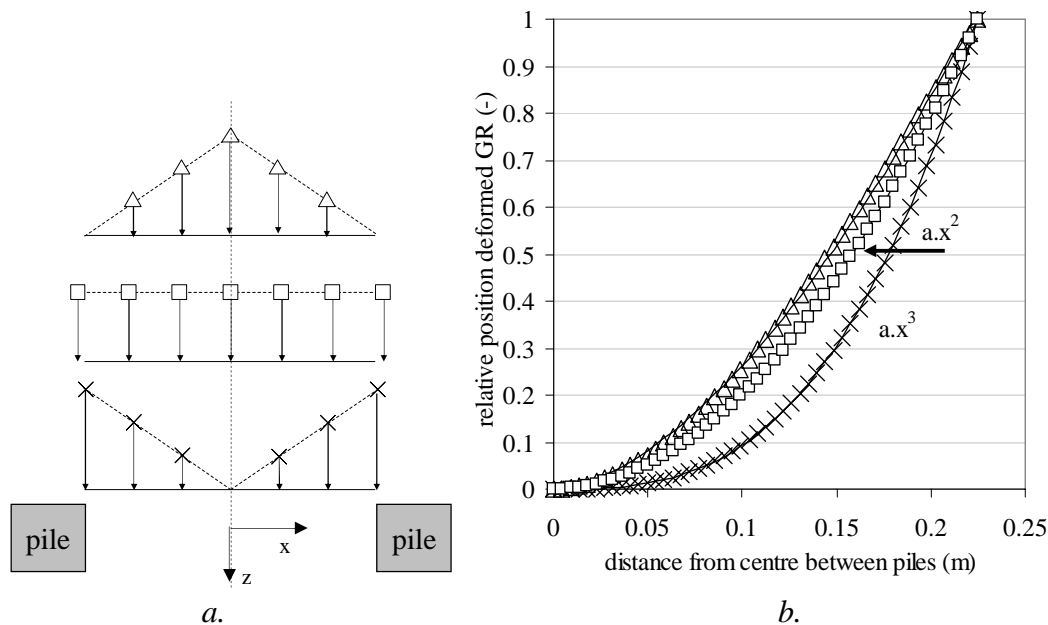
Figure 2.9 Relationship between (*a*) assumed distribution of load on GR tensile strip and (*b*) shape of half a deformed GR tensile strip, calculated analytically from the assumed load distribution.
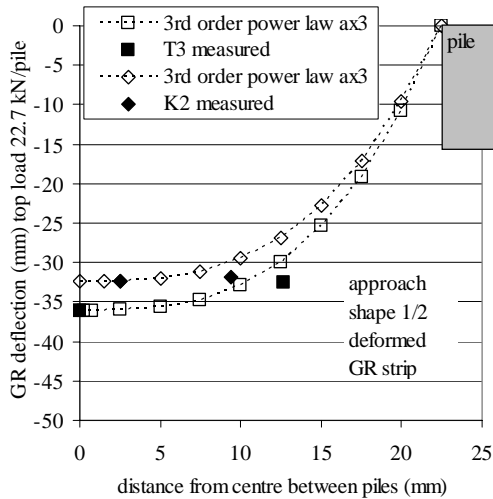
Figure 2.10 Comparison of measured vertical deflection (separate black dots) with third order power law function, which closely matches the shape of the deformed GR strip; measured vertical deflection for top load $p = 22.7$ kN/pile and subsoil $C = 2.4$ kN/pile.

Figure 2.10 shows the GR vertical deflection measured with a top load of 22.7 kN/pile for the tests K2 and T3, with subsoil support $C = 1.8$ and 0.8 kN/pile respectively. It should be noted that the exact locations (Figure 2.3) of the measurements vary per test. The figure shows $z2$ and $z3$, and a vertical deflection curve that follows a third order power law (ax^3), assuming that $z2$ lies on the curve. The figure shows that the shape of the deformed GR follows a power law of the third order, or even a higher order. The deformed GR does not follow a power law in any of the tests that is lower than the third order. This proves that the load on the GR strip is at least the same as in the inverse triangle shown in Figure 2.9. This conclusion is also confirmed in further measurements (including phases without subsoil support), as presented in Van Eekelen et al. (2011b). The analytical elaboration of this new model is presented in Van Eekelen et al (2012b, adopted in Chapter 3 of this thesis).

The load may even be more concentrated around the pile caps than the inverse triangular distribution indicates. A possible reason is found when the fill settlement around the pile is compared to the situation when a pile is pushed into the soil. This will also result in localisation of stresses in the area just around the pile.

The load distribution is of importance for loading on the GR, and thus for the GR design. For this geometry, the same total load with the inverse triangular load gives a tensile force (and thus GR strain) in the geosynthetic that is only 75% of the tensile force for the triangular load. For the maximum vertical deflection, this ratio is 70%.

2.5   Analysis of influencing factors

Chapter 4 presented general test results, mainly based on the representative test K2. This chapter considers the influence of several variations, such as the properties or specifications of the fill, subsoil, or reinforcement.

2.5.1   Embankment fill

Tests T2 and T3 were identical except for the fill; T2 used sand, T3 used granular material. As mentioned earlier in this paper, the sand used has a lower friction angle ($\varphi = 39\text{-}40^{o}$) than the granular material ($\varphi = 45\text{--}49^{o}$, both for 2-5% strain).

Figure 2.11 shows that the higher shear resistance of the granular fill improves arching, as shown by the faster increase of load part *A* during the consolidation steps in particular. The sand fill gives only limited improvement of arching during the consolidation steps, with only a quarter of the increase in load part *A* compared to the increase measured in a test using granular fill. Consequently, the corresponding load part *B* increases more in sand than in the granular tests. The load on the GR in sand will therefore be higher when the subsoil consolidates. At the end of tests T2 and T3, load part *B* on the GR is some 39% larger for sand than for granular fill. The sand fill therefore has less arching, resulting in more vertical deflection (as shown in Figure 2.12). In practical applications, the influence of a lower internal friction angle should therefore be taken into account during the design phase.
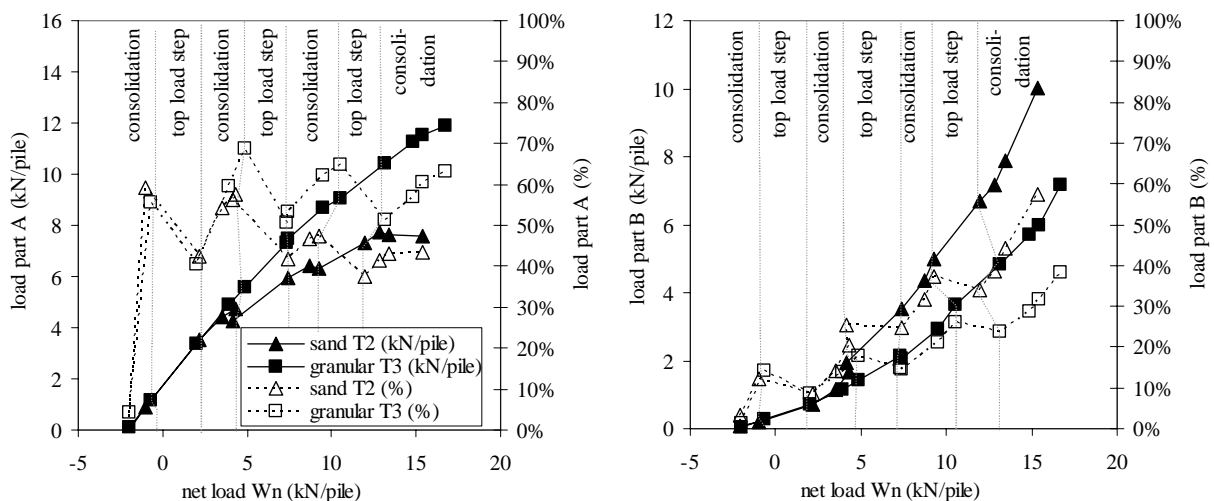
Figure 2.11 Comparison of measured load distribution for tests T2 (sand) and T3 (granular)
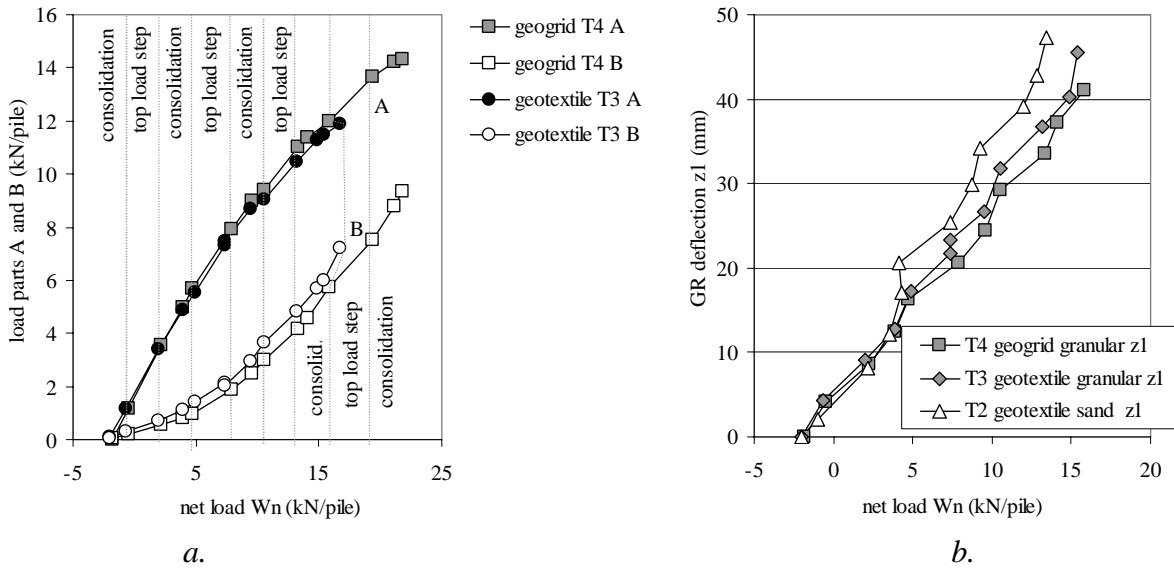
Figure 2.12 (*a*) comparison of measured load distribution for geotextile (T3) and geogrid (T4); (*b*) measured vertical deflection *z1* for T2 (sand, geotextile), T3 (granular, geotextile) and T4 (granular, geogrid).

2.5.2   Geogrid or geotextile

Test T4 is identical to T3, except that a geogrid is used instead of a geotextile, and the maximum top load in T4 is higher. The stiffness behaviour of the two materials is more or less the same (see Table 2.1). It is generally expected that the grains of the granular material become trapped in the gaps of the geogrid, so improving the arching mechanism of the system.

Figure 2.12 shows that the differences between the use of the geogrid and the geotextile are negligible, and are far less than the differences demonstrated between sand and granular fill (see Figure 2.11). Thus, the concept of trapping grains within the geogrid gaps either does not occur in these tests or (if it does) does not lead to any observable benefits over surface friction alone.

2.5.3   Single GR layer consisting of one biaxial or two uniaxial grids

Most design methods assume a geosynthetic reinforcement design consisting of one biaxial layer. However, the width limitation of rolls of geosynthetic reinforcements means that it would not be possible to guarantee the strength in the cross direction of the roll. Therefore, two layers of uniaxial material are normally used instead of a single biaxial layer. These two uniaxial layers are placed perpendicular to, and directly on top of each other.
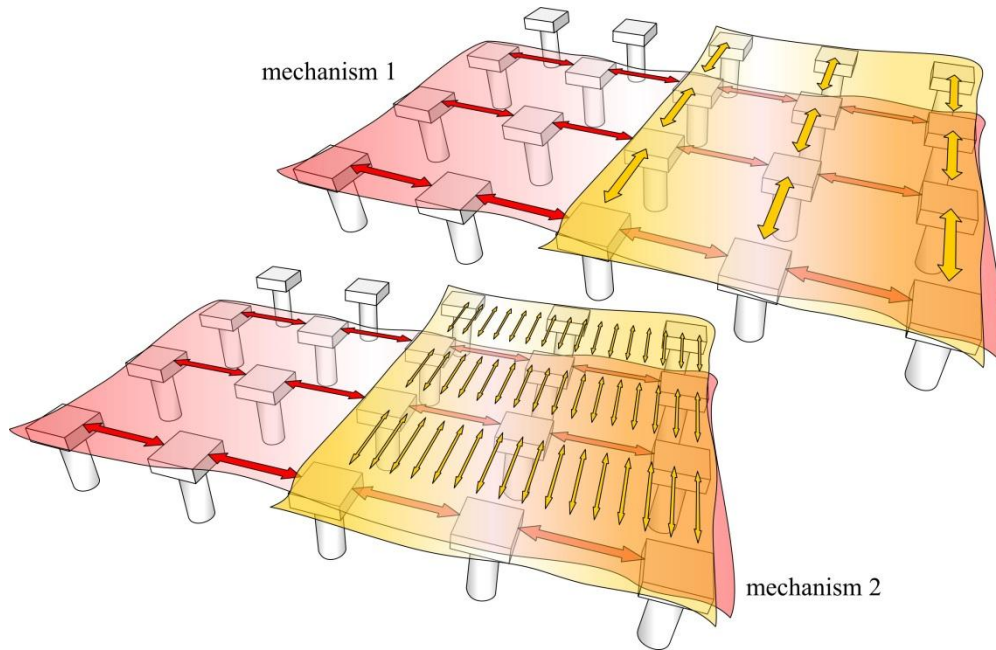
Figure 2.13 Two possible mechanisms for load transfer in reinforcement of two layers of uniaxial grid.

Model tests K1 and K2 were carried out to validate whether the behaviour of a single biaxial and two uniaxial layers is the same. It was expected that the single layer biaxial grid (K1) would behave according to mechanism 1 shown in Figure 2.13[3]. It was uncertain whether K2 would behave in the same way, or whether the load would travel in the longitudinal direction in the top GR layer until it met the second layer of reinforcement with members spanning between the pile caps (mechanism 2 in Figure 2.13).
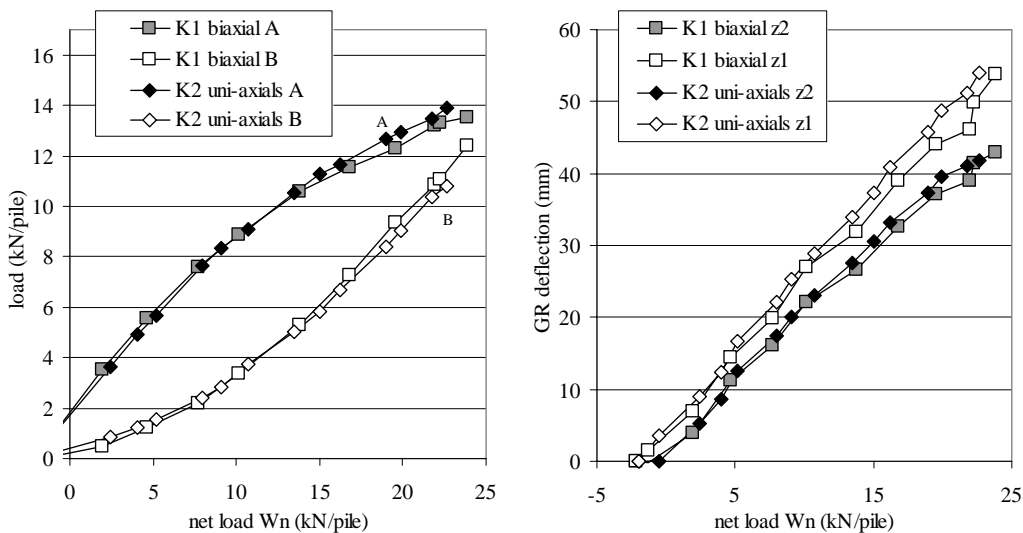
Figure 2.14 Comparison of a GR layer consisting of one biaxial GR grid (K1) or two uniaxial GR grids (K2). Left: measured load distribution, right: measured vertical deflection of GR (locations *z1* and *z2* in Figure 2.3).

---

[3] This figure has been changed by comparison with the original paper, Van Eekelen et al. (2012a).

Figure 2.14 show that both tests behave the same, and Figure 2.7 shows that mechanism 1 occurs in test K2. The load travels in both directions, mainly along the strips between adjacent pile caps, as shown by mechanism 1 in Figure 2.13. Differences between the two tests (a higher load part *B* in the final phase of test K1) must be due to differences in friction between the box and fill, as the top load, load parts *A* and *C* (and vertical deflection of the GR) are nearly the same.

2.5.4 Stiffness of GR[4]
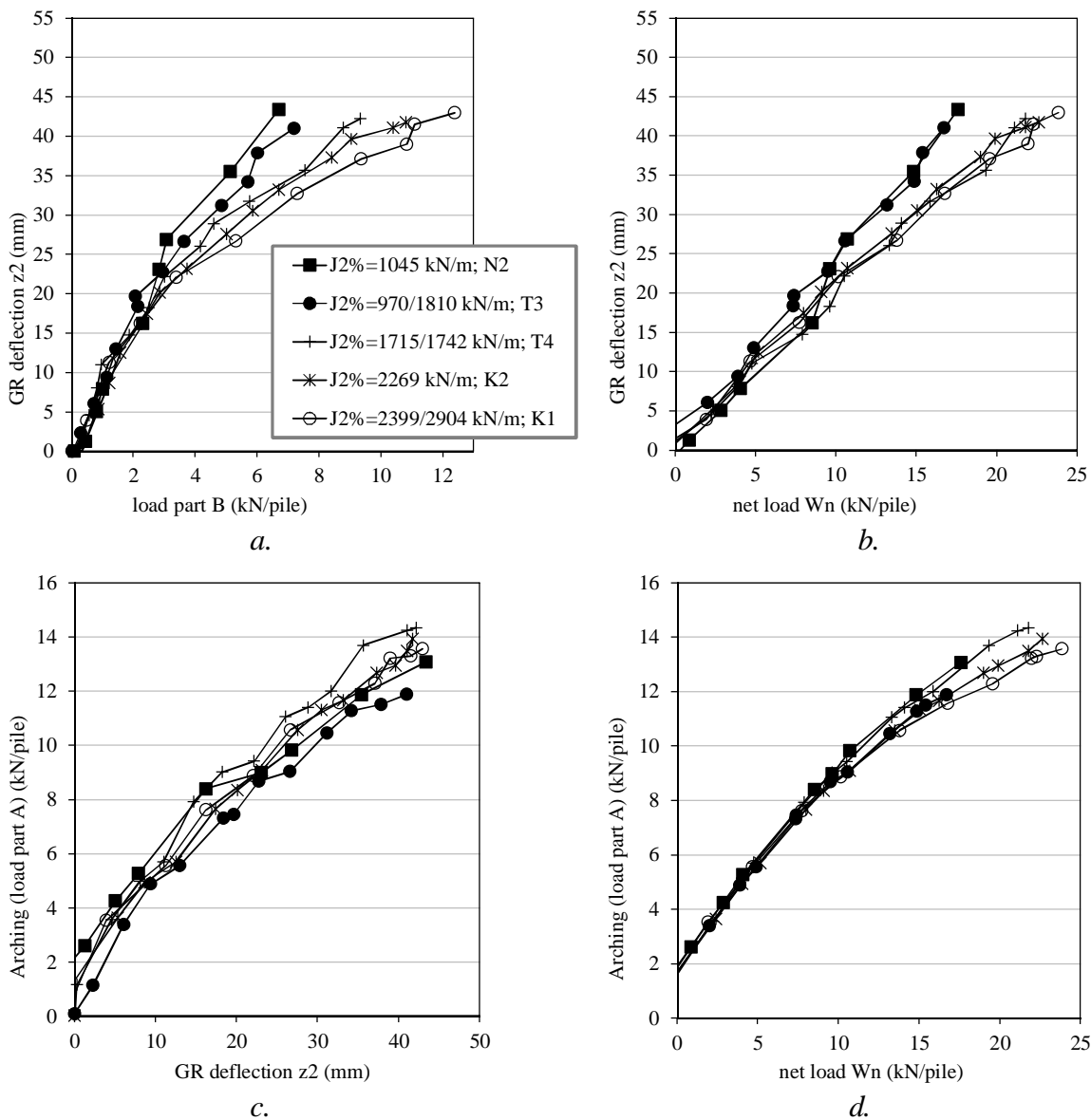
Figure 2.15 Vertical GR deflection and arching in relation to GR stiffness *J* for tests with a granular fill.

---

[4] This chapter has been extended by comparison with the original paper, Van Eekelen et al. (2012a).

Figure 2.15 and Figure 2.16 consider the dependency of GR stiffness *J* in single-layered tests for granular and sand fills respectively.

Figure 2.15*a* and *b* show the influence of *J* in granular fills. The figures show clearly that the stiffer the GR, the less vertical deflection there is. This is due to the fact that there is less GR strain.
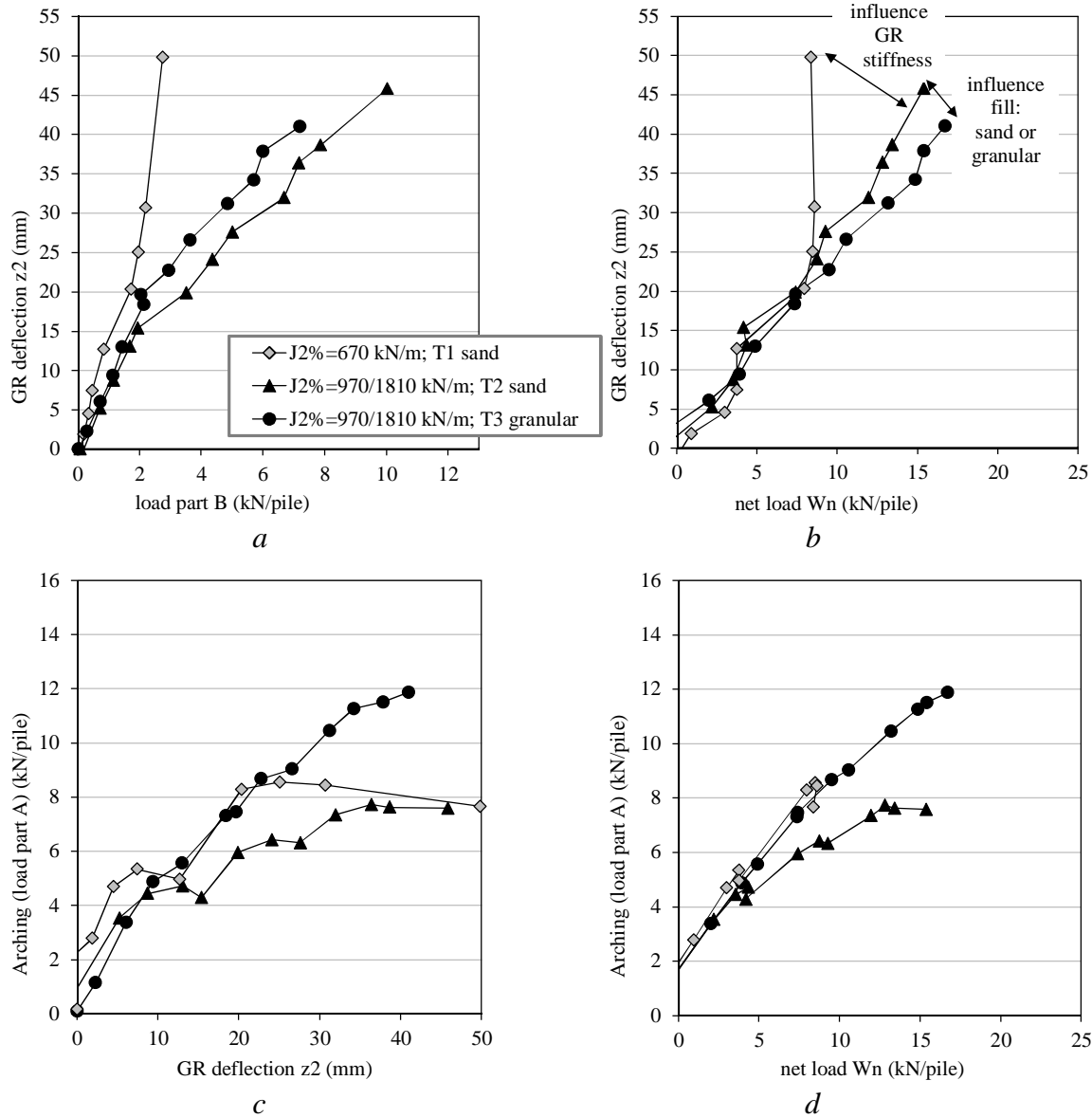
Figure 2.16 Vertical GR deflection and arching in relation to GR stiffness and fill type. The GR stiffness in test T1 is so low that the behaviour in test T1 resembles the situation without GR.

Figure 2.16*a* and *b* show a similar picture for sand fills and include one granular fill test, T3, for comparison purposes. Test T1, in which the GR stiffness was the lowest in the entire test series, shows ongoing GR deflection, with no increase in the net load W_n: the GR was so flexible that it followed the subsoil deformation and it was not possible to reduce subsoil support *C* to zero by draining the foam cushion. Nor did the application of vacuum pressure to the foam cushion help to

further reduce subsoil support. The piled embankment in test T1 is therefore comparable with the situation without GR because the GR is so flexible.

Figure 2.15*c* and *d* and Figure 2.16*c* and *d* show how GR stiffness affects arching. These figures show that GR stiffness *J* does not affect the amount of arching as long as the GR is stiffer than in test T1. Van der Peet and Van Eekelen (2014) also found, with finite element calculations, that GR stiffness does not affect arching *A* in the GR stiffness range that they investigated.

2.5.5 *Two layers of reinforcement*

Most design models, such as EBGEO (2010), CUR226 (2010) and BS8006-1 (2010), calculate the required strength and stiffness for one GR layer, located in the base of the embankment. In practice, the required strength and stiffness is frequently divided into two GR layers with a layer of granular material in between. This chapter compares the 'single-layered test' using one layer of GR, and the 'double-layered test', using two layers of GR with a layer of granular material in between. In the 'double-layered tests', the second GR layer as indicated in Figure 2.2 and Figure 2.3*d* is applied.

Test K2 and K3 are particularly suitable for comparison purposes as the GR is identical. However, the two GR layers in the K2 test lie directly on top of each other to give a single reinforcement layer, whilst the two GR layers in test K3 are separated by 0.05 m of granular material.
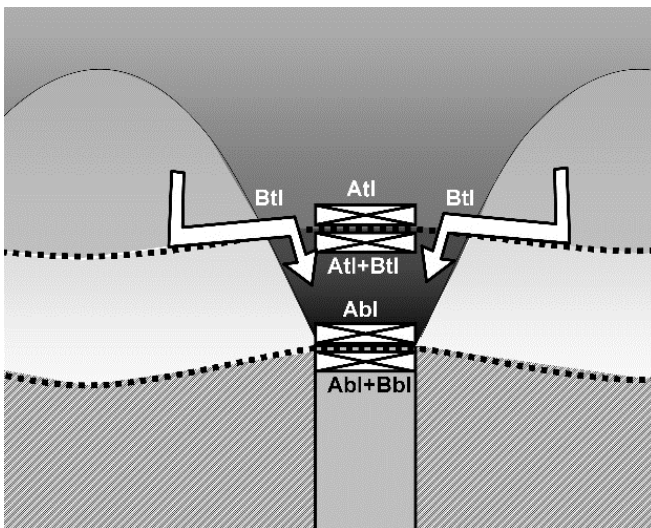
Figure 2.17 Interpretation of measured load distribution in a double-layered system (an embankment with a GR divided into two layers with a granular layer in between).

Figure 2.17 shows that the A_{bl} in a double-layered test cannot be compared with load part *A* in a single-layered test, because A_{bl} will increase as load B_{tl} is

transferred through the top grid layer. Another limitation is that, due to arching, the top grid layer will experience a pile that is virtually wider. The total pressure cells are intended to measure the total load on the pile, and therefore have exactly the same diameter as the pile. The diameter of A_{tl} is therefore smaller than the virtual diameter below the top grid layer. Both A_{tl} and B_{tl} may be larger than the measured A_{tl} and B_{tl}.

While being aware of these limitations, the measured load part B in a single-layered test can be compared (approximately) with $B_{tl} + B_{bl}$ in a double-layered test, and load part A in a single-layered test can be compared with $A_{bl} - B_{tl}$ in a double-layered test.
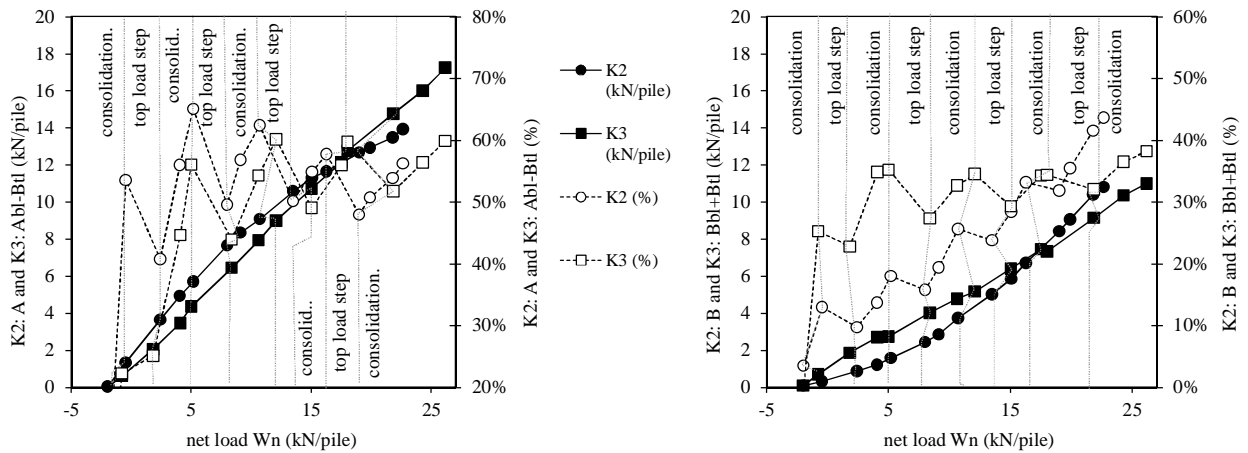
Figure 2.18 Comparison of double-layered test (K3) and single-layered test (K2); measured load distribution in kN/pile. The total stiffness of the reinforcement is the same for K2 and K3.

Figure 2.18 compares the load distribution for the single-layered K2 test and the double-layered K3 test. It can be concluded that arching in the double-layered test develops more slowly, and remains more stable during the test. The final value is higher than in the single-layered test. This is shown by the K3 measurements in Figure 2.18, as the curves are straighter than those of K2. During the entire K3 test, $B_{bl} + B_{tl}$ is slightly larger than load B in K2.
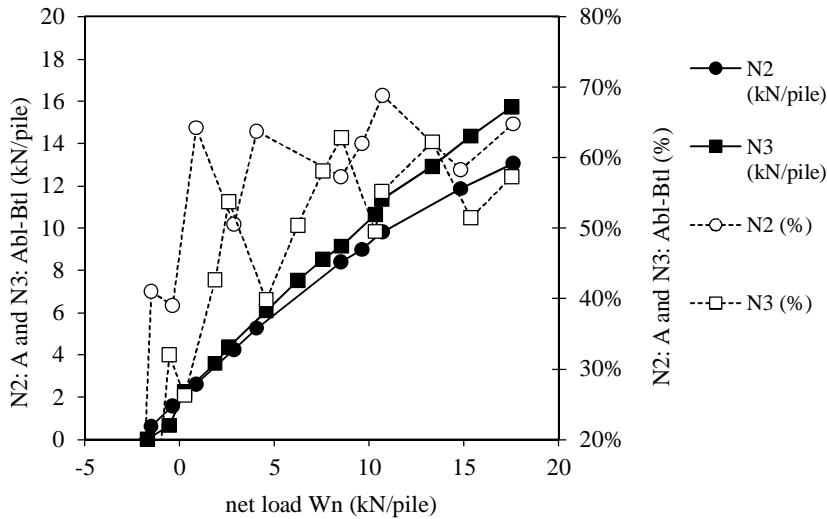
Figure 2.19 Comparison of double-layered test (N3) and single-layered test (N2); measured load distribution in kN/pile. The total stiffness of the N3 reinforcement is twice the total stiffness of N2.
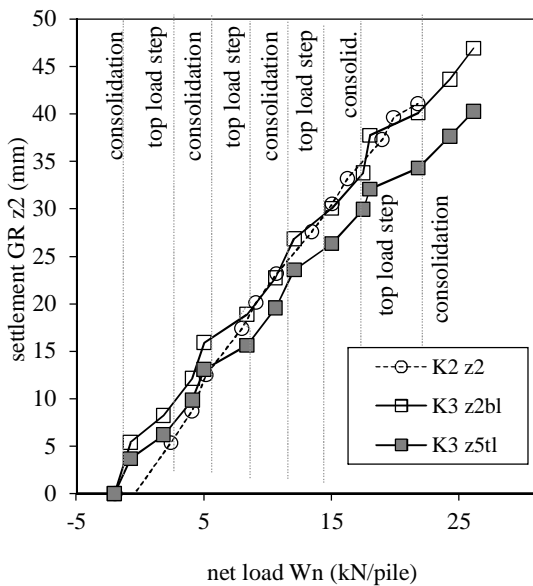
Figure 2.20 Comparison of single-layered test (K2) and double-layered test (K3); measured vertical deflection of the bottom grid layer (z2) and top grid layer (z5).
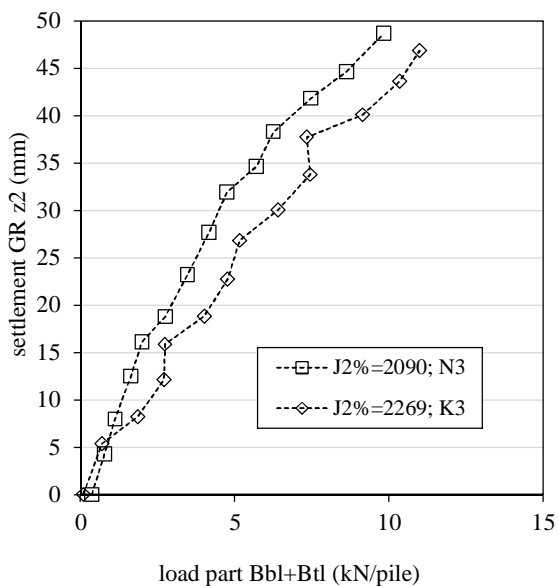
Figure 2.21 Measured dependency of the GR stiffness in double-layered tests, compare with Figure 2.15.

These conclusions can also be drawn for the other single- and double-layered tests in the test series, for example when N2 and N3 are compared (see Figure 2.19). Here, the reinforcement is not identical for both tests. The total stiffness of the N3 reinforcement is twice the stiffness of N2. The arching in N3 is thus relatively higher in comparison to N2. Furthermore, the type of GR used in N2 and N3 is different to that used in K2 and K3 (see Table 2.1). Figure 2.19 also shows that

arching develops at a slower rate in the double-layered tests, but remains more stable during the test, in the same way as in K3 (see Figure 2.18).

Figure 2.20 shows that there are also only limited differences in the measured vertical deflection in K2 and K3. Figure 2.20 also shows that the top grid layer settles less than the bottom grid layer. The same tendency is found for the GR strains. The top layer shows the same GR strain pattern as the bottom grid layer, but the GR strains are lower. Figure 2.21 shows that a GR with lower stiffness also results in more vertical deflection in a double-layered system.

2.5.6 Differences between types of GR

No differences in behaviour were found between the types of reinforcement that were used, except for the differences described in the previous chapters, namely: the stiffness of the GR, the strength of the fill, the use of geotextile or geogrid, and the number of GR layers.

2.5.7 Angle of arching

The angle of arching can be determined for the tests K3 and N3 where the total pressure cells *A* are placed at two levels, and where the distance between the pressure cells is determined before the test. To do so, it is assumed that (1) the arch has a straight conical shape with arching angle $\alpha = 90^o\text{-}\beta$, as shown in Figure 2.22, (2) the load within the cone seen in the left-hand side of Figure 2.22 is equally distributed.
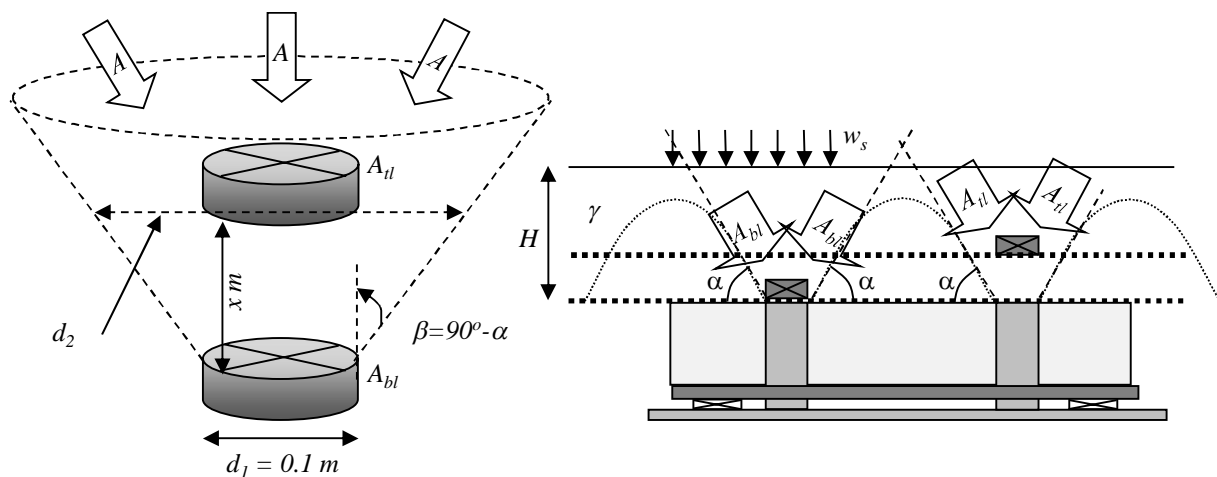
Figure 2.22 Measuring the angle *β* of arching.
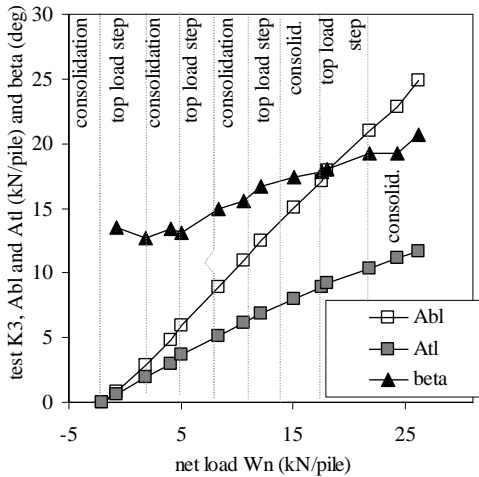
Figure 2.23 Angle β of arching in test K3, calculated from measured A_{bl} and A_{tl}.

Table 2.2 Angle β of arching.

	height between the total pressure cells[a]	angle β
	m	deg
K3	0.059[a]	16.7
N3	0.087[a]	16.9

[a] measured before the start of the test

The diameter d_1 of the arching cone at the base (at A_{bl}) is 0.1 m, which is the diameter of the piles and the total pressure cells. The arching angle β is given by:

$$\tan\beta = \frac{d_1\sqrt{\dfrac{A_{bl}}{A_{tl}}} - d_1}{2x} = \frac{0.1\sqrt{\dfrac{A_{bl}}{A_{tl}}} - 0.1}{2x} \tag{2.4}$$

Figure 2.23 gives A_{bl}, A_{tl} and β for test K3. For this test, the average β is 16.7°. Table 2.2 gives the average β for the four double-layered tests. The average angle β lies between 16.7° and 16.9°. This is in the same range as the observed angle of 13.5° in the 2D experiments with sand fill and no GR, as reported in Van Eekelen et al. (2003).

2.6 Conclusions

An experimental programme was undertaken to investigate the mechanism of arching within a piled embankment. In the test series, it was possible to measure the distribution of the load in three parts (kN/pile): load part *A* ('the arching load part') that is transferred directly to the piles; load part *B* that travels through the GR to the piles; and load part *C* ('subsoil') that is carried by the soft subsoil.

The measured load parts *A* and *B*, both in kN/pile as well as GR vertical deflection, follow a smoothly ascending curve when plotted against net load (top load minus subsoil support *C*). This means that the actual surcharge load on the fill is not

particularly important – it is the net load on the fill and the GR that determines its behaviour.

Consolidation of the subsoil results in an increasing load through the GR (increasing load part *B*), and also an increase of arching (increasing load part *A*). This is different from results obtained using calculation models. A higher friction angle of the fill gives more arching during consolidation. This results in load part *B* on the GR being some 39% larger for sand than for granular fill at the end of tests T2 (sand fill) and T3 (granular fill).

The measurements show that, without consolidation of the subsoil, top load increase results in a load part *A* that increases in kN, but decreases as a percentage of the total measured load. Thus, top load increase results in less arching.

All the tests show that the GR strains occur mainly in the tensile strips that lie on top of and between adjacent piles. This is in agreement with the assumptions of the calculation models BS8006-1 and EBGEO, and is also proven by numerical calculations (Den Boogert, 2011). For the test conditions (smooth, small-scale piles), the largest GR strains are measured on top of the piles.

The line load on a GR strip between piles has the distribution of an inverse triangle, although the load may be even more concentrated around the pile caps than this indicates. This follows from the shape of the deformed GR, measured at two points between two piles.

The difference in performance when applying a geotextile or a geogrid with the same mechanical characteristics is negligible. The difference between, for example, applying a sand or granular fill is much larger.
No difference is found between the use of a single biaxial grid layer and two uniaxial grid layers positioned directly on top of each other as one layer.

The GR stiffness *J* does not influence the measured arching *A*.
In a double-layered test, the reinforcement consists of two grids, with a layer of granular material in between. Arching in the double-layered tests develops more slowly, but increases slightly more steadily throughout. At the end of the test, arching is higher than in the single-layered test in the test series. The differences for the GR are small throughout the entire test series.

No significant difference in behaviour is seen between the different types of reinforcement tested in single-layered tests and in comparable double layered-tests (except for differences due to differences in fill, GR stiffness, and whether a geotextile or geogrid is used).

3 Load-deflection Behaviour of the Geosynthetic Reinforcement (step 2)
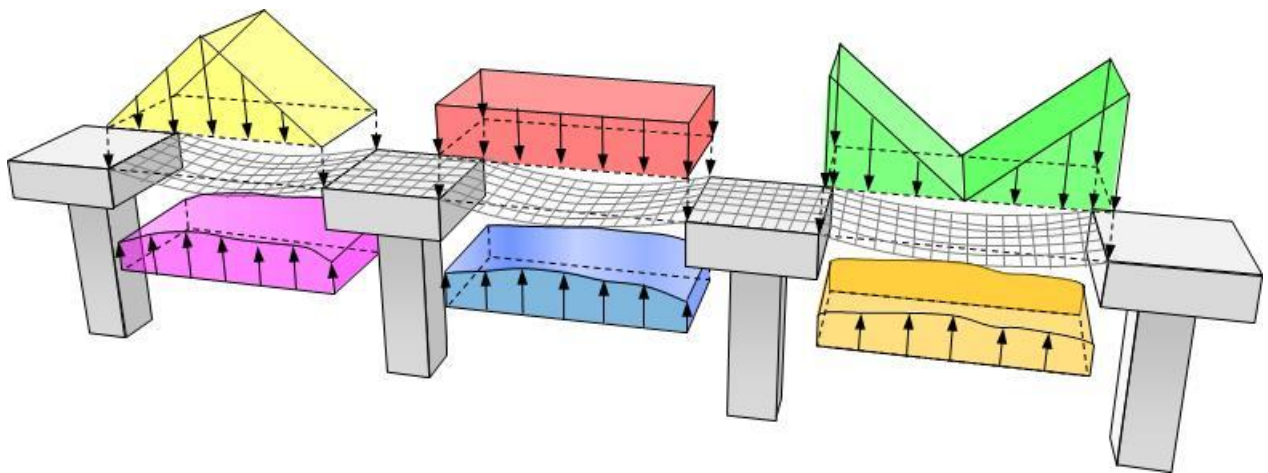
Abstract

This two-part study concerns a series of twelve 3D laboratory model tests on piled embankments. In the first part (Chapter 2), the measured load distribution, deformation, and strains were presented and analysed. In this second part, the measurements are compared with calculations made using the EBGEO (2010) and CUR (2010) analytical model, hereafter called 'EBGEO'. Possible improvements to the analytical model are also suggested, and the resultant calculations are compared with the measurement results.

EBGEO calculations consist of two steps: (step 1) load distribution in the fill i.e. arching behaviour, and (step 2) the load-deflection behaviour of the geosynthetic reinforcement (GR). For the test conditions (static load, laboratory scale), it was found that the GR strains calculated using EBGEO are larger than the measured GR strains (approximately a factor of two for GR strains larger than 1%). The EBGEO calculations are therefore too conservative. The following reasons were found. In step 1, the response of arching to subsoil consolidation in the experiments is different from that assumed in EBGEO. In step 2, the distribution of loading on the 'GR strips' lying between adjacent piles is quite different from that assumed by EBGEO, and EBGEO only takes part of the subsoil support into account. Modifications are suggested for the second calculation step. It is shown that this modified step 2 model results in significantly closer agreement with the test measurements.

3.1   Introduction

The first part (Van Eekelen et al., 2012a, Chapter 2 of this thesis) of this two-part study presented and analysed the measured load distribution, deformation, and strains in a series of 12 model laboratory model tests on piled embankments. In this second part of the study, the measurements are compared with calculations using EBGEO (2010). EBGEO (2010) as well as CUR 226 (2010) adopted the analytical model of Zaeske (2001), hereafter called 'EBGEO'. The EBGEO model describes (step 1) the arching behaviour in the fill and (step 2) the load-deflection behaviour of the geosynthetic reinforcement (GR), see Figure 3.1. These two steps will be summarised and compared with the test measurements, and modifications for step 2 are suggested.
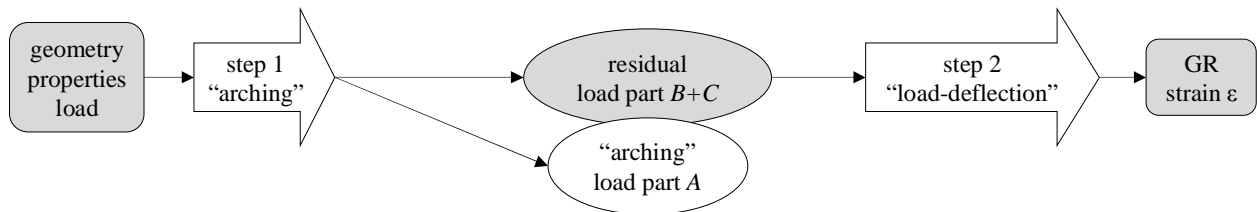
Figure 3.1 EBGEO and CUR226 calculations are in two steps: (step 1) load distribution in the fill (arching), (step 2): load-deflection behaviour of the GR (membrane behaviour).

To compare the calculated and measured results of steps 1 and 2 separately, the load distribution within the embankment is considered, as introduced in Van Eekelen et al. (2012a, Chapter 2 of this thesis). According to this approach (see Figure 3.2), the vertical load is distributed into three parts: part *A* ('arching' or 'arching load part') is transferred directly to the piles, part *B* goes through the GR to the piles, and part *C* ('subsoil') is carried by the soft subsoil. Load parts *A, B* and *C* are expressed in kN/pile. Horizontal loads, for example spreading forces, are outside the scope of this research.
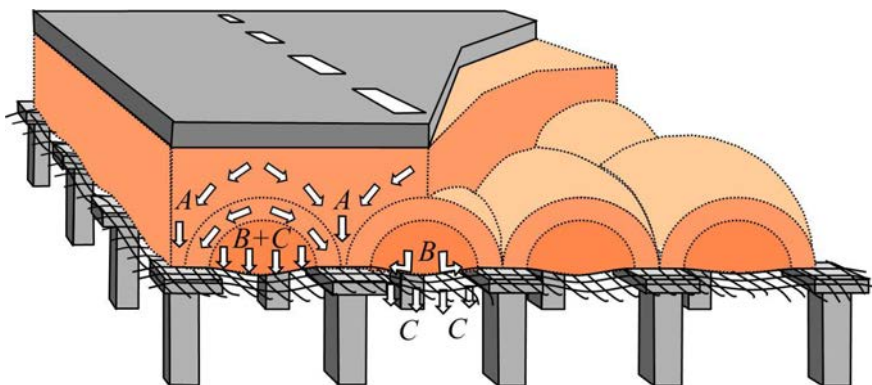
Figure 3.2 distribution in piled embankments. Distribution of the load is in three parts: *A* (arching) directly to the piles; *B* via the GR to the piles; *C* (subsoil) to the soft subsoil between the piles.

EBGEO was chosen as the basis for this study as it is widely accepted and applied in the design of piled embankments in the Netherlands, Germany, Poland and several other countries.

However, many more models are available to calculate the tensile forces in the geosynthetic reinforcement (GR). These models usually distinguish step 1 (arching) and step 2 (membrane behaviour) in the same way as in EBGEO. Several of them are 2D, for example R.P. Chen et al. (2008b, without GR), Abusharar et al. (2009, assuming a circular deformed GR), and Deb (2010, focussing on the application of geosynthetic encased stone columns in a piled embankment). Filz and Smith (2008) developed the axial symmetric load-deflection relationships for each of the components of the piled embankment separately (step 2). They suggest describing the arching mechanism (step 1) using the Adapted Terzaghi Method of

Russell and Pierpoint (1997), but any other realistic method to describe the arching can be used in their model.

Jones et al. (2010), Halvordson et al. (2010) and Plaut and Filz (2010) adopted Filz and Smith's starting point (2008), and presented the load-deflection relationship for the GR ('step 2') in a three-part study. They used respectively a 3D plate model, a 3D cable-net model, and an axial symmetric model.

Other 3D models are BS8006-1 (2010, discussed and modified in Van Eekelen et al, 2011a, see appendix A of this thesis), Hewlett and Randolph (1998), and several Scandinavian contributions such as Svanø et al (2000) and Rogbeck et al. (1998), also discussed and modified in Van Eekelen et al. (2003). Several authors have shown that these methods produce results that differ widely from each other, such as Filz and Smith (2006) and R.P. Chen et al. (2010).

Several studies compared the results of analytical models with field- or laboratory measurements. For example, Y.M. Chen et al. (2008a) conducted 2D experiments both with and without GR. They compared the results of their experiments without GR with three 2D analytical models without GR, namely Terzaghi (1943) and Low et al. (1994) and the original 2D equation of Marston and Anderson (1913) that formed the basis of the BS8006-1 3D equations (1995, see Van Eekelen et al., 2011a, adopted in appendix A of this thesis). R.P. Chen et al. (2010) compared BS8006-1995, Nordic handbook (NGI 2003), EBGEO, version 2004 and R.P. Chen et al, 2008b with the results of three field studies. Zaeske (2001), Heitz (2006) and Farag (2008) compared the results of laboratory model tests with calculations.

The three load parts *A, B* and *C* were not measured separately in any of the studies mentioned above. For example Zaeske (2001) and Heitz (2006) measured *A+B* together. As it was not possible to validate steps 1 and 2 separately for their tests using GR, they compared the results of their calculation models with their tests without GR. However, they also showed that use of GR considerably influenced mechanisms within the piled embankment in their tests.

In the study presented in this paper, load parts *A, B* and *C* are measured separately, as explained in Van Eekelen et al. (2012a, Chapter 2 of this thesis). This makes it possible to validate EBGEO's calculation steps 1 and 2 separately.

The relevant parts (steps 1 and 2) of EBGEO's analytical calculation method are summarised in Chapter 3.2, and the EBGEO results are compared with the measured results for both steps in Chapter 3.3. Chapter 3.4 suggests improvements for the analytical model of step 2 (membrane behaviour). Chapter 3.5 considers the

influence of the fill's friction angle, the GR stiffness, and the application of one or two GR layers in both the measurements and the calculations (Chapter 3.5). In this last chapter, the modifications suggested for step 2 are applied.

3.2 EBGEO: the two calculation steps

Both the German EBGEO (2010) and the Dutch CUR 226 (2010) adopted the model developed by Zaeske (2001), hereafter called 'EBGEO'. EBGEO uses two calculation steps (see Figure 3.1): (step 1) arching and (step 2) the load-deflection behaviour of the GR, or the 'membrane step'.

3.2.1 Calculation step 1: arching

For this 'arching step', Zaeske used a 3D-arching model to divide the total load into two parts: (1) part A and (2) part $B+C$:

$$A = A_p \cdot \sigma_{v;p} = A_p \left[\left(\left(\gamma \cdot h + w_s \right) - \sigma_{v;r} \right) \cdot \frac{A_i}{A_p} + \sigma_{v;r} \right] \tag{3.1}$$

$$B + C = A_r \cdot \sigma_{v;r} =$$

$$A_r \cdot \left[\lambda_1^\chi \cdot \left(\gamma + \frac{w_s}{h} \right) \cdot \left(\begin{array}{c} h \cdot \left(\lambda_1 + h_g^2 \cdot \lambda_2 \right)^{-\chi} + \\ h_g \cdot \left(\left(\lambda_1 + \frac{h_g^2 \cdot \lambda_2}{4} \right)^{-\chi} - \left(\lambda_1 + h_g^2 \cdot \lambda_2 \right)^{-\chi} \right) \end{array} \right) \right] \tag{3.2}$$

where:

$$K_{crit} = \tan^2 \left(45^o + \frac{\varphi'}{2} \right)$$

$$\chi = \frac{d \cdot \left(K_{crit} - 1 \right)}{\lambda_2 \cdot s}$$

$$\lambda_1 = \frac{1}{8} \cdot (s - d)^2$$

$$\lambda_2 = \frac{s^2 + 2 \cdot d \cdot s - d^2}{2 \cdot s^2}$$

and *A, B* and *C* are the load parts in kN/pile as defined in Figure 3.2 and Chapter 3.1, *h* is the fill height above the bottom layer of the GR in m, A_p is the area of pile caps (per pile) in m^2, A_i is the area of influence of one pile; $A_i = s_x \cdot s_y$ in m^2, A_r area GR (per pile) in m^2, $A_r = A_i - A_p$, d is the diameter of the pile (cap) in m, *s* is the diagonal pile spacing in m, $\sigma_{v;r}$ is the vertical stress on the GR between the pile caps in kPa, $\sigma_{v;p}$ is the stress on the pile caps in kPa, γ is the fill unit weight in kN/m^3, w_s is the top load (static + dynamic) in kPa and h_g is the arch height in m: $h_g = s/2$ for $h \geq s/2$ or $h_g = h$ for $h < s/2$.

It should be noted that this first calculation step only depends on the geometry of the piled embankment and the friction angle φ of the fill. Subsoil support and GR properties do not influence the calculation of load part *A*.

3.2.2   Calculation step 2: membrane behaviour

The 'membrane step' determines the GR strain, and thus the tensile force *T* from the load part *(B+C)*. For this load step, EBGEO considers the GR strip as presented in Figure 3.3. The width of the strip equals B_{ers}. For circular pile caps with diameter *d*, B_{ers} is the equivalent size of a square pile cap:

$$B_{ers} = \frac{1}{2} \cdot d \cdot \sqrt{\pi} \tag{3.3}$$
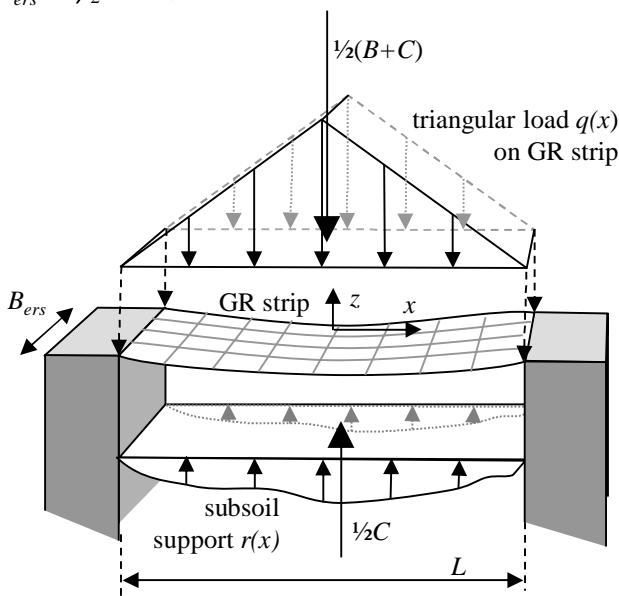
Figure 3.3 Calculation step 2 (membrane) of EBGEO; the GR strip is loaded by a triangular load *q(x)* and supported by the subsoil *r(x)* below the GR strip.

The length of the GR strip equals $L_{x,y} = s_{x,y} - B_{ers}$. The GR strip is loaded by a triangular load $q(x)$ in kPa (see Figure 3.3), with (assuming that $s_x = s_y$)[5]:

$$A_s \cdot q_{average}(x) = \tfrac{1}{2}(B + C) \tag{3.4}$$

where $A_s = L_{x,y} \cdot B_{ers}$ is the area of GR strip. The strip is supported by the subsoil below the GR strip. The subsoil is modelled as an elastic spring with a constant modulus of subgrade reaction k_s in kN/m^3. The subsoil support results in an 'upward load' $r(x)$ in kPa:

$$r(x) = K \cdot z(x) \tag{3.5}$$

with $z(x)$ the vertical deflection of the GR strip. In this paper, the calculation value for the subgrade reaction K is introduced. In accordance with EBGEO, it follows that $K = k_s$. K is considered more specifically in Chapter 4.1. The GR vertical deflection due to the loading situation, illustrated in Figure 3.3, can be described with the following differential equation (see appendix 3.B):

$$\frac{d^2 z}{dx^2} = \frac{q(x) - r(x)}{T_H} = \frac{q(x) - K \cdot z(x)}{T_H} \tag{3.6}$$

where T_H is the horizontal component of the tensile force in the GR (kN/m) and $q(x)$ is the triangular load given in Figure 3.3 in kPa.

Zaeske (2010) solved this differential equation and presented the results in the graph shown in Figure 3.4. It should be noted that the vertical axis shows the average GR strain, and not the maximum GR strain. This is a misprint in EBGEO, as shown by Lodder (2010). Heitz (2006) expresses this graph in several high order polynomial equations. The calculation factors F_1 and F_2 in Figure 3.4 are defined as follows (assuming $s_x = s_y$):

$$\text{EBGEO:} \quad F_1 = \frac{\tfrac{1}{2}(B+C)/B_{ers}}{J} \qquad F_2 = \frac{K \cdot L_{x,y}^2}{J} \tag{3.7}$$

where J is the stiffness of the GR (usually determined from the isochronic curves of the specific GR), and L the distance between the piles, as indicated in Figure 3.3.

---

[5] EBGEO distributes $B+C$ to the GR strips in the x- and y-directions relative to the diamond areas in equation (5.8). If $s_x = s_y$, equation (3.4) is true and gives the same result as equation (5.9) for the CA model presented in Chapters 4 and 5. If $s_x \neq s_y$, the EBGEO load on the GR strips in the x- and y-directions differ slightly. The differences are much smaller than in the case of the CA model (equation (5.9)).

Finally, the tensile force T is determined as follows:

$$T = J \cdot \varepsilon \tag{3.8}$$
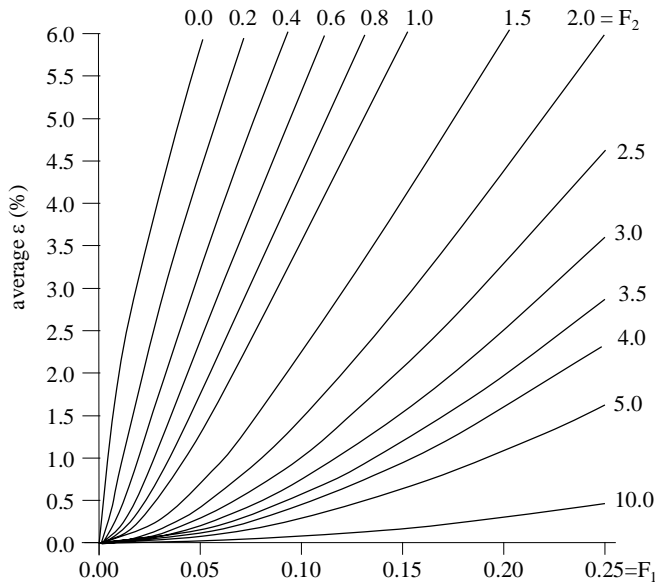
Figure 3.4 Design graph of EBGEO; average GR strain ε between the pile caps. Source: EBGEO (2010), graph 9.16[a].

[a] This graph is identical to that in EBGEO, except that the text along the vertical axis differs: EBGEO names the given GR strain ε as the maximum GR strain, Lodder (2010) showed that this must be the average strain.

3.3 Comparison of EBGEO and measurements

Appendix 3.A describes how the input and output parameters of the calculations from the tests were determined.
Table 3.2 and Table 3.3 (page 57) give the resulting input properties for the calculations of test K2.

3.3.1 Calculation step 1: arching

EBGEO's step 1 divides the load into two parts: A and $B+C$. Figure 3.5 shows the measured and calculated value for A (left) and $B+C$ (right) for the typical test K2 (see van Eekelen et al., 2012a, Chapter 2 of this thesis). The figure shows that the A parameter from the EBGEO calculation is lower, and that EBGEO's $B+C$ value is higher. Use of EBGEO in a design is therefore on the 'safe' side. This observation is confirmed by field measurements along the Kyoto Road (Van Eekelen et al., 2010a), the N210 in the Netherlands (Haring et al., 2008), the

Houten Railway (Van Duijnen et al., 2010) as well as in HafenCity Hamburg in Germany (Weihrauch et al, 2010).

Figure 3.5 clearly shows that an increase in the top load leads to an increase in load part *A*, both in the calculations and the measurements. However, subsoil consolidation leads to an increase in load part *A* in the measurements, but not in the EBGEO calculations. The same holds for load part *B+C*; the measurements show that *B+C* decreases with consolidation, but the calculations show no change. Figure 3.5 also shows that EBGEO always calculates *A* and *B+C* as a constant percentage of the load if the geometry and the fill properties are constant. The figure also shows an increase in measured *A%* in response to subsoil consolidation, while the calculated *A%* remains constant. This means that according to EBGEO, arching is independent from subsoil deformation (that changes during the consolidation phase), although subsoil deformation in the experiments resulted in more arching. Subsoil deformation is even required to increase the amount of arching (*A%*).
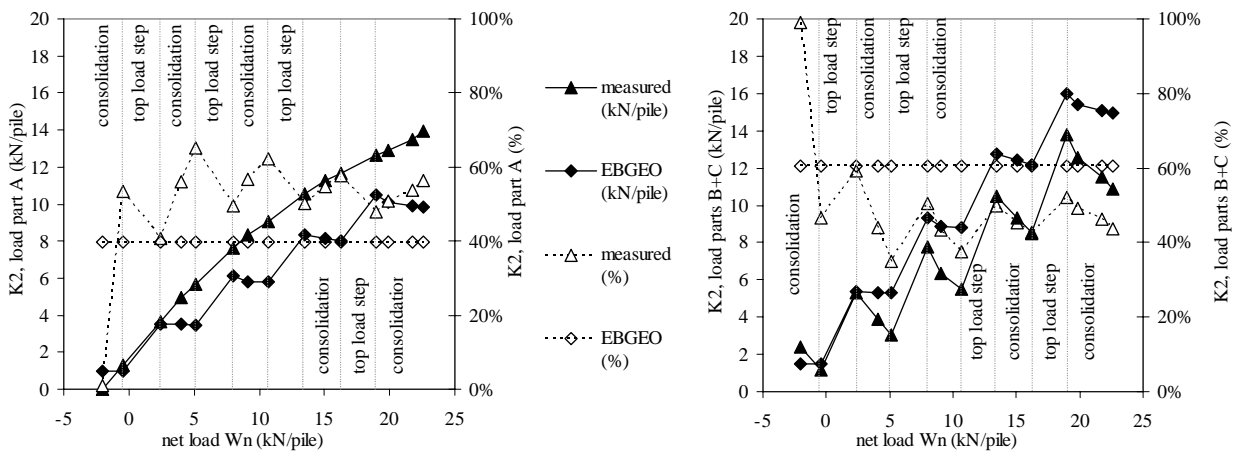
Figure 3.5 Calculation step 1 (arching); distribution load into arching *A* (left) and *B+C* (right); comparison between measurements and calculations for test K2.

It can be concluded that consolidation or an increase of top load give a different response (expressed in %) in EBGEO compared to the test measurements. The net load W_n is normative for the measurements in kN/pile, which is not confirmed by the calculations (van Eekelen et al., 2012a, adopted in Chapter 2 of this thesis).

It is recommended that EBGEO step 1 should be improved to give a more accurate response to consolidation. This would require a modification to the EBGEO calculation, resulting in closer agreement between measured and calculated arching. This improvement is currently a subject for further study, and will be published at a later date[6].

---

[6] Published in Van Eekelen et al. (2013), adopted in Chapter 4 of this thesis.

3.3.2   Calculation step 2: membrane behaviour

Figure 3.6 compares the results of the second calculation step with the test measurements. The 'measured' average GR strains in all strain diagrams in this paper are calculated using the measured vertical deflection $z2$, using a third order power law function, as explained in Van Eekelen et al. (2012a, Chapter 2 of this thesis). It should be noted that the *measured B+C* value in Figure 3.6 was *direct* input for the calculations. This makes it possible to compare the measurements and calculation results of step 2 only. The results in this figure are presented chronologically from left to right. It should be noted that the values for $(B+C)$ decrease for each top load. The figure shows that the calculated GR strains for identical $B+C$ values are much higher than the measured GR strains.
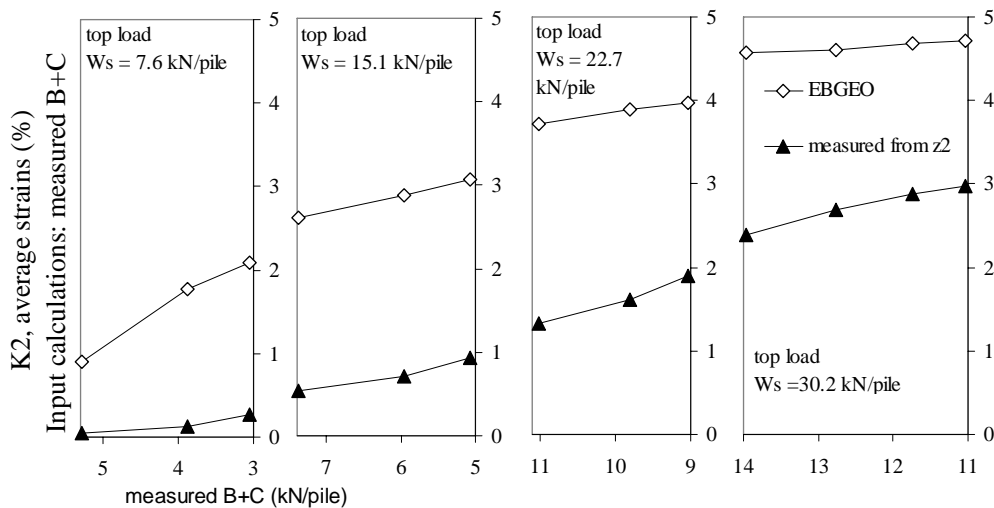
Figure 3.6 Calculation step 2 (membrane): GR strains are calculated from $(B+C)$; comparison between measurements and EBGEO calculations for test K2. It should be noted that $B+C$ decreases during each top load. All calculations are carried out using the measured $B+C$ value as an input parameter.

3.3.3   Conclusions: step 1+2

It can be concluded that step 1 of the EBGEO calculations results in a value for GR load $(B+C)$ that is higher than that shown by the model tests, mainly because subsoil consolidation leads to an increase in load part A in the measurements, but not in the EBGEO calculations. In addition, step 2 of the EBGEO calculations results in a GR strain value that is higher than that shown by the model tests. Chapter 3.4 shows that this has two reasons: (1) the wrong EBGEO-assumption for the load distribution on the GR, as shown in Van Eekelen et al. (2012a, Chapter 2 of this thesis) and (2) EBGEO assumes that only a part of the subsoil is mobilised. Because of the over-estimation of the load on the GR in step 1, and the over-estimation of the strain in step 2, EBGEO (step 1+2) calculations give GR strain

values that are higher than those shown in the test measurements, as shown in Figure 3.7.
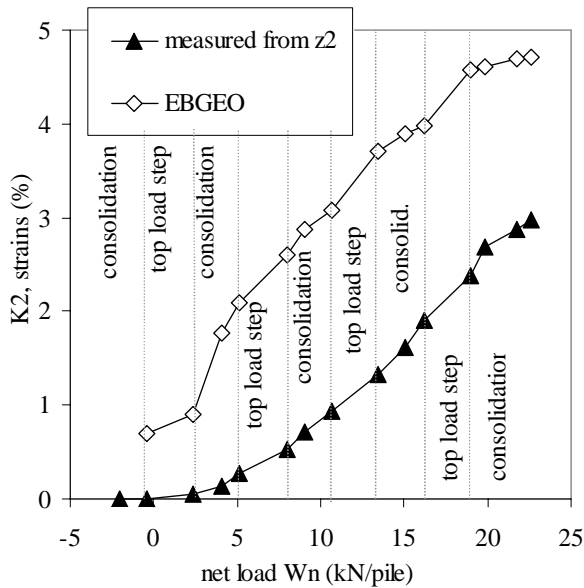
Figure 3.7 Calculation steps 1+2: comparison between measurements and EBGEO calculations for test K2.
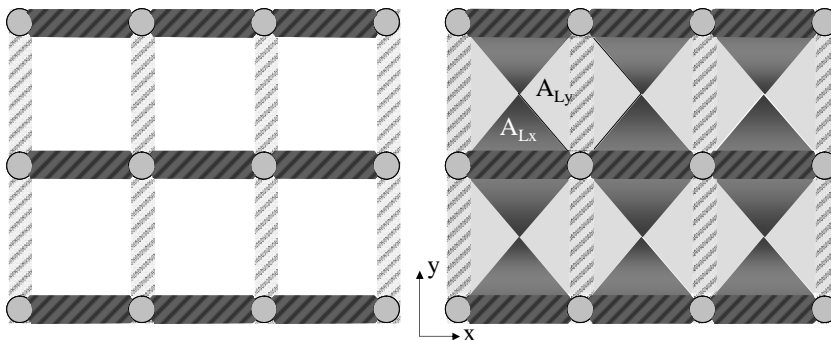
Figure 3.8 First suggestion for improvement to calculation step 2: subsoil support taken into account below the area of the tensile GR strips (left, EBGEO), or (right, suggested modification) the entire area below the GR (a diamond-shaped area per tensile GR strip).

3.4   Suggestions for improving step 2 of the analytical model

3.4.1   Subsoil support

Figure 3.3 shows that EBGEO mobilises only part of the subsoil, namely the area below the GR strips. This paper suggests that the subsoil below the entire GR area A_r should be taken into account. The difference between the areas below the GR strip and the entire GR area is shown in Figure 3.8. Lodder (2010) elaborated this modification by changing equation (3.5) into:

$$r(x) \;=\; K \cdot z(x) = \frac{A_{L_{x,y}}}{L_{x,y} \cdot B_{ers}} \cdot k_s \cdot z(x) \tag{3.9}$$

As the calculation value K for the subsoil has been changed, we find:

$$K_{EBGEO} = k_s$$

$$K_{Modified\ Subsoil} = \frac{A_{L_{x,y}} \cdot k_s}{L_{x,y} \cdot B_{ers}} \tag{3.10}$$

Using this $K_{Modified\ Subsoil}$[7] in equation (3.6) results in a differential equation that is solved in a way similar to that used to solve equation (3.6). Assuming that there are no other changes in the EBGEO calculations, this results in the same design graph given in Figure 3.4[8], with the same F_1, (equation (3.7)). However, F_2 changes into:

$$F_2 = \frac{K \cdot L_{x,y}^2}{J} = \frac{k_s \cdot A_{L_{x,y}} \cdot L_{x,y}}{J \cdot B_{ers}} \tag{3.11}$$

It should be noted that subsoil support should not always be taken into account. If the subsoil is expected to disappear over time, for example due to groundwater changes, the design should be based on an end situation without subsoil support. For cases of rather stiff subsoil on the other hand, for example preloaded subsoil, it is sufficiently safe to calculate on the basis of subsoil support. Of course, in cases when subsoil support is not taken into account, the presented modification has no influence.

3.4.2 Load on GR strip

EBGEO uses a triangular-shaped line load on the reinforcement strip between two piles (Figure 3.3). However, the measured GR vertical deflection shows that the distribution of the load is similar to an inverse triangle (Van Eekelen et al., 2012a, (Chapter 2 of this thesis) and Van Eekelen et al., 2011b), as shown in Figure 3.9. Assuming the apex of the axis between the pile caps is as shown in Figure 3.9, we find for $0 \le x \le 0.5L$:

$$q(x) = \frac{-2Q}{L} \cdot x \tag{3.12}$$

---

[7] This chapter uses the term "modified subsoil", which is referred to as "all subsoil" in Chapter 5.
[8] Appendix B gives the same graph, presented differently.
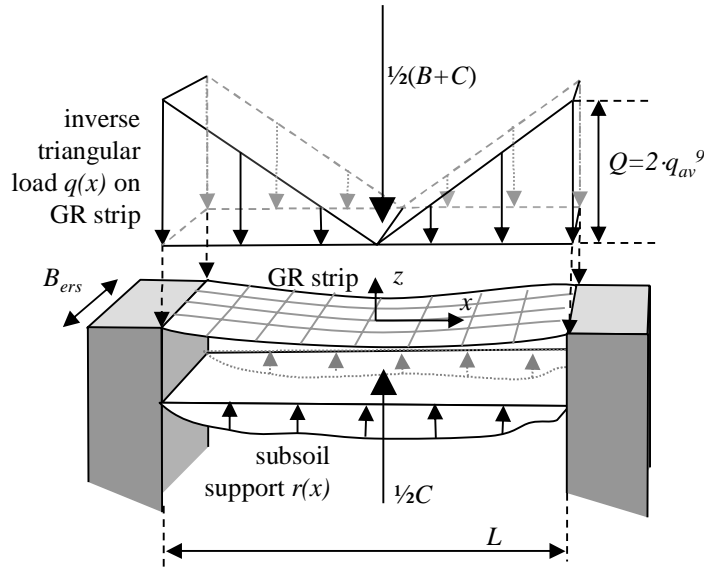
Figure 3.9 Second suggestion for improvement to calculation step 2: inverse triangular load $q(x)$ on GR strip.

with (assuming $s_x = s_y$)[9]: $Q = \dfrac{B+C}{A_s}$ (3.13)

This means that equation (3.6) changes into:

$$\frac{d^2z}{dx^2} - \frac{K}{T_H} \cdot z(x) = -\frac{2Q}{LT_H} \cdot x$$ (3.14)

Appendix 3.B shows how this equation is solved, resulting in[10]:

$$z(x) = -\frac{Q}{KL\alpha}\left(Me^{\alpha x} + (M-2)e^{-\alpha x} - 2\alpha x\right)$$

$$z'(x) = \frac{T_V}{T_H} = -\frac{Q}{KL\alpha}\left(M\alpha e^{\alpha x} - (M-2)\alpha e^{-\alpha x} - 2\alpha\right)$$

$$T(x) = T_H\sqrt{1 + \left(\frac{T_V}{T_H}\right)^2}$$ (3.15)

$$\varepsilon(x) = \frac{T(x)}{J}$$

where:

---

[9] Compare this definition of the maximum load on the GR strip Q, see Figure 3.17, with the definition of the average load on the GR strips q_{av}, see equation (5.9) and appendix 5.A. If $s_x = s_y$; $Q = 2q_{av}$. If $s_x \neq s_y$; the definition of q_{av} should be used as described in appendix 5.A..

[10] Appendix B of this thesis gives design graphs which can be used instead of these equations.

$$M = \frac{L\alpha + 2e^{-\frac{1}{2}\alpha L}}{e^{\frac{1}{2}\alpha L} + e^{-\frac{1}{2}\alpha L}} \quad \text{and:} \tag{3.16}$$

$$\alpha^2 = \frac{K}{T_H} \tag{3.17}$$

The unknown constant T_H can be determined from equalising the geometric GR strain and the constitutive GR strain over (half) the length of the GR strip:

$$\varepsilon_{geometric,average} = \frac{\int\limits_{x=0}^{x=\frac{1}{2}L} dx \sqrt{1 + \left(\frac{dz}{dx}\right)^2} - \frac{1}{2}L}{\frac{1}{2}L} = \tag{3.18}$$

$$\varepsilon_{constitutive,average} = \frac{\frac{1}{J}\int\limits_{x=0}^{x=\frac{1}{2}L} T(x)dx}{\frac{1}{2}L}$$

For the situation without subsoil support ($K \to 0$), the solution changes to:

$$z(x) = -\frac{Q}{3T_H L}\left(x^3 - \frac{1}{8}L^3\right)$$

$$z'(x) = -\frac{Q}{T_H L}\cdot x^2 \quad \left(= \frac{T_V}{T_H}\right) \tag{3.19}$$

as shown in Appendix 3.B.

3.4.3   GR strain on pile caps

EBGEO calculations do not incorporate GR strains on pile caps. However, the test measurements presented in this paper show that these are the largest GR strains. Incorporating GR strain on the pile caps in the EBGEO calculations would result in a lower GR strain, but more vertical deflection of the GR between the piles. However, as discussed in Van Eekelen et al., 2012a (Chapter 2 of this thesis), although this conclusion is true for smooth, small diameter piles such as used in the test series presented in Van Eekelen et al., 2012a (Chapter 2 of this thesis) or by Zaeske (2001), it is not necessarily true for larger pile caps with a frictional surface, such as those used along the N210 (Haring at al., 2008). Therefore, this finding was not implemented in the model modifications.

3.4.4 Results of modifications: step 2 calculation[11]
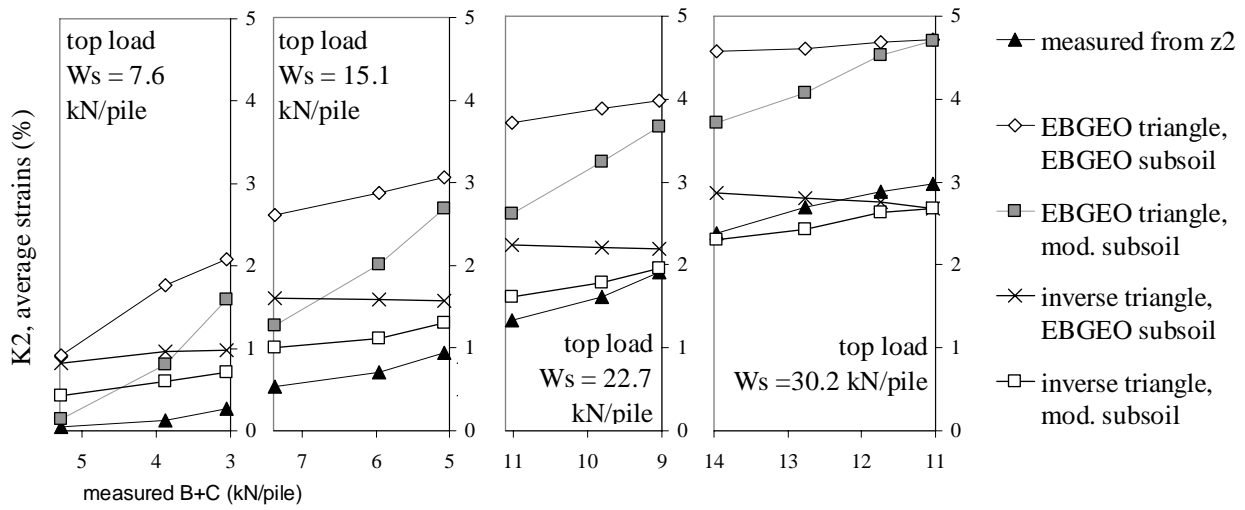
Figure 3.10 Calculation step 2: comparison measurements with EBGEO and the two suggested improvements (modified subsoil and inverse triangle, separately and together). It should be noted that $B+C$ decreases during each top load. All calculations are carried out using the measured $B+C$ value as an input parameter.
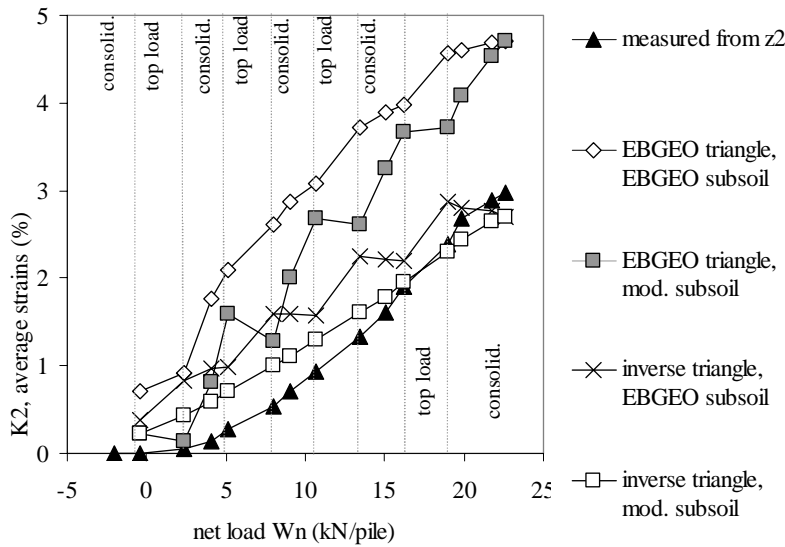
Figure 3.11 Calculation step 2: comparison measurements with EBGEO and the two suggested improvements (modified subsoil and inverse triangle, separately and together). All calculations are carried out using the measured $B+C$ value as an input parameter.

Figure 3.10 and Figure 3.11 compare the measured and calculated results of step 2. All calculations in these figures were carried out using the measured $(B+C)$ value as an input parameter. The figures clearly show that both modifications (subsoil and load distribution) result in an improvement. The closest agreement with the

---

[11] See also Van Eekelen and Bezuijen, 2012a, 2012c and 2013a.

test measurements is seen when the modifications are combined. For example, the combination of modified subsoil and the EBGEO-triangular load distribution gives a large overestimation of the consolidation response.

It can be concluded that the model using both modifications gives GR strain values that are more than 40% lower in the final phase of the test, and results in good agreement with the measurements.

3.5 Comparing the influence of fill, GR, and the use of double-layered systems in measurements and calculations

This chapter compares the calculated and measured influence of the fill, the stiffness of the GR, and the use of single- or double-layered systems, as described in Chapter 2.5 of this thesis (Chapter 5 of Van Eekelen et al. (2012a)). In the step 2 calculations, the suggested improvements for the EBGEO model are applied.

3.5.1 Friction angle of the fill: step 1 calculations

For step 1, Figure 3.12 compares the measured and calculated results for the sand test T2 and the corresponding granular test T3. The figure shows that the higher friction angle φ in test T3 leads to a larger increase in arching, both in the measurements and in the calculations. A higher φ value gives a larger increase in measured arching during the consolidation phases in particular. With EBGEO, however, subsoil consolidation results in no increase in load part A (kN/pile) and thus no dependency on the friction angle φ in response to subsoil consolidation.
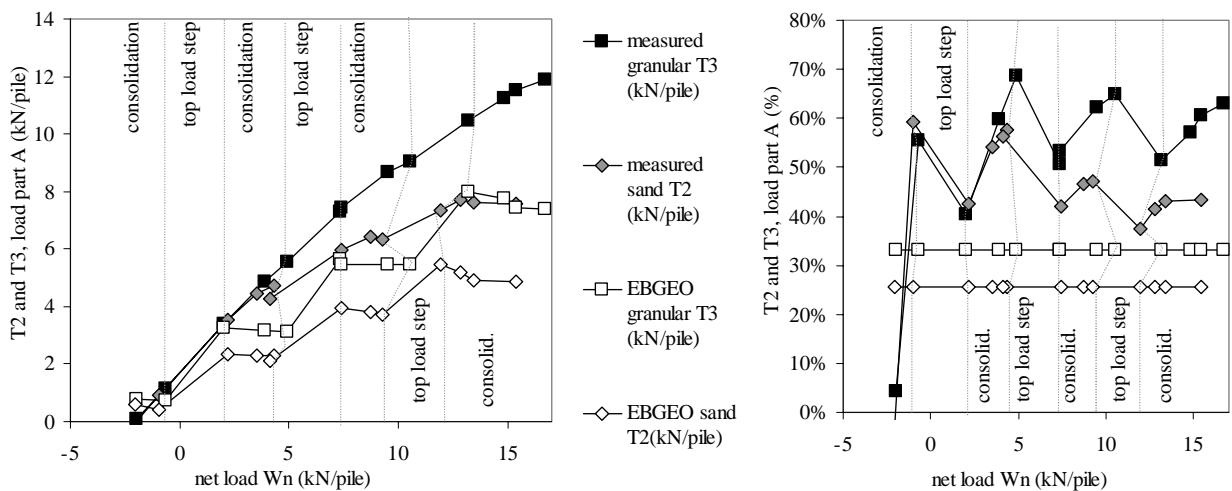
Figure 3.12 Tests T2 (sand, $\varphi = 40.9^{\circ}$) and T3 (granular, $\varphi = 49^{\circ}$), measurements and results from EBGEO step 1 calculations.

An increase in top load results in a decreasing value for the measured *A%*. EBGEO, however, always predicts a constant *A%*. This value is dependent on the geometry and the *φ*, not on changes in top load or subsoil support.

It can be concluded that EBGEO's lack of response to consolidation (in step 1) is dominant, so that EBGEO considerably underestimates arching load *A*. Fill with a lower *φ* value (sand) responds much less to consolidation than granular fill. It therefore seems that EBGEO predicts the behaviour of sand better than that of granular fill.

3.5.2   Stiffness of the GR

The GR stiffness *J* does not influence the arching behaviour (step 1) of the piled embankment in the measurements: virtually an identical *A* value is found for each GR if other factors remain the same. The measurements (Figure 2.14) and calculations using EBGEO (= step 1, see Chapter 3.3.1) correspond with this.
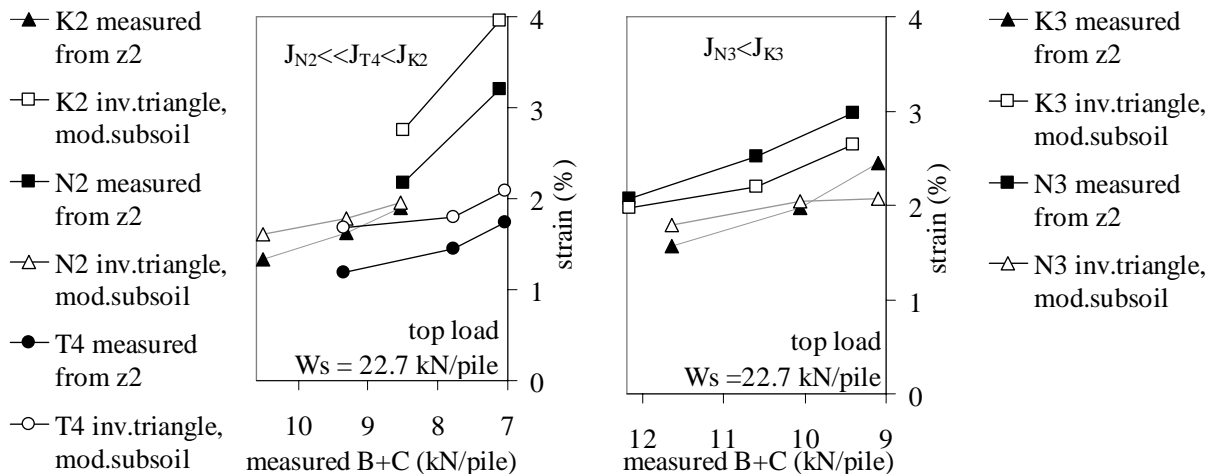
Figure 3.13 The influence of GR stiffness *J* on average GR strain; comparison measurements and step 2 calculations using both suggested modifications (inverse triangle and modified subsoil). Compare with Figure 3.10. Left: Tests K2, N2 and T4, all with a single GR layer and granular fill. Right: Tests N3 and K3, both with a double GR layer and granular fill.

However, the GR stiffness *J* influences the GR strain (step 2), both in the measurements and the calculations. Figure 3.13 shows that measured and calculated GR strains are in the same range when they are considered as a function of *B+C* (thus step 2), and that the influence of *J* is approximately the same in the measurements and the calculations. Figure 3.14 shows that the tendency of the measured and calculated GR strains is also the same when they are considered as a function of the net load.

Table 3.1 gives the stiffness properties of the GR for tests presented in Figure 3.13 and Figure 3.14. The GR stiffness is strain-dependent and therefore depends on the GR strain that occurs.
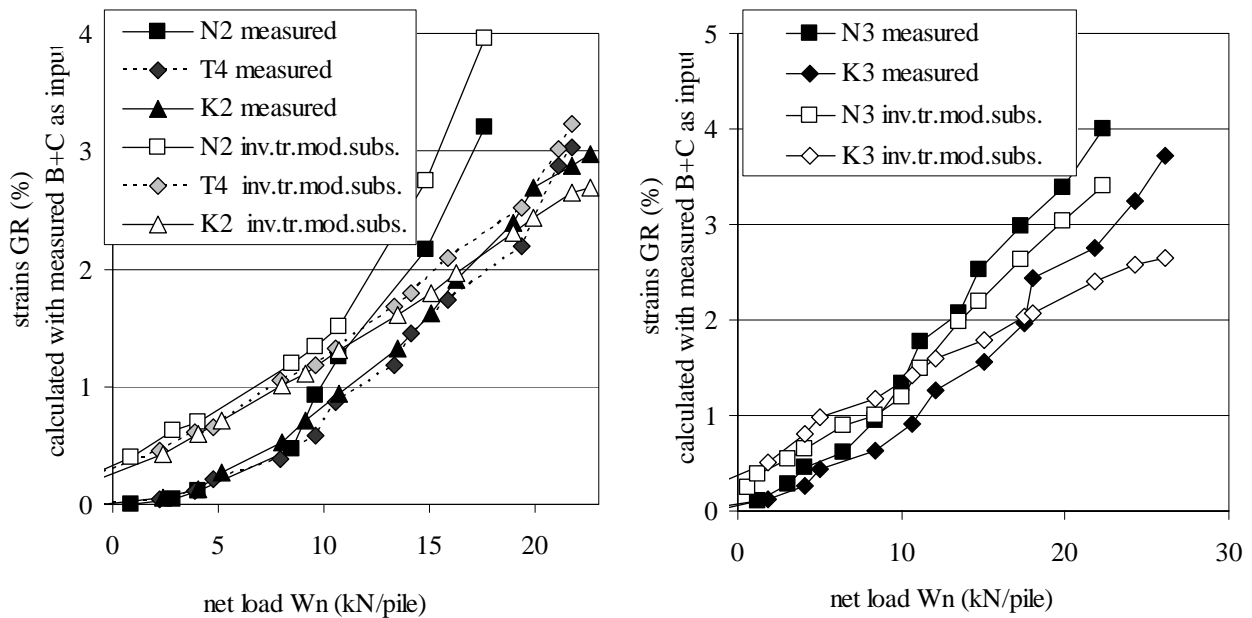
Figure 3.14 Comparison of the influence of GR stiffness *J* on measured average strain, and GR strain calculated using the two suggested modifications (inverse triangle and modified subsoil). Left: one grid layer, right: two grid layers.

Table 3.1 Strain-dependent stiffness; stiffness calculated from measured GR strains (calculated from measured vertical deflection GR *z2*) and strain-stiffness graphs determined in accordance with CEN ISO 10319.

| top load[a] | one geogrid layer | | | two geogrid layers[b] | | |
| | K2 | N2 | | K2 | N2 | |
kN/pile	kN/m	kN/m	kN/pile	kN/m	kN/m	kN/pile
15.2	2269[c]	1551[c]	15.2	2269[c]	1551[c]	15.2
22.7	2269	787	22.7	2269	787	22.7
30.3	2255		30.3	2255		30.3

[a] stiffness calculated for this top load and a maximum consolidated subsoil (consolidated situation)

[b] stiffness for both grid layers summed

[c] strain-stiffness graphs were not available for very small GR strains and are therefore taken as constant until the minimum strain given in the graphs

Table 3.2 Input properties for post-calculations.

height of the embankment	H	m	0.42
diameter of the pile (no caps were applied)	d	m	0.10
centre-to-centre distance piles	s_x, s_y	m	0.55
diagonal centre-to-centre distance piles	s	m	0.78
arching reduction coefficient[a]	κ	-	1.00
internal friction angle granular material[b]	φ_{peak}	deg	49.00
internal friction angle sand test T1	φ_{peak}	deg	40.33
internal friction angle sand test T2	φ_{peak}	deg	40.90

[a] suggested by Heitz (2006) and adopted in EBGEO and CUR 226 for relatively high dynamic loads, $\kappa = 1.0$ means that the calculations have been carried out without arching reduction.
[b] determined with large diameter triaxial tests (Den Boogert, 2011)

Table 3.3 Input properties for test K2.

step in test	input top load = top load W_s – friction R p-R kN/pile	subgrade reaction k_s kN/m³	average GR stiffness $J_{2\%}$ kN/m	load parts B+C kN/pile
2	0.37	548	2269	1.14
3	6.82	2923	2269	5.28
4	6.71	881	2269	3.88
5	6.65	330	2269	3.06
6	13.34	1194	2269	7.79
7	12.60	583	2269	6.35
8	12.45	233	2269	5.48
9	18.97	733	2269	10.51
10	18.51	383	2269	9.30
11	18.09	175	2269	8.53
12	24.34	512	2263	13.77
13	23.40	294	2259	12.57
14	22.92	85	2256	11.55
15	22.67	2	2255	10.84

3.5.3   One or two GR layers

Figure 3.15 compares the measured and calculated results of step 1 (left) and step 2 (right) for tests K2 and K3. As in all comparisons, the calculations of step 1 give a lower load A than the measured value. The step 1 measurements show that development of arching is slower in the double-layered system, but is steadier than in the single-layered system, as explained in Van Eekelen et al. (2012a, chapter 2 of this thesis). This tendency is also observed in the (trend lines through the) calculations.
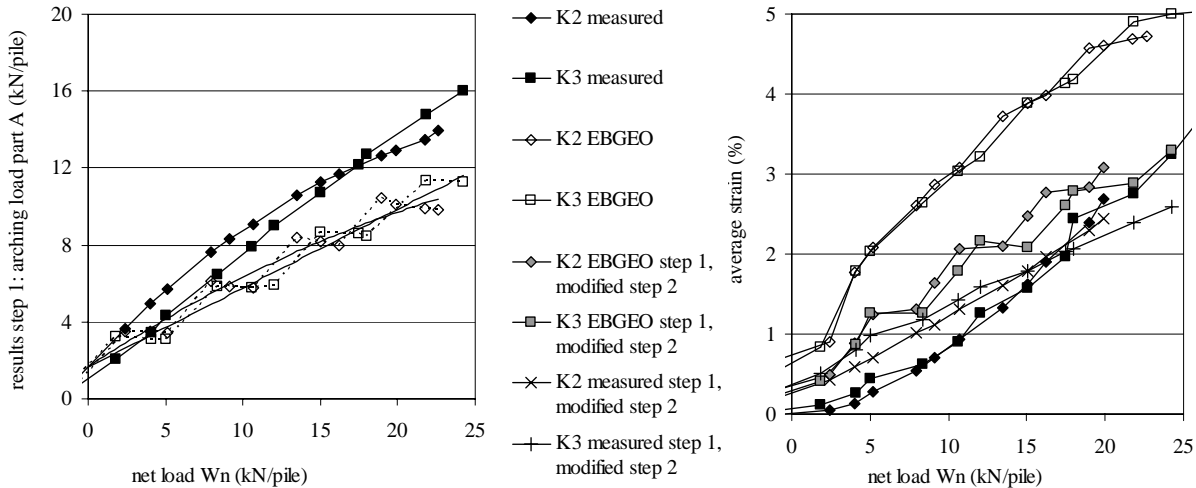
Figure 3.15 Load distribution, comparison of reinforcement divided in one (K2) or two (K3) grid layers, comparison of EBGEO with and without subsoil modifications and measurements. The thick lines are second order polynomial fits through the measurements.

For both steps 1 and 2, it can be concluded that the calculations do not match the measurements in the single-layered systems any more closely than they match measurements in the double-layered systems.

3.6   Conclusions

EBGEO consists of two calculation steps; step 1 and step 2. Step 1 calculates the loading on the piles *A* due to arching and consequently the resulting value *B+C* (load on GR and subsoil), and step 2 calculates the resulting strains in the GR. It is shown that step 1 calculates a higher *B+C* value (load on GR and subsoil) than the measured value, and step 2 calculates higher GR strains than are seen in the measurements. Any design calculations made using EBGEO are therefore on the safe side. This over-prediction is mainly due to the following reasons:

3.6.1   Step 1

Consolidation of the subsoil results in increased measured arching in the fill. Consolidation (subsoil deformation) is in fact necessary for the development of arching. In addition, the measured response to consolidation depends on the internal friction angle of the fill. If EBGEO is used, consolidation leads to no increase in arching. This results in a value for arching load part *A* that is lower than shown in the model tests, and in turn gives a calculation for load part *B+C* that is higher than shown in the model tests. This agrees with the conclusion that the net load on the fill determines the behaviour of the

system. The improvement of step 1 is a subject for further study, and will be published in 'Geotextiles and Geomembranes' at a later date.

3.6.2   Step 2

EBGEO mobilises only part of the subsoil, namely the area below the GR strips between the piles. This paper suggests how the supporting subsoil area can be increased, and shows that this gives much better agreement with the measurements.

The measured GR vertical deflection shows that the distribution of the line load on the reinforcement strip between two piles tends to have the distribution of an inverse triangle. However, EBGEO calculations are based on a triangular-shaped line load.

EBGEO calculations do not take GR strains on the pile caps into account, although these can be the largest GR strains under specific conditions, such as for the smooth, small-diameter pile caps in the test set-up. As this will generally not be the case in the field, it was decided not to modify the step 2 calculations on the basis of this conclusion.

This paper presents equations for modifying step 2 by improving both the subsoil support and the load distribution. It has been shown that this gives more than 40% less GR strain than the EBGEO assumptions, so providing much better agreement with the test measurements.

The influence of the GR stiffness *J* is comparable in the modified EBGEO step 2 calculations and in the measurements. The agreement between calculated and measured results is neither better nor worse for single-layered systems than for double-layered systems.

Appendix 3.A Procedure for analytical calculations to compare with experimental results

The measurements were calculated using EBGEO (2010). No safety factors were applied, and only vertical load was considered as no thrust forces occur within the test box. Without safety factors, calculations in accordance with EBGEO (2010) are the same as calculations in accordance with CUR 226 (2010), as described (in English) in Van Eekelen et al., (2010b).

BS8006-1 (2010) and Modified BS8006 (Van Eekelen and Bezuijen, 2008 and Van Eekelen et al., 2011a, adopted in appendix A of this thesis) do not take subsoil support into account, and are therefore not suitable for comparing the measurements under consideration.

EBGEO input parameters

Table 3.2 (page 57) shows the input parameters that are identical for each test. Table 2.1 gives the unit weight of the fills.

For each equilibrium point, the following input parameters were determined separately.

(1)   The top load w_s in kPa; the friction R (kN/pile) measured in each test was subtracted from the measured top load W_s (kN/pile) and converted to kPa by

$$w_{s,input} = 4(W_s - R) / A_{fill} \tag{3.20}$$

(2)   The GR stiffness. Each supplier determined the strain-dependent stiffness behaviour of their GR, in accordance with CEN ISO 10319. This value was used to determine the stiffness for each equilibrium point from the measured vertical deflection $z2$, using the following steps. (a) The average strain ε of the GR strip was determined from the measured $z2$, assuming a third order power law deformation pattern (this procedure appeared to be more reliable than using the results of the cable measurement system, see Van Eekelen et al., 2012a) (b) The supplied stiffness behaviour graphs from the suppliers of the various GRs provide a stiffness value for this ε. Where GR strains were less than the lowest given strain, the same stiffness was assumed as that given for the smallest strain in the suppliers' data. Therefore, the stiffness is assumed to be constant for small GR strains. The stiffness along and perpendicular to the machine direction is determined separately.

(3)   The modulus of the foam's subgrade reaction, k_s, in kN/m^3, while the tap is closed in between the loading or drainage steps. The somewhat 'artificial' modulus of subgrade reaction has been determined as follows:

$$k_s = \frac{C}{A_{foam} \cdot z}$$ (3.21)

where z (m) is the average settlement of the foam cushion due to consolidation (calculated from the measured volume of water drained from the foam cushion).

In the measurements, the soaked foam cushion gives a more constant loading over the whole area. EBGEO assumes that deformation of the subsoil is proportional to loading on the subsoil. This will be closer to reality. In EBGEO and in the field, the GR will experience more support in the centre between two piles. The shape of the deformed GR will therefore approach an even higher order power law function than the foam cushion construction. Table 3.3 (page 57) presents the input parameters for test K2.

EBGEO output parameters
The calculation results of calculation step 1 are given in terms of *A* equation (3.1), and *B+C* (equation (3.2)), for load distribution, see Figure 3.2). The results of calculation step 2 (membrane behaviour) are given in terms of average GR strain: Figure 3.4 and equation (3.7) for EBGEO, and equation (3.44) for the suggested modification of step 2.

Appendix 3.B Derivation of the step 2 equations for inverse triangle load distribution[12]

The tensile force is calculated from the inverse triangular load $q(x)$. A tension membrane is considered with a tensile force T, components T_V and T_H, and a load $q(x)$ in kN/m. The equilibrium of a small particle is first considered as given in Figure 3.16.
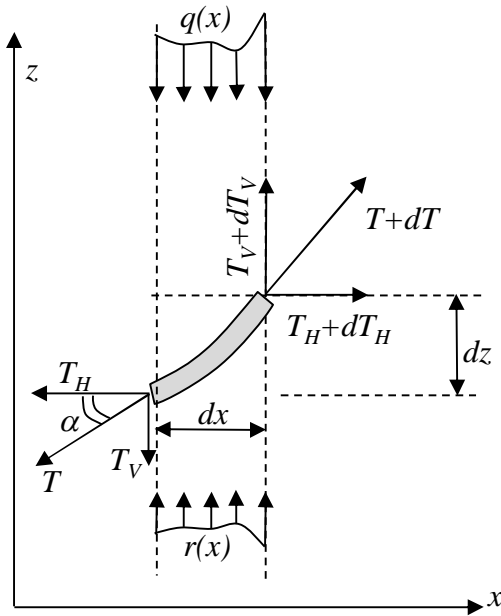
Figure 3.16 Equilibrium tension membrane.
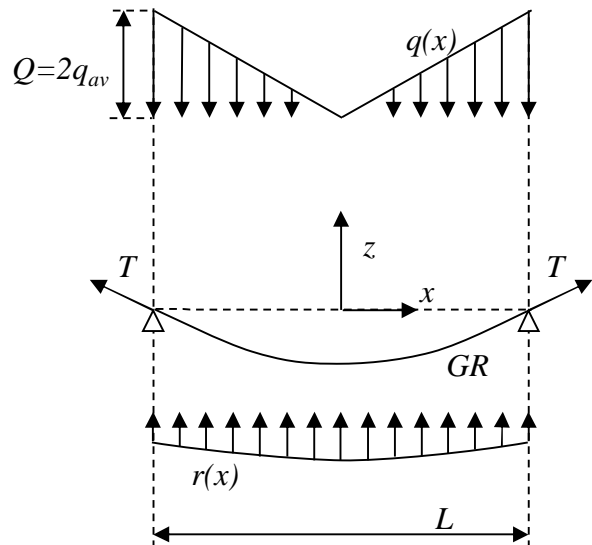
Figure 3.17 Deformed GR with inverse triangular load.

From the horizontal equilibrium, it follows:

$$T_H - T_H - dT_H = 0 \qquad \rightarrow \qquad dT_H = 0 \tag{3.22}$$

From the vertical equilibrium, it follows:

$$-T_V - q(x)dx + r(x)dx + T_V + dT_V = 0 \qquad \rightarrow \qquad q(x) - r(x) = \frac{dT_V}{dx} \tag{3.23}$$

The relationship between the components T_H and T_V of the tensile force, dz and dx, and the angle α is:

$$\tan \alpha = \frac{T_V}{T_H} = \frac{dz}{dx} \qquad \rightarrow \qquad T_V = T_H \frac{dz}{dx} \tag{3.24}$$

---

[12] Appendix 5.A summarizes the equations for both the uniformly distributed and inverse-triangular distributed load on the GR strips. Appendix 4.B gives calculation examples.

This gives:

$$\frac{dT_V}{dx} = \frac{dT_H}{dx}\frac{dz}{dx} + T_H\frac{d^2z}{dx^2} \tag{3.25}$$

Using equation (3.22) and thus $\frac{dT_H}{dx} = 0$ it follows:

$$\frac{dT_V}{dx} = T_H\frac{d^2z}{dx^2} \tag{3.26}$$

Using equation (3.23), this gives the differential equation for reinforcement strips:

$$\frac{d^2z}{dx^2} = \frac{q(x) - r(x)}{T_H} = \frac{q_{net}(x)}{T_H} \tag{3.27}$$

Where $q_{net}(x)$ is the net load on the GR strip. For the inverse triangular load, we find for $0 < x < L/2$ (see Figure 3.17):

$$q(x) = -\frac{2Q}{L}\cdot x \tag{3.28}$$

With

$$Q = \frac{2\cdot\frac{1}{2}\cdot(B+C)}{A_s} = \frac{B+C}{A_s} \tag{3.29}$$

Thus:

$$\frac{d^2z}{dx^2} + \frac{r(x)}{T_H} = -\frac{2Q}{LT_H}\cdot x \tag{3.30}$$

Using equation (3.5) or (3.9) it follows that the differential equation to be solved is:

$$\frac{d^2z}{dx^2} - \frac{K}{T_H}z(x) = -\frac{2Q}{LT_H}\cdot x \tag{3.31}$$

Homogeneous solution

The corresponding homogeneous equation is:

$$\frac{d^2z}{dx^2} - \frac{K}{T_H} z(x) = 0 \tag{3.32}$$

If a solution is assumed to be:

$$z(x) = A \cdot e^{\alpha x} \tag{3.33}$$

substitution in equation (3.32) gives:

$$A\alpha^2 e^{\alpha x} - \frac{K}{T_H} A e^{\alpha x} = 0 \tag{3.34}$$

Thus: $\alpha^2 = \dfrac{K}{T_H}$ $\tag{3.35}$

and the complementary function is:

$$z(x) = A_1 \cdot e^{\alpha x} + A_2 \cdot e^{-\alpha x} \tag{3.36}$$

Particular solution

If a solution is assumed to be:

$$z(x) = A_3 \cdot \frac{Q}{LT_H} \cdot x \tag{3.37}$$

substitution in equation (3.31) gives:

$$0 - \frac{K}{T_H} \cdot A_3 \cdot \frac{Q}{LT_H} \cdot x = -\frac{2Q}{LT_H} \cdot x \quad \rightarrow \quad A_3 = 2\frac{T_H}{K}\left(=\frac{2}{\alpha^2}\right) \tag{3.38}$$

and the particular term is:

$$z(x) = 2 \cdot \frac{Q}{KL} \cdot x \tag{3.39}$$

General solution
The following general solution results (for $0 < x < L/2$):

$$z(x) = A_1 \cdot e^{\alpha x} + A_2 \cdot e^{-\alpha x} + \frac{2Q}{KL} \cdot x$$

$$z'(x) = A_1\alpha \cdot e^{\alpha x} - A_2\alpha \cdot e^{-\alpha x} + \frac{2Q}{KL}$$

(3.40)

Boundary conditions
Two constraints give expressions for A_1 and A_2:

$$z'(0) = 0 \quad \rightarrow \quad A_1\alpha - A_2\alpha + \frac{2Q}{KL} = 0 \quad \rightarrow \quad A_2 = A_1 + \frac{2Q}{KL\alpha}$$

$$z\left(\frac{L}{2}\right) = 0 \quad \rightarrow \quad A_1 e^{\frac{1}{2}\alpha L} + \left(A_1 + \frac{2Q}{KL\alpha}\right)e^{-\frac{1}{2}\alpha L} + \frac{Q}{K} = 0$$

(3.41)

For the second constraint it is assumed that the pile and pile cap behave rigidly. We find that the critical height decreases:

$$A_1 = -\frac{Q}{KL\alpha} \cdot \frac{L\alpha + 2e^{-\frac{1}{2}\alpha L}}{e^{\frac{1}{2}\alpha L} + e^{-\frac{1}{2}\alpha L}} \quad and \quad A_2 = -\frac{Q}{KL\alpha} \cdot \left(\frac{L\alpha + 2e^{-\frac{1}{2}\alpha L}}{e^{\frac{1}{2}\alpha L} + e^{-\frac{1}{2}\alpha L}} - 2\right)$$

(3.42)

It follows that:

$$z(x) = -\frac{Q}{KL\alpha} \cdot \left(Me^{\alpha x} + (M-2)e^{-\alpha x} - 2\alpha x\right)$$

(3.43)

$$where \quad M = \frac{L\alpha + 2e^{-\frac{1}{2}\alpha L}}{e^{\frac{1}{2}\alpha L} + e^{-\frac{1}{2}\alpha L}}$$

From this, the tensile force in the GR and the GR strain can be calculated as follows:

$$z'(x) = -\frac{Q}{KL\alpha} \cdot \left(M\alpha e^{\alpha x} - (M-2)\alpha e^{-\alpha x} - 2\alpha\right)$$

$$T(x) = T_H\sqrt{1 + z'(x)^2}$$

$$\varepsilon(x) = \frac{T(x)}{J}$$

(3.44)

The average strain can be calculated numerically, as shown in equation (3.45). Because the average strains were measured (see appendix 3.A), average strains are calculated for comparisons with the measurements presented in this paper. EBGEO always determines average strains. However, it is preferable to base a design on the calculated maximum strains, calculated from (3.44) using $x = L/2$.

The unknown constant T_H can be determined by equalising the geometric strain and the constitutive strain over (half) the length of the GR strip:

$$\varepsilon_{geometric,average} = \frac{\int\limits_{x=0}^{x=\frac{1}{2}L} dx\sqrt{1+\left(\frac{dz}{dx}\right)^2} - \frac{1}{2}L}{\frac{1}{2}L} = \varepsilon_{constitutive,average} = \frac{\frac{1}{J}\int\limits_{x=0}^{x=\frac{1}{2}L} T(x)\,dx}{\frac{1}{2}L} \qquad (3.45)$$

Situation without subsoil support ($K \to 0$):
If the Maclaurin series is applied:

$$
\begin{aligned}
e^{\alpha x} &= 1 + \alpha x + \tfrac{1}{2}\alpha^2 x^2 + \tfrac{1}{6}\alpha^3 x^3 + \tfrac{1}{24}\alpha^4 x^4 + \tfrac{1}{120}\alpha^5 x^5 ..... \\
e^{-\alpha x} &= 1 - \alpha x + \tfrac{1}{2}\alpha^2 x^2 - \tfrac{1}{6}\alpha^3 x^3 + \tfrac{1}{24}\alpha^4 x^4 - \tfrac{1}{120}\alpha^5 x^5 ..... \\
e^{\frac{1}{2}\alpha L} &= 1 + \tfrac{1}{2}\alpha L + \tfrac{1}{2}\left(\tfrac{1}{2}\alpha\right)^2 L^2 + \tfrac{1}{6}\left(\tfrac{1}{2}\alpha\right)^3 L^3 + \tfrac{1}{24}\left(\tfrac{1}{2}\alpha\right)^4 L^4 + \tfrac{1}{120}\left(\tfrac{1}{2}\alpha\right)^5 L^5 ..... \\
e^{-\frac{1}{2}\alpha L} &= 1 - \tfrac{1}{2}\alpha L + \tfrac{1}{2}\left(\tfrac{1}{2}\alpha\right)^2 L^2 - \tfrac{1}{6}\left(\tfrac{1}{2}\alpha\right)^3 L^3 + \tfrac{1}{24}\left(\tfrac{1}{2}\alpha\right)^4 L^4 - \tfrac{1}{120}\left(\tfrac{1}{2}\alpha\right)^5 L^5 ....
\end{aligned}
\qquad (3.46)
$$

And thus:

$$
\begin{aligned}
e^{\alpha x} + e^{-\alpha x} &= 2 + \alpha^2 x^2 + \tfrac{1}{12}\alpha^4 x^4 ..... \\
-2e^{-\alpha x} &= -2 + 2\alpha x - \alpha^2 x^2 + \tfrac{1}{3}\alpha^3 x^3 - \tfrac{1}{12}\alpha^4 x^4 + \tfrac{1}{60}\alpha^5 x^5 ..... \\
e^{\frac{1}{2}\alpha L} + e^{-\frac{1}{2}\alpha L} &= 2 + \left(\tfrac{1}{2}\alpha\right)^2 L^2 + \tfrac{1}{12}\left(\tfrac{1}{2}\alpha\right)^4 L^4 .... \\
2e^{-\frac{1}{2}\alpha L} &= 2 - \alpha L + \left(\tfrac{1}{2}\alpha\right)^2 L^2 - \tfrac{1}{3}\left(\tfrac{1}{2}\alpha\right)^3 L^3 + \tfrac{1}{12}\left(\tfrac{1}{2}\alpha\right)^4 L^4 - \tfrac{1}{60}\left(\tfrac{1}{2}\alpha\right)^5 L^5 .....
\end{aligned}
\qquad (3.47)
$$

Equation (3.43) is written as:

$$z(x) = -\frac{Q}{T_H L}\cdot\frac{1}{\alpha^3}\cdot\left[\left(\frac{L\alpha + 2e^{-\frac{1}{2}\alpha L}}{e^{\frac{1}{2}\alpha L} + e^{-\frac{1}{2}\alpha L}}\right)\left(e^{\alpha x} + e^{-\alpha x}\right) - 2e^{-\alpha x} - 2\alpha x\right] \qquad (3.48)$$

Substituting equation (3.47) in equation (3.48) gives:

$$z(x) = -\frac{Q}{T_H L} \cdot \frac{1}{\alpha^3} \cdot \left[\left(\frac{L\alpha + 2 - \alpha L + \left(\frac{1}{2}\alpha\right)^2 L^2 - \frac{1}{3}\left(\frac{1}{2}\alpha\right)^3 L^3 + \frac{1}{12}\left(\frac{1}{2}\alpha\right)^4 L^4 - \frac{1}{60}\left(\frac{1}{2}\alpha\right)^5 L^5}{2 + \left(\frac{1}{2}\alpha\right)^2 L^2 + \frac{1}{12}\left(\frac{1}{2}\alpha\right)^4 L^4} \right) \cdot \right.$$

$$\left. \cdot \left(2 + \alpha^2 x^2 + \frac{1}{12}\alpha^4 x^4\right) - 2 + 2\alpha x - \alpha^2 x^2 + \frac{1}{3}\alpha^3 x^3 - \frac{1}{12}\alpha^4 x^4 + \frac{1}{60}\alpha^5 x^5 - 2\alpha x \right]$$

(3.49)

Thus:

$$z(x) = -\frac{Q}{T_H L} \cdot \frac{1}{\alpha^3} \cdot \left[\left(1 + \frac{-\frac{1}{3}\left(\frac{1}{2}\alpha\right)^3 L^3 - \frac{1}{60}\left(\frac{1}{2}\alpha\right)^5 L^5}{2 + \left(\frac{1}{2}\alpha\right)^2 L^2 + \frac{1}{12}\left(\frac{1}{2}\alpha\right)^4 L^4} \right) \cdot \left(2 + \alpha^2 x^2 + \frac{1}{12}\alpha^4 x^4\right) \right.$$

$$\left. - 2 - \alpha^2 x^2 + \frac{1}{3}\alpha^3 x^3 - \frac{1}{12}\alpha^4 x^4 + \frac{1}{60}\alpha^5 x^5 \right]$$

(3.50)

Therefore:

$$z(x) = -\frac{Q}{T_H L} \cdot \left[\left(\frac{-\frac{1}{3}\left(\frac{1}{2}\right)^3 L^3 - \frac{1}{60}\left(\frac{1}{2}\right)^5 \alpha^2 L^5}{2 + \left(\frac{1}{2}\alpha\right)^2 L^2 + \frac{1}{12}\left(\frac{1}{2}\alpha\right)^4 L^4} \right) \cdot \left(2 + \alpha^2 x^2 + \frac{1}{12}\alpha^4 x^4\right) + \frac{1}{3}x^3 + \frac{1}{60}\alpha^2 x^5 \right]$$

(3.51)

For $K \to 0$, we find $\alpha \to 0$, thus:

$$z(x) = -\frac{Q}{3T_H L} \cdot \left(x^3 - \frac{1}{8}L^3 \right)$$

(3.52)

4   An Analytical Model for Arching in Piled Embankments (step 1)
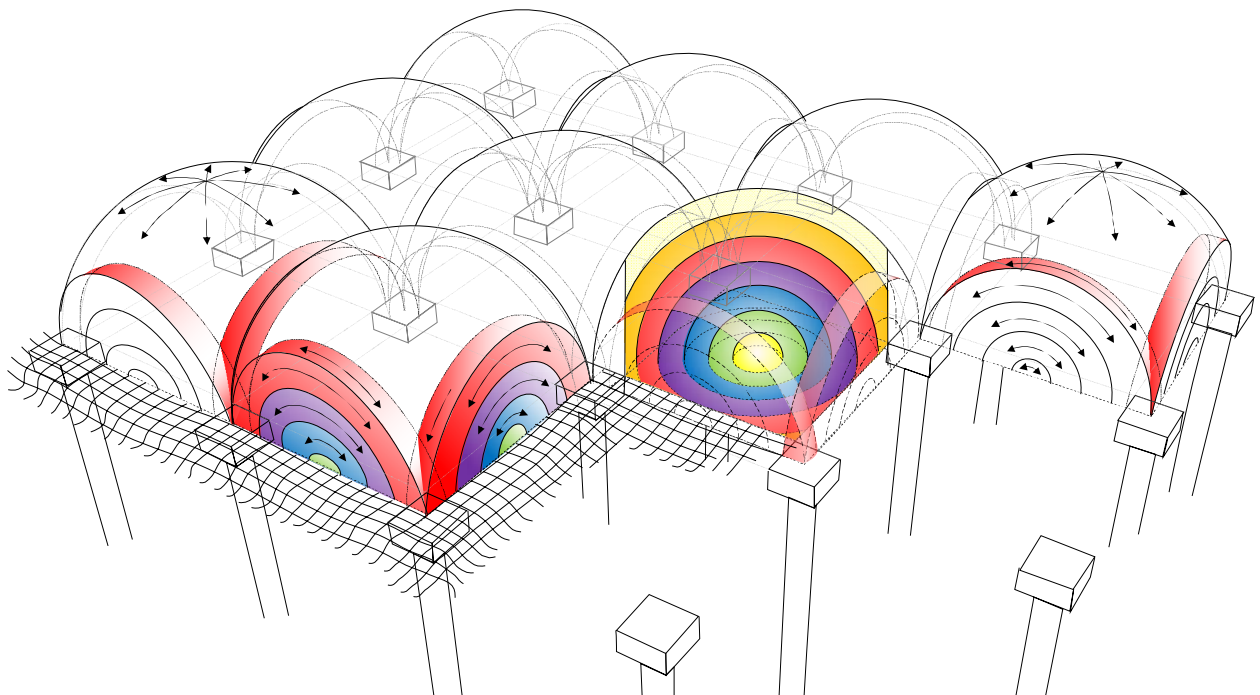
Abstract

Most analytical models for the design of piled embankments or load transfer platforms with geosynthetic reinforcement (GR) include two calculation steps. Step 1 calculates the arching behaviour in the fill and step 2 the load-deflection behaviour of the GR. A calculation method for step 2 based on the results of model tests has been published by Van Eekelen et al., 2012a (Chapter 2) and 2012b (Chapter 3). The present paper analyses and presents a new model for step 1, which is the arching step. Additional tests, which are also presented in this paper, were conducted for this purpose.
The new model is a limit-state equilibrium model with concentric arches. It is an extension of the models of Hewlett and Randolph (1988) and Zaeske (2001). The new model results in a better representation of the arching measured in the experiments than the other models mentioned, especially for relatively thin fills.

Introducing GR in a piled embankment results in a more efficient transfer of load to the piles in the form of an arching mechanism. The load is then exerted mainly on the piles and the GR strips between the piles, on which the load is approximately distributed as an inverse triangle. The new model presented in this paper describes this behaviour and is therefore meant to describe the situation with GR. The new model provides a physical explanation for observations of the arching mechanism, especially the load distribution on the GR. Other observations with which this model concurs are the dependency on fill height and friction angle. The amount of arching increases with increasing subsoil consolidation and GR deflection. The paper describes how the new model relates to the development of arching as a result of subsoil consolidation.

4.1   Introduction

Many analytical design models for the design of piled embankments include two calculation steps. The first step calculates the arching behaviour in the fill. This step divides the total vertical load into two parts: load part A, and the 'residual load' ($B+C$ in Figure 4.1). Load part A, called 'arching A' in the present paper, is the part of the load that is transferred to the piles directly.

The second calculation step describes the load-deflection behaviour of the geosynthetic reinforcement (GR, see Figure 4.1). In this calculation step, the 'residual load' is applied to the GR strip between each pair of adjacent piles and the GR strain is calculated. An implicit result of step 2 is that the 'residual load' is divided into a load part B which passes through the GR to the piles, and a part C resting on the subsoil, as indicated in Figure 4.1.

70

Van Eekelen et al. (2012b, Chapter 3 of this thesis) analysed and made proposals for calculation step 2. The present paper analyses and puts forward a new model for step 1, the arching step. Both papers compare the results with measurements from a model test series presented in the first part of this three-part study (Van Eekelen et al., 2012a, Chapter 2 of this thesis). These tests are particularly suitable for the validation of calculation steps 1 and 2 separately because *A, B* and *C* were measured separately. For the present paper, a number of additional tests were carried out with the same test set-up.
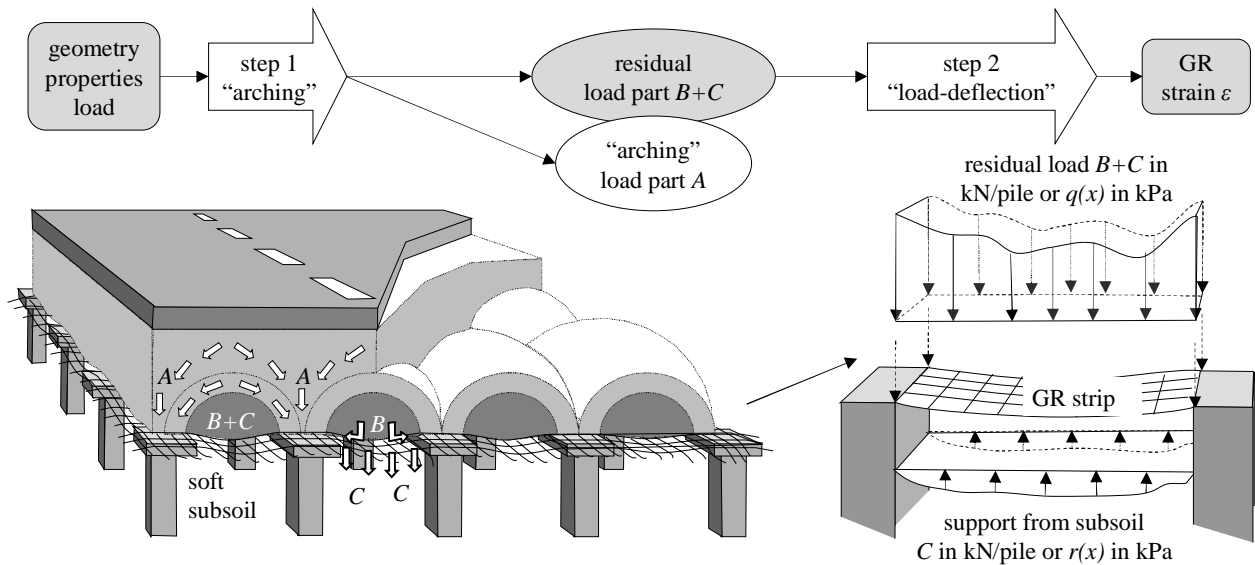
Figure 4.1 Calculating the geosynthetic reinforcement (GR) strain comprises two calculation steps.

Several families of analytical models describing step 1 (arching) are available in the literature. Terzaghi (1943) listed a number of them. Current arching models comprise:

Rigid arch models, such as several Scandinavian models (Carlsson (1987), Rogbeck et al. (1998, modified by Van Eekelen et al. (2003)), Svanø et al. (2000)) and the Enhanced Arching model (also called the Bush-Jenner model or the Collin (2004) model) and the present design method of the Public Work Research Centre in Japan (2000, discussed in Eskişar et al. (2012)). In this class of models, it is assumed that an arch is formed that has a fixed shape. The shape of the arch is usually 2D or 3D triangular. It is assumed that the entire load above the arch, including the soil weight and the traffic load, is transferred directly to the piles (load part *A,* or arching *A*, see Figure 4.1). The weight of the soil wedge is carried by the GR + subsoil (*B+C*). These models do not consider the mechanical properties of the fill, such as the friction angle, in their equations and they are therefore not discussed further in the present paper.

In equilibrium models, an imaginary limit-state stress-arch is assumed to appear above the GR + soft subsoil between the stiff elements. In the 3D situation, these stiff elements are piles; in the 2D situation, they are beams or walls. The pressure on the GR + subsoil ($B+C$) is calculated by considering the equilibrium of the arch. In most models, the arch has a certain thickness.

Two limit-state equilibrium models are frequently used in piled embankment design today. One of them is the Hewlett and Randolph model (1988, explained in Figure 4.2), which was adopted in the French ASIRI guideline (2012) and suggested in BS8006 (2010) as an alternative for the original empirical model in BS8006. The other frequently used equilibrium model is Zaeske's model (2001, and also described in Kempfert et al., 2004), which is explained in Figure 4.3. This model was adopted in the German EBGEO (2010) and the Dutch CUR226 (2010, described in Van Eekelen et al., 2010b), and we refer to it here as 'EBGEO'.
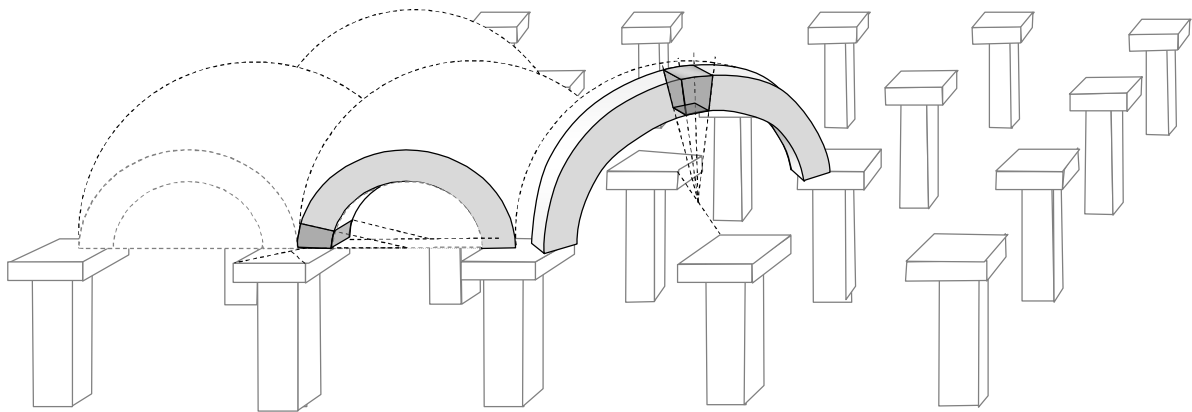
Figure 4.2 Hewlett and Randolph (1988) consider the 'crown' element of the diagonal arch and the 'foot' element (just above the pile cap) of the plane strain arch as indicated in this figure.
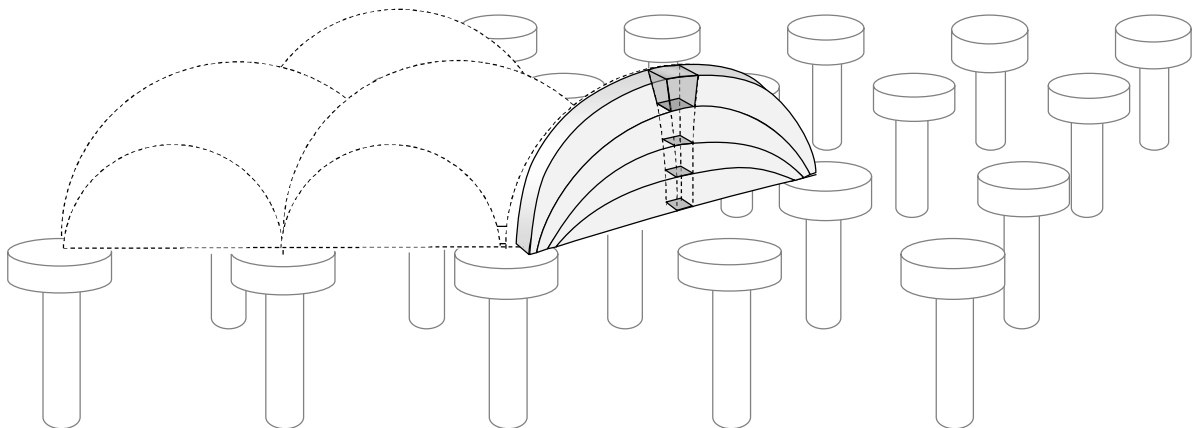
Figure 4.3 Zaeske (2001) considers the equilibrium of the crown elements of the diagonal arches.

Another family of arching models is the family of frictional models. Several authors have adopted the frictional model proposed by Terzaghi (1943), who in turn based his model on previous work from other authors such as Cain (1916) and Völlmy (1937). McKelvey (1994) extended Terzaghi by assuming that a 'plane of equal settlement' exists and combined this with a tensioned membrane theory.

Russell and Pierpoint (1997) extended the Terzaghi model to include a third dimension by assuming the presence of friction in the vertical planes along the edges of the square pile caps. McGuire et al. (2012) also adopted the idea of a 'plane of equal settlement', which they described as the 'critical height'. They conducted numerous tests and collected field data to determine and validate their equation for the critical height. This critical height should be used in combination with Russell and Pierpoint's (1997) version of Terzaghi (1943). Naughton (2007) determined the critical height with log spiral shear planes. Britton and Naughton (2008) presented 3D experiments validating the critical height of this model.

Although the ideas underlying the frictional models are extremely important, these models are not generally used in Europe for piled embankment design and they will not be discussed further. A possible reason for the infrequent use of these models in Europe is that the results depend to a large extent on the value of K_0 (the ratio between horizontal and vertical pressure) and the fact that it is difficult to determine an accurate value for K_0.

Other examples of models considered in the literature are the models using mechanical elements, like the load displacement compatibility method of Filz et al. (2012), the one-dimensional model of R.P. Chen et al. (2008b) and the plane strain models of Deb (2010), Deb and Mahapatra (2012) and Zhang et al. (2012). Filz et al. (2012) model the fill, the GR and the piles + subsoil as separate elements. The boundary condition for each of the elements is that deformation must match neighbouring elements. This determines the load transferred to the piles directly (arching *A*, see Figure 4.1). Filz et al. (2012) limit arching *A* with 3D Terzaghi (cross-shaped, according to Russell and Pierpoint, 1997), plus critical height.

A familiar empirical model is the modified Marston and Anderson model (1913) that was modified by Jones et al. (1990) and adopted in BS8006 and the Finnish design guideline (Liikennevirasto, 2012). Marston and Anderson (1913) carried out numerous experiments to determine arching above a pipe in soil. They found a 2D equation that was modified by Jones et al. (1990) for the 3D piled embankments, as explained and further modified in Van Eekelen et al.

(2011a, adopted in appendix A of this thesis). This model is very important because of the widespread application of BS8006.

The final type of model that should be mentioned is the family of hammock models, such as the 'path of minor principal stress' model described by Handy (1985).

Most step 1 models calculate one average pressure on the GR. EBGEO uses, in its step 2, a triangular pressure distribution. This is an assumption following from figure 9.15 of EBGEO (2010), not the result of a calculation. Van Eekelen et al. (2012a and b, Chapters 2 and 3 of this thesis) showed that the measured pressure distribution on the GR strip between the piles can be better approximated with an 'inverse triangle'.

The present paper presents a new equilibrium model for step 1 that is a better match for several experimental, numerical and field observations, particularly the measured inverse triangle in the pressure distribution. The starting point for this study consisted of the design models in general use in Europe. The new model is an extension of the Hewlett and Randolph (1988) and EBGEO (2010) models.

4.2   Additional laboratory tests

4.2.1   Measurements of steps 1 and step 2 separately

Van Eekelen et al. (2012a, Chapter 2 of this thesis) presented and analysed a series of twelve model laboratory model tests on piled embankments. Since then, eight additional model tests have been carried out with the same set-up. Six of them were carried out specifically to validate variations in calculation step 1. These tests are presented here. One of the strengths of the test set-up was that it was possible to validate calculation steps 1 and 2 (Figure 4.1) separately because the values of *A, B* and *C* are measured separately.

4.2.2   Description tests

Figure 4.4 shows the test set-up for both the first and the second series, except for two additional total pressure cells (TPCs), which were used in the second series only. The insides of the box walls were located on the lines of symmetry. A foam cushion modelled the soft soil around the four piles. This cushion was a saturated and watertight sealed foam rubber cushion. A tap allowed drainage of the cushion during the test to model the soft-soil consolidation process.

A stiff steel frame was installed to which the GR was attached. The steel frame could move freely in a vertical direction. Since it fitted precisely in the container, no horizontal movement was possible. Differential settlement along the frame bars was not possible. It is assumed that this has a negligible influence on differential settlement between the piles.
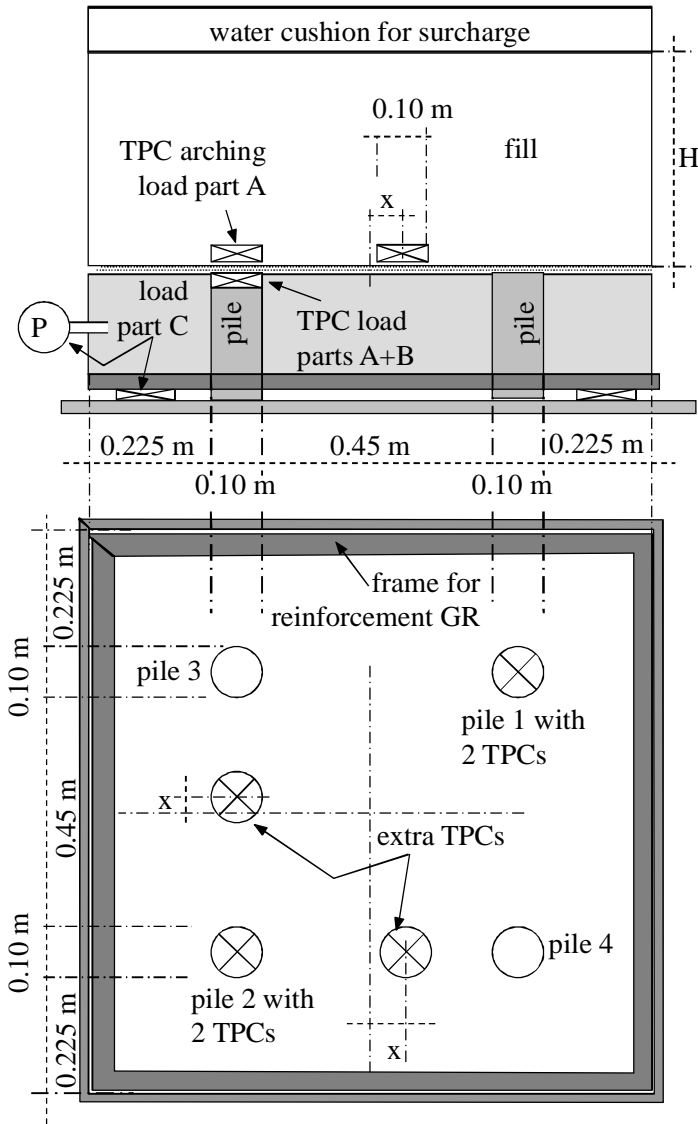
Figure 4.4 Test set-up for piled embankment model experiments. The stress distribution is measured with total pressure cells (TPCs). See also Van Eekelen et al., 2012a (Chapter 2 of this thesis), which includes an extensive presentation of the test series, including measurements of strains and deformations.

Table 4.1 Specification of the additional series 2 scaled model tests, and a selection of the series 1 tests. The series 2 tests were a variation on test K2 presented in Chapter 2 of this thesis (Van Eekelen et al., 2012a).

se-quence of tests	Code	GR $J_{2\%}$ = 2269 kN/m except tests T2 and T3	fill height granular fill[13] φ = 49.0° except test T2 m	fill unit weight kN/m³	top load p^a. kPa and kN/pile
SELECTION OF TESTS OF SERIES 1 (Van Eekelen et al., 2012a, Chapter 2 of this thesis)					
6	K2	2x PVA grid	0.420	16.59	p = 0-25-50-75-100 kPa (= 0-7.6-15.1-22.7-30.2 kN/pile) p-R = 1.2-22.0-41.1-59.8-74.9 kPa
5	T2	**1x PP geotextile** $J_{2\%}$ = **970/1810 kN/m**	0.420 **sand** φ=40.9°	16.55	p = 0-25-50-75 kPa (= 0-7.6-15.1-22.7 kN/pile) p- R = -1.8-18.3-37.4-50.9 kPa
7	T3	**1x PP geotextile** $J_{2\%}$ = **970/1810 kN/m**	0.420	16.70	p = 0-25-50-75 kPa (= 0-7.6-15.1-22.7kN/pile) p-R = -0.2-19.7-39.0-55.2 kPa
SERIES 2					
13	K4	2x PVA grid	**0.655**	16.80	p = 0-25-50-75 kPa (= 0-7.6-15.1-22.7 kN/pile) p-R = -0.9-13.9-28.5-44.7 kPa
14	K5	2xPVA grid	**0.343**	17.95	p = 0-25-50-75-100 kPa (= 0-7.6-15.1-22.7-30.2 kN/pile) p-R = -2.7-14.3- 31.9-49.9-67.2 kPa
15	K6	2xPVA grid	0.429	16.35	**p = 0-50-100 kPa (= 0-15.1-30.2 kN/pile)** p-R = -1.3-31.7-66.1 kPa
16	K7	**bottom layer PVA geotextile, top layer PVA grid**	0.426	16.42	p = 0-25-50-75-100 kPa (= 0-7.6-15.1-22.7-30.2 kN/pile) p-R = 0.0-17.3- 33.9-51.4-68.0 kPa
17	K8	2x PVA grid	**0.227**	17.13	p = 0-25-50-75-100 kPa (= 0-7.6-15.1-22.7-30.2 kN/pile) p-R = -0.1-18.0-35.6-57.7-73.8 kPa
18	K9	2x PVA grid	**0.655**	16.82	p = 0-25-50-75-100 kPa (= 0-7.6-15.1-22.7-30.2 kN/pile) p-R = -4.8-12.4-28.6-43.5-63.8 kPa

[a] After each top load increase, controlled drainage of the foam cushion ('subsoil') follows in one or more steps until the subsoil support C is nearly gone. The calculations were carried out with surcharge load p-R, where R is the measured friction between fill and box walls. The listed values for p-R are given for the moments just before top load increase (and therefore for minimal subsoil support C).

[13] Mainly concrete.

The embankment in most tests was granular fill (crushed recycled construction material 1-16 mm, $\varphi = 49^o$ at a unit weight of 16.4 kN/m^3). The friction angle $\varphi = 49^o$ of the granular fill was measured in large diameter ($\phi = 0.3$ m) triaxial tests. The average relative density in the triaxial tests and scale model tests was nearly the same at 61.0% and 62.9% respectively. The top load was applied with a water cushion that made it possible to apply stresses comparable with field stresses.

The area replacement ratio $a^2/(s_x \cdot s_y)$ in the test series described was 2.6%, while the area replacement ratio in Dutch practice is between 4.5 and 12%. This was a deliberate decision with the aim of generating enough GR tensile forces at this smaller scale.

After the introduction of the fill, each test was carried out as follows: (1) one drainage step foam cushion (subsoil consolidation), (2) first top load increment, (3) one or more drainage steps (4) second top load increment, (5) one or more drainage steps and so on, up to the maximum top load (varying between 50 and 100 kPa) and the subsequent drainage steps. The test concluded with the complete removal of the subsoil support by applying vacuum to the foam cushion. Table 4.1 lists a selection of the tests in the first series, and all the tests in the new second series presented in the present paper. The tests from the second series are all variations on test K2, except that each test included one variation, which is indicated in bold in Table 4.1. Furthermore, additional total pressure cells were added to measure the load distribution on the GR strips

The GR in these additional tests consisted of two layers of woven PVA grid, except for test K7, where the bottom layer was replaced by a similar PVA geotextile. The two uniaxial reinforcement layers were placed directly upon each other on one frame. The strength direction of one geogrid was perpendicular to the other. There was no distance between these two GR layers. The two layers are therefore considered to be a single GR layer that is completely biaxial.

GR stiffness depends on GR strain and the duration of loading, as well as other factors. The stiffness values of the weak direction of one GR layer and the stiff direction of the other layer were aggregated, resulting in a total GR stiffness $J_{2\%} = 2269$ kN/m in each direction. $J_{2\%}$ is the GR stiffness for a GR strain of 2%, and is determined in accordance with ISO 10319. These ISO tests are much faster than the piled embankment model tests (that took 3 days each). This means that the GR in the model tests is loaded longer and will behave differently (less stiffly) from the behaviour suggested by this $J_{2\%}$. However, GR stiffness is not a parameter in analytical step 1: the arching calculations considered in the present paper. Van Eekelen et al. (2012a, Chapter 2 of this thesis) confirmed that using GR has a

major impact on the arching mechanism, but GR stiffness (as long as the stiffness complies with a good-quality design model) does not have a measurable influence.

4.2.3 Results of the additional tests

Figure 4.5 compares the measurements of arching *A* in the new model tests with several old model tests. The numbers between brackets refer to the sequence of tests.

The granular fill was re-used for each test. It was observed that large numbers of grains were crushed during the successive tests. This will probably have caused a reduction of the friction angle. A lower friction angle results in less arching, as shown by the figure. Arching was also relatively low in test T2, in which a sand fill was used.

The friction angle $\varphi = 49^{o}$ of the granular fill was measured with large triaxial tests carried out between experiments 12 and 13. This effect of reducing friction is neglected in the present paper. In the calculations, friction angle $\varphi = 49^{o}$ was applied. More results from the additional tests are presented in Figure 4.7, Figure 4.15, Figure 4.17, Figure 4.19, and Figure 4.21 of this paper.
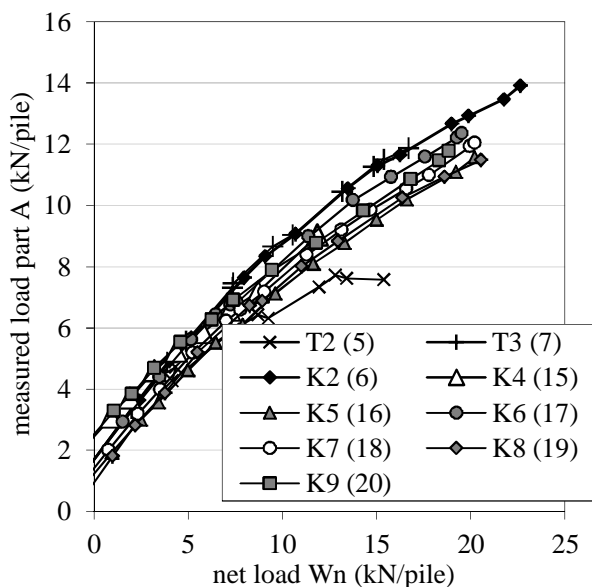
Figure 4.5 Measurements of arching *A* in a selection of the experiments in series 1 (Van Eekelen et al., 2012a, Chapter 2 of this thesis) and the additional tests in series 2. The numbers between the brackets refer to the sequence of tests.

4.3 Observations of arching in experiments, field tests and numerical calculations

4.3.1 Measuring arching

This paper focuses on the description of the arching mechanism, and therefore on calculation step 1 in Figure 4.1. Arching divides the vertical load into two parts, as shown in Figure 4.1. One part is load part *A* (called 'arching *A*' in this paper), which is the load that is transferred to the pile caps directly. The remaining load part is *B+C*.

Direct validation of arching in a GR reinforced piled platform with measurements is only possible when *A* is measured separately, as shown in Figure 4.4. This figure shows how load *A* was measured in the tests, using total pressure cells (TPCs) with a diameter equal to the pile diameter. They were located on top of the piles and on top of the GR. In addition, two total pressure cells measured *A+B*. They were located below the GR on top of the piles. This paper gives arching *A* in kN/pile. In several figures, arching is presented as a percentage of the total load, which is referred to as "*A%*". *A%* corresponds to efficacy ("*E*") as used by several authors, where $E = A\% = A/(A+B+C)$, with *A, B* and *C* given in kN/pile, *A%* in % and *E* as a ratio (-).

Many researchers (such as Zaeske, 2001; Blanc et al., 2013) have measured *A+B* or measured *A* in a piled platform without GR (Hewlett and Randolph, 1988; Ellis and Aslam, 2009a, for example). As far as we are aware, only the Dutch research programme has reported measurements of *A* in experiments with GR (Van Eekelen et al., 2012a and b, adopted in Chapters 2 and 3 of this thesis) and three field tests with GR (Van Duijnen et al., 2010, Van Eekelen et al., 2010a, 2010b and Van Eekelen et al., 2012c, 2013).

4.3.2 Comparison of predictions and measurements of arching A

Van Eekelen et al. (2012b, Chapter 3 of this thesis) measured *A* in their experiment series and showed that EBGEO generally under-predicts the measured *A*. This paper presents additional tests of the same type. Van Duijnen et al. (2010) measured *A* in field tests under a railway in Houten, the Netherlands. They showed that EBGEO considerably under-predicts *A*, as also shown in Figure 4.16*a*.
More recently, Van Eekelen and Bezuijen (2013b) showed that EBGEO only slightly under-predicts *A* as a result of the permanent load in field measurements in Woerden, the Netherlands, as shown in Figure 4.16*b*.

It should be noted that the results of the predictions are highly dependent on the friction angle of the fill and that this friction angle is difficult to determine in the field. The presented EBGEO prediction for Woerden, for example, is calculated with a best-guess friction angle $\varphi = 43^o$, resulting in $A = 113$ kN/pile, as indicated in Figure 4.16*b*. However, this EBGEO-prediction of A falls to 96 kN/pile for $\varphi = 37.5^o$ and rises to 132 kN/pile for $\varphi = 49^o$.

It is also not certain that this fill friction angle or fill cohesion remains constant in all circumstances, such as heavy rain or long dry, hot periods: the arching in Figure 4.16*b* increased in the spring of 2011 during a dry, hot period.

4.3.3   Impact of fill height

Several researchers have reported that the efficiency of arching increases with increasing fill height. Examples are Y.M. Chen et al. (2008a) in 2D experiments with GR and Zaeske (2001) with 3D experiments (although the latter only showed the differences in his experiments without GR), Han and Gabr (2002) with numerical analysis with GR, Le Hello and Villard (2009) with numerical analysis with GR (see Figure 4.18), Jenck et al. (2009) with 2D experiments without GR and numerical analysis, Ellis and Aslam (2009a) with centrifuge tests without GR, and Deb and Mohapatra (2013) with 2D analytical calculations. All these researchers showed that a higher fill results in relatively more load being transferred to the piles, either directly or via the GR. A higher fill therefore results in a relative reduction in the load exerted on the GR and/or the subsoil between the piles.

The experiments presented in this paper also show that fill height has an impact, as seen in Figure 4.17. *A*% increases with fill height and seems to stabilise with increasing embankment height, as shown in Figure 4.17 and Figure 4.18. When *A*% stabilises, the absolute values of *A* and *B+C* (kN/pile or kPa) will increase with increasing fill height. This tendency towards increasing arching is followed by many design models, such as Carlson (1987), Guido et al. (1987), Hewlett and Randolph (1988), Russel and Pierpoint (1997), Sintef (2002) and Kempfert et al. (2004), which was adopted in EBGEO (2010), as Le Hello and Villard (2009) have shown.

The critical height is the height at which the shear forces in the embankment fill are reduced to zero (Naughton, 2007), which is the case at the 'plane of equal settlement', defined by McKelvey (1994) as the lowest plane where no differential settlement occurs. Lally and Naughton (2012) carried out a series of 2D GR-reinforced centrifuge tests. They found close agreement between the observed

critical heights and the critical height suggested by Hewlett and Randolph's model (1988).

4.3.4   Load distribution on the GR; influence of using GR

There is a considerable difference between piled embankments with or without GR. GR, when stiff enough, leads to (1) more efficient arching and therefore a higher *A*, (2) a concentration of load on the GR strips (3) an inverse triangular load distribution on the GR strips and (4) a larger fall in stress between the piles with depth in the embankment above the GR. Each of these features will be explained in this chapter.

Y.M. Chen et al. (2008a), Abusharar et al. (2009) and Deb and Mohapatras (2013) showed that the efficiency of the piled embankment improves greatly when GR is used. They found that the load on the piles was much larger with, respectively, a 2D analytical model, an axial-symmetric analytical model and in 2D experiments.
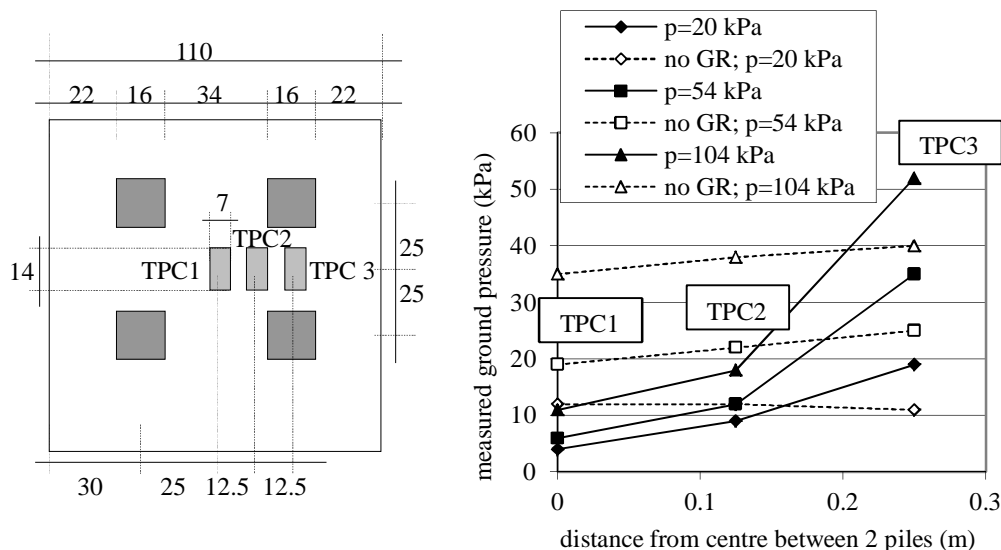
Figure 4.6 Comparison of results of the Zaeske test series (2001, page 60, GR is a woven grid PET 60/60-20). Top view. Zaeske measured the load distribution at 5 cm above the GR, at the locations TPC1, TPC2 and TPC3. See also Figure 4.20. Sizes in cm. $H = 0.7$ m, $\varphi_{fill} = 38^{o}$. The size of the TPCs was adapted in comparison to the original paper of Van Eekelen et al., 2012a. The TPCs were 0.07x0.14 m^2.

The localisation of the load on the GR strips has been shown by, for example, Zaeske (2001) by measuring the pressure at three locations on the GR square and the GR strips (Figure 4.6). Note that, in this paper, the square between four piles is referred to as the 'GR square', even when no GR is in place, as indicated in Figure 4.11*a*. Figure 4.6 shows that introducing GR clearly transfers the load towards the GR strips. This results in a load distribution that is concentrated mainly on the

GR strips (and probably the piles, but Zaeske did not measure *A*). As a result, it is expected that the strains in the GR occur mainly in the GR strips between the piles. This was indeed found in both Zaeske (2001) and Van Eekelen et al. (2012b, Chapter 3 of this thesis).

The pressure on the GR strips is not equally distributed; it rises towards the piles. In the additional tests presented in this paper, the load distribution on the GR strip was measured with additional total pressure cells on the GR strip (Figure 4.4). These measurements (Figure 4.7) do indeed show that the load on the GR rises towards the piles. This load distribution can be approximated by a model with an inverse triangular load distribution. The inverse triangular model has advantages since it is a relatively simple analytical model. Van Eekelen et al. (2012a and b (Chapters 2 and 3 of this thesis) and 2013) showed that this simplified analytical model provides a good match with measurements of deformation in laboratory experiments.
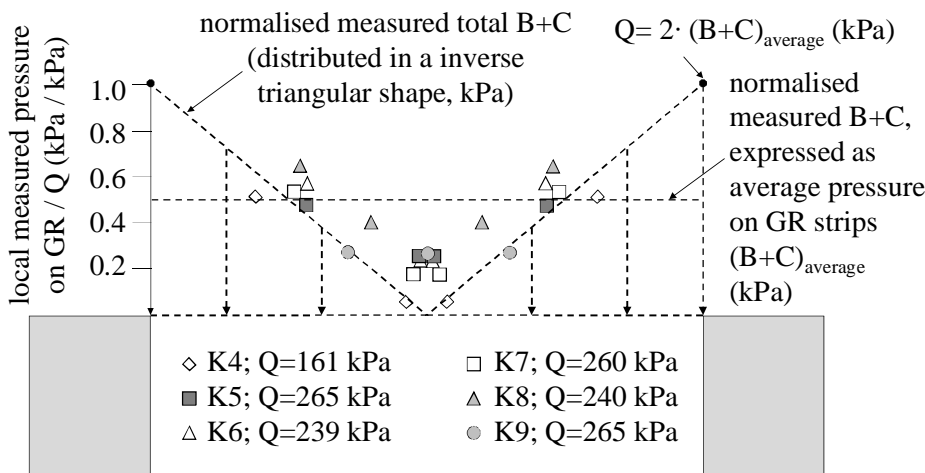
Figure 4.7 Measured load distribution on GR in newly presented tests (Table 4.1) compared with the total measured load *B+C* on the GR, presented as an equally distributed load and with the inverse triangular load distribution of Van Eekelen et al., 2012a and b (Chapters 2 and 3 of this thesis). The total measured *B+C* (kN/pile) was measured with the transducers that measure *A, A+B* and *C* indicated in Figure 4.4. These values were divided by the area of a GR strip to get the equally distributed load $(B+C)_{average}$ in kPa. The local pressures were measured in kPa with the extra TPC's indicated in Figure 4.4.

Furthermore, the inverse triangle (or at least the concentration of load close to the piles, and the minimum load in the centre between piles) was also found in, for example, finite element calculations on a soldier pile wall by Vermeer et al. (2001), discrete element calculations on a heap of grains on a deflecting subsurface (Nadukuru and Michalowski, 2012), numerical calculations by Han et al. (2012), with a inversed triangle in their Figure 9, and by Den Boogert et al. (2012a,b), settlement measurements in a field test (Van Eekelen et al., 2012c and 2013) and the large-scale model tests of Filz and Sloan (2013).

GR also has a major effect on ground pressure in the fill above the GR between the piles. Zaeske (2001, pages 55 and 63) showed that this ground pressure declines with increasing fill depth. When GR is applied, the fall in ground pressure with depth is much larger than without GR, as shown by the comparison of Zaeske's measurements in the situations with and without GR in Figure 4.20.

Zaeske's findings (2001) showed that there is an interaction between the GR and the fill. Without GR, the arch is much less efficient than with GR. The GR attracts the load to the GR strips between the pile caps and then further to the pile caps, approximately resulting in the inverse triangular load distribution on the GR strips. This ultimately results in larger vertical loads on the pile caps and on the GR close to the pile caps. GR therefore makes arching much more efficient.

The current analytical models do not give the localisation of the load on the GR strips. Nor do they result in a concentration of load on the GR in the area around the pile cap or, therefore, lead to an inverse triangular load distribution. This paper describes a new equilibrium model that is a better match for load distribution observations. The resulting model is only applicable to load transfer platforms with GR.

4.3.5 *Influence of subsoil consolidation or GR deflection and fill properties*

A. Consolidation or compaction of the subsoil results in an increase of arching *A*, as shown by Van Eekelen et al. (2012a, Chapter 2 of this thesis), and in Figure 4.8. Most analytical models, like EBGEO, do not calculate with increased arching due to subsoil consolidation. An exception is the model of Deb (2010), which agrees with this influence of consolidation.
B. A lower friction angle of the fill gives less arching during consolidation. This results in load part *B+C* on the GR being some 39% larger for sand than for granular fill at the end of the tests presented by Van Eekelen et al. (2012a, Chapter 2 of this thesis) and Figure 4.8*b*.

Most of the existing arching models assume that a slight deflection of the geotextile is sufficient to create a 'full arch'. However, the measurements showed that *A* increases with increasing GR deflection (due to subsoil consolidation). The influence of deformation cannot be incorporated in rigid-plastic models such as the equilibrium models or frictional models. A new class of models would be needed. This would, however, conflict with the initial principle of keeping as closely as possible to existing design models, and it is beyond the scope of this paper. A 'work-around' is presented in Chapter 4.4.2: the development of concentric arches.
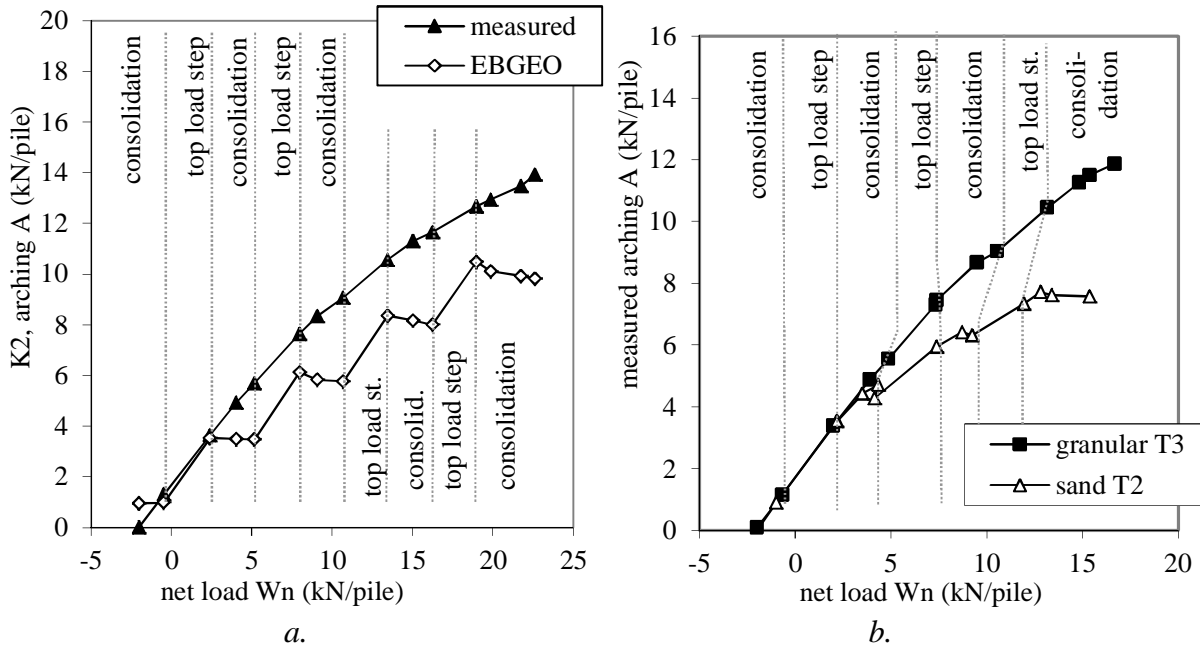
Figure 4.8 Measurements showing that arching increases with subsoil consolidation (*a*): Comparison of measured values and EBGEO calculations for test K2. (*b*): The increase in arching is larger for the stronger material 'granular' (test T3) than for sand (Test T2, source: Van Eekelen et al., 2012a (Chapter 2 of this thesis), see Table 4.1 for specifications of tests K2, T2 and T3).

4.3.6 Summary of Chapter 4.3

Comparing the existing models with measurements, it can be concluded that none of the analytical models considered (equilibrium, frictional, empirical) can explain the measurements. In several cases, they under-predict the arching *A* measured in the field. They do not describe the load and strain localisation on and in the GR strips. They do not give an explanation for the approximately inverse triangular load distribution on the GR strips. However, they do give decreasing ground pressure with depth in the fill above the GR square, and they do give increasing efficiency in arching with increasing fill height.

4.4 A new equilibrium model: the Concentric Arches model

4.4.1 Introduction

With equilibrium models, the pressure on the GR is calculated by considering the equilibrium of the arch. The models of Hewlett and Randolph (1988) and Zaeske (2001), which are in widespread use, are shown in Figure 4.2 and Figure 4.3. These two models give quite satisfactory results when used in a design (the predicted loading on the GR is reasonable and on the safe side), but (1) do not

explain the concentration of load on the GR strip, (2) do not explain or derive an inverse triangular load distribution on the GR strips and (3) do not give increasing arching during subsoil consolidation. Furthermore, the Hewlett and Randolph model is not meant for arching with GR, and not particularly suitable for partial arching situations, which are situations where the fill or embankment is thinner than the full arch height, in other words when $H < s_d/2$. The Zaeske model can work with these low embankments.

This chapter introduces a new model, the concentric hemispheres model. This model accounts for increased arching with subsoil consolidation and finds load localisation on the GR strips. Furthermore, it gives a physical explanation for the inverse triangular load distribution and is therefore a better match for the observations in Chapter 4.3.

However, in practical applications, a limit-state version of the model will be applied. In that case, the Concentric Arches model behaves in a rigid-plastic way and will no longer describe the influence of subsoil consolidation or deformation.
It should be noted that in this paper a hemisphere is a 3D arch as indicated in Figure 4.13, and an arch is a 2D arch, as indicated in Figure 4.12.

4.4.2   Development of concentric arches

Figure 4.9 introduces a 2D picture of the new model that describes the development of arching during subsoil consolidation, accompanied by an increasing GR deflection.

In Figure 4.9*a*, a small GR deflection results in the start of arch formation at the edge of the pile cap. At this location (the edge of the pile cap), the differential settlement between GR and pile cap is at a maximum and the load starts to be attracted to the stiffer pile cap, resulting in an increasing pile load *A*. Subsequently, increasing GR deflection closes the arch *(b)*.

Now, the piece of GR close to the pile behaves in a relatively stiff way because it is 'attached' to the pile and can move less freely than the GR in the middle. Another arch therefore starts to develop inside the first one (*c*). After this, more arches develop, each one smaller than the preceding one (*d*). Each smaller arch exerts a smaller force on its subsurface than the preceding larger arch. The arches give the directions of the main principal stresses: the major principal stress in the tangential direction and the minor principal stress in the radial direction.
The creation of new arches is accompanied by increasing load transfer in the direction of the piles and a reduction of the load on the GR area between the piles. This results in a more or less inverse triangular load distribution on the GR strip.

The process of arch development terminates in a set of concentric hemispheres which Figure 4.10 shows in 3D. The GR is essential in this model because, without GR, there will be a more or less even settlement of the area between the piles and the Concentric Arches cannot develop, as shown with 2D experiments by for example Hong et al. (2007) and Jenck et al. (2009).

The development of arching in a basal reinforced piled embankment has never been observed through, for example, a glass wall. However, the formation of subsequent new Concentric Arches as a result of settlement underground has been observed in experiments at the University of Cambridge (Casarin, 2011). In these experiments, sand was poured onto a rubber tunnel. The largest differential settlements started, in this case, in the centre of the tunnel. In that case, a small arch in the fill occurred first, followed by a succession of larger arches.

a. *b.*

c. *d.*
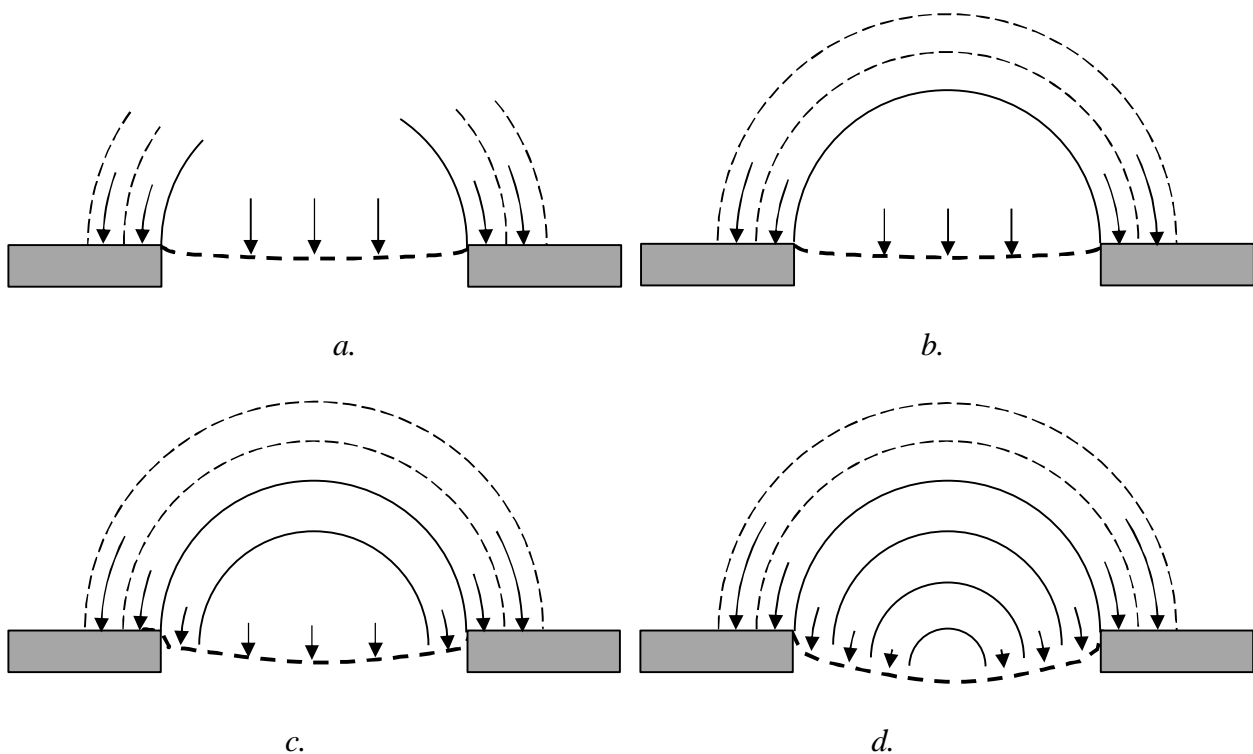
Figure 4.9 Increasing GR defection results in an increasing lateral transport of load via concentric arch-shaped stress paths and an inverse triangular load distribution on the GR.

The theory that base deflection results in Concentric Arches has also been stated by several authors presenting numerical analyses. For example, Han et al. (2012) carried out 2D DEM piled embankment analysis and showed (in their Figure 11) force chains that resemble concentric arches, with smaller forces in the smaller arches. Vermeer et al. (2001) found main stress directions following Concentric Arches when they studied the horizontal stress distribution in the soil behind a soldier pile wall. A soldier pile wall of this kind consists of relatively weak timber

laggings (comparable with GR) between stiff anchored steel piles (comparable with piles).

Another example is Nadukuru and Michalowski (2012), who carried out discrete element simulations. After a wedge-shaped heap of particles was formed, a basal deflection was prescribed. In this way, maximum subsidence at the centre equal to 0.67% of the heap's height was observed. Nadukuru and Michalowski showed their calculated force chains in the particles. The force chains follow the shapes of concentric arches. They also demonstrated that the load on the central part of the base was reduced in the process of deflection at the expense of the parts farther away from the centre. Each larger arch therefore exerts a larger stress on the base. This stress distribution resembles the inverse stress distribution presented in Van Eekelen et al. (2012a and b, adopted in Chapters 2 and 3 of this thesis). Sloan (2011) also concluded from his large scale tests that it is possible that secondary arches form below the primary arch. His idea is similar to the Concentric Arches model presented in the present paper.
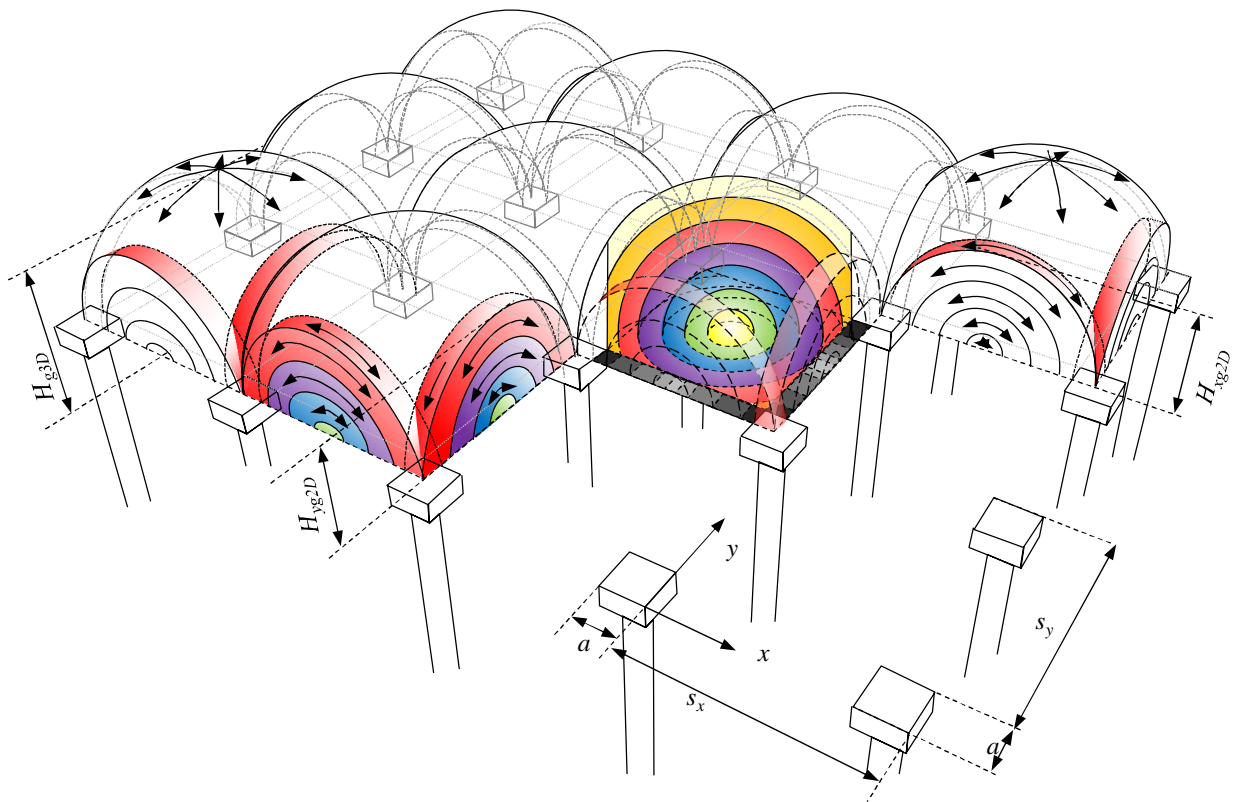
Figure 4.10 New proposed analytical model: the Concentric Arches model. The load is transferred along the concentric 3D hemispheres towards the GR strips and then via the concentric 2D arches towards the pile caps. The geometry parameters shown are: H_{g3D} (m): height of the largest 3D hemisphere; H_{xg2D} and H_{yg2D} (m): height of the 2D arches respectively along the *x-axis* and the *y-axis*; s_x and s_y (m): the pile spacing parallel to the *x*-axis or the *y*-axis and *a* (m) the width of the pile caps.

The new proposed model assumes that 3D Concentric Arches (hemispheres) are formed above the square between each four piles (Figure 4.10 and Figure 4.11*b*). These hemispheres transfer the load outward in all directions along the hemispheres towards the GR strips. The process continues with the further transfer of the load along the 2D arches above the GR strips toward the pile caps (Figure 4.10 and Figure 4.11*c*).

Force on piles *A*

Force $F_{GRsquare}$ exerted by 3D hemispheres on the GR square

Force $F_{GRstrips}$ exerted by the 2D arches on the GR strips
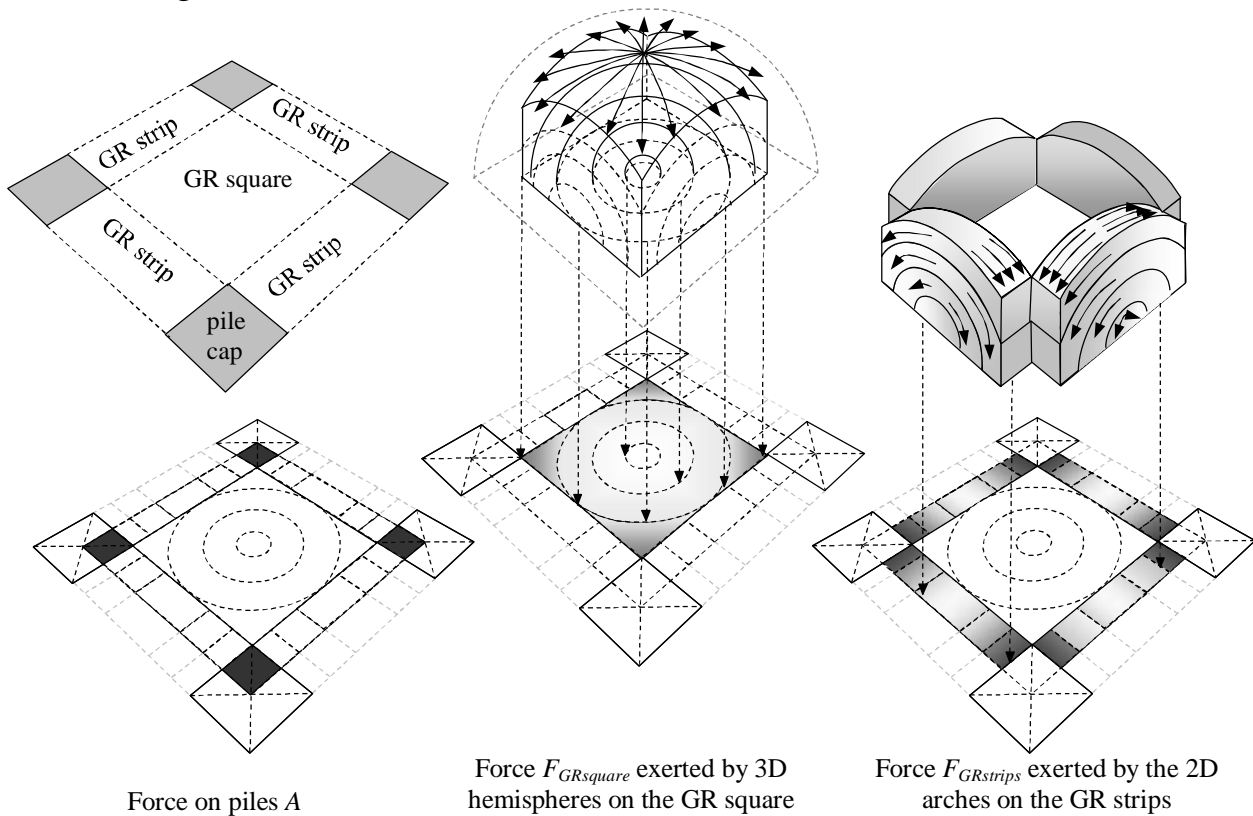
Figure 4.11 Basic idea underlying the proposed Concentric Arches model: distribution of the load on the GR area between the piles and the determination of arching part $A = (\gamma H + p) \cdot s_x \cdot s_y - F_{GRsquare} - F_{GRstrips}$ going to the pile directly (see also Figure 6.5).

Both the 3D hemispheres and the 2D arches exert a load on the GR subsurface which increases towards the outside. The part of the load not resting on the GR is arching *A*, which is the load part transferred directly to the pile caps, as explained in Figure 4.11*a*. Figure 4.11 depicts the three components of the model – (*a*) the load part (arching *A*) that is applied directly to the pile caps (Figure 4.11*a*), (*b*) the load part that is applied on the GR square between the pile caps diagonally between the pile caps (Figure 4.11*b*) and (*c*) the load part that is applied between adjacent pile caps on the GR strips (Figure 4.11*c*) – plus the interaction that must exist between the last two components. With this model, it is possible to approximate the observed load distribution on the piles and the entire GR area between the piles.

The following chapters present the equations for the 2D Concentric Arches and the 3D concentric hemispheres and these 2D and 3D equations will then be combined to form the new arching model.

4.4.3   2D Concentric Arches
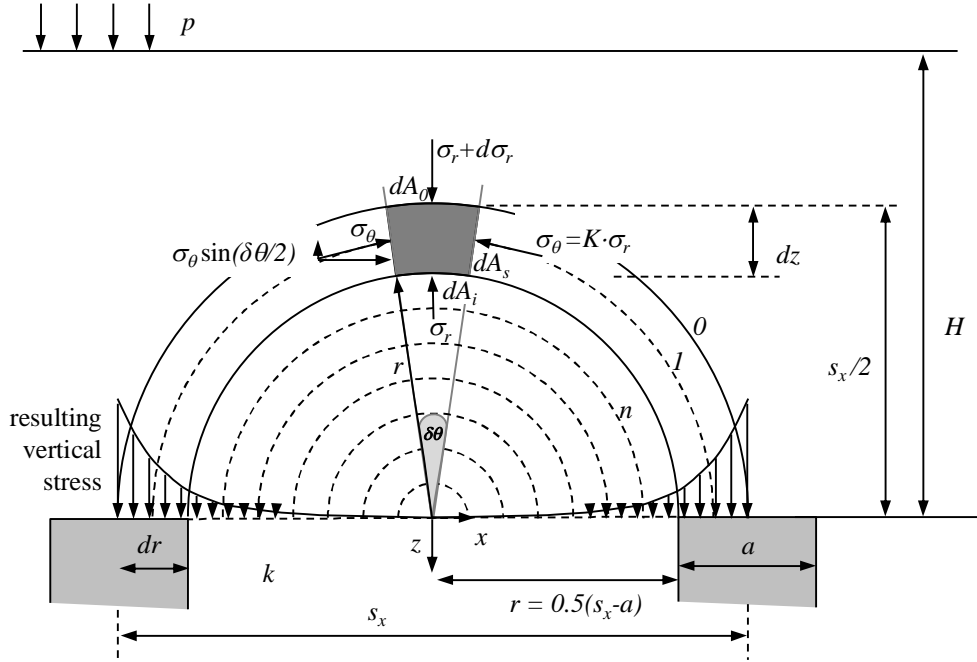
Figure 4.12 2D Concentric arches, the tangential stress in the arches result in a vertical stress exerted on the subsurface that resembles the simplified inverse triangle.

Figure 4.10, Figure 4.11*c* and Figure 4.12 show 2D concentric arches. It should be noted that this paper states the radius for 3D hemispheres as an upper-case *R*, and the radius of 2D arches as a lower-case *r*. The radial sBStress σ_r in the 2D arch is found by considering the radial equilibrium of the crown element of the 2D arch and assuming that the stress state in the arch is uniform around the semi-circle and that the limit state occurs in the entire arch, which gives the tangential stress $\sigma_\theta = K_p \cdot \sigma_r$. This leads, after some derivation given in appendix 4.A.1, to the following tangential stress (in kPa) for a 2D arch in the *x*-direction:

$$\sigma_\theta = P_{x2D} \cdot r^{(K_p - 1)} + Q_{2D} \cdot r$$

where

$$P_{x2D} = K_p \cdot H_{xg2D}{}^{1-K_p} \cdot \left[\gamma H + p - \gamma H_{xg2D} \frac{(K_p - 1)}{(K_p - 2)} \right] \text{ and } Q_{2D} = K_p \cdot \frac{\gamma}{K_p - 2} \tag{4.1}$$

and, where γ (kN/m^3) is the fill unit weight, p is the uniformly distributed surcharge load on top of the fill, H_{xg2D} (in m) is the height of the largest 2D arch (see Figure 4.10 and Figure 4.12):

$$H_{g2D} = \frac{s_x}{2} \qquad \text{For} \quad H \geq \frac{s_x}{2} \qquad \text{(full arching)}$$

$$H_{g2D} = H \qquad \text{for} \quad H < \frac{s_x}{2} \qquad \text{(partial arching)}$$

(4.2)

and

$$K_p = \frac{1 + \sin\varphi}{1 - \sin\varphi}$$

The explanation of these equations is similar to Hewlett and Randolph's 2D explanation (1988), except that soil weight and top load are taken into account here. Hewlett and Randolph limit the thickness of their arch and therefore the crown element to half the width of a pile cap and calculate the vertical (radial) stress immediately below the crown element. For the Concentric Arches model, however, the arch is extended downwards towards the subsoil, resulting in a set of concentric arches. These arches exert a force on their subsurface, which comprises the GR strips, in the case of the 2D arches, as shown in Figure 4.11c. The larger the arch, the larger the exerted force. This 'imprint' of load on the GR strip is shown in Figure 4.12 and resembles the inverse triangle described in Chapter 4.3.
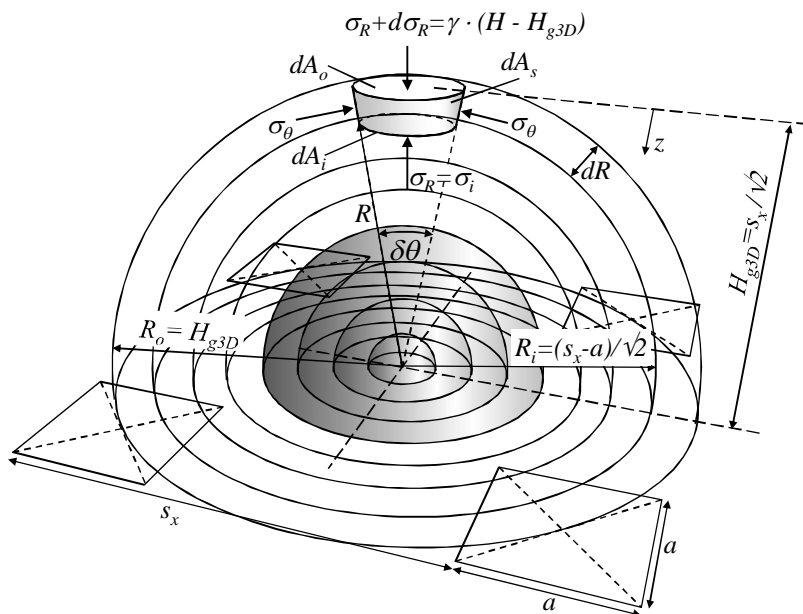
Figure 4.13 3D Concentric hemispheres, the tangential stress in the arches result in a vertical stress exerted on the subsurface.

4.4.4 3D concentric hemispheres

Figure 4.10, Figure 4.11*b* and Figure 4.13 show 3D concentric hemispheres. The tangential stress (kPa) in the 3D arches is found in a similar way as for the 2D arches, as explained in appendix 4.A.2,

$$\sigma_{\theta(p=0)} = P_{3D} \cdot R^{2(K_p-1)} + Q_{3D} \cdot R$$

where (4.3)

$$P_{3D} = \gamma \cdot K_p \cdot H_{g3D}^{2-2K_p} \cdot \left[H - H_{g3D} \cdot \left(\frac{2K_p-2}{2K_p-3} \right) \right] \text{ and } Q_{3D} = K_p \cdot \frac{\gamma}{2K_p-3}$$

and where K_p is given by equation (4.2) and H_{g3D} (m) by:

$$H_{g3D} = \frac{s_d}{2} \quad \text{for } H \geq \frac{s_d}{2} \quad \text{full arching}$$

(4.4)

$$H_{g3D} = H \quad \text{for } H < \frac{s_d}{2} \quad \text{partial arching}$$

With surcharge load *p* (kPa) the tangential stress (kPa) becomes (analogous to Hewlett and Randolph, 1988; Zaeske, 2001):

$$\sigma_\theta = \left(\frac{\gamma(H-z)+p}{\gamma(H-z)} \right) \left(P_{3D} \cdot R^{2(K_p-1)} + Q_{3D} \cdot R \right)$$

(4.5)

Where *z* is the vertical distance between the considered point and the GR. So far, the explanation of the 3D equations is the same as Hewlett and Randolph's (1988). Hewlett and Randolph now limit the thickness of the arch and therefore the crown element to half the diagonal of a pile cap and calculate the vertical (radial) stress immediately below the crown element which gives Hewlett and Randolph's equation (10) (1988).

In the concentric hemispheres model, however, the arch is extended downwards towards the subsoil, resulting in a set of concentric hemispheres. These hemispheres exert a force on their subsurface. The larger the radius, the larger the force exerted on the subsurface.

4.4.5 Concentric Arches model: combination of 2D arches and 3D hemispheres

The new calculation model is derived in appendix 4.A and summarised in this chapter. Note that the equations in the appendix are for a situation in which the piles are placed in a grid with the same centre-to-centre distance in both directions: $s_x = s_y$, while this chapter extends the equations for the situation $s_x \neq s_y$. The model should be applied as follows:

A. Determine the total vertical load $F_{GRsquare}$ (in kN/pile) exerted by the 3D hemispheres on their square subsurface (Figure 4.11*b*). This load $F_{GRsquare}$ is derived by integrating the tangential stress of the 3D hemispheres over the area of this square (see appendix 4.A.3, equations (4.53) to (4.85)), resulting in:

$$F_{GRsquare} = F_{GRsquare1} + F_{GRsquare2} + F_{GRsquare3} =$$

$$\left(\frac{\gamma H + p}{\gamma H} \right) \cdot \left(F_{GRsq1\,p=0} + F_{GRsq2\,p=0} + F_{GRsq3\,p=0} \right)$$

where

$$F_{GRsq1\,p=0} = \frac{\pi P_{3D}}{K_p} \cdot \left(\frac{L_{x3D}}{2} \right)^{2K_p} + \tfrac{2}{3} \pi Q_{3D} \cdot \left(\frac{L_{x3D}}{2} \right)^{3}$$

$$F_{GRsq2\,p=0} = {}_1F_{GRsq2} + {}_2F_{GRsq2} + {}_3F_{GRsq2} + {}_4F_{GRsq2}$$

where

$${}_1F_{GRsq2} = \frac{2\pi P_{3D}}{2K_p} \left(2^{K_p} - 1 \right) \left(\frac{L_{x3D}}{2} \right)^{2K_p}$$

(4.6)

$${}_2F_{GRsq2} = \frac{2\pi Q_{3D}}{3} \left(\sqrt{2}^{\,3} - 1 \right) \left(\frac{L_{x3D}}{2} \right)^{3}$$

$${}_3F_{GRsq2} = \frac{P_{3D} \cdot 2^{2-2K_p} \cdot L_{x3D}^{2K_p}}{K_p} \cdot \left(-\frac{\pi}{2^{2-K_p}} + \sum_{n=0}^{\infty} \frac{1}{2n+1} \binom{K_p - 1}{n} \right)$$

$$= \frac{P_{3D} \cdot 2^{2-2K_p} \cdot L_{x3D}^{2K_p}}{K_p} \cdot \left(\begin{array}{l} -\dfrac{\pi}{2^{2-K_p}} + 1 + \tfrac{1}{3}\left(K_p - 1 \right) + \tfrac{1}{10}\left(K_p - 1 \right)\left(K_p - 2 \right) \\[2mm] + \tfrac{1}{42}\left(K_p - 1 \right)\left(K_p - 2 \right)\left(K_p - 3 \right) \\[2mm] + \tfrac{1}{216}\left(K_p - 1 \right)\left(K_p - 2 \right)\left(K_p - 3 \right)\left(K_p - 4 \right) + \tfrac{1}{1320} .... \left(K_p - 5 \right)... \end{array} \right)$$

$${}_4F_{GRsq2} = \tfrac{1}{6} Q_{3D} L_{x3D}^{3} \cdot \left(\sqrt{2}\,(1 - \pi) + \ln\left(1 + \sqrt{2} \right) \right)$$

where

$$P_{3D} = \gamma \cdot K_p \cdot H_{g3D}^{2-2K_p} \cdot \left[H - H_{g3D} \cdot \left(\frac{2K_p - 2}{2K_p - 3} \right) \right] \text{ and } Q_{3D} = K_p \cdot \frac{\gamma}{2K_p - 3} \tag{4.7}$$

H_{g3D} (m) is the height of the largest hemisphere given in equation (4.4) and Figure 4.10 and L_{x3D} is given by:

$$L_{x3D} = \frac{1}{\sqrt{2}} \sqrt{(s_x - a)^2 + (s_y - a)^2} \qquad \text{for} \quad H \geq \frac{1}{2} \sqrt{(s_x - a)^2 + (s_y - a)^2}$$

$$L_{x3D} = \sqrt{2} \cdot H_{g3D} \qquad \text{for} \quad H < \frac{1}{2} \sqrt{(s_x - a)^2 + (s_y - a)^2} \tag{4.8}$$

where a (m) is the width of a square pile cap or the equivalent width of a circular pile cap and $F_{GRsquare}$ given in kN/pile. $F_{GRsquare1}$ and $F_{GRsquare2}$ (kN/pile) are indicated in Figure 4.22. L_{x3D} (m) is the width of the square upon which the hemispheres exert a load, as indicated in Figure 4.22. When the area between the four piles $(s_x - a) \cdot (s_y - a) > L_{x3D}^2$, the area outside L_{x3D} but inside the GR square is assumed to be loaded by $\gamma H + p$. This gives an extra term, $F_{GRsq3p=0}$, where

$$F_{GRsq3p=0} = \gamma H \cdot \left((s_x - a) \cdot (s_y - a) - L_{x3D}^2 \right) \quad \text{for} \quad L_{x3D}^2 < (s_x - a) \cdot (s_y - a)$$

$$F_{GRsq3p=0} = 0 \qquad\qquad \text{for} \quad L_{x3D}^2 \geq (s_x - a) \cdot (s_y - a) \tag{4.9}$$

The load that does not rest on the GR square is supposed to be transferred to the ring of GR strips and pile caps. This load is therefore applied as an equally distributed surcharge load on the 2D arches. This surcharge load on the 2D arches is in kN/pile:

$$F_{transferred} = \gamma H \cdot (s_x - a) \cdot (s_y - a) - \left(F_{GRsq1p=0} + F_{GRsq2p=0} + F_{GRsq3p=0} \right) \tag{4.10}$$

Distributed equally on the 2D arches, this results in a surcharge load in kPa (2 full GR strips and a pile cap per pile):

$$p_{transferred} = \frac{F_{transferred}}{a \cdot \left(L_{x2D} + L_{y2D} \right) + a^2} \tag{4.11}$$

Where L_{x2D} is the length of the part of the GR strip upon which the 2D arches exert their force, as indicated in Figure 4.23:

$$L_{x2D} = s_x - a \qquad \text{for} \quad H \geq \frac{1}{2}(s_x - a)$$

$$L_{x2D} = 2 \cdot H_{xg\,2D} \qquad \text{for} \quad H < \frac{1}{2}(s_x - a)$$

$$L_{y2D} = s_y - a \qquad \text{for} \quad H \geq \frac{1}{2}(s_y - a)$$

$$L_{y2D} = 2 \cdot H_{yg\,2D} \qquad \text{for} \quad H < \frac{1}{2}(s_y - a)$$

(4.12)

and

$$H_{xg\,2D} = \frac{s_x}{2} \qquad \text{for} \quad H \geq \frac{s_x}{2} \qquad \text{(full arching)}$$

$$H_{xg\,2D} = H \qquad \text{for} \quad H < \frac{s_x}{2} \qquad \text{(partial arching)}$$

$$H_{yg\,2D} = \frac{s_y}{2} \qquad \text{for} \quad H \geq \frac{s_y}{2} \qquad \text{(full arching)}$$

$$H_{yg\,2D} = H \qquad \text{for} \quad H < \frac{s_y}{2} \qquad \text{(partial arching)}$$

(4.13)

B. Determine the total load $F_{GRstrips}$ (kN/pile) on the GR strips. $F_{GRstrips}$ is derived by integrating the tangential load of the 2D arches over the area of the GR strips (see appendix 4.A.3, equations (4.86) to (4.91)), resulting in:

$$F_{GRstrip;p>0} = \left(\frac{\gamma H + p}{\gamma H}\right) \cdot \left(2a \frac{P_{x2D}}{K_p}\left(\tfrac{1}{2}L_{x2D}\right)^{K_p} + \tfrac{1}{4}aQ_{2D} \cdot \left(L_{x2D}\right)^2 + F_{xGRstr2\,p=0} \right.$$

(4.14)

$$\left. + 2a \frac{P_{y2D}}{K_p}\left(\tfrac{1}{2}L_{y2D}\right)^{K_p} + \tfrac{1}{4}aQ_{2D} \cdot \left(L_{y2D}\right)^2 + F_{xGRstr2\,p=0} \right)$$

Where:

$$P_{x2D} = K_p \cdot H_{xg\,2D}^{(1-K_p)} \cdot \left[\gamma H + p_{transferred} - \gamma H_{xg\,2D} \cdot \left(\frac{K_p - 1}{K_p - 2}\right) \right]$$

$$P_{y2D} = K_p \cdot H_{yg\,2D}^{(1-K_p)} \cdot \left[\gamma H + p_{transferred} - \gamma H_{yg\,2D} \cdot \left(\frac{K_p - 1}{K_p - 2}\right) \right]$$

$$Q_{2D} = K_p \cdot \frac{\gamma}{K_p - 2}$$

$$F_{xGRstr2\,p=0} = \gamma Ha\left(s_x - a - L_{x2D}\right) \quad \text{for} \quad H < \tfrac{1}{2}\left(s_x - a\right)$$

$$F_{GRstr2\,p=0} = 0 \qquad\qquad\qquad \text{for} \quad H \geq \tfrac{1}{2}\left(s_x - a\right)$$

$$F_{yGRstr2\,p=0} = \gamma Ha\left(s_y - a - L_{y2D}\right) \quad \text{for} \quad H < \tfrac{1}{2}\left(s_y - a\right)$$

$$F_{GRstr2\,p=0} = 0 \qquad\qquad\qquad \text{for} \quad H \geq \tfrac{1}{2}\left(s_y - a\right)$$

And where L_{x2D} and L_{y2D} are given in equation (4.12). A practical limitation is a minimum embankment height of $H \geq 0.5 \cdot s_x$ and $H \geq 0.5 \cdot s_y$, so that the 2D arches always have enough height to develop fully. Furthermore, the largest 2D arches are wide enough to rest on the pile caps, as the width of the largest arch is equal to s_x or s_y. Figure 4.14 shows that this requirement is not additional to EBGEO (2010) and CUR226 (2010) and only increases the minimum height in a limited, less realistic, number of cases for the British Standard (BS8006, 2010). However, the equations for the case $H < 0.5 \cdot s_{x,y}$ are stated here for calculations for the construction phase.
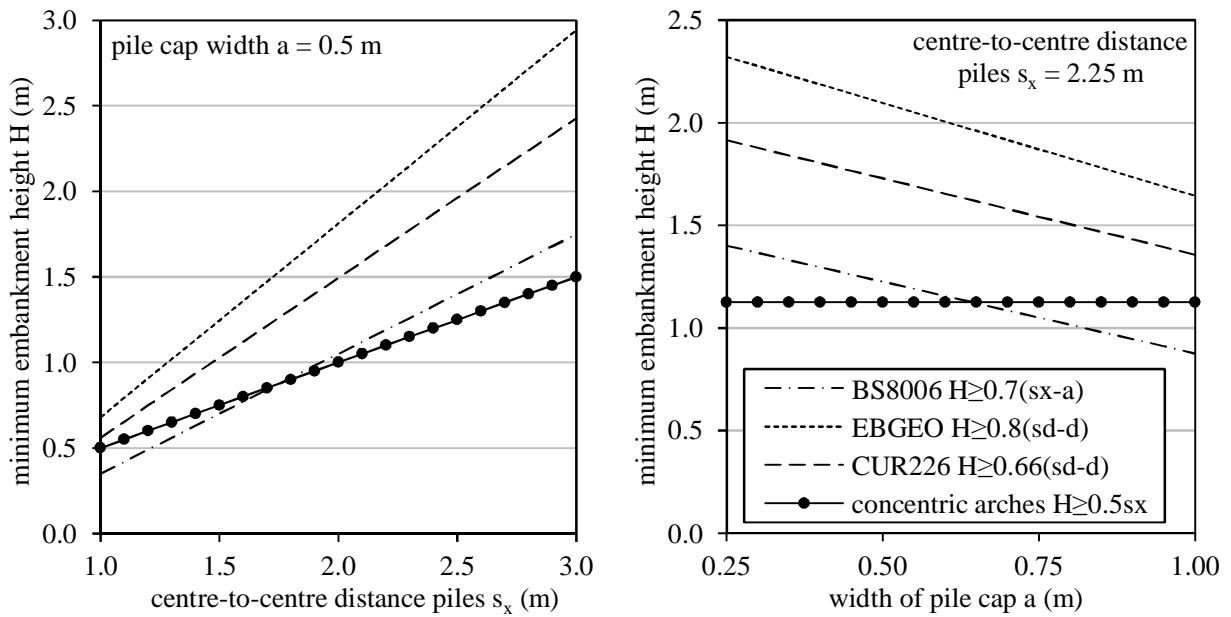
Figure 4.14 Comparison of required minimum embankment heights for the new Concentric Arches model, BS8006 (2010), EBGEO (2010) and CUR226 (2010).

C. Determine the load distribution. The part transferred to the piles directly (arching *A* in kN/pile) is:

$$A = F_{pile} = \left(\gamma H + p\right) \cdot s_x \cdot s_y - F_{GRsquare} - F_{GRstrips} \tag{4.15}$$

as indicated in Figure 4.11. The total load resting on GR+subsoil is therefore:

$$B + C = F_{GRsquare} + F_{GRstrips} \tag{4.16}$$

Calculation step 2 derives the GR strain from this load part *B+C* (Van Eekelen et al., 2012b, Chapter 3.4.2 of this thesis). Appendix 4.B gives a calculation example using the Concentric Arches model for step 1 and the inverse triangular load distribution for step 2 following Van Eekelen et al. (2012b, adopted in Chapter 3 of this thesis).

4.4.6   Line-shaped foundations

The concentric 2D arches also apply in the 2D situation where the embankment is supported by line-shaped supporting elements, such as diaphragm walls or beams. The equations for this case are given in appendix 4.A.4.
When a 2D situation with line-shaped foundation is compared to its corresponding 3D situation with square pile caps (same centre-to-centre distance, same width of square pile caps and line foundation), the resulting average pressure on the GR is lower for the 2D situation than for the 3D situation. This is different from the model of Zaeske, that finds a slightly higher average pressure on the GR in the 2D case.

4.5   Comparison with laboratory experiments, field tests and numerical calculations

4.5.1   Introduction

Step 1 of the calculation model calculates the arching expressed in arching *A,* and also calculates the load distribution on the GR + subsoil. Both results of step 1 should concur with measurements, including the observed dependency on fill height and friction angle.

The calculations for this chapter have been carried out with the newly presented concentric-arches model described in Chapter 4.4, EBGEO (2010) and Hewlett and Randolph (1988), all without safety factors.

Most of the presented experimental results are measurements during a minimum of subsoil support, in other words just before a top load increase in the experiments described in Chapter 4.2.

4.5.2 Arching A

Figure 4.15 compares measured and calculated arching *A* of the experiments described in Chapter 4.2. Calculations that agree exactly with a measurement are located on the dotted diagonal line. The figure shows that the measurements agree much better with the Concentric Arches model than with EBGEO.

The Concentric Arches model has a better match than EBGEO for the embankments with a fill height of 0.34 - 0.42 m (K2, K5, K6, K7, T2 and T3, thus for $H/(s_d\text{-}d) = 0.51$ - 0.62, where s_d is the diagonal centre-to-centre pile spacing). EBGEO under-predicts these measurements much more than the Concentric Arches model. These heights are important in design when making calculations for the construction phase. For the thinnest fill, K8, however, where $H/(s_d\text{-}d) = 0.33$, neither model works properly, but remains on the 'safe side' for the GR design: the models predict more load on the GR than measured.
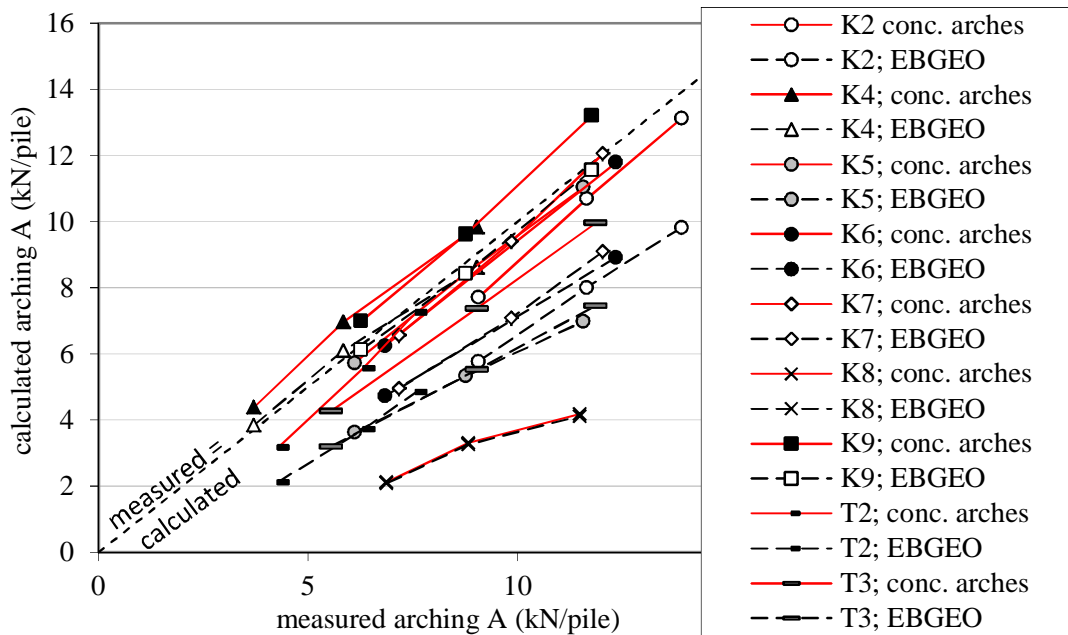
Figure 4.15 Comparison of measured and calculated arching *A* in model experiments specified in Table 4.1.

It should be noted that EBGEO predicted the measurements for the thickest fills (K4 and K9, $H/(s_d\text{-}d) = 0.97$) very well. The Concentric Arches model, however, gives a slight over-prediction in cases with this relatively thick, but realistic, fill. However, in the following paragraphs, it is shown that measurements in two full-scale field tests, and numerical calculations with a full-scale geometry, produce a satisfying match with the results of the Concentric Arches model.

Figure 4.16 compares full-scale field measurements with calculations. The figure shows that EBGEO and the Concentric Arches model agree better or equally well

with the measurements. This is an important result, as it is dangerous to base the conclusions only on scaled model tests. It should be noted that it is difficult to determine the friction angle φ in the fill in the field, while even though φ has a major influence on the calculation results in each of the calculation models, as mentioned before in Chapter 4.3.2.

$\varphi = 43°$, d=0.4m, s_x=1.45m, s_y=1.90m, H=2.60 m, γ=18.3 kN/m³, design load p=26.83 kPa, subsoil: 1m sand, 3m soft clay, 20m sand: k= 310 kN/m³

$\varphi = 43°$, average values geometry: d=0.85 m, s_x=s_y=2.25 m, H=1.86 m, γ=18.3 kN/m³, p=0 kPa, subsoil: 17 m soft soil: k= 0 kN/m³
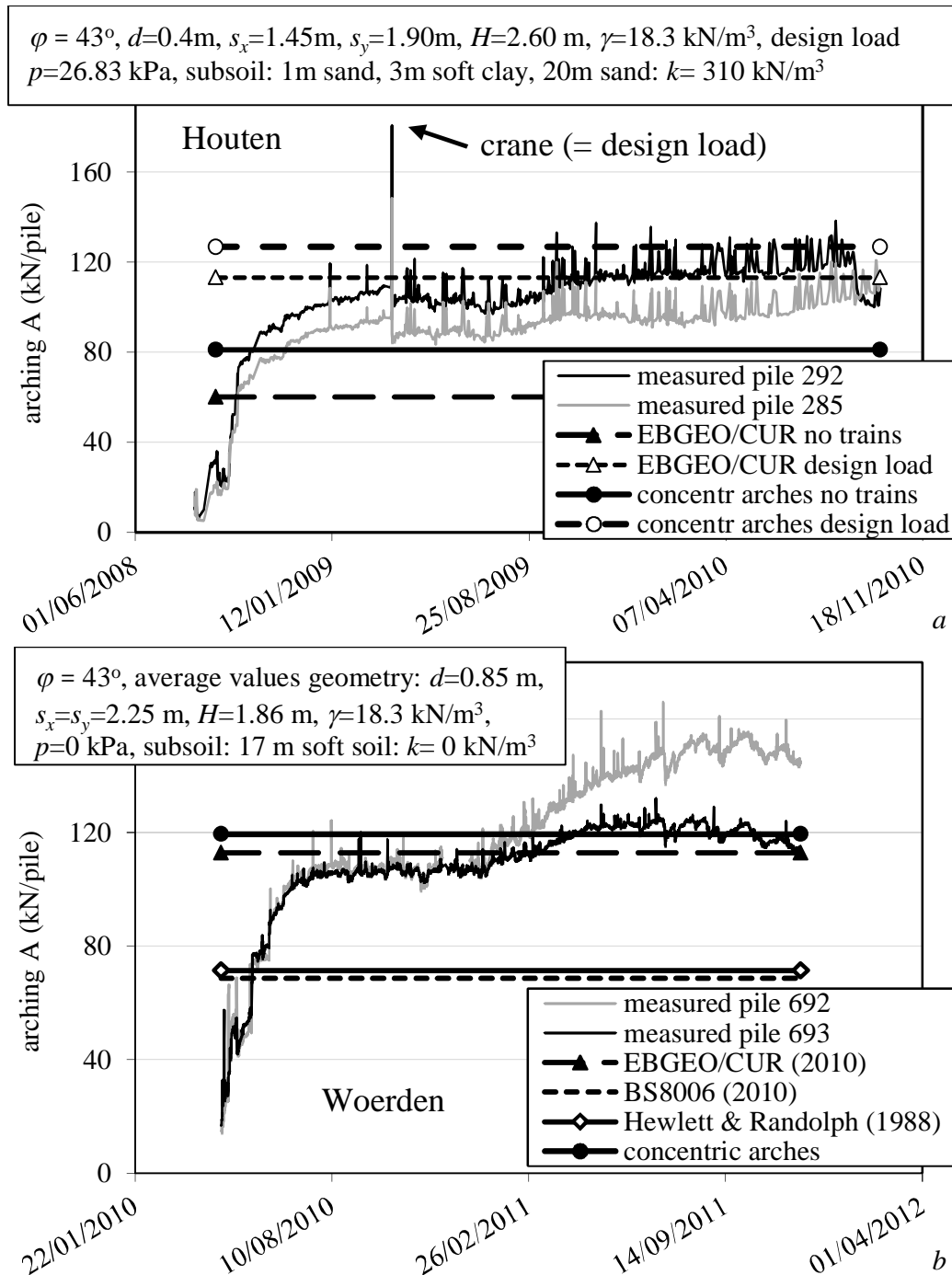
Figure 4.16 Comparison of measured and calculated arching A in two field cases: (*a*) railway Houten, Netherlands, described in Van Duijnen et al., 2010 and (*b*) highway exit Woerden, Netherlands, described in Van Eekelen et al., 2012c, see also appendix 4.B for a calculation example of this case.

4.5.3   The influence of fill height

Figure 4.17 and Figure 4.18 show the influence of embankment height *H*. Figure 4.17 compares measurements of the model tests with predictions. The figure shows that the Concentric Arches model agrees better with the measurements than the other models. The measurements indicate that *A*% increases with embankment height and seems to stabilise for the higher embankments. This finding concurs with Le Hello and Villard's numerical calculations (2009). They developed a numerical model that combined the 3D discrete element method and the finite element method. They also found increasing arching with fill height, stabilising for higher embankments. Figure 4.18 shows that the Concentric Arches model is a reasonable match with the numerical calculations of Le Hello and Villard.
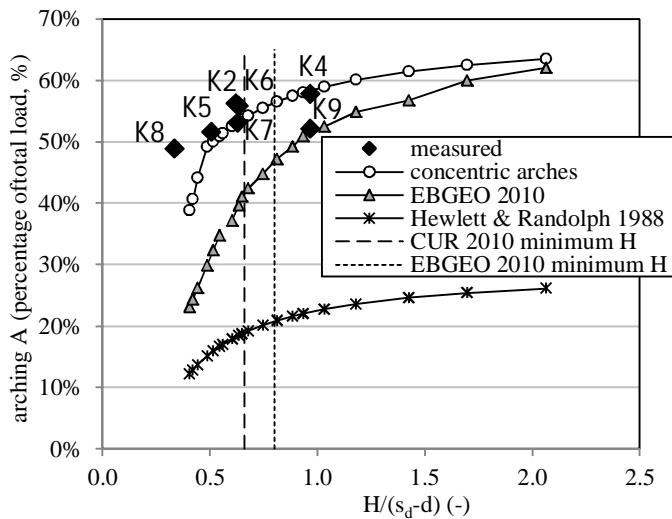
Figure 4.17 Variation of embankment height *H*. Comparison of measured and calculated arching *A*% in model experiments specified in Table 4.1.
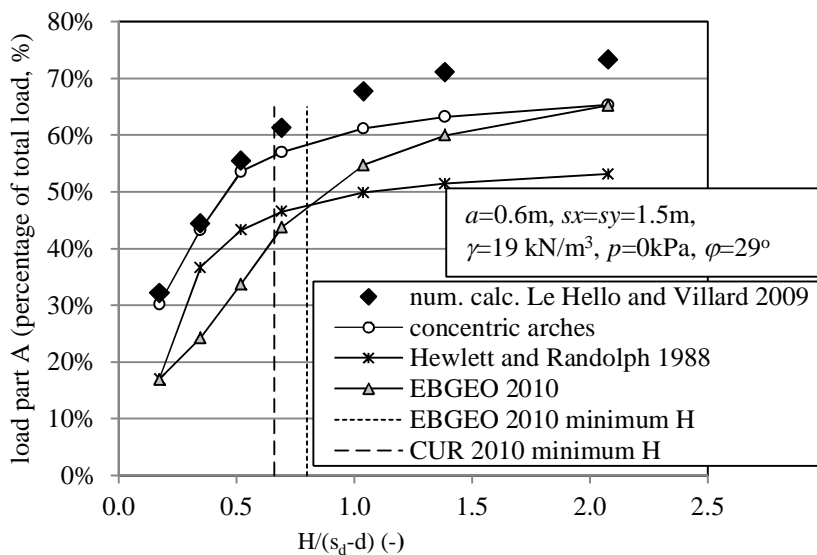
Figure 4.18 Variation of embankment height *H*, comparison of analytical models with numerical calculations of Le Hello and Villard (2009).

4.5.4   Load distribution on GR

Figure 4.19 shows the measured and calculated load distribution on the GR strip. The figure presents the actual results from the new model. It is suggested that the step 2 calculations suggested in Van Eekelen et al. (2012b, Chapter 3 of this thesis) should be followed for design purposes using the simplified inverse triangular load distribution.

The result of step 1 of EBGEO is pressure on a single point of the GR + subsurface. It is assumed that this pressure is the same everywhere between the pile caps, not only on the GR strip. This load is relatively low. For comparison purposes, the EBGEO pressure on GR + subsurface in Figure 4.19 has been concentrated on the GR strip and expressed as the triangular load distribution as used in calculation step 2 of EBGEO.
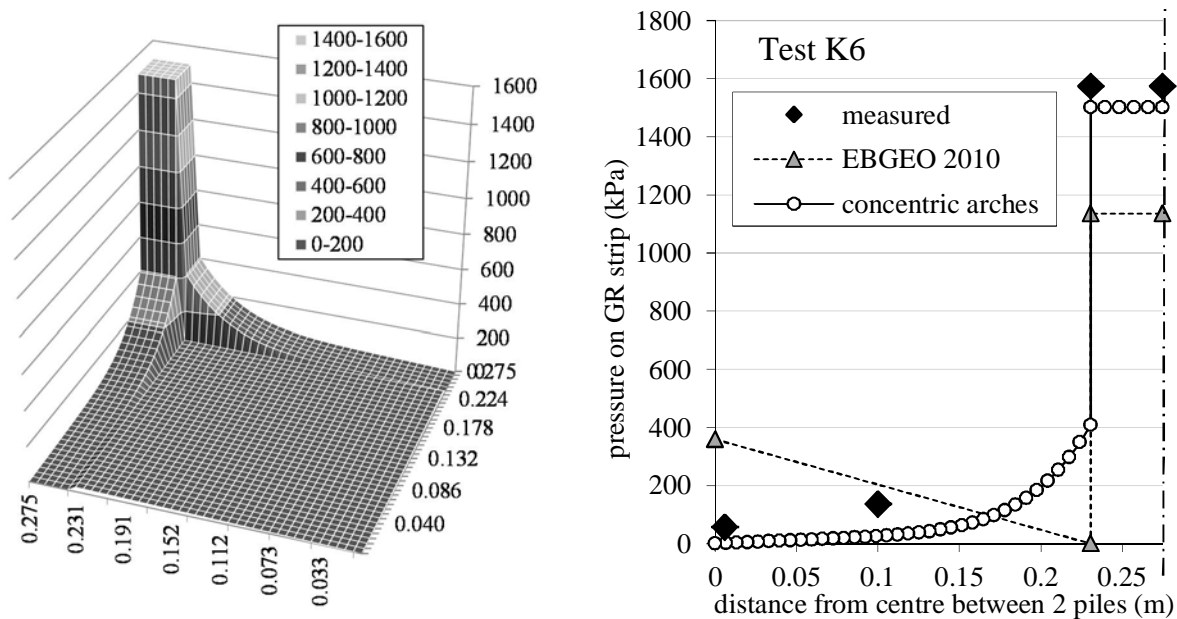
Figure 4.19 Load distribution for test K6 for p-R_b = 66.1 kPa, which equals 20.0 kN/pile and minimum subsoil support: C = 0.5kN/pile, (see Table 4.1). Left: load distribution calculated with concentric model in kPa. Right: cross-section through GR strip and pile. EBGEO gives an equally distributed load, which is translated in calculation step 2 into a triangular load distribution, which is given here.

The figure shows that the measured *A* agrees well with the *A* calculated with the Concentric Arches model. It can therefore be concluded that the total measured *B+C* per pile also agrees well with the calculated *B+C*, as *B+C = total load – A*. The figure also shows clearly that the Concentric Arches model concentrates the load on the GR strips. And the load on the GR strips is concentrated near the pile cap in a way resembling the inverse triangular load distribution. The concentric arches obviously explain the observed concentration of load near the pile caps. The

Concentric Arches model agrees better with the observed load distribution than any of the other available analytical models.

4.5.5   Ground pressure versus depth

Figure 4.20 compares the measured ground pressure (Zaeske, 2001) with the results of the Concentric Arches model, EBGEO, and Hewlett and Randolph (1988). The figure shows that the Concentric Arches model over-predicts the fall in ground pressure with depth, but that it is the only model that more or less follows the measured tendency of falling pressures with depth.
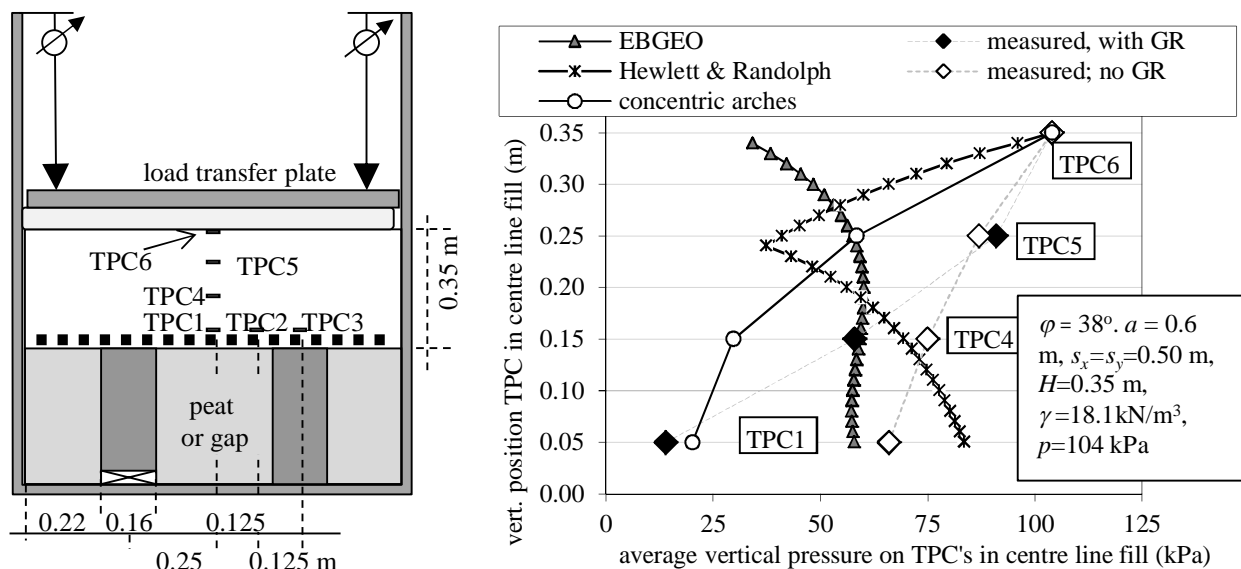
Figure 4.20 Comparison of analytical calculations with measurements in Zaeske (2001, page 63). For comparison reasons, measurements for the situation with and without GR are given (2001, page 55 and 63), see also Figure 4.6.

4.5.6   Parameter study

Figure 4.21*a* shows that an increasing friction angle φ gives increasing arching. The figure shows the measured results for tests T2 and T3. These tests are the same, except for the embankment fill, as indicated in the figure and in Table 4.1.

The figure shows that the Concentric Arches model is a better fit for the measurements than the others. The influence of φ is limited in the Hewlett and Randolph model for $\varphi > 30°$. Within this model of Hewlett and Randolph, the situation of one of two elements is normative: the crown element or the foot element as indicated in Figure 4.2. For $\varphi < 30°$, the foot element is normative,

for $\varphi > 30°$, the crown element is normative. For the crown element, the pressure on the subsurface consists of two terms: the radial stress immediately below the arch, σ_i, and the soil weight below the arch. For $\varphi > 30°$, σ_i is so small that the soil weight below the arch dominates. Soil weight is independent of φ and therefore constant.

a.

b.

c.

d.
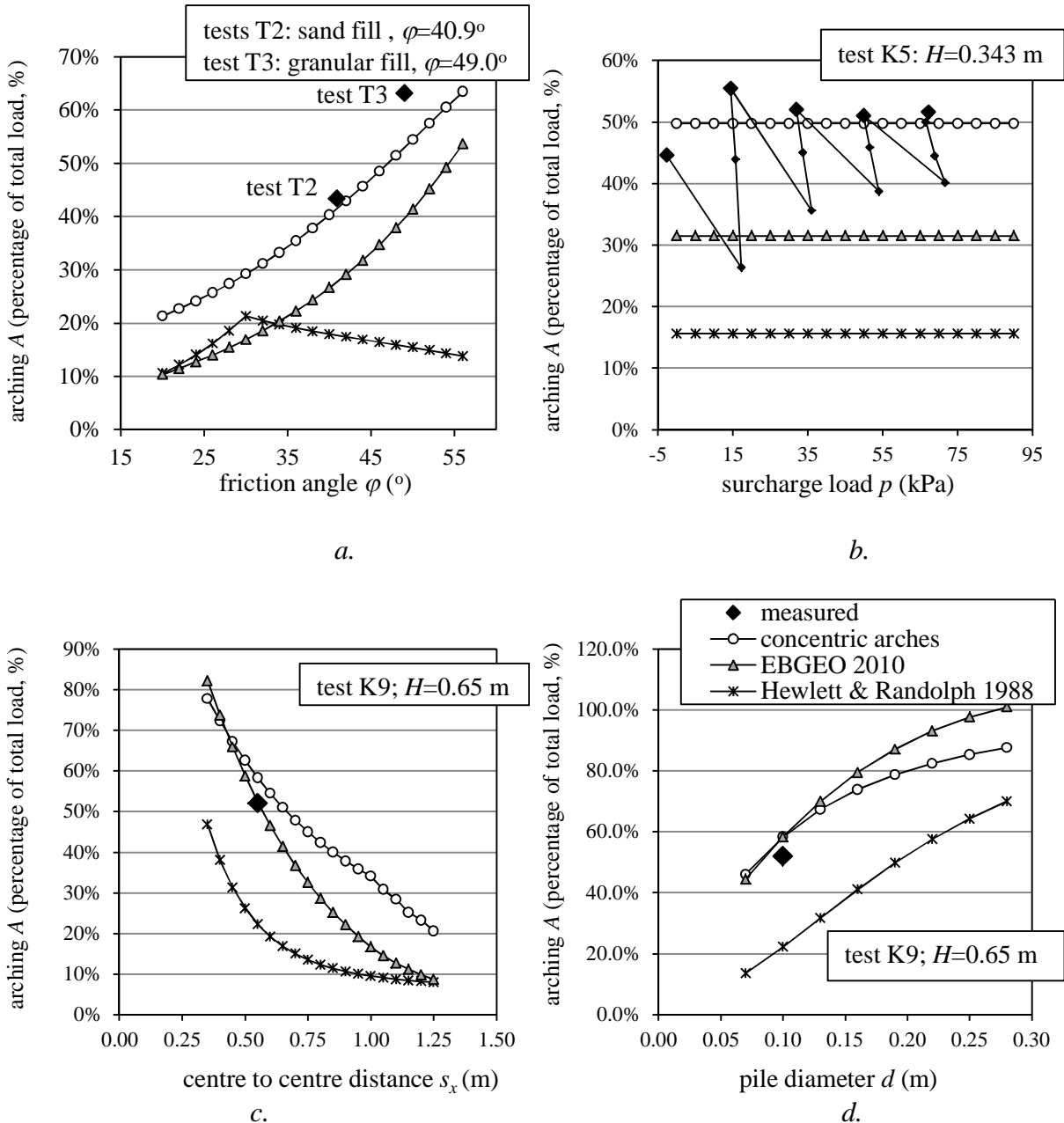
Figure 4.21 Comparison of calculations and measurements in tests T2, T3, K5 and K9. See Table 4.1for test specifications. Parameter study: variation of (*a*) friction angle φ, (*b*) surcharge load *p*. The large dots show the situation with a minimum of subsoil support measured just before a surcharge load increase, (*c*) centre-to-centre distance $s_x = s_y$ and (*d*) pile diameter *d*.

A% in all three models considered is independent of the surcharge load. This is because the models first calculate the load distribution for the situation without surcharge load ($p = 0$ kPa) and then multiply the result by the factor $(\gamma H + p)/(\gamma H)$. This is shown in Figure 4.21*b*. This figure compares the measurements and calculations for test K5. The large dots are the measurements for the situations with a minimum of subsoil support. The figure shows that the measured *A*%, for the situation with a minimum of subsoil support, is indeed more or less constant: the large dots, especially with the higher surcharges, are located more or less on a horizontal line.

Figure 4.21*c* and *d* show variation in the geometric properties; the centre-to-centre distance s_x of the piles and the pile diameter *d*. It is not possible to compare this with the measurements because these features were not varied in the tests. The tendency in the figures confirms expectations: larger pile spacing gives less arching; larger pile cap diameter gives more arching.

4.6   Conclusions

In model tests, numerical studies and field measurements of geosynthetic reinforced piled embankments, the following features were observed:

There is a major difference between piled embankments with or without GR. GR makes arching much more efficient: the load is transferred to the piles much more efficiently. With GR, the load on the GR is concentrated on the GR strips and can be described approximately as an inverse triangular load distribution on the GR strips. The difference between piled embankments with or without GR requires a distinction between models describing one or the other situation.

The observed load distribution in the piled embankments with GR is neither described nor explained by any of the available analytical models.

EBGEO tends to under-predict arching, although prediction accuracy is acceptable in one of the field tests considered. Arching *A*% increases with embankment height and seems to stabilise for the higher embankments. Consolidation of the subsoil results in an increase in arching (increasing arching *A*). This is different from results obtained using most of the available calculation models. A higher friction angle of the fill gives more arching, especially during subsoil consolidation.

A new equilibrium model was presented in this paper: the Concentric Arches model. It is a variation on the Hewlett and Randolph (1988) and EBGEO (Zaeske, 2001) equilibrium models. The model consists of a set of concentric

hemispheres and arches. Larger hemispheres or arches exert more pressure on their subsurface.

A set of concentric 3D hemispheres transfer their load to a set of 2D arches between adjacent piles. These 2D arches transfer their load further to the piles. The model results in a load distribution on the GR that resembles the load distribution observed in experiments, field measurements and numerical analysis: the load is mainly concentrated on the GR strips with an approximately inverse triangular load distribution. The model therefore provides a satisfactory physical explanation for this observed load distribution. The concentric stress arches were also found by several authors presenting numerical studies on arching such as Vermeer et al. (2001), Nadukuru and Michalowski (2012) and Han et al. (2012).

The Concentric Arches model explains increasing arching with subsoil consolidation (GR deflection). The explanation is that new arches are formed in succession as GR deflection progresses. However, in the limit-state version of the model presented in this paper, the model behaves in a rigid-plastic way and no longer describes the influence of subsoil consolidation or deformation.

The new model describes both full and partial arching, the latter with a relatively thin embankment.

Agreement between measured arching *A* and calculations made with the Concentric Arches model is good, and generally better than the EBGEO/CUR results, especially for relatively thin embankments. This finding is important for design calculations for the construction phase. The Concentric Arches model is dependent on the embankment height and the fill friction angle φ in a way similar to that found in the experiments and in the numerical calculations of Le Hello and Villard (2009).

Ground pressure in the embankment decreases with depth and the tendency for decreasing pressure is similar in the Zaeske measurements (2001) and the Concentric Arches model. Furthermore, this model matches Zaeske's observations better than any of the other models considered.

Parameter variation indicates that the response of the Concentric Arches model to variations of surcharge load and geometry is reasonable.

Appendix 4.A. Derivation of the equations of the Concentric Arches model

4.A.1 The 2D arch: radial equilibrium

Consider Figure 4.12. The areas and volume of the crown element are (neglecting terms with a product of more than one increment):

$$
\begin{aligned}
&\text{area below}: dA_i = r \cdot \delta\theta \\
&\text{top area}: dA_o = (r + dr) \cdot \delta\theta = r \cdot \delta\theta + dr \cdot \delta\theta \\
&\text{side area}: dA_s = dr \\
&\text{volume crown element}: dV \approx r \cdot \delta\theta \cdot dr
\end{aligned}
\tag{4.17}
$$

For this 2D plane strain situation, these properties (areas and volume) apply for a unit length in the third dimension. For example $dA_i = r \cdot \delta\theta \cdot 1$, where the '1' is 1 m. The areas dA_i, dA_o and dA_s are therefore expressed in m^2, and dV in m^3. From the vertical (radial) equilibrium of the crown element, it follows that:

$$
-\sigma_r \cdot dA_i + (\sigma_r + d\sigma_r) \cdot dA_0 - 2 \cdot \sigma_\theta \cdot dA_s \cdot \sin\left(\frac{\delta\theta}{2}\right) + \gamma \cdot dV = 0
\tag{4.18}
$$

The stresses σ_r and σ_θ are expressed in kPa and γ in kN/m^3. From substituting equations (4.17), and assuming that $\sin(\delta\theta) \approx \delta\theta$, it follows that:

$$
-\sigma_r \cdot r \cdot \delta\theta + (\sigma_r + d\sigma_r) \cdot (r \cdot \delta\theta + dr \cdot \delta\theta) - 2 \cdot \sigma_\theta \cdot dr \cdot \left(\frac{\delta\theta}{2}\right) + \gamma \cdot r \cdot \delta\theta \cdot dr = 0
\tag{4.19}
$$

$$
\frac{d\sigma_r}{dr} + \frac{d\sigma_r}{r} + \frac{\sigma_r - \sigma_\theta}{r} + \gamma = 0
\tag{4.20}
$$

where σ_r is expressed in kPa. From $\dfrac{d\sigma_r}{r} \to 0$, it follows that:

$$
\frac{d\sigma_r}{dr} + \frac{(\sigma_r - \sigma_\theta)}{r} = -\gamma
\tag{4.21}
$$

We assume that the stress state in the arch is uniform around the semi-circle and that the limit state occurs in the entire arch.

$$
\sigma_\theta = K_p \cdot \sigma_r = \frac{1 + \sin\varphi}{1 - \sin\varphi} \cdot \sigma_r
\tag{4.22}
$$

This results in the 2D differential equation for the radial stress in 2D arches:

$$\frac{d\sigma_r}{dr}+\frac{\left(1-K_p\right)}{r}\cdot\sigma_r=-\gamma \tag{4.23}$$

To solve this differential equation, it can be rewritten as

$$\frac{d\sigma_r}{dr}+p(r)\cdot\sigma_r=q(r) \tag{4.24}$$

Where

$$p(r)=\frac{\left(1-K_p\right)}{r} \quad \text{and} \quad q(r)=-\gamma \tag{4.25}$$

The left-hand and right-hand sides of Equation (4.23) are multiplied by an integration factor: $e^{\int p(r)dr}$. This standard procedure to solve this kind of differential equation results in:

$$\frac{d}{dr}\left(e^{\int p(r)dr}\cdot\sigma_r\right)=e^{\int p(r)dr}q(r) \tag{4.26}$$

We find:

$$e^{\int p(r)dr}=e^{\int\frac{1-K_p}{r}dr}=e^{\left(1-K_p\right)\ln r}=r^{1-K_p} \tag{4.27}$$

Thus (4.26) becomes:

$$\frac{d}{dr}\left(r^{1-K_p}\cdot\sigma_r\right)=q(r)\cdot r^{1-K_p}=-\gamma\cdot r^{1-K_p} \tag{4.28}$$

$$\rightarrow r^{1-K_p}\cdot\sigma_r=-\gamma\int r^{1-K_p}dr=-\frac{\gamma}{2-K_p}\cdot r^{2-K_p}+C \tag{4.29}$$

where C is a constant. Thus

$$\sigma_r=-\frac{\gamma}{2-K_p}\cdot\frac{r^{2-K_p}}{r^{1-K_p}}+\frac{C}{r^{1-K_p}} \tag{4.30}$$

Thus

$$\sigma_r = C \cdot r^{K_p - 1} + \frac{\gamma}{K_p - 2} \cdot r \tag{4.31}$$

For the weightless case we find equation 3 of Hewlett and Randolph's 1988:

$$\sigma_r = C \cdot r^{K_p - 1} \tag{4.32}$$

The boundary condition on the outside of the 2D arch is:

$$r = H_{g2D} \quad \rightarrow \quad \sigma_r = \gamma \left(H - H_{g2D} \right) + p \tag{4.33}$$

Where H_{g2D} is the height of the largest 2D arch and given by equation (4.2). Substitution of this condition into equation (4.31) gives:

$$C \cdot \left(H_{g2D} \right)^{\left(K_p - 1 \right)} + \frac{\gamma}{K_p - 2} \cdot H_{g2D} = \gamma \left(H - H_{g2D} \right) + p$$

$$\rightarrow C = H_{g2D}{}^{\left(1 - K_p \right)} \cdot \left[\gamma H + p - \gamma H_{g2D} \frac{\left(K_p - 1 \right)}{\left(K_p - 2 \right)} \right] \tag{4.34}$$

thus

$$\rightarrow \sigma_r = \left(\frac{2}{s_x} \right)^{\left(K_p - 1 \right)} \cdot \left[\gamma H + p - \frac{s_x \gamma}{2} \frac{\left(K_p - 1 \right)}{\left(K_p - 2 \right)} \right] \cdot r^{\left(K_p - 1 \right)} + \frac{\gamma}{K_p - 2} \cdot r \tag{4.35}$$

As the tangential stress $\sigma_\theta = K_p \cdot \sigma_r$ in kPa, we find:

$$\sigma_\theta = P_{2D} \cdot r^{\left(K_p - 1 \right)} + Q_{2D} \cdot r$$

where we have defined P_{2D} and Q_{2D} as:

$$\tag{4.36}$$

$$P_{2D} = K_p \cdot \left(\frac{2}{s_x} \right)^{\left(K_p - 1 \right)} \cdot \left[\gamma H + p - \frac{s_x \gamma}{2} \frac{\left(K_p - 1 \right)}{\left(K_p - 2 \right)} \right] \quad \text{and} \quad Q_{2D} = K_p \cdot \frac{\gamma}{K_p - 2}$$

4.A.2 The 3D arch: radial equilibrium

Consider Figure 4.13. The areas and volume of the crown element are (neglecting terms with a product of more than one increment):

$$\text{area below}: dA_i = \tfrac{1}{4}\pi \cdot \left(R \cdot \delta\theta\right)^2 = \tfrac{1}{4}\pi \cdot R^2 \cdot \delta\theta^2$$

$$\text{top area}: dA_o = \tfrac{1}{4}\pi \cdot \left(R + dR\right)^2 \cdot \delta\theta^2 \approx \tfrac{1}{4}\pi \cdot \left(R^2 \cdot \delta\theta^2 + 2R \cdot dR \cdot \delta\theta^2\right)$$

$$\text{side area}: dA_s \approx \pi \cdot R \cdot \delta\theta \cdot dR$$

$$\text{volume crown element}: dV \approx \tfrac{1}{4}\pi \cdot R^2 \cdot \delta\theta^2 \cdot dR$$

(4.37)

From the vertical (radial) equilibrium of the crown element, it follows that:

$$-\sigma_R \cdot dA_i + \left(\sigma_R + d\sigma_R\right) \cdot dA_0 - \sigma_\theta \cdot \sin\left(\frac{\delta\theta}{2}\right) \cdot dA_s + \gamma \cdot dV = 0 \tag{4.38}$$

From substituting equations (4.37), and assuming $\sin\left(\delta\theta\right) \approx \delta\theta$, it follows that:

$$-\sigma_R \cdot \tfrac{1}{4}\pi \cdot R^2 \cdot \delta\theta^2 + \left(\sigma_R + d\sigma_R\right) \cdot \tfrac{1}{4}\pi \cdot \left(R^2 \cdot \delta\theta^2 + 2R \cdot dR \cdot \delta\theta^2\right)$$
$$-\sigma_\theta \cdot \left(\frac{\delta\theta}{2}\right) \cdot \pi \cdot R \cdot \delta\theta \cdot dR + \gamma \cdot \tfrac{1}{4}\pi \cdot R^2 \cdot \delta\theta^2 \cdot dR = 0 \tag{4.39}$$

From neglecting terms with a product of more than one increment, it follows that:

$$\frac{d\sigma_R}{dR} + \frac{2\left(\sigma_R - \sigma_\theta\right)}{R} + \gamma = 0 \tag{4.40}$$

In the weightless case, the stress state in the arch is uniform around the semi-circle. It is assumed that the limit state occurs in the entire arch.

$$\sigma_\theta = K_p \cdot \sigma_R = \frac{1 + \sin\varphi}{1 - \sin\varphi} \cdot \sigma_R \tag{4.41}$$

This results in:

$$\frac{d\sigma_R}{dR} + \frac{2\left(1 - K_p\right)}{R} \cdot \sigma_R = -\gamma \tag{4.42}$$

which is the differential equation for the radial stress in the 3D hemisphere. So far, the explanation is the same as Hewlett and Randolph's (1988). To solve this differential equation, equation (4.23) can be rewritten as:

$$\frac{d}{dR}\left(e^{\int p(R)dR} \cdot \sigma_R\right) = e^{\int p(R)dR} q(R) \tag{4.43}$$

with:

$$p(R) = \frac{2(1-K_p)}{R} = \frac{\alpha}{R} \text{ and } q(R) = -\gamma \tag{4.44}$$

and $\alpha = 2(1-K_p)$

We find:

$$e^{\int p(R)dR} = e^{\int \frac{\alpha}{R}dR} = e^{\alpha \ln R} = R^{\alpha} \tag{4.45}$$

Thus equation (4.43) becomes:

$$\frac{d}{dR}\left(R^{\alpha} \cdot \sigma_R\right) = q(R) \cdot R^{\alpha} = -\gamma \cdot R^{\alpha} \tag{4.46}$$

$$\rightarrow R^{\alpha} \cdot \sigma_R = -\frac{\gamma}{\alpha+1} \cdot R^{\alpha+1} + C \tag{4.47}$$

where C is a constant. Thus

$$\sigma_R = -\frac{\gamma}{\alpha+1} \cdot R + \frac{C}{R^{\alpha}}$$

$$\rightarrow \sigma_R = C \cdot R^{2(K_p-1)} + \frac{\gamma}{2K_p-3} \cdot R \tag{4.48}$$

The outer radius of the hemisphere is $R_o = s_x/\sqrt{2}$. The surcharge load will first be neglected and taken into account afterwards, analogous to Zaeske (2001) and Hewlett and Randolph (1988). The boundary condition on the outside of the arch is:

$$R = R_o = H_{g3D} \quad \rightarrow \quad \sigma_R = \gamma\left(H - H_{g3D}\right) \tag{4.49}$$

where the arch height H_{g3D} is given by equation (4.4). Substitution of this condition into equation (4.48) gives:

$$C \cdot H_{g3D}^{2(K_p-1)} + \frac{\gamma}{2K_p - 3} \cdot H_{g3D} = \gamma \left(H - H_{g3D} \right)$$

$$\rightarrow C = \gamma \cdot H_{g3D}^{2-2K_p} \cdot \left[H - H_{g3D} \cdot \left(\frac{2K_p - 2}{2K_p - 3} \right) \right]$$

(4.50)

Thus

$$\rightarrow \sigma_R = \gamma \cdot H_{g3D}^{2-2K_p} \cdot \left[H - H_{g3D} \cdot \left(\frac{2K_p - 2}{2K_p - 3} \right) \right] \cdot R^{2K_p-2} + \frac{\gamma}{2K_p - 3} \cdot R$$

(4.51)

As $\sigma_\theta = K_p \cdot \sigma_r$, we find:

$$\sigma_\theta = P_{3D} \cdot R^{2K_p-2} + Q_{3D} \cdot R$$

where we have defined P_{3D} and Q_{3D} as:

$$P_{3D} = \gamma \cdot K_p \cdot H_{g3D}^{2-2K_p} \cdot \left[H - H_{g3D} \cdot \left(\frac{2K_p - 2}{2K_p - 3} \right) \right] \text{ and } Q_{3D} = K_p \cdot \frac{\gamma}{2K_p - 3}$$

(4.52)

So far, Hewlett and Randolph used the same explanation. However, a difference is that they limit the height of their arch to half the width of the pile cap, while the equation of the Concentric Arches model is extended downwards to the subsurface where $R = 0$. Hewlett and Randolph (1988) therefore use equation (4.52) for $R_i < R < R_o$, and we use the equation for $0 < R < R_o$, where for full arching: $R_o = H_{g3D} = 0.5s_d$ and $R_i = 0.5(s_d\text{-}d)$.

4.A.3 Derivation of load exerted on GR

Arching is assumed to transfer the load in two steps. The first step is that the load is transferred in the direction of the ring of GR strips and pile caps. This is done along the 3D hemispheres. The second step is that the load is transferred further in the direction of the pile caps along the 2D arches between each two adjacent pile caps. The 2D and 3D arches exert a total force on the subsurface. The total force

exerted on the GR ($B+C$ in kN/pile) may be obtained by integrating the tangential stress σ_θ across the area of the GR. The general equation is:

$$B+C = F_{GR} = \int_{GRarea} \sigma_\theta dA_{GR} = F_{GRsquare} + F_{GRstrips} \tag{4.53}$$

The total load $B+C$ on the subsurface, F_{GR}, consists of two parts along the two arching steps described above: $F_{GRsquare}$ and $F_{GRstrips}$:

1. 3D hemispheres transfer the load in the direction of the ring of GR strips and pile caps. The 3D hemispheres exert a vertical load on their GRsquare (indicated in Figure 4.11*b*). This is the first load part, $F_{GRsquare}$, of the load on the subsurface.
2. The 2D arches above the GR strips transfer the load further in the direction of the pile caps. The 2D arches exert a vertical load on the GR strips (indicated in Figure 4.11*c*). This is the second load part, $F_{GRstrips}$, of the load on the subsurface.
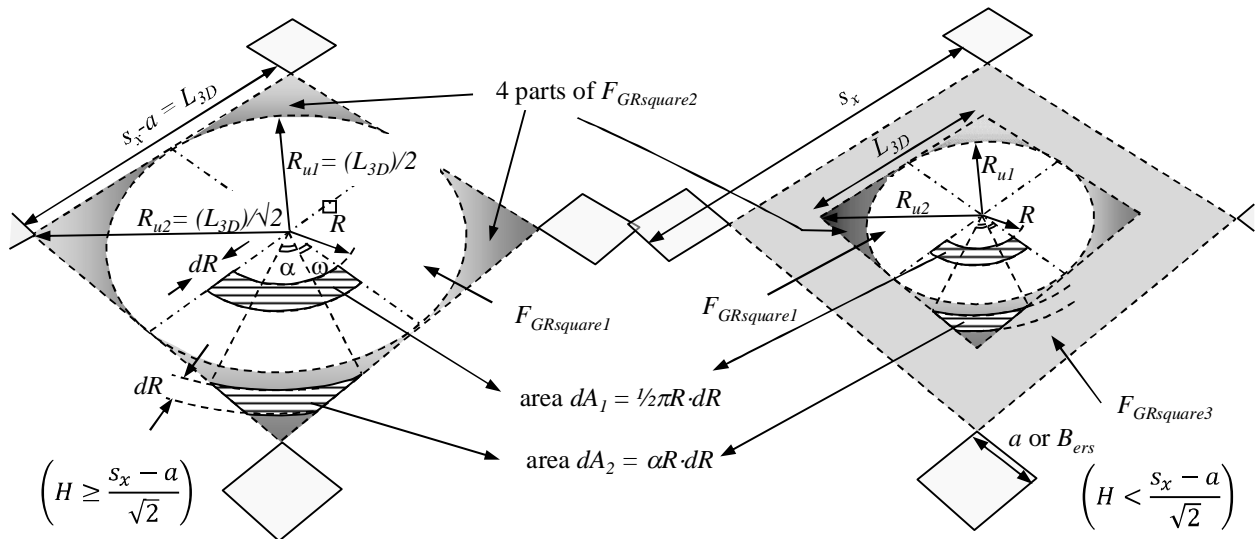
Figure 4.22 Integrating the tangential stress σ_θ across the square area where the 3D hemispheres exert their load.

Total force on the GR square; determination of $F_{GRsquare}$

Consider Figure 4.22. As long as $H \geq \dfrac{s_x - a}{\sqrt{2}}$, $F_{GRsquare}$ consists of the load exerted by the hemispheres only. In that case (on the left of Figure 4.22), the total force exerted on the GRsquare may be obtained by integrating the tangential stress σ_θ in the 3D hemispheres across the GRsquare. When $H < \dfrac{s_x - a}{\sqrt{2}}$, the total force exerted on the GRsquare may be obtained by integrating the tangential stress σ_θ across the smaller ($L_{x3D} \cdot L_{x3D}$ -)square, with width L_{x3D}, as indicated on the right of Figure 4.22. The load F_{GRsq3} on the area outside this $L_{x3D} \cdot L_{x3D}$ -square and inside the GRsquare is assumed to be $\gamma H + p$, which will be derived for later on. L_{x3D} is defined as follows:

$$
\begin{aligned}
L_{x3D} &= s_x - a && \text{for} \quad H \geq \frac{s_x - a}{\sqrt{2}} \\
L_{x3D} &= \sqrt{2} \cdot H_{g3D} && \text{for} \quad H < \frac{s_x - a}{\sqrt{2}}
\end{aligned}
\tag{4.54}
$$

where H_{g3D} in defined in equation (4.4). For the situation in which $s_x \neq s_y$ the integration is carried out for an imaginary square with width L_{x3D}. This width is determined as:

$$
\begin{aligned}
L_{x3D} &= \frac{1}{\sqrt{2}} \sqrt{\left(s_x - a\right)^2 + \left(s_y - a\right)^2} && \text{for} \quad H \geq \frac{1}{2}\sqrt{\left(s_x - a\right)^2 + \left(s_y - a\right)^2} \\
L_{x3D} &= \sqrt{2} \cdot H_{g3D} && \text{for} \quad H < \frac{1}{2}\sqrt{\left(s_x - a\right)^2 + \left(s_y - a\right)^2}
\end{aligned}
\tag{4.55}
$$

Considering the situation that $H \geq \dfrac{1}{2}\sqrt{\left(s_x - a\right)^2 + \left(s_y - a\right)^2}$, the square with width L_{x3D} has the same diagonal as the area between the four piles. Integrating the tangential stress across this imaginary square gives the same or a higher force on the GR square than numerical integration of the tangential stress over the rectangular between the four piles. In the remainder of this appendix, the situation with $s_x = s_y$ applies.

The total force $F_{GRsquare}$ on the GR square is derived by dividing the square into three sections:

- part $F_{GRsquare1}$, inside the largest circle in the $L_{x3D} \cdot L_{x3D}$ -square (white in Figure 4.22)
- part $F_{GRsquare2}$, outside the circle but inside the $L_{x3D} \cdot L_{x3D}$ -square (dark grey Figure 4.22).
- part $F_{GRsquare3}$, outside the $L_{x3D} \cdot L_{x3D}$-square but inside the GR square (light grey in the right-hand figure in Figure 4.22).

The three terms are calculated with surcharge load $p = 0$, and will afterwards be multiplied by the term $\dfrac{\gamma H + p}{\gamma H}$ to find the total load on the GR square:

$$F_{GRsquare} = F_{GRsquare1} + F_{GRsquare2} + F_{GRsquare3} =$$
$$\left(\frac{\gamma H + p}{\gamma H} \right) \cdot \left(F_{GRsq1\,p=0} + F_{GRsq2\,p=0} + F_{GRsq3\,p=0} \right) \tag{4.56}$$

The first load part, $F_{GRsquare1}$, which rests on the circular area in the largest circle, is determined as follows:

$$F_{GRsq1\,p=0} = 4 \int_0^{R_{u1}} \sigma_\theta dA_{GR} = 4 \int_0^{R_{u1}} \sigma_\theta \tfrac{1}{2} \pi R dR = 2\pi \int_0^{R_{u1}} \left(P_{3D} \cdot (R)^{2K_p - 1} + Q_{3D} \cdot R^2 \right) dR$$

$$F_{GRsq1\,p=0} = 2\pi \left[\frac{P_{3D}}{2K_p} \cdot (R)^{2K_p} + \tfrac{1}{3} Q_{3D} \cdot R^3 \right]_0^{R_{u1}=\frac{L_{x,3D}}{2}} \tag{4.57}$$

$$F_{GRsquare1} = \left(1 + \frac{p}{\gamma H} \right) \cdot \left(\frac{\pi P_{3D}}{K_p} \cdot \left(\frac{L_{x3D}}{2} \right)^{2K_p} + \tfrac{2}{3} \pi Q_{3D} \cdot \left(\frac{L_{x3D}}{2} \right)^3 \right)$$

where σ_θ, P_{3D} and Q_{3D} are given in equation (4.52). The second load part, $F_{GRsquare2}$, which rests on the area within the square but outside the circle, is dependent on angle α. This angle α is a function of R, and can be read from Figure 4.22, as the complementary angle $\omega = \arccos\left(\dfrac{R_{u1}}{R} \right) = \arccos\left(\dfrac{L_{x3D}}{2R} \right)$. We therefore find, for α:

$$\alpha = \frac{\pi}{2} - 2\arccos\left(\frac{L_{x3D}}{2R} \right) \tag{4.58}$$

The force on the grey areas in Figure 4.22 (outside the circle, inside the GR square) should therefore be determined by:

$$F_{GRsquare2} = \left(1 + \frac{p}{\gamma H}\right) \cdot F_{GRsq2\,p=0} \quad \text{where}$$

$$F_{GRsq2\,p=0} = 4\int_{R_{u1}}^{R_{u2}} \sigma_\theta dA_{GRsq2} = 4\int_{R_{u1}}^{R_{u2}} \sigma_\theta \alpha R dR = 4\int_{R_{u1}}^{R_{u2}} \left(P_{3D} \cdot (R)^{2K_p-2} + Q_{3D} \cdot R\right) \alpha R dR \quad (4.59)$$

$$\rightarrow F_{GRsq2\,p=0} = 4\int_{R_{u1}}^{R_{u2}} \left(P_{3D} \cdot (R)^{2K_p-2} + Q_{3D} \cdot R\right)\left(\frac{\pi}{2} - 2\arccos\left(\frac{L_{x,3D}}{2R}\right)\right) R dR$$

This integral can be separated into four terms, which will be solved separately:

$$F_{GRsq2\,p=0} = {}_1F_{GRsq2} + {}_2F_{GRsq2} + {}_3F_{GRsq2} + {}_4F_{GRsq2}$$

where

$${}_1F_{GRsq2} = 2\pi P_{3D} \int_{R_{u1}}^{R_{u2}} R^{2K_p-1} dR$$

$${}_2F_{GRsq2} = 2\pi Q_{3D} \int_{R_{u1}}^{R_{u2}} R^2 dR \quad (4.60)$$

$${}_3F_{GRsq2} = -8P_{3D} \int_{R_{u1}}^{R_{u2}} R^{2K_p-1} \arccos\left(\frac{L_{x3D}}{2R}\right) dR$$

$${}_4F_{GRsq2} = -8Q_{3D} \int_{R_{u1}}^{R_{u2}} R^2 \arccos\left(\frac{L_{x3D}}{2R}\right) dR$$

The first two terms are solved as follows (R_{u2} and R_{u1} are indicated in Figure 4.22):

$${}_1F_{GRsq2} = \frac{2\pi P_{3D}}{2K_p} R^{2K_p}\Big|_{R_{u1}}^{R_{u2}} = \frac{\pi P_{3D}}{K_p}\left(2^{K_p} - 1\right)\left(\frac{L_{x3D}}{2}\right)^{2K_p}$$

$$(4.61)$$

$${}_2F_{GRsq2} = \frac{2\pi Q_{3D}}{3} R^3\Big|_{R_{u1}}^{R_{u2}} = \frac{2\pi Q_{3D}}{3}\left(\left(\sqrt{2}\right)^3 - 1\right)\left(\frac{L_{x3D}}{2}\right)^3$$

The other two integral terms are re-written as:

$$-\frac{3F_{GRsq2}}{8P_{3D}} = \int_{R_{u1}}^{R_{u2}} R^{2K_p - 1} \arccos\left(\frac{L_{x3D}}{2R}\right) dR$$

$$-\frac{4F_{GRsq2}}{8Q_{3D}} = \int_{R_{u1}}^{R_{u2}} R^2 \arccos\left(\frac{L_{x3D}}{2R}\right) dR$$

(4.62)

We continue with solving the fourth term, $_4F_{GRsq2}$, and substitute:

$$\rho = \frac{L_{x3D}}{2R} \quad \text{thus} \quad R = \frac{L_{x3D}}{2\rho} \quad \text{and} \quad dR = -\frac{L_{x3D}}{2\rho^2} d\rho$$

$$\rightarrow \int_{R_{u1} = \frac{L_{x3D}}{2}}^{R_{u2} = \frac{L_{x3D}}{\sqrt{2}}} dR = \int_{\frac{L_{x3D}}{2R_{u1}} = \frac{L_{x3D}}{2 \cdot \frac{L_{x3D}}{2}} = 1}^{\frac{L_{x3D}}{2R_{u2}} = \frac{L_{x3D}}{2 \cdot \frac{L_{x3D}}{\sqrt{2}}} = \frac{1}{2}\sqrt{2}} d\rho$$

(4.63)

where ρ is the cosine of the complementary angle $\omega = \arccos\left(\frac{L_{x3D}}{2R}\right)$ in Figure 4.22.

Thus

$$\frac{4F_{GRsq2}}{8Q_{3D}} = \int_{1}^{\frac{1}{2}\sqrt{2}} \left(\frac{L_{x3D}}{2\rho}\right)^2 \arccos\rho \left(\frac{L_{x3D}}{2\rho^2}\right) d\rho$$

$$\rightarrow \frac{4F_{GRsq2}}{Q_{3D}\left(L_{x3D}\right)^3} = \int_{1}^{\frac{1}{2}\sqrt{2}} \rho^{-4} \arccos\rho \, d\rho$$

(4.64)

We bring the power to the increment

$$-\frac{3 \cdot {}_4F_{GRsq2}}{Q_{3D}\left(L_{x3D}\right)^3} = \int_{1}^{\frac{1}{2}\sqrt{2}} \arccos\rho \, d\left(\rho^{-3}\right)$$

(4.65)

Partial integration gives:

$$-\frac{3 \cdot {}_4F_{GRsq2}}{Q_{3D}\left(L_{x3D}\right)^3} = \rho^{-3} \arccos\rho \Big|_{1}^{\frac{1}{2}\sqrt{2}} - \int_{1}^{\frac{1}{2}\sqrt{2}} \rho^{-3} d\left(\arccos\rho\right)$$

(4.66)

As $\dfrac{d}{d\rho}\left(\arccos\rho\right)=-\dfrac{1}{\sqrt{1-\rho^2}}$, we find:

$$-\frac{3\cdot {_4}F_{GRsq2}}{Q_{3D}\left(L_{x3D}\right)^3}=\frac{\pi}{\sqrt{2}}+\int_{1}^{\frac{1}{2}\sqrt{2}}\frac{\rho^{-3}}{\sqrt{1-\rho^2}}\,d\rho \tag{4.67}$$

We substitute:

$$\frac{1}{\sqrt{1-\rho^2}}=\frac{\sqrt{u^2+1}}{u}$$

$$\rightarrow \rho^{-2}=u^2+1$$

$$\rightarrow -\rho^{-3}\,d\rho=u\,du \tag{4.68}$$

$$\rightarrow \int_{\rho=1}^{\rho=\frac{1}{2}\sqrt{2}} d\rho = \int_{u=\sqrt{\frac{1}{(1)^2}-1}=0}^{u=\sqrt{\frac{1}{\left(\frac{1}{2}\sqrt{2}\right)^2}-1}=1} du$$

This gives:

$$-\frac{3\cdot {_4}F_{GRsq2}}{Q_{3D}\left(L_{x3D}\right)^3}=\frac{\pi}{\sqrt{2}}-\int_{0}^{1}\sqrt{u^2+1}\,du \tag{4.69}$$

This gives, with any integral table:

$$-\frac{3\cdot {_4}F_{GRsq2}}{Q_{3D}\left(L_{x3D}\right)^3}=\frac{\pi}{\sqrt{2}}-\tfrac{1}{2}\sqrt{2}-\tfrac{1}{2}\ln\left(1+\sqrt{2}\right) \tag{4.70}$$

Thus

$${_4}F_{GRsq2}=\tfrac{1}{6}Q_{3D}\left(L_{x3D}\right)^3\cdot\left(\sqrt{2}\left(1-\pi\right)+\ln\left(1+\sqrt{2}\right)\right) \tag{4.71}$$

The derivation of the third term, ${_3}F_{GRsq2}$, follows the same procedure as for ${_4}F_{GRsq2}$. With equations (4.63) and (4.62) we find:

$$\frac{_3F_{GRsq2} \cdot 2^{2K_p-3}}{P_{3D} \cdot \left(L_{x3D}\right)^{2K_p}} = \int_{1}^{\frac{1}{2}\sqrt{2}} \rho^{-2K_p-1} \arccos\rho \, d\rho \tag{4.72}$$

We bring the power to the increment:

$$\rho^{-2K_p-1} = \frac{1}{-2K_p} d\rho^{-2K_p}$$

$$\rightarrow -\frac{2K_p \cdot {}_3F_{GRsq2} \cdot 2^{2K_p-3}}{P_{3D} \cdot \left(L_{x3D}\right)^{2K_p}} = \int_{1}^{\frac{1}{2}\sqrt{2}} \arccos\rho \, d\rho^{-2K_p} \tag{4.73}$$

Partial integration:

$$-\frac{K_p \cdot {}_3F_{GRsq2} \cdot 2^{2K_p-2}}{P_{3D} \cdot \left(L_{x3D}\right)^{2K_p}} = \rho^{-2K_p} \arccos\rho \Big|_{1}^{\frac{1}{2}\sqrt{2}} - \int_{1}^{\frac{1}{2}\sqrt{2}} \rho^{-2K_p} d\left(\arccos\rho\right) \tag{4.74}$$

Thus

$$-\frac{K_p \cdot {}_3F_{GRsq2} \cdot 2^{2K_p-2}}{P_{3D} \cdot \left(L_{x3D}\right)^{2K_p}} = \frac{\pi}{2^{2-K_p}} - \int_{1}^{\frac{1}{2}\sqrt{2}} \frac{\rho^{-2K_p}}{\sqrt{1-\rho^2}} d\rho \tag{4.75}$$

Finally, the substitution of:

$$\frac{1}{\sqrt{1-\rho^2}} = \frac{\sqrt{u^2+1}}{u}$$

$$\rightarrow \rho^{-2} = u^2+1 \rightarrow -\rho^{-3}d\rho = u\,du$$

$$\rightarrow \rho^{-2K_p} = \left(u^2+1\right)^{K_p}$$

$$\rightarrow \rho^3 = \left(u^2+1\right)^{-\frac{3}{2}} \tag{4.76}$$

$$\rightarrow d\rho = -u\rho^3 du = -u\left(u^2+1\right)^{-\frac{3}{2}} du$$

$$\rightarrow \int_{\rho=1}^{\rho=\frac{1}{2}\sqrt{2}} d\rho = \int_{u=\sqrt{\frac{1}{(1)^2}-1}=0}^{u=\sqrt{\frac{1}{\left(\frac{1}{2}\sqrt{2}\right)^2}-1}=1} du$$

gives:

$$-\frac{K_p \cdot {}_3F_{GRsq2} \cdot 2^{2K_p-2}}{P_{3D} \cdot \left(L_{x3D}\right)^{2K_p}} =$$

$$\frac{\pi}{2^{2-K_p}} + \int_0^1 \frac{\sqrt{u^2+1}}{u}\left(u^2+1\right)^{K_p} u\left(u^2+1\right)^{-\frac{3}{2}} du$$

$$\rightarrow -\frac{K_p \cdot {}_3F_{GRsq2} \cdot 2^{2K_p-2}}{P_{3D} \cdot \left(L_{x3D}\right)^{2K_p}} = \frac{\pi}{2^{2-K_p}} + \int_0^1 \left(u^2+1\right)^{K_p-1} du$$

(4.77)

This last term can be rewritten with a binomial series:

$$\int_0^1 \left(u^2+1\right)^{K_p-1} du = \int_0^1 \sum_{n=0}^{\infty} \binom{K_p-1}{n} u^{2n}\, du$$

(4.78)

where:

$$\sum_{n=0}^{\infty} \binom{K_p-1}{n} u^{2n} =$$

$$1+\left(K_p-1\right)u^2+\frac{\left(K_p-1\right)\left(K_p-2\right)}{2!}u^4+\frac{\left(K_p-1\right)\left(K_p-2\right)\left(K_p-3\right)}{3!}u^6+...$$

(4.79)

From this, it follows that:

$$\int_0^1 \left(u^2+1\right)^{K_p-1} du = \frac{1}{2n+1}\sum_{n=0}^{\infty} \binom{K_p-1}{n} u^{2n+1}\Bigg|_0^1 = \sum_{n=0}^{\infty} \frac{1}{2n+1}\binom{K_p-1}{n}$$

(4.80)

$$\rightarrow -\frac{K_p \cdot {}_3F_{GRsq2} \cdot 2^{2K_p-2}}{P_{3D} \cdot (L_{x3D})^{2K_p}} = \frac{\pi}{2^{2-K_p}} + \int_0^1 (u^2+1)^{K_p-1} \, du$$

$$-\frac{K_p \cdot {}_3F_{GRsq2} \cdot 2^{2K_p-2}}{P_{3D} \cdot (L_{x3D})^{2K_p}} = \frac{\pi}{2^{2-K_p}} + \sum_{n=0}^{\infty} \frac{1}{2n+1} \binom{K_p-1}{n}$$

$$\rightarrow {}_3F_{GRsq2} = -\frac{P_{3D} \cdot 2^{2-2K_p} \cdot (L_{x3D})^{2K_p}}{K_p} \cdot \left(\frac{\pi}{2^{2-K_p}} + \sum_{n=0}^{\infty} \frac{1}{2n+1} \binom{K_p-1}{n} \right)$$

$$= -\frac{P_{3D} \cdot 2^{2-2K_p} \cdot (L_{x3D})^{2K_p}}{K_p} \cdot \begin{pmatrix} \frac{\pi}{2^{2-K_p}} + 1 + \frac{1}{3}(K_p-1) + \frac{1}{10}(K_p-1)(K_p-2) \\ + \frac{1}{42}(K_p-1)(K_p-2)(K_p-3) \\ + \frac{1}{216}(K_p-1)(K_p-2)(K_p-3)(K_p-4) \\ + \frac{1}{1320}(K_p-1)(K_p-2)(K_p-3)(K_p-4)(K_p-5) \\ + \frac{1}{9360}(K_p-1)(K_p-2)(K_p-3)(K_p-4)(K_p-5)(K_p-6) \\ + ... \end{pmatrix}$$

(4.81)

The resulting total load on the GR square for the case $s_x \neq s_y$ is given by equation (4.6) of this paper.

An alternative is to solve this numerically. This means that the GR square is divided into a large number of small areas. The average vertical stress on each increment is determined and multiplied by its area. The sum gives the total force on the GR square with $F_{GRsquare}$ in kN/pile. $F_{GRsquare1}$ and $F_{GRsquare2}$ (kN/pile) are indicated in Figure 4.22, where H_{g3D} (m) is the height of the largest hemisphere and L_{x3D} is the width of the square upon which the hemispheres exert a load, as indicated in Figure 4.22. When $L_{x3D} < (s_x - a)$, the area outside L_{x3D} but inside the GR square is assumed to be loaded by $\gamma H + p$. This gives an extra term, $F_{GRsq3p=0}$, where

$$F_{GRsq3p=0} = \gamma H \cdot \left((s_x - a)^2 - L_{x3D}^2 \right) \qquad \text{for} \quad L_{x3D} < s_x - a$$

$$F_{GRsq3p=0} = 0 \qquad \text{for} \quad L_{x3D} \geq s_x - a$$

(4.82)

Note that it is assumed that $s_x = s_y$ in this appendix. In Chapter 4.4.5 the equations are given for $s_x \neq s_y$. It is supposed that the load not resting on the GR square is transferred to the ring of GR strips and pile caps. This load is therefore applied as an equally distributed surcharge load on the 2D arches. This surcharge load on the 2D arches is, in kN/pile:

$$F_{transferred} = \gamma H \cdot (s_x - a)^2 - \left(F_{GRsq1p=0} + F_{GRsq2p=0} + F_{GRsq3p=0} \right) \tag{4.83}$$

Where a is the width of a square pile cap or the equivalent width of a circular pile cap. Distributed equally on the 2D arches, this results in a surcharge load in kPa (2 full GR strips and a pile cap per pile):

$$p_{transferred} = \frac{F_{transferred}}{2a \cdot (L_{x2D}) + a^2} \tag{4.84}$$

Where

$$L_{x2D} = s_x - a \qquad \text{for} \quad H \geq \frac{1}{2}(s_x - a)$$

$$L_{x2D} = 2 \cdot H_{g2D} \qquad \text{for} \quad H < \frac{1}{2}(s_x - a) \tag{4.85}$$

where H_{g2D} in defined in equation (4.13)

Total force on the GR strip; determination of $F_{GRstrip}$

In this appendix, for reasons of clarity, it is assumed that $s_x = s_y$. The tangential stress σ_θ (kPa) in the 2D arches above the GR strips is now given by:

$$\sigma_\theta = P_{2D} \cdot r^{K_p - 1} + Q_{2D} \cdot r \tag{4.86}$$

(2D arch), where

$$P_{2D} = K_p \cdot H_{g2D}^{(1-K_p)} \cdot \left[\gamma H + p_{transferred} - \gamma H_{g2D} \cdot \left(\frac{K_p - 1}{K_p - 2} \right) \right]$$

$$Q_{2D} = K_p \cdot \frac{\gamma}{K_p - 2}$$

Where $p_{transferred}$ (kPa) is the load transferred from the 3D hemispheres to the 2D arches and given by equation (4.84) and H_{g2D} (m) is the height of the 2D arch and given by equation (4.13). When $s_x \neq s_y$, a distinction should be made between P_{x2D} versus P_{y2D} and H_{xg2D} versus H_{yg2D}. The rest of the equation is equal to equation (4.1) in this paper. The total force on the GR strip (without surcharge load p) may

be obtained by integrating the tangential stress σ_θ across the area of the GR strip as shown in Figure 4.23.
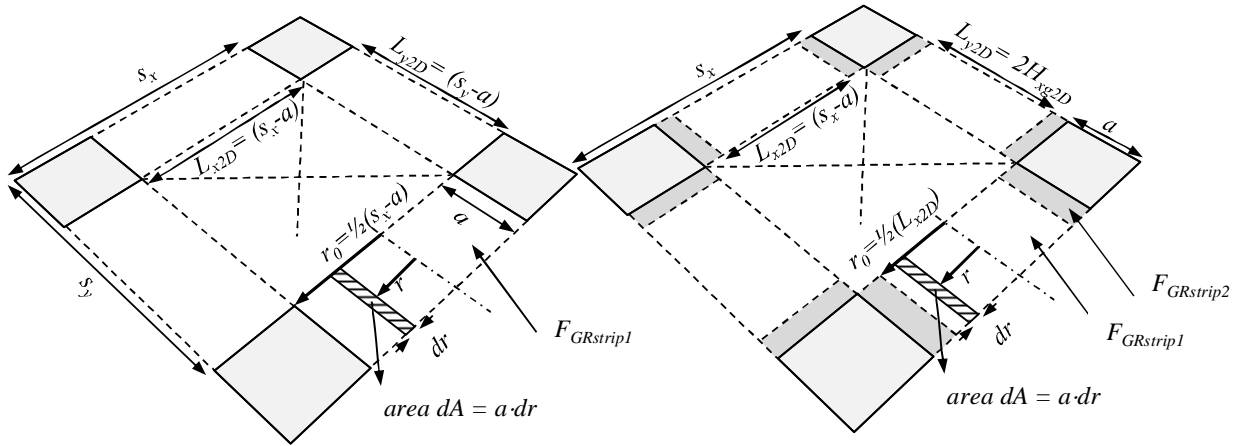
$$\left(H \geq \frac{s_x - a}{2} \quad and \quad H \geq \frac{s_y - a}{2} \right) \qquad\qquad \left(H < \frac{s_x - a}{2} \quad and \quad H < \frac{s_y - a}{2} \right)$$

Figure 4.23 Integrating the tangential stress σ_θ across the area of the GR strip where the 2D arches exert their load.

The total force on two GR strips (in kN/pile) is therefore:

$$F_{GRstrip} = F_{GRstrip1} + F_{GRstrip2} = \left(\frac{\gamma H + p}{\gamma H} \right) \cdot \left(F_{GRstr1p=0} + F_{GRstr2p=0} \right) \qquad (4.87)$$

Where

$$F_{GRstr1p=0} = 4 \int_0^{r_0} \sigma_\theta dA_{GRstrip} = 4 \int_0^{r_0} \sigma_\theta \cdot a dr = 4a \int_0^{\frac{1}{2}L_{x2D}} \left(P_{2D} \cdot r^{(K_p - 1)} + Q_{2D} \cdot r \right) dr \qquad (4.88)$$

Thus

$$F_{GRstr1p=0} = 4a \left[\frac{P_{2D}}{K_p} \cdot r^{K_p} + \tfrac{1}{2} Q_{2D} \cdot r^2 \right]_0^{\frac{1}{2}L_{x2D}}$$

$$\rightarrow F_{GRstr1p=0} = a \cdot \left(4 \frac{P_{2D}}{K_p} \left(\tfrac{1}{2} L_{x2D} \right)^{K_p} + \tfrac{1}{2} Q_{2D} \cdot L_{x2D}^2 \right) \qquad (4.89)$$

And

$$F_{GRstr2\,p=0} = 2\gamma Ha\left(s_x - a - L_{x2D}\right) \quad \text{for } H < \tfrac{1}{2}\left(s_x - a\right)$$
$$F_{GRstr2\,p=0} = 0 \qquad\qquad\qquad\quad \text{for } H \geq \tfrac{1}{2}\left(s_x - a\right)$$
(4.90)

With surcharge load $p > 0$:

$$F_{GRstrip;p>0} = \left(\frac{\gamma H + p}{\gamma H}\right)\cdot\left(4a\frac{P_{2D}}{K_p}\left(\tfrac{1}{2}L_{x2D}\right)^{K_p} + \tfrac{1}{2}aQ_{2D}\cdot L_{x2D}^{\;2} + F_{GRstr2\,p=0}\right)$$
(4.91)

For the situation $s_x \neq s_y$, this equation changes into equation (4.14).

4.A.4 2D variant: line-shaped support

The 2D equations can be worked out easily for the situation in which the embankment is supported by line-shaped supporting elements (such as diaphragm walls). In this case, equation (4.86) is applicable, where $p_{transferred} = 0$ kPa, as this is the load transferred from the 3D hemispheres that do not exist in the 2D case.

The total load in kN/m' on a 1-m-wide line foundation is (in accordance with equation (4.87)):

$$F_{GR\,line} = F_{GR\,line1} + F_{GR\,line2} = \left(\frac{\gamma H + p}{\gamma H}\right)\cdot\left(F_{GR\,line1\,p=0} + F_{GR\,line2\,p=0}\right)$$
(4.92)

where

$$F_{GR\,line1\,p=0} = 2\int_0^{r_0}\sigma_\theta dA_{GR\,line} = 2\int_0^{r_0}\sigma_\theta\cdot dr = 2\int_0^{\frac{1}{2}L_{x2D}}\left(P_{2D}\cdot r^{(K_p-1)} + Q_{2D}\cdot r\right)dr$$
(4.93)

Thus

$$F_{GR\,line1\,p=0} = 2\left[\frac{P_{2D}}{K_p}\cdot r^{K_p} + \tfrac{1}{2}Q_{2D}\cdot r^2\right]_0^{\frac{1}{2}L_{x2D}}$$
$$\rightarrow F_{GR\,line1\,p=0} = 2\frac{P_{2D}}{K_p}\left(\tfrac{1}{2}L_{x2D}\right)^{K_p} + \tfrac{1}{4}Q_{2D}\cdot L_{x2D}^{\;2}$$
(4.94)

and

$$F_{GR\,line\,2\,p=0} = \gamma H\left(s_x - a - L_{x2D}\right) \qquad \text{for} \quad H < \tfrac{1}{2}\left(s_x - a\right)$$
$$F_{GR\,line\,2\,p=0} = 0 \qquad\qquad\qquad \text{for} \quad H \geq \tfrac{1}{2}\left(s_x - a\right) \tag{4.95}$$

With surcharge load $p > 0$:

$$F_{GR\,line;\,p>0} = \left(\frac{\gamma H + p}{\gamma H}\right)\cdot\left(2\frac{P_{2D}}{K_p}\left(\tfrac{1}{2}L_{x2D}\right)^{K_p} + \tfrac{1}{4}Q_{2D}\cdot L_{x2D}{}^2 + F_{GR\,line\,2\,p=0}\right) \tag{4.96}$$

Appendix 4.B. Calculation examples[14]

This appendix gives two calculation examples. The first is the Woerden field test in Figure 4.16, the second is a variation with $s_x \neq s_y$.

Input parameters		example 1	example 2	
diameter circular pile cap	d	0.85	0.85	m
height embankment	H	1.86	1.86	m
transverse ctc distance piles	s_x	2.25	**2.00**	m
longitudinal ctc distance piles	s_y	2.25	2.25	m
unit weight	γ	18.3	18.3	kN/m^3
surcharge load	p	6	6	kPa
cohesion	c	0	0	kPa
internal friction angle	φ	43	43	deg

Calculated parameters		example 1	example 2		equation
equivalent width pile cap	$a = B_{ers}$	0.75	0.75	m	$a = \sqrt{\tfrac{1}{4}\pi d^2}$
passive earth pressure coefficient	K_p	5.29	5.29	-	(4.2)
height 3D hemisphere	H_{g3D}	1.59	1.51	m	(4.4)
width square loaded by 3D arches (Figure 4.22)	L_{x3D}	1.50	1.38	m	(4.8)
Length of GR strip loaded by 2D arches (Figure 4.23)	L_{x2D}	1.50	1.25	m	(4.12)
	L_{y2D}	1.50	1.50	m	(4.12)
calculation parameter	P_{x2D}	90.63	155.65	kPa/m$^{Kp\text{-}1}$	(4.14)
	P_{y2D}	90.63	84.39		(4.14)
calculation parameter	$Q_{x2D} = Q_{y2D}$	29.43	29.43	kN/m^3	(4.14)
calculation parameter	P_{3D}	0.11	0.45	kPa/m$^{2Kp\text{-}2}$	(4.7)
calculation parameter	Q_{3D}	12.77	12.77	kN/m^3	(4.7)

---

[14] Example 2 has been added to the original paper (Van Eekelen, S.J.M, Bezuijen, A., Van Tol, A.F., 2013). Some changes were made in calculation example 1 to correct mistakes.

Determination of the force exerted by the 3D hemispheres on the GR square (no surcharge load yet: $p = 0$)

		example 1	example 2		
force inside circle in GR square (Figure 4.22)	$F_{GRsq1;p=0}$	11.21	8.74	kN/pile	(4.6)
part 1 of force on area inside $L_{x3D} \cdot L_{x3D}$ square, but outside circle (Figure 4.22)	$_1F_{GRsq2}$	0.11	0.20	kN/pile	(4.6)
part 2 of force on area inside $L_{x3D} \cdot L_{x3D}$ square, but outside circle (Figure 4.22)	$_2F_{GRsq2}$	20.50	15.98	kN/pile	(4.6)
part 3 of force on area inside $L_{x3D} \cdot L_{x3D}$ square, but outside circle (Figure 4.22)	$_3F_{GRsq2}$	-0.10	-0.17	kN/pile	(4.6)
part 4 of force on area inside $L_{x3D} \cdot L_{x3D}$ square, but outside circle (Figure 4.22)	$_4F_{GRsq2}$	-15.33	-11.94	kN/pile	(4.6)
total force on area inside $L_{x3D} \cdot L_{x3D}$ square, but outside circle (Figure 4.22)	$F_{GRsq2;p=0}$	5.19	4.06	kN/pile	$_1F_{GRsq2} +$ $_2F_{GRsq2} +$ $_3F_{GRsq2} +$ $_4F_{GRsq2}$ (4.6)
force on area outside $L_{x3D} \cdot L_{x3D}$ square, but inside GR square)	$F_{GRsq3;p=0}$	0.00	0.00	kN/pile	(4.9)
total force on GR square (Figure 4.22) for $p = 0$ kPa	$F_{GRsquare;p=0}$	16.40	12.80	kN/pile	(4.6)

Determination of the force transferred along the 3D hemispheres to the 2D arches; to be applied as surcharge load on the 2D arches

		example 1	example 2		
force transferred	$F_{transferred}$	59.85	50.71	kN/pile	(4.10)
resulting surcharge load on 2D arches	$p_{transferred}$	21.20	19.25	kPa	(4.11)

Determination of the force exerted by the 2D arches on the GR strips (no surcharge load yet: $p = 0$) and no load outside the arches on the GR strip (equation (4.14))

		example 1	example 2		
total force on GR strips for $p = 0$ kPa	$F_{GRstrips;p=0}$	35.97	29.86	kN/pile	(4.14)

Determination of load distribution (no surcharge load yet: $p = 0$)

		example 1	example 2		
total force on GR for $p = 0$	$F_{GR}=B+C$	52.37	42.66	kN/pile	(4.16)
total force on pile cap with $p = 0$	A	119.94[a]	110.51	kN/pile	(4.15)

[a] this is the value given in Figure 4.16*b*.

Determination of load distribution (with surcharge load: $p = 6$ kPa)

		example 1	example 2		
total force on GR for $p = 6$ kPa	$F_{GR}=B+C$	61.61	50.18	kN/pile	(4.16)
Average load on GR strips	q_{av}	27.32	24.28	kPa	(5.9)
total force on pile cap for $p = 6$ kPa	A	141.09	129.99	kN/pile	(4.15)
total pressure on pile cap for $p = 6$ kPa	p_A	248.63	229.09	kPa	$p_A = A / A_p$
percentage of total force transferred to the pile cap directly for $p = 6$ kPa	$A\%$	69.6	72.2	%	$A\% = A/((\gamma H+p)\cdot s_x \cdot s_y)$

Step 2 with the inverse triangular load distribution according to Van Eekelen et al., (2012b, Chapter 3 of this thesis)

Additional parameters:

Subgrade reaction	k	0.00	kN/m^3
GR Stiffness[b]	J	5000	kN/m

[b] J is stress and time dependent and should be determined from isochronic curves.

The average geometric and constitutive strains should be equalised numerically:

$$\varepsilon_{geometric,average} \;=\; \frac{\int\limits_{x=0}^{x=\frac{1}{2}L} dx\sqrt{1+\left(\frac{dz}{dx}\right)^2} - \frac{1}{2}L}{\frac{1}{2}L} \;=\; \varepsilon_{constitutive,average} \;=\; \frac{\frac{1}{J}\int\limits_{x=0}^{x=\frac{1}{2}L} T(x)\,dx}{\frac{1}{2}L} \qquad (4.97)$$

We find[15]:

Inverse-triangular load distribution		example 1	example 2 transverse	example 2 longitu-dinal		
Horizontal component tensile force	T_H	58.79	54.38	48.19	kN/m	(4.97)
Term for graphs in appendix B	$q_{av}{\cdot}L/J$	0.0082	0.0073	0.0061	-	App B
Term for graphs in appendix B	$k{\cdot}A_L{\cdot}L/(J{\cdot}a)$	0.0000	0.0000	0.0000	-	App B
max GR strain at the edge of the pile cap	ε_{max} at $x=\frac{1}{2}(s_x-a)$	1.24%	1.15%	1.01%	%	(3.15)[a]
max tensile force at the edge of the pile cap	T_{max} at $x=\frac{1}{2}(s_x-a)$	62.24	57.35	50.51	kN/m	(3.15)
average GR strain	$\varepsilon_{average}$	1.19%	1.10%	0.97%	%	(4.97)
max GR deflection		0.087	0.083	0.065	m	(3.15)
GR inclination at edge pile cap	dz/dx at $x=\frac{1}{2}(s_x-a)$	-0.34	-0.33	-0.31	m/m	(3.15)

[a] or from graphs in appendix B

---

[15] Appendix B of this thesis gives design graphs which can be used instead of these equations.

For the case with subsoil support[16], with $k = 100$ kN/m^3 both load distributions need to be considered (inverse-triangular and uniform):

Inverse-triangular *load distribution*		example 1	example 2 transverse	example 2 longitu- dinal		
Modified subgrade reaction	K	199.3	176.3	207.1	kN/m^3	(5.7)
Calculation parameter	M	0.67	0.69	0.72		(5.5)
Horizontal component tensile force	T_H	39.06	36.68	33.39	kN/m	(4.97)
Calculation parameter	α	2.26	2.19	2.49		(5.6)
Term for graphs in appendix B	$q_{av} \cdot L/J$	0.0082	0.0073	0.0061	-	App B
Term for graphs in appendix B	$k \cdot A_L \cdot L/(J \cdot a)$	0.0893	0.0790	0.0644	-	App B
max GR strain at the edge of the pile cap	ε_{max} at $x = \frac{1}{2}(s_x - a)$	0.83%	0.77%	0.70%	%	(3.15)[a]
max tensile force at the edge of the pile cap	T_{max} at $x = \frac{1}{2}(s_x - a)$	41.30	38.62	34.96	kN/m	(3.15)
Max GR deflection	z_{max}	0.058	0.057	0.046	m	(3.15)
GR inclination at edge pile cap	dz/dx at $x = \frac{1}{2}(s_x - a)$	-0.33	-0.32	-0.30	m/m	(3.15)
average GR strain	$\varepsilon_{average}$	0.79%	0.74%	0.67%	%	(4.97)

[a] *or from graphs in appendix B*

Uniform load distribution		example 1	example 2 transverse	example 2 longitu-dinal		
Modified subgrade reaction	K	199.3	176.3	207.1	kN/m^3	(5.7)
Horizontal component tensile force	T_H	44.21	41.74	38.35	kN/m	(4.97)
Calculation parameter	α	2.12	2.05	2.32		(5.6)
Term for graphs in appendix B	$q_{av} \cdot L/J$		0.0073	0.0061	-	App B
Term for graphs in appendix B	$k \cdot A_L \cdot L/(J \cdot a)$		0.0790	0.0644	-	App B
max GR strain at the edge of the pile cap	ε_{max} at $x=\frac{1}{2}(s_x-a)$	0.92%	0.86%	0.79%	%	(5.4) [a]
max tensile force at the edge of the pile cap	T_{max} at $x=\frac{1}{2}(s_x-a)$	45.78	43.11	39.47	kN/m	(5.4)
Max GR deflection	z_{max}	0.083	0.081	0.065	m	(5.4)
GR inclination at edge pile cap	dz/dx at $x=\frac{1}{2}(s_x-a)$	-0.26	-0.25	-0.24	m/m	(5.4)
average GR strain	$\varepsilon_{average}$	0.89%	0.84%	0.77%	%	(4.97)

[a] or from graphs in appendix B

The inverse triangular load distribution gives smaller strains than the uniform load distribution and the inverse triangular is therefore normative in this case, as explained in Chapter 5.5.

5 Validation of Analytical Models for the Design of Basal Reinforced Piled Embankments

Field measurements in Woerden, the Netherlands

Abstract

Van Eekelen et al. (2012a, b and 2013, Chapters 2, 3 and 4 of this thesis) have introduced an analytical model for the design of the geosynthetic reinforcement (GR) in a piled embankment. This paper further validates this model with measurements from seven full-scale tests and four series of scaled model experiments. Most of these measurements have been reported earlier in the literature.

The new model describes arching with the "Concentric Arching model" (CA model). This model is an extension of the single arch model of Hewlett and Randolph (1988) and the multi-scale model of Zaeske (2001), which is also described in Kempfert et al. (2004). For load-deflection behaviour, Van Eekelen et al. (2012a, b and 2013, Chapters 2, 3 and 4 of this thesis) proposed the use of a net load distribution that is inverse triangular instead of uniform or triangular. These authors also proposed the inclusion of all the subsoil support beneath the GR in the calculations.

On the basis of comparisons between the measurements and calculations, it is concluded that the CA model matches the measurements better than the models of Zaeske or Hewlett and Randolph.

Where there is no subsoil support, or almost no subsoil support, the inverse triangular load distribution on the GR strips between adjacent piles gives the best match with the measurements. Cases with subsoil support generally lead to less GR strain. In the cases with significant subsoil support, the load distribution is approximately uniform. In the cases with limited subsoil support, it should be determined which load distribution gives the minimum GR strain to find the best match with the measurements.

5.1   Introduction

Basal reinforced piled embankments are increasingly popular due to the good performance of these structures, mainly in areas with soft soil. They can be constructed quickly, they do not exert horizontal soil pressure on adjacent sensitive structures and residual settlement is very limited or absent. As a result, they require very limited maintenance. Several design guidelines have been published or updated lately in Europe, including the German EBGEO (2010), the Dutch CUR226 (2010, described in Van Eekelen et al., 2010b), the British BS8006 (2010, described and analysed in Van Eekelen et al., 2011a, see appendix A of this thesis) and the French ASIRI (2012). The CUR226 committee is currently working on an update to bring the CUR226 in line with recent research results. This paper presents a validation study that has been carried out to support the choices made for the update of CUR226 (2015).

Analytical design models for the design of the basal reinforcement in piled embankments include two calculation steps. The first step calculates the arching behaviour in the fill. This step divides the total vertical load into two parts: load part *A*, and the 'residual load' (*B+C* in Figure 5.1). Load part *A*, which is also referred to as 'arching *A*', is the part of the load that is transferred to the piles directly.

The second calculation step describes the load-deflection behaviour of the geosynthetic reinforcement (GR, see Figure 5.1). In this calculation step, the 'residual load' is applied to the GR strip between each pair of adjacent piles and the GR strain is calculated. The GR strip may or may not be supported by the subsoil, depending on the local circumstances.

An implicit result of step 2 is that the 'residual load' is divided into a load part *B*, which passes through the GR to the piles, and a load part *C*, resting on the subsoil, as indicated in Figure 5.1.
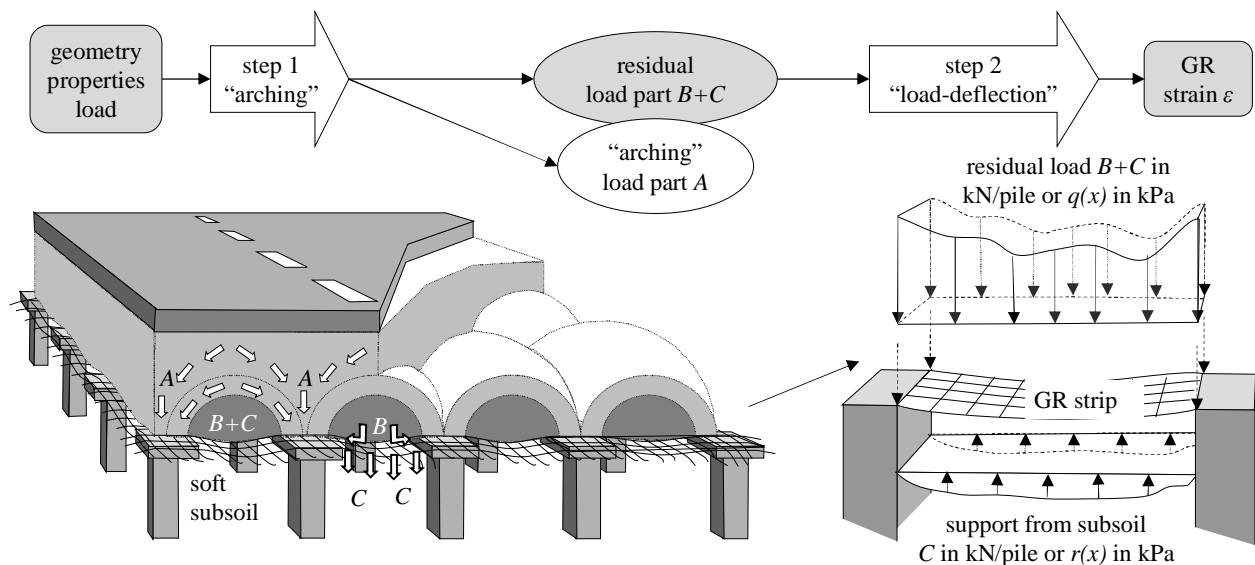
Figure 5.1 Calculating the geosynthetic reinforcement (GR) strain comprises two calculation steps.

Several analytical models have been proposed in the literature to calculate the first calculation step, the arching. They are listed and explained in Van Eekelen et al. (2013, see Chapter 4 of this thesis). They include frictional models, rigid arch models, models using mechanical elements and limit equilibrium models. The frictional models, which are based on Terzaghi (1943), include McKelvey (1994), Russell and Pierpoint (1997), McGuire et al., (2012), Naughton (2007) and Britton and Naughton (2008) and the model of Marston and Anderson (1913), which was modified by Jones et al. (1990) and adopted in the British Standard

BS8006 (2010). The rigid arch models include Scandinavian models such as Carlsson (1987), Rogbeck et al. (1998, modified by Van Eekelen et al., 2003), Svanø et al. (2000), the enhanced arch model described in, for example, Collin (2004), the design method of the Public Work Research Centre in Japan (2000, discussed in Eskişar et al., 2012). The models that consider the behaviour of the separate mechanical elements and match their boundaries are described in, for example, Filz et al. (2012), Deb (2010), Deb and Mohapatra (2013) and Zhang et al. (2012). The present paper focuses on the last family of arching models: limit equilibrium models. The following Chapter describes these models.

Several approaches for the second calculation step have also been presented in the literature. The German approach (adopted in EBGEO, 2010 and CUR226, 2010), including some variations, is described in the following chapter. An approach using finite differences and minimisation of the total energy has been presented by Jones et al. (2010) with a 3D plate model, Halvordson et al. (2010) with a 3D cable-net model and Plaut et al. (2010) with an axisymmetric model.
This paper validates three variations of limit equilibrium models for the arching of step 1 in combination with several variations of load-deflection membrane theory for step 2. Results obtained with the combination of these models are compared with measurements in seven full-scale cases and four series of scaled model experiments.

This paper specifically considers piled embankments with GR. Any reported measurements without GR were therefore not suitable for this paper. Examples are Hong et al. (2014) with 2D full-scale experiments, Ellis and Aslam (2009a, b) and Lally and Naughton (2012) with centrifuge tests, Britton and Naughton (2008, 2010) with model experiments, and Hewlett and Randolph (1988) with scaled 2D trapdoor experiments.

Specific measurements are necessary to validate steps 1 and 2 separately. To validate step 1 separately, arching A needs to be measured. When GR is present, A needs to be measured above the GR. To validate a step 2 model, both arching A and the GR strain ε need to be measured. Only a very limited number of researchers have reported measurements of A in full-scale tests with GR (Van Eekelen et al., 2010a, 2012c; and Van Duijnen et al., 2010) or scaled experiments with GR (Oh and Shin, 2007; Van Eekelen et al., 2012a (Chapter 2 of this thesis). Van Eekelen et al. (2012b and 2013 (Chapter 4 of this thesis), Van Eekelen and Bezuijen, 2013b) used most of these measurements to validate their proposed steps 1 and 2 separately.

When validating steps 1 and 2 together, measurements of A are not necessary and measurements of the GR strain suffice. Seven full-scale cases have been reported

with the data that will be considered in the present paper: in Brazil (Spotti, 2006; and Almeida et al., 2007 and 2008), in Houten, the Netherlands (Van Duijnen et al., 2010), near Woerden, the Netherlands (Van Eekelen et al., 2012c), in Finland (Huang et al., 2009, including FDM calculations), in the Krimpenerwaard, the Netherlands (Haring et al., 2008), in Hamburg, Germany (Weirauch et al., 2013) and in France (Briançon and Simon, 2012). Additionally, four series of model experiments reported in the literature are considered in the present paper: from Virginia (Sloan, 2011 and McGuire et al., 2012), the Republic of Korea (Oh and Shin, 2007), Germany (Zaeske, 2001, also reported in Kempfert et al., 2004) and the Netherlands (Van Eekelen et al., 2012a and b, adopted in Chapter 2 and 3 of this thesis).

Several other measurements reported in the literature were not suitable for use in the present paper because GR strains were not measured or not reported. They include Chen et al. (2008a), Blanc et al. (2013 and 2014) and Van Eekelen et al. (2010a). Zhuang et al. (2014) used this last reference for the validation of their simplified model, and calculated the 'measured' GR deflection from the measured load distribution.

Chapter 5.2 summarises the analytical models included for consideration. Chapter 5.3 includes a summary of the cases considered. Special attention is paid to the determination of the calculation parameters for each case. Chapter 5.4 compares the analytical calculation results with the measurements for each of the considered cases. Chapter 5.5 discusses the results.

5.2 Description of the considered analytical models

This paper validates several combinations of analytical models for step 1, the arching and step 2, the load-deflection behaviour. See Figure 5.1 and Table 5.13.

5.2.1 Step 1: arching

The two most frequently used arching models in Europe are Hewlett and Randolph's single arch model (1988, see Figure 5.2*a*) and Zaeske's multi-scale model (2001, also cited in Kempfert et al., 2004, see Figure 5.2*b*). An extension of these two models is the Concentric Arches model (CA model, see Figure 5.2*c*) presented recently by Van Eekelen et al. (2013, Chapter 4 of this thesis). This model was specifically developed in response to the observation that a major part of the load on the GR concentrates on the GR strips between adjacent piles, and that the load distribution on these strips approaches the inverse triangular shape, as shown in Figure 5.3*c*. This is further discussed in the next chapter.
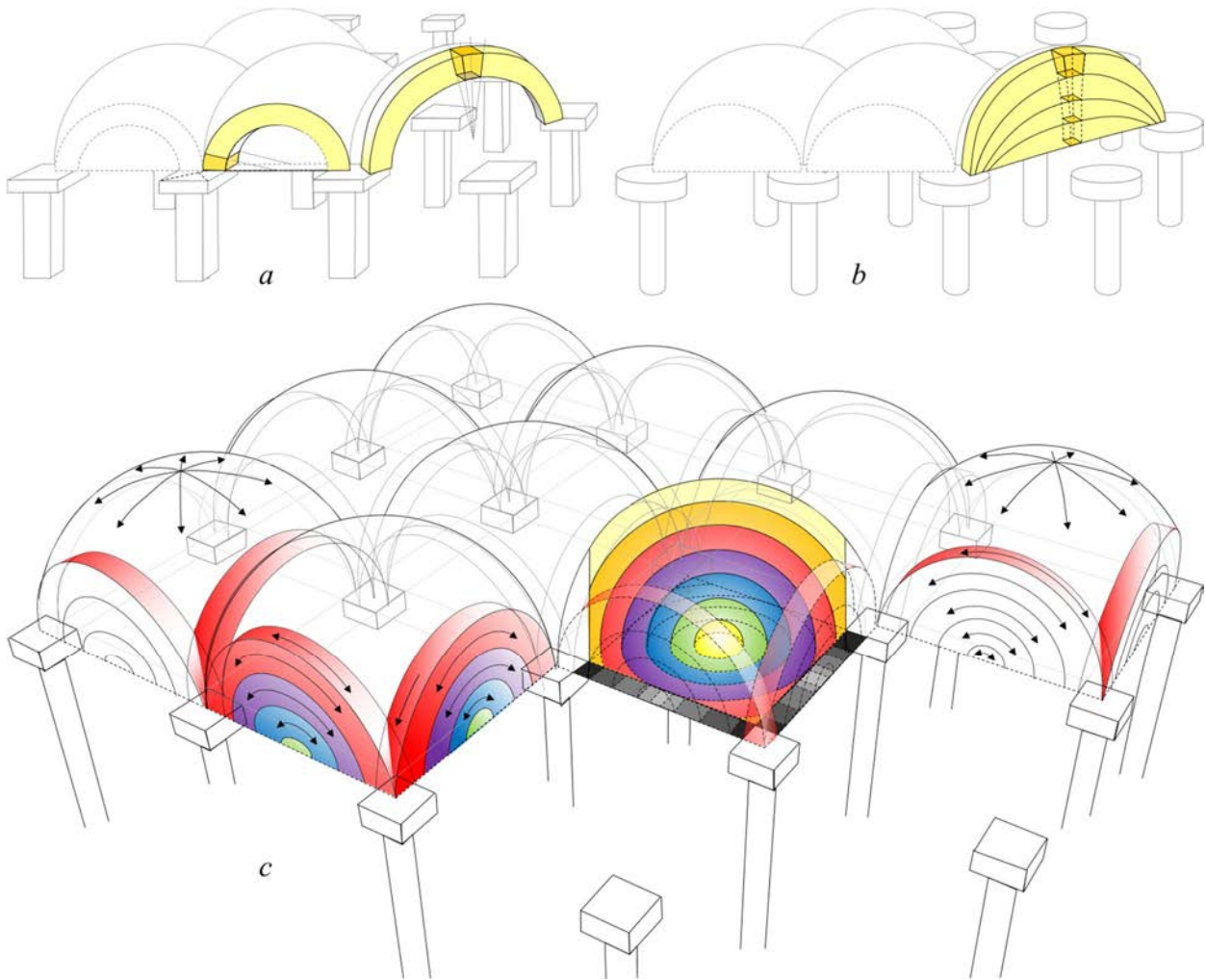
Figure 5.2 Models for calculation step 1: arching, see Figure 5.1. (*a*) Hewlett and Randolph's single arch model (1988), (*b*) Zaeske's multi-scale model (2001, also described in Kempfert et al, 2004, adopted in EBGEO, 2010 and CUR226, 2010) and (*c*) the Concentric Arches model (CA model, Van Eekelen et al., 2013, adopted in Chapter 4 of this thesis).
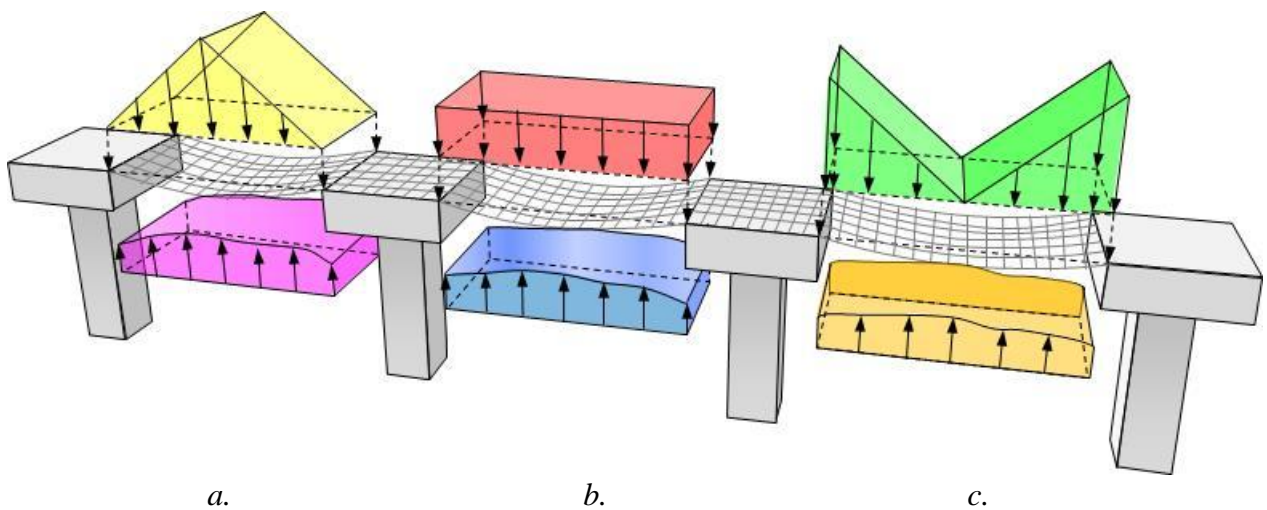
Figure 5.3 Calculation step 2 with three different load distributions: (*a*) triangular (Zaeske, 2001; EBGEO, 2010; CUR, 2010) (*b*) uniform (BS8006, 2010) (*c*) inverse triangular (Van Eekelen et al., 2012a and b).

The applicability of arching models should be limited to situations where the distance between the piles is comparable to those applied in the considered cases. When the distance between the pile caps becomes too large, the arching or rather punching here is less efficient, as shown by Hong et al. (2014).

5.2.2 Step 2: load-deflection behaviour

In the second calculation step, the 'residual load' that results from step 1 is applied to the GR strip between each two adjacent piles. The GR strip may be supported by subsoil. The GR strain is then calculated using differential equations based on membrane theory, as explained in Van Eekelen et al. (2012b, Chapter 3 of this thesis).

Two issues are of major importance in step 2. Firstly, the load distribution on the GR strip has a strong influence on the calculated GR strain (see Figure 3). Van Eekelen et al. (2012a,b, Chapter 2 and 3 of this thesis, also discussed in Filz and Sloan, 2013) concluded that this distribution approaches the inverse triangular distribution as opposed to the triangular distribution of EBGEO(2010); CUR (2010) and Zaeske (2001) and the uniform distribution of BS8006 (2010). This is also confirmed by the findings of, for example, Han and Gabr (2002). These three load distributions are all considered in the present paper.

Secondly, subsoil support has a major influence. The most extreme situations occur when the subsoil support is lost. This can happen, for example, due to lowering the water table in the subsoil, the settlement of soft subsoil under the weight of a working platform below the GR, or migrating voids, for example due to old mine workings. To stay on the safe side in design, BS8006 disregards subsoil support.

Some design guidelines, such as EBGEO (2010) and CUR (2010), accept taking subsoil support into account. However, they only consider the subsoil beneath the GR strip under consideration between adjacent piles. Lodder et al. (2012) and Van Eekelen et al. (2012b, Chapter 3 of this thesis) suggested using a modified value for the subgrade reaction k to take into account all subsoil[17] underneath the entire GR. This suggestion is in line with the work of Jones et al. (2010), Halvordson et al. (2010), Plaut et al. (2010) and Filz et al. (2012).

---

[17] In Chapter 3, "all subsoil" is referred to as "Modified Subsoil".

5.2.3   *Validation of arching, load distribution and subsoil support*

Van Eekelen et al. (2013, Chapter 4 of this thesis) recommend using the CA model, an inverse triangular load distribution and taking into account all soil support underneath the GR between the piles. They validated the CA model with laboratory experiments, numerical calculations of Le Hello and Villard (2009) and measurements in two full-scale cases (Van Eekelen et al., 2012c and 2015b, c, d; Van Duijnen et al., 2010). Van Eekelen et al. (2012b, Chapter 3 of this thesis) validated the inverse triangular load distribution with or without subsoil support with model experiments. The present paper gives additional validations for the variations in steps 1 and 2 described in the previous chapters.

5.3   Case study descriptions

5.3.1   *Introduction*

This chapter briefly describes seven full-scale cases and four series of model experiments. Mean (best-guess) values for the parameters used in the calculations are determined. Characteristic values, which are the values generally used in design, cannot be used here.

The analytical models considered have been developed for cohesion-less frictional fills. In practice, however, fills often have some level of cohesion. For design purposes, it is advisable to disregard this cohesion. This simplification results in a 'safe' design: greater GR strain will be calculated than if cohesion is taken into account.

For the purposes of validation, however, cohesive fill is less suitable. It is possible to take cohesion into account by increasing the friction angle. However, for small stresses, the maximum difference between the two principal stresses is much larger for cohesive fills than for a fill with an artificially high friction angle. This means that higher tangential stresses can develop in a highly cohesive fill. This can result in a lot of arching and therefore low GR strains that are lower than any calculated GR strain with an artificially high friction angle. This paper focuses exclusively on piled embankments with frictional fills.

The subgrade reaction coefficient k (kN/m^3) was determined as follows, in order of preference:

- In some cases the relationship between the vertical pressure p and settlement z is known, for example for an adjacent unreinforced area subjected to the same surcharge load. In those cases the value of k was determined using the relationship $k = p/z$. However, if the settlement measured in the adjacent field is much larger than the settlement in the piled embankment, the value selected for k should be lower. For example, in the case of Woerden (Chapter 5.3.3), it is expected that the weight of the working platform below the GR will have caused so much settlement that the contact between the subsoil and the GR will be lost, resulting in $k = 0$ kN/m^3. In other cases, subsoil support decreases when the contact between the GR and the subsoil is reduced during subsoil settlement.

- In some cases calculations were carried out using a simple 1D consolidation model. In those cases, the soil profile and the required soil parameters were determined with the results of the original soil investigation.

- In other cases, the Young's modulus E of the subsoil in combination with the thickness of the soft soil layer t or layers t_i is known. In those cases the value of k was determined using the relationships given in EBGEO (2010): $k = E/t$, or in the case of multiple layers: $k = E_1 \cdot E_2 / (E_1 \cdot t_2 + E_2 \cdot t_1)$. It is possible that this leads to an underestimation of the subgrade soil reaction because the stiffness of the subsoil can increase due to the pre-loading caused by the pile installation or due to the negative friction along the pile shafts. Given this negative friction, it is not advisable to calculate k using large thicknesses for soft soils.

The installation of piles in soft soil results in (1) an increase in soft soil stiffness due to increasing stress and (2) negative friction along the pile shafts resulting in an apparent increase of stiffness. These effects are disregarded in the present paper.

A limitation of the study in this paper is that most field tests and numerical calculations did not continue until failure occurred and so no information is available about the ultimate limit state. However, model experiments by Zaeske (2001, Chapters 5.3.11 and 5.4.11) and Van Eekelen et al. (2012a, see Chapters 5.3.12 and 5.4.12) did continue in many cases until failure occurred. Furthermore, the authors of the present paper believe that the available data for the working condition are sufficient to determine the reliability of the analytical models for the working condition.

5.3.2 Full-scale test in Rio de Janeiro

Almeida et al. (2007, 2008) present measurements in a full-scale experiment carried out in the Barra da Tijuca District of Rio de Janeiro. The project has also been described in Spotti (2006), McGuire et al. (2009), Van Eekelen et al. (2014) and Zhuang et al. (2014). Part of the test area is shown in Figure 5.4.
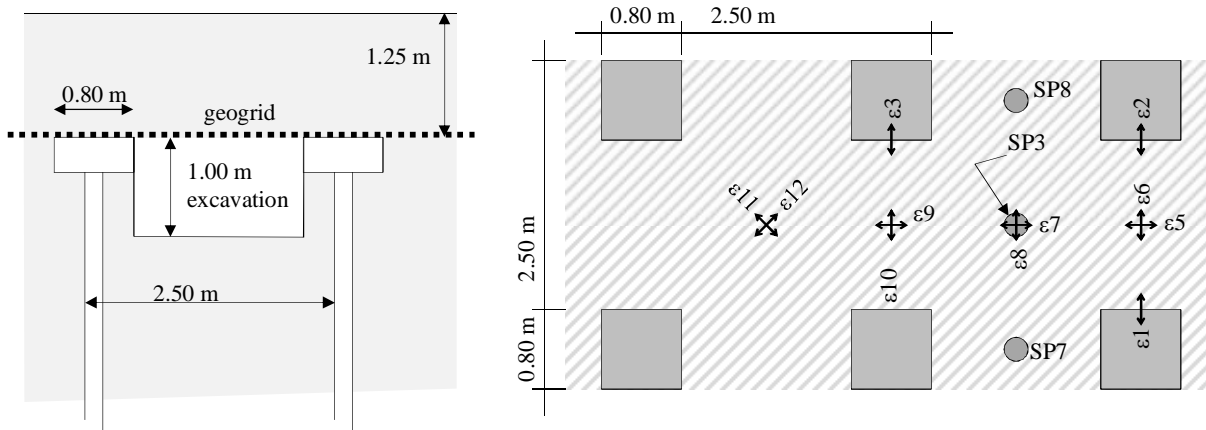
Figure 5.4 Layout of the part of the experimental site under consideration in the Barra da Tijuca District, Brazil Drawing modified after Spotti (2006) and Almeida et al., (2007). The shaded area was excavated prior to the installation of the reinforced embankment.

The embankment is relatively thin: at the test location, the average $H = 1.25$ m and so $H/(\sqrt{2}\cdot(s_x - a)) = 0.52$. This value is less than the minimum values allowed in the EBGEO (0.80) or CUR (0.66) for the usability phase. However, the low height is interesting for the construction phase and for research purposes.

A 1.0 m deep excavation was made before GR installation, as indicated in Figure 5.4. The GR was kept taut by loading the edges with fill. Photos taken at the site show that the geogrid was indeed relatively taut but that some parts of the reinforcement did sag a little prior to placement of the fill. Compaction of the lower fill layers was carried out with care using light equipment.
A single layer of knitted Fortrac PET biaxial geogrid 200/200 was placed over the pile caps with an underlying layer of non-woven geotextile to reduce abrasion between the pile cap and the geogrid. The failure strain of PET geogrids is around 10%. The fill material consisted of a clayey sand compacted to at least 95% of the standard Proctor maximum. It has a compacted unit weight $\gamma = 18.0$ kN/m^3. Adjacent geogrids were joined together by seaming.

The GR deflection was measured with settlement plates (SP) installed at the GR level at the locations indicated in Figure 5.4. GR strain gauges (ε in Figure 5.4) consisted of an ingenious system described by Almeida et al. (2007) which measured the strain using strain gauges on a steel bar that had been attached with a reaction spring to the GR.

138

Determination of parameters

The stiffness J (kN/m) of the geogrid depends on the tensile force and the loading time. The average of the larger values for the measured GR strains is 1.5% (see Figure 5.15). The total loading time is 188 days. The isochronous curves of the applied geogrid give $J_{1.5\%,1\ month}$ = 1637 kN/m and the $J_{1.5\%,1\ year}$ = 1594 kN/m. We assume that the average of these values is $J_{1.5\%,188\ days}$ = 1615 kN/m.

Table 5.1 Parameters used in the calculations of case Almeida et al. (2007, 2008).

centre-to-centre distance piles	width square pile caps	height fill	unit weight fill	friction angle fill	subgrade reaction	stiffness GR	surcharge load
$s_x = s_y$	a	H	γ	φ	k	$J_x = J_y$	p
m	m	m	kN/m^3	deg	kN/m^3	kN/m	kPa
2.50	0.80	1.25	18.0	43-68^a	0	1615	0

^{a} In the comparison in Chapter 5.4.2, the value of φ has been varied. In Chapter 5.5, $\varphi = 68^o$ has been used because this value gives the lowest GR strains of the two possibilities given in this chapter.

Direct shear tests on fill samples given in Spotti (2006) show an average friction angle $\varphi = 42^o$ and an average cohesion $c = 18.9$ kPa. As described in Chapter 5.3.1, the high cohesion value results in a limitation for validation purposes. However, it was believed worthwhile to include this case in this study because of the excavation below the GR and the low embankment. It was therefore necessary to find an equivalent friction angle φ for $c = 0$. An equivalent φ can be found by determining the fill strength at the average pressure at GR level ($\sigma_v = \gamma \cdot H + p = 18 \cdot 1.25 = 22.5$ kPa). From this, it follows that:

$$\varphi_{virtual;c=0} = \text{atan}\left(\frac{\sigma_v \tan\varphi + c}{\sigma_v}\right) = \text{atan}\left(\frac{22.5 * \tan 42^o + 18.9}{22.5}\right) = 60^o \tag{5.1}$$

However, McGuire et al. (2009) have found (after back-calculations from measurements in nearby 2D test fields): $\varphi = 68^o$ for $c = 0$ kPa. McGuire et al. consider these results satisfying, although their value for φ seems unreasonably high.

To prevent misinterpretation as a result of selecting the wrong friction angle, a wide range of values for φ was used in the calculations of this paper. Table 5.1 summarises the parameters used in the calculations.

5.3.3   *Full-scale case in Woerden*

A motorway exit was rebuilt near Woerden, a city in the centre of the Netherlands. The work involved building a new road on a piled embankment. Van Eekelen et al. (2012c and 2015b, c, d) reported monitoring results from this project.

The part of the test area considered in this paper is shown in Figure 5.5. The subsoil consists of 17 m of very soft clay. Over 900 precast square pile caps were placed on precast driven piles. The amount of arching was measured with total pressure cells on top of pile caps 692 and 693, above the GR. These pile caps were accordingly replaced by circular pile caps with the same area as the square ones. The pressure cells had the same diameter as the circular pile caps.

The embankment fill consisted of 0.18 m asphalt, 0.25 m asphalt gravel mixture and, below that, a fill of crushed recycled construction material, mainly concrete. The distance between asphalt surface and pile cap ranges from 2.11 m above pile cap 691 and 1.70 m above pile cap 682.
In the transverse direction, a layer of knitted PET geogrid reinforcement Fortrac 600/50 was installed with an underlying layer of 0.05 to 0.16 m of sand to protect the reinforcement. A second layer of the same material was installed on top of and perpendicular to the first layer. The failure strain of PET geogrids and PET geotextiles is around 10%.

The GR strains were measured with optic fibres at the locations "ε" in Figure 5.5. Additionally, the GR strains were measured at three locations elsewhere in this
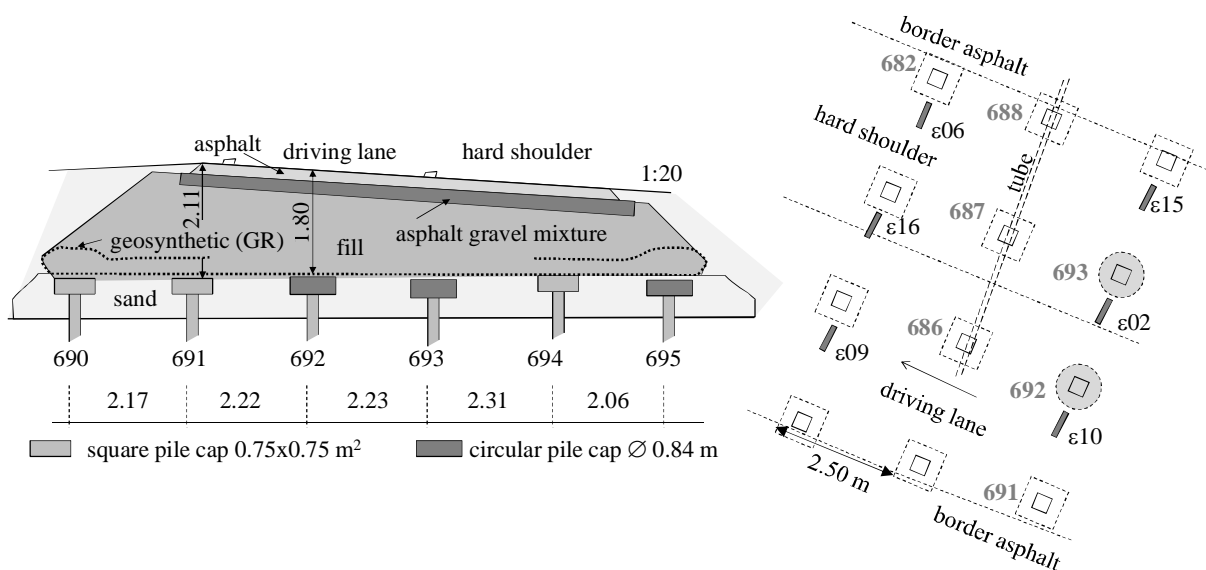
Figure 5.5 Layout of the part of the monitored site under consideration in Woerden, the Netherlands, including the instrumentation relevant for the present paper (Van Eekelen et al., 2012c).

Table 5.2 Parameters used in the calculations for Woerden (Van Eekelen et al., 2012c).

centre-to-centre distance piles	width square pile caps	height fill	unit weight fill	friction angle fill	subgrade reaction	stiffness GR	surcharge load
$s_x = s_y$	a	H	γ	φ	k	$J_x = J_y$	p
m	m	m	kN/m^3	deg	kN/m^3	kN/m	kPa
2.25	0.75	1.79	18.3	51	0	4936	0

piled embankment with a system of steel cables, as explained in Van Eekelen et al. (2012c). The GR strains measured with the last system were 0.2% during the first six weeks. As the optic fibres started measuring after these six weeks, the initial 0.2% GR cable strain was added to the optic-fibre measurements, as shown later in Chapter 5.4.3 of this paper. The resulting GR strains correspond to the GR deflection measured with a liquid levelling system in tubes, as described by Van Eekelen et al. (2012c).

The new exit went operational in June 2010. The present paper reports the average strains measured during six weeks in August and September 2013, in other words 38 months after the road was opened.

Determination of parameters
The friction angle of the fill of compacted crushed recycled material is assumed to be around 51 degrees. This value is based on large triaxial tests on similar material by both Den Boogert et al. (2012a,b) and Van Niekerk et al. (2002).
The stiffness of the GR layers in both directions can be summed, as shown by Van Eekelen and Bezuijen (2014). In each direction 600+50 = 650 knitted PET geogrid was installed. It has, at small strains (less than 1.5%) and with a loading time of three years, a tensile stiffness of ca. 4936 kN/m. This value was determined with the isochronous curves provided by the GR supplier.

Before the installation of the piles, a working platform was installed on the soft subsoil. The working platform consisted of 0.75 m of sand. The working platform was left underneath the GR and caused subsoil settlement.
This settlement of the subsoil underneath the GR caused by the weight of 0.75 m of sand was predicted using a simple 1D consolidation model based on CPT and triaxial test results. The calculations resulted in values for subsoil settlement that were well in excess of the 0.11 m measured after the road went operational.
However, the maximum measured settlement after the road went operational was less than 0.11 m. It is therefore concluded that the subgrade reaction k must have reached a minimum and is approximately 0 kN/m^3. This value is given in Table 5.2, along with the other properties and the geometry used in the calculations.

5.3.4   Full-scale case in Houten

Van Duijnen et al. (2010) and Van Duijnen (2014) presented monitoring results from a railway widening project described by Van der Stoel et al. (2010). The railway is located in Houten, the Netherlands. Figure 5.6 shows the test area that is considered in this paper. The subsoil consists (top-down) of 1 m of sand, 3 m of soft clay and 20 m of sand. The piles and pile caps are cast in situ. The embankment fill consisted (top-down) of 0.4 m of ballast of crushed stones below the sleepers, 0.1 m blinding layer, 1.0 m of sand and 1.0 m of crushed granular fill (recycled construction material, mainly concrete).
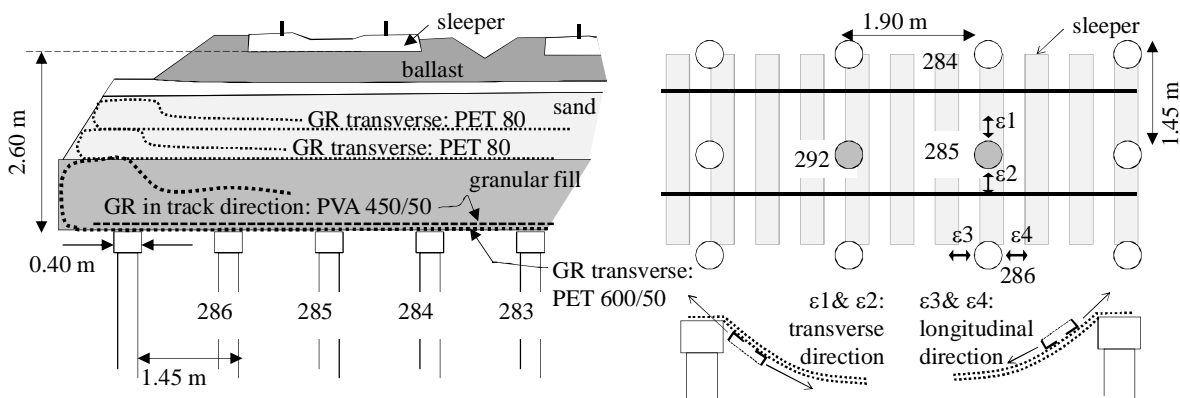
Figure 5.6 Layout of the part of the monitored site under consideration in Houten, the Netherlands. Drawing modified after Van Duijnen et al. (2010). Detail in bottom right-hand corner: location of strain gauges.

Three layers of Fortrac reinforcement were installed in the transverse direction. The basal layer is a knitted PET geogrid 600/50 installed upon the pile caps with an underlying layer of sand to protect the reinforcement. Higher in the fill, two layers of knitted PET geogrid 80 were installed, as indicated in Figure 5.6. In the direction of the track, a layer of knitted PVA geogrid 450/50 was installed on top of the basal GR layer. The failure strain of PET geogrids is around 10%, the failure strain of PVA geogrids is around 5%.

The arching in the embankment was measured with total pressure cells on top of piles 285 and 292, above the GR layer, with the same diameter as the pile caps. Other measurements have been reported by Van Duijnen et al. (2010).

GR strains in the basal reinforcement layer were measured with Glötzl strain gauges at the locations "εx" in Figure 5.6. Strain gauges ε1 and ε2 measure the strains in the transverse direction and they were installed below the bottom GR layer. Strain gauges ε3 and ε4 measure the strain in the direction of the track and they were installed on top of the longitudinal (in other words, in the direction of the track) GR layer. As shown in the picture at the bottom right-hand side of

Figure 5.6, it is expected that strain gauges ε1 and ε2 could result in a higher GR strain than the real GR strain due to the curvature of the deflected GR. Strain gauges ε3 and ε4, however, might measure a smaller strain than the real GR strain due to the bending.

The railway went operational in November 2008. This paper reports the average of the strains measured in 2010.

Determination of parameters

The fill material consists of different layers, as indicated in Figure 5.6. It is assumed that the bottom level is decisive for the arching. This layer is comparable to the fill in Woerden and its friction angle is also assumed to be around 51 degrees, as explained in Chapter 5.3.3.

The stiffness of the reinforcement was determined as follows. In the longitudinal direction, the total reinforcement consists of woven PVA geogrid 450 + woven PET geogrid 50. The stiffness of the separate layers may be summed, as described in Van Eekelen and Bezuijen (2014). At a maximum 1.5 % strain and a loading time of two years, this gives a tensile stiffness J_{along} = 5237 kN/m. In the transverse direction, the two upper layers were installed quite a large distance above the pile caps and it is therefore assumed that it is not correct to add their stiffness to the total stiffness. The total reinforcement is therefore woven PET grid 600 + woven PVA grid 50. At small strains (max 1.5%) and a loading time of two years, this gives a tensile stiffness J_{across} = 5208 kN/m. These values were determined with the isochronous curves provided by the GR supplier.

Table 5.3 Parameters used in the calculations for Houten (Van Duijnen et al., 2010).

centre-to-centre distance piles	centre-to-centre distance piles	dia-meter circular pile caps	height fill	unit weight fill	friction angle fill	subgrade reaction	stiffness GR along	stiffness GR across	sur-charge load
s_x along	s_y across	d	H	γ	φ	k	J_x	J_y	p
m	m	m	m	kN/m^3	deg	kN/m^3	kN/m	kN/m	kPa
1.90	1.45	0.40	2.60	18.3	51	480	5237	5208	0

The subgrade reaction k was calculated using a 1D consolidation model that included parameters derived from CPT and triaxial test results. Later, settlement measurements became available for a nearby embankment on the same subsoil. It was concluded that the measured settlement was 30% less than predicted. The subgrade reaction was therefore divided by 0.7 to obtain a more realistic value. The resulting value is given in Table 5.3, along with the other properties and the geometry used in the calculations.

5.3.5 Large-scale French experiments

Briançon and Simon (2012) and, for example, Nunez et al. (2013) reported a series of large-scale tests. The researchers carried out tests in four test fields. Two of them are considered in this paper: test fields 3R and 4R. The researchers placed 8 · 4 circular concrete piles in a square arrangement in each test field, as indicated in Figure 5.7. No pile caps were installed.

The load transfer platform in test field 3R consisted of (bottom-up) a 0.15 m working platform, 0.2 m of industrial gravel (0-31.5 mm), a layer of biaxial PET geotextile and 0.2 m of industrial gravel. The failure strain of PET geotextiles is around 10%. The industrial gravel consisted of crushed recycled road construction material.
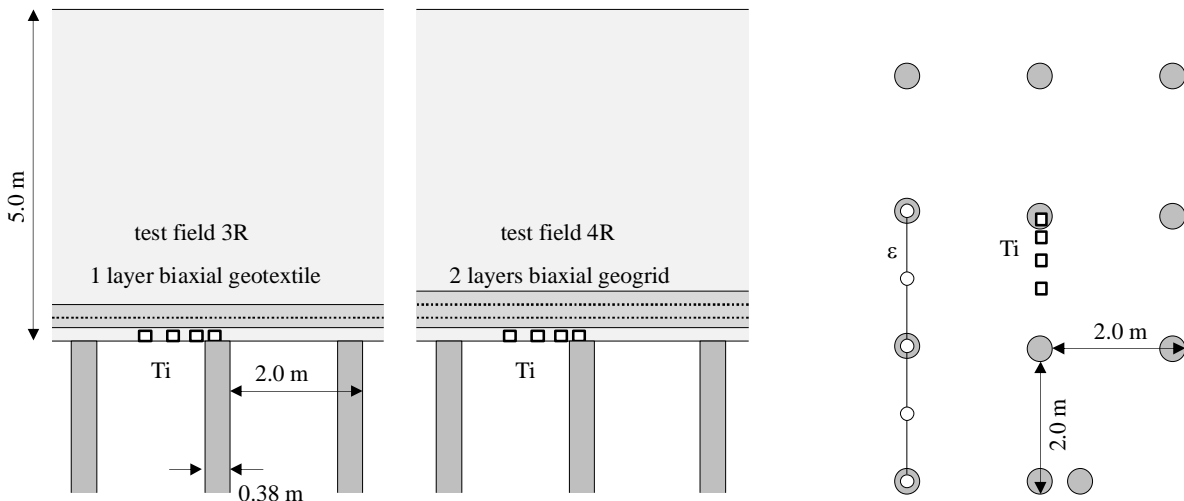
Figure 5.7 Layout of the part of fields 3R and 4R under consideration in the large-scale tests in France with settlement transducers Ti. Drawing modified after Briançon and Simon (2012).

The load transfer platform of test field 4R consisted of (bottom-up) a 0.15 m working platform, 0.2 m of industrial gravel (0-31.5 mm), a layer of biaxial geogrid, 0.2 m of industrial gravel, another biaxial geogrid and 0.1 m of industrial gravel. At the embankment edges, the GR was wrapped around and anchored back into the embankment.

The rest of the embankment was a marly and chalky natural soil. The total height of the embankment was 5.0 m. Settlement was measured at locations Ti in Figure 5.7. Optic fibres (Geodetect® strips) were used to measure GR strains in field 3R, as indicated with ε in Figure 5.7.

Determination of parameters

In one of the neighbouring test fields, no GR or piles were applied. The pressure of the embankment was 92.5 kPa. An average maximum settlement of 0.26 m was measured at the original ground level after 165 days. The subgrade reaction k is therefore $92.5/0.26 = 356$ kN/m^3. The subsoil therefore provides considerable support.

Table 5.4 Parameters used in the calculations of the large-scale tests in France of Briançon and Simon (2012).

test	centre-to-centre distance piles s_x along $= s_y$ across m	dia-meter circu-lar pile caps d m	height fill H m	unit weight fill γ kN/m^3	friction angle fill φ deg	subgrade reaction k kN/m^3	stiffness GR $J_x = J_y$ kN/m	surcharge load p kPa
3R	2.00	0.38	5.00	20	40-78[a]	356	600	0
4R	2.00	0.38	5.00	20	40-78[a]	356	750	0

[a] In the comparison in Chapter 5.4.5, the value of φ has been varied. In Figure 5.18 and Chapter 5.5, $\varphi = 53°$ has been used.

Briançon and Simon (2012) give a friction angle $\varphi = 36°$ and an effective cohesion $c = 60$ kPa for the fill of industrial gravel. As described in Chapter 5.3.2, a cohesive fill is less suitable for comparing measurements with analytical models not meant for cohesive material.

An equivalent φ can be found by determining the fill strength at the average pressure at GR level ($\sigma_v = \gamma \cdot H + p = 20 \cdot 5 + 0 = 100$ kPa). From this, it follows that:

$$\varphi_{virtual;c=0} = \text{atan}\left(\frac{\sigma_v \tan\varphi + c}{\sigma_v}\right) = \text{atan}\left(\frac{100 * \tan 36° + 60}{100}\right) = 53° \tag{5.2}$$

In their Table 3, Briançon and Simon (2012) give the results of EN ISO 10319 tensile tests on the GR. The short-term tensile stiffness for 2% GR strain was determined at 800 kN/m for test field 3D and 500 kN/m per GR layer for test field 4R. The measurements in the test field were carried out over a period of approximately six months. The stiffness of the GR was therefore reduced by 25% in a loading time of six months, which is a normal reduction for PET for this loading period. The resulting values are listed in Table 5.4.

5.3.6   Finnish full-scale test and 2D FDM calculations

A geosynthetic reinforced embankment was constructed on deep mixing (DM) columns and DM walls for an approach to a new bridge over the Sipoo River in Hertsby, Finland. Forsman et al. (1999) and Forsman (2001) give detailed information about the project. Huang et al. (2009) presented monitoring results and compared the measurements with 2D FDM (Finite Difference Method) calculations.
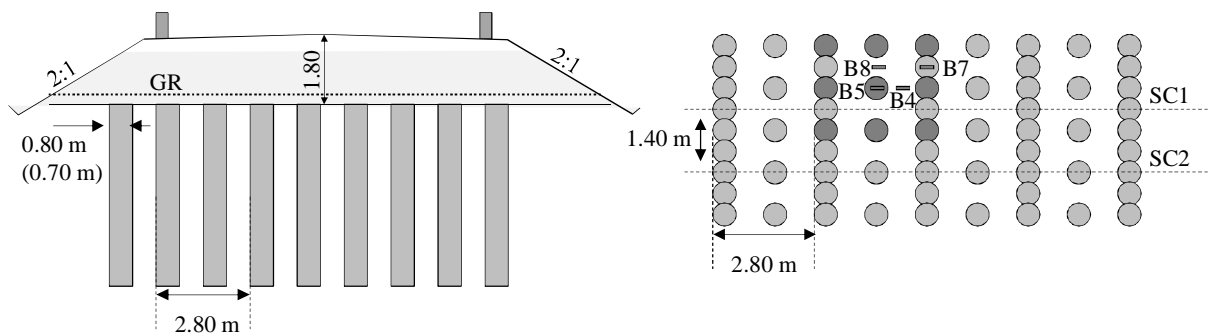
Figure 5.8 Layout of the monitored site on DM columns in Hertsby, Finland. Drawing modified after Huang et al. (2009).

Figure 5.8 presents the test area. The subsoil consists of a crust of 1 to 1.5 m, 10 to 14 m of soft clay, 1 to 6 m of silt and 1 to 5 m of glacial till. Deep mixing (DM) columns with a diameter of 0.80 m were installed following the pattern shown in Figure 5.8. Some of the DM columns were installed in such a way as to effectively create a wall. The average thickness of these DM walls was estimated to be 0.70 m. No pile caps were installed.

The embankment consisted (top-down) of 0.05 m of asphalt, a base course of 0.20 m of crushed stone, a sub-base of 1.05 m of gravel and a 0.50 m sand working platform above the existing ground.

A layer of woven biaxial geotextile 200/200 was installed with a 0.3 m thick underlying layer of sand to protect the reinforcement. Huang et al. (2009) did not specify the material used for the reinforcement but they indicated the stiffness of the GR used in their 2D FDM calculations: $J = 1700$ kN/m.

GR strains were measured at the locations indicated in Figure 5.8 (B4, B5, B7 and B8). The bridge approach was constructed in 1996 and 1997. This paper compares the GR strains measured during the first five years after putting the road into use. Huang et al. (2009) simulated the project with 2D FDM calculations using FLAC. They used coupled mechanical and hydraulic modelling. This means that the pore water pressure changes and effective stress changes were calculated alternately in a continuous loop. To convert the 3D problem to a 2D one, they investigated two

cases: (SC1) without mid-columns and (SC2) with mid-columns as indicated in Figure 5.8.

This paper presents the following two analytical calculations: (1) a 2D calculation (with a 2D plane strain version of the CA model) like cross-section SC2 of Huang et al., see Figure 5.8 Accordingly, the walls have a centre-to-centre distance $s_x = 1.40$ m and a wall width of 0.70 m. It is expected that this calculation will result in smaller GR strains than measured. And (2) a fully 3D configuration, with only columns and no walls. This simulates the situation with only the dark-coloured columns in Figure 5.8. The centre-to-centre distances are $s_x = s_y = 1.40$ m and the column diameter $d = 0.80$ m. It is expected that this calculation will result in slightly higher values for GR strain than measured.

Huang et al. (2009) included a traffic load as a uniformly distributed load of 12 kPa. This value was adopted for the calculations presented in the current paper.

Table 5.5 Parameters used in the calculations to compare with Huang et al. (2009).

	centre-to-centre distance DM piles/ walls	width DM walls a / diameter columns	height fill	unit weight fill	friction angle fill	subgrade reaction	stiffness GR	surcharge load
	$s_x = s_y$	d	H	γ	φ	k	$J_x = J_y$	p
	m	m	m	kN/m^3	deg	kN/m^3	kN/m	kPa
$2D^a$	1.40	0.70	1.80	20	41.5	19.5	1700	12
3D	1.40	0.80	1.80	20	41.5	19.5	1700	12

^{a} plane strain

Determination of parameters
Huang et al. (2009) give a friction angle $\varphi = 38^o$ and a cohesion $c = 5.0$ kPa. It is necessary to find an equivalent friction angle φ for $c = 0$ using the method given in Chapter 5.3.2:

$$\varphi_{virtual;c=0} = \text{atan}\left(\frac{\sigma_v \tan\varphi + c}{\sigma_v}\right) = 41.5^o \tag{5.3}$$

The subgrade reaction k is calculated from the thickness of the soft soil layers in combination with the Young's modulus E of these layers. The 15 m thick layer of soft clay has an E of 300 kPa. The 2 m thick layer of silt has an E of 1600 kPa. The resulting subgrade reaction is: $k = (300 \cdot 1600)/(2 \cdot 300 + 15 \cdot 1600) = 19.5$ kN/m^3. Subsoil support in this case was therefore very limited. This value has been listed in Table 5.5, along with the other parameters.

5.3.7 The Krimpenerwaard N210 piled embankment

A new 14 km long regional road was built on a 15 m layer of extremely compressible organic soil. Haring et al. (2008) reported monitoring results from this project.

The part of the test area considered in this paper is shown in Figure 5.9. The same precast square pile caps as in Woerden (see Chapter 5.3.3) were installed on driven precast piles. The embankment fill consisted of 0.18 m of asphalt on top of an embankment of gravel consisting of crushed recycled construction material, mainly concrete. During the measurements, however, the asphalt had not yet been laid. An extra 0.18 m layer of gravel was placed to compensate for this.

The test field was established in 2007, which was during the optimisation process of the construction process. The space between the pile caps in the test field was not filled and the GR was installed on top of the pile caps with gaps in between. This construction method made it difficult to get the GR taut and so it was decided to fill the gaps between the pile caps with loose soil before GR installation for the rest of the road. The problems with the GR installation in the test field may have resulted in unexplainable measurements. The road surface, however, has remained settlement-free during the first four years of using the road.

In the transverse direction, a layer of woven PET Stabilenka geotextile reinforcement 350/50 was installed with underlying pieces of non-woven on top of the pile caps to protect the reinforcement. This geotextile was wrapped back, as indicated in Figure 5.9. This effectively results in two layers of cross-reinforcement. The reinforcement in the direction of the road consisted of knitted PET geogrid Fortrac 600/50. The failure strain of PET geogrids and PET geotextiles is around 10%. The GR strains were measured with Glötzl strain gauges at the locations "ε" in Figure 5.9.

The new road was opened in 2010. This paper reports the average strains measured on 29 September 2007, which was 2 months after the building of the embankment but before the road went operational.
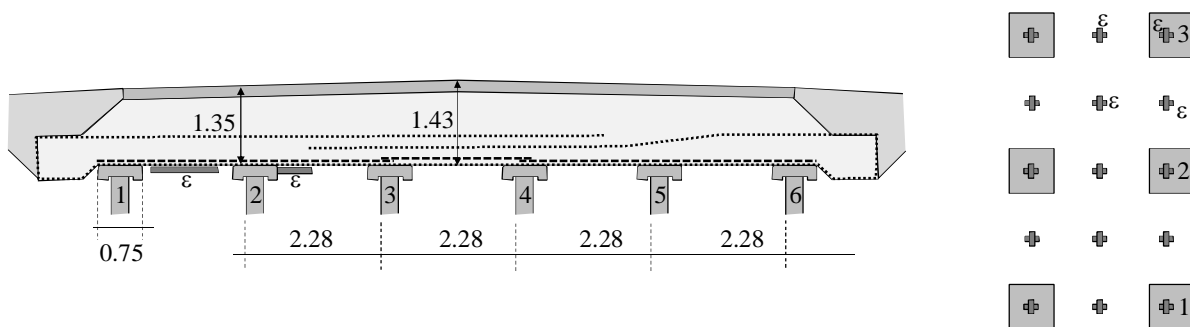
Figure 5.9 Layout of the part of the monitored site under consideration in the N210 in the Krimpenerwaard, the Netherlands, indicating the location of the strain gauges applied for measuring GR strains. Drawing modified after Haring et al. (2008).

Determination of parameters

The fill material was comparable to the fill in Woerden and Houten (Chapters 5.3.3 and 5.3.4) and its friction angle is also assumed to be around 51 degrees, as explained in Chapter 5.3.3.

The stiffness of the GR layers in both directions may be summed, as proposed by Van Eekelen and Bezuijen (2014). All the reinforcement consisted of knitted or woven PET. In the longitudinal direction, the short-term strength of this material is 600+50+50 = 700 kN/m. In the transverse direction, the short-term strength is 350+350+50 = 750 kN/m. The isochronous curves give, at 2.5% strain and a loading time of approximately 1 year, stiffness values J of 5548 kN/m and 5240 kN/m respectively for these materials. However, a better approach could be to disregard the upper GR layer since the distance between the bottom and top layers is considerable, as shown in Figure 5.9. If the embankment is considered as a bending beam, the top layer cannot contribute much. In that case, the short-term strength will be 400 kN/m. This results in a stiffness J of 2959 kN/m. Both approaches will be considered.

Table 5.6 Parameters used in the calculations for the Krimpenerwaard N210 road (Haring et al., 2008).

	centre-to-centre distance piles along	centre-to-centre distance piles across	width square pile caps	height fill	unit weight fill	friction angle fill	subgrade reaction	stiffness GR along	stiffness GR across	surcharge load
	s_x	s_y	a	H	γ	φ	k	J_x	J_y	p
	m	m	m	m	kN/m^3	deg	kN/m^3	kN/m	kN/m	kPa
2 GR layers across	2.35	2.28	0.75	1.35	19.0	51	250	5178	5548	0
1 GR layer across[a]	2.35	2.28	0.75	1.35	19.0	51	250	5178	2959	0

[a] These cases are included in Figure 5.27.

The pressure on the subsoil below the GR is approximately 13.5 kPa. It is assumed that this pressure is the same for the entire area between the pile caps and it is therefore concluded that the subgrade reaction $k \cong 250$ kN/m^3. This was concluded from the pressure below the GR $\cong 13.5$ kPa, which was measured at two locations: between two piles and four piles in combination with a measured GR deflection of 45 to 70 mm at these locations, which were averaged to assess the subgrade reaction. Table 5.6 lists the parameters used in the calculations for the Krimpenerwaard.

5.3.8   Hamburg full-scale test

The level of several streets in Hamburg's HafenCity is being raised by around 3 m to ensure safety from flooding. Weihrauch et al. (2010, 2013) reported measurements in a piled embankment constructed in the Hongkongstrasse. Vollmert (2014) supplied more data.

Part of the test area is presented in Figure 5.10. Later, the right-hand part of the piled embankment was removed and a wall was installed as indicated. The subsoil consists of 15 m of layered soft soil. Top-down the layers consist of very loose sandy, partially clayey fills, clay-soft peaty clay, soft sandy clay, peat and sand. The average layer thickness of the organic layers is approximately 8.2 m. There were no significant differences between the geotechnical properties of the top fill layer and that of the original ground before filling up.
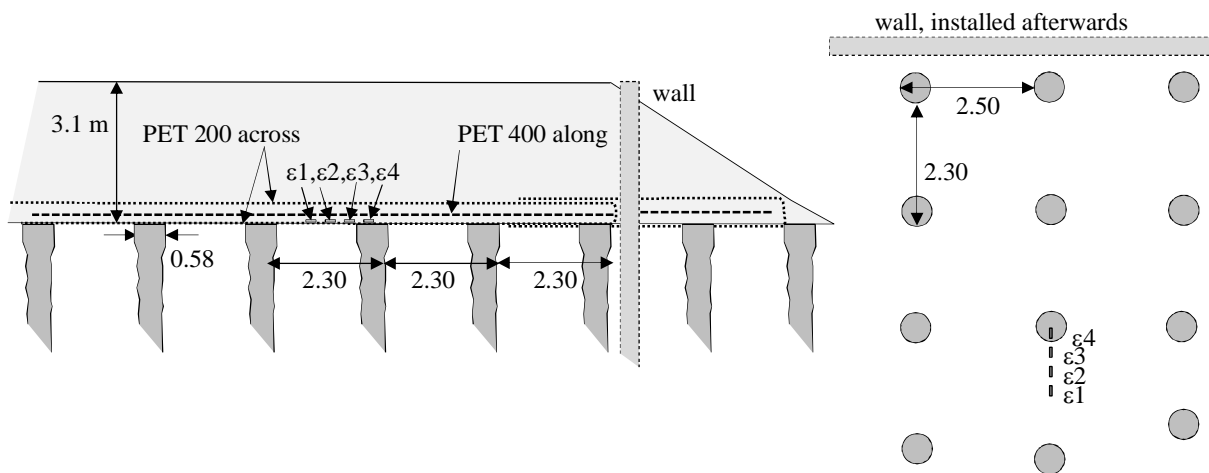
Figure 5.10 Layout of the part of the test field under consideration in the Hongkongstrasse, Hamburg, Germany Drawing modified after Weihrauch et al. (2010, 2013).

Unreinforced lime-cement treated gravel columns were installed at a centre-to-centre distance $s_{along} \cdot s_{across} = 2.50 \cdot 2.30$ m. The pile caps were widened with cast in situ unreinforced concrete to a diameter of 0.60 m.

The fill consists of a sand layer with a 0.30 m layer of asphalt and its foundation. In the direction perpendicular to the road axis, a laid Secugrid PET-200 geogrid layer was installed 0.15 m above the columns and wrapped back 0.25 higher in the fill across the entire road. In the longitudinal direction (along the road axis), a laid PET-400 geogrid layer of the same type was installed at 0.30 m above the columns. The failure strain of PET geogrids is around 10%. The GR strains were measured at the four locations indicated in Figure 5.10.

Determination of parameters

Table 5.7 Parameters used in the calculations for Hamburg (Weihrauch et al., 2010, 2013).

	centre-to-centre distance piles along s_x m	centre-to-centre distance piles across s_y m	dia-meter columns d m	height fill H m	unit weight fill γ kN/m^3	friction angle fill φ deg	sub-grade reaction k kN/m^3	stiff-ness GR $J_x = J_y$ kN/m	sur-charge load p kPa
during install-ation	2.50	2.30	0.58	2.50	19.0	35	1765	7480	18
long term	2.50	2.30	0.58	3.10	19.0	35	1200	6050	20

The stiffness *J* (kN/m) of the geogrid was determined using the isochronous curves, the loading time and the measured GR strains. Table 5.7 gives the resulting GR stiffness, along with the other parameters provided by Vollmert (2014). He determined the subgrade reaction *k* with the measured GR deflection and the measured pressure beneath the GR.

5.3.9 Sloan's large-scale experiments (2011)

Sloan (2011, also reported in McGuire et al., 2012) carried out five large-scale tests. This paper considers two of the tests, namely CSE#3 and CSE#4 (Table 5.8). Nine circular ∅ 0.61 m concrete columns were placed in a square arrangement within a square of concrete walls, as indicated in Figure 5.11. The spaces between the box walls and piles were filled with a geofoam of expanded polystyrene (EPS) to model the soft subsoil between the piles. After installing a reinforced embankment on top of the columns and the EPS, the EPS was dissolved using D-limonene through a network of PVC pipes. D-limonene is a natural oil obtained from orange peels that dissolves EPS easily.
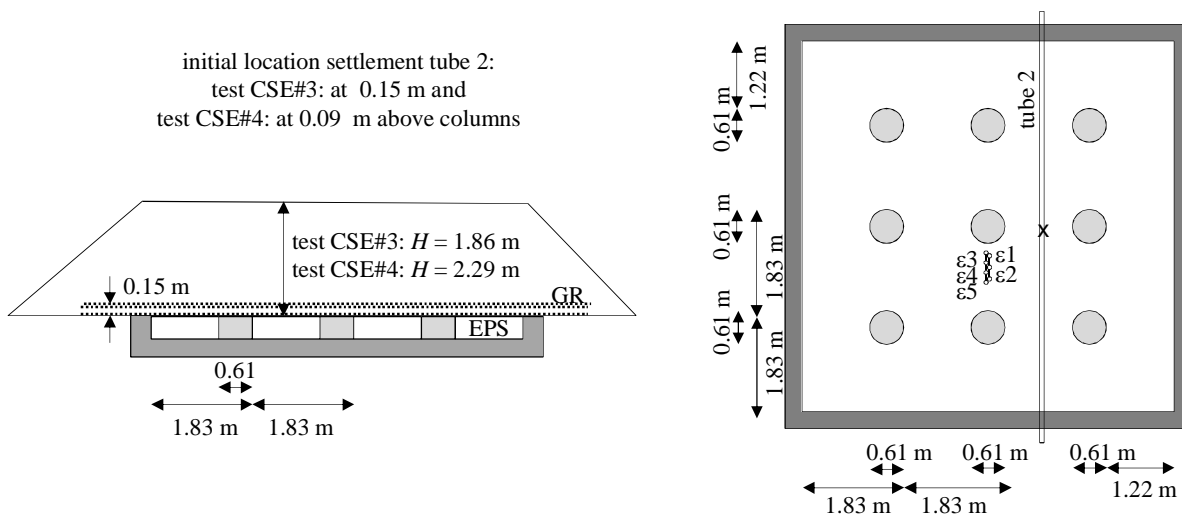
Figure 5.11 Layout of large-scale tests CSE#3 and CSE#4 carried out in the USA (Sloan, 2011). Drawing modified after Sloan (2011).

After dissolving the geofoam, the researchers waited 7 days and then loaded the embankment with a small working truck weighing 1878 kg with 4 wheels and measuring length · width = 3.0 · 1.4 m^2.

Three layers of biaxial punched/drawn Tensar® BX1500 geogrid of PP were installed. The authors of this paper did not have the failure strain for these PP geogrids at their disposal. One layer was placed directly on the columns. The other two GR layers were placed transversely with respect to each other at an elevation of 0.15 m above the first GR layer. GR strain measurements were made with wire extensometers, attached to the base layer of the GR. The locations of the GR strain transducers "ε" are indicated in Figure 5.11. Transducers ε1, ε2 have been installed in test CSE#3 and ε3, ε4, ε5 in test CSE#4.

Table 5.8 Parameters used in the calculations for the large-scale experiments of Sloan (2011).

test	centre-to-centre distance piles $s_{along} = s_{across}$ m	dia-meter circu-lar pile caps d m	height fill H m	unit weight fill γ kN/m^3	friction angle fill φ deg	subgrade reaction k kN/m^3	stiffness GR along J_x kN/m	stiffness GR across J_y kN/m	sur-charge load p kPa
CSE#3	1.83	0.61	1.86	22.00	45	0	493 [a]	569 [a]	0
CSE#4	1.83	0.61	2.29	21.53	45	0	493 [a]	569 [a]	0

[a] On the basis of the illustrations in Sloan (2006), it is assumed that the GR strain measurements were made in the transverse direction, and therefore that J_x = 493 kN/m.

The fill consisted of gravel with 5% fines. This relatively low fines content was chosen to reduce the risk of an artificially high strength due to negative pore water pressure. The fill was compacted dry to avoid capillarity and increased strength due to negative pore water pressures.

Determination of parameters
Large GR strains were measured during the piled embankment tests. Sloan (2006, table 7.3) gives the rapid loading tensile stiffness of the reinforcement for several strains and states that stiffness falls by approximately 55% during the experiments. At 8% strain and a loading time of 7 days, this results in the following tensile stiffness: in machine direction (MD) 139 kN/m and in XMD direction 215 kN/m per layer. Consequently, the total stiffness in one direction (MD+MD+XMD) is 2·139+215 = 493 kN/m. In the other direction, the total stiffness is (XMD+XMD+MD) = 569 kN/m. It is possible that the reduction of the stiffness by 55% is not accurate as PP is a material that creeps considerably. The resulting values are stated in Table 5.8, along with the other geometry and material properties. The value for the fill friction angle was taken from Sloan (2011).

5.3.10 Oh and Shin's scaled tests (2007)

Scaled field experiments were performed at the Geotechnical Experimentation Site of the University of Incheon in the Republic of Korea (Oh and Shin, 2007). Figure 5.12 presents part of the test area. A test box with length · width · depth = 13.0 m · 3.0 m · 1.6 m³ was excavated in a firm composed granite and filled with marine clay obtained from the Bay of Incheon. After a consolidation period of 3 months, five test fields were installed, one with no piles or GR, one with only piles, and three with both piles and GR. In these three test fields, the centre-to-centre distance of the piles was 0.75, 0.60 and 0.95 meters respectively. In each test field nine concrete piles with a diameter of 0.10 m were driven into the clay and a concrete pile cap with a diameter of 0.15 m was installed on each of the piles.
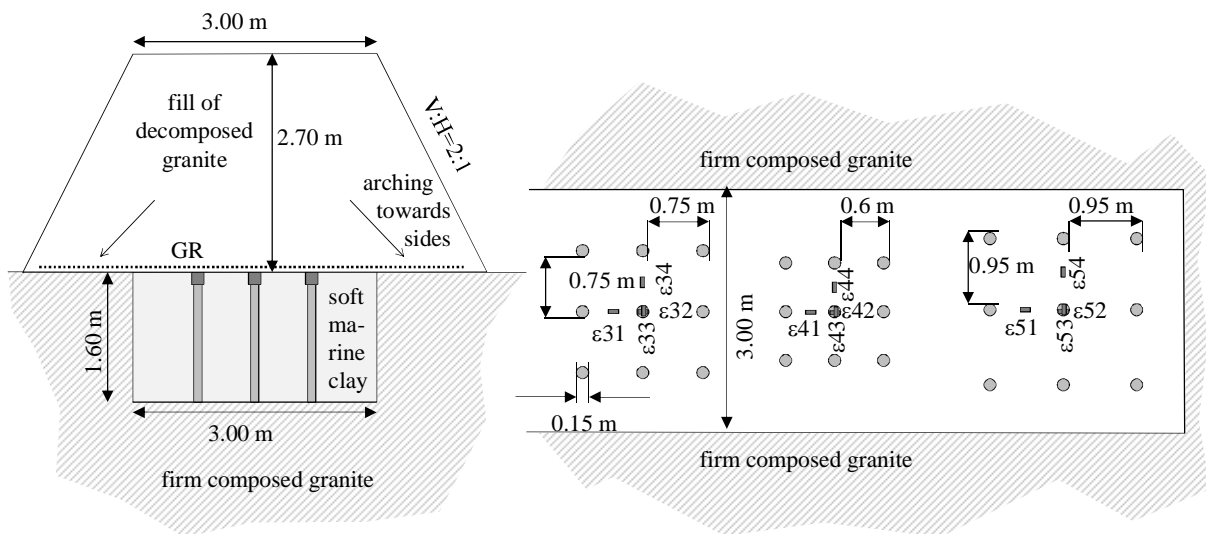
Figure 5.12 Layout of the three test fields with piles and GR. Drawing modified after Oh and Shin (2007).

The embankment was built in three stages to heights of 0.67 m, 1.65 m and 2.70 m respectively. It consisted of a granite weathered soil, which is a poorly graded silty sand according to the authors.

A limitation of the structure is that arching occurs towards the sides of the test box, as indicated in Figure 5.12. Oh and Shin (2007) indeed found, in their Figure 13, that the total measured load was approximately 60% lower than the embankment weight.

A biaxial punched/drawn PP geogrid type Tensar® BX1100 was installed directly on top of the pile caps. The authors of this paper did not have the failure strain for these PP geogrids at their disposal. GR strains were measured with a plastic gauge (type YFLA-5) in both directions, both on top of a pile and mid-way between adjacent piles.

154

Determination of parameters

The value for the fill friction angle φ in Table 5.9 was taken from Oh and Shin's table 4 (2007). The cohesion given in this table is $c = 1.0$ kPa, which is considered negligible.

For the test field without piles or GR, Oh and Shin found, at $H = 1.65$ m, a maximum value for settlement of $z = 0.063$ m. These values are considered to be normative for the determination of the subgrade reaction k, as this settlement is comparable to the final settlement in the test fields with piles and GR for the embankment height of 2.70 m. At this embankment height, they also found arching towards the test box sides. The total measured load in the piled areas was more than 60% lower than expected. In this paper, it is assumed that the loss of load due to arching in the test field without piles is slightly less: 50%. This gives the subgrade reaction: $50\% \cdot \gamma \cdot H/z = 0.5 \cdot 18 \cdot 1.65/0.063 = 236$ kN/m^3.

Table 5.9 Parameters used in the calculations for the comparison with the Oh and Shin's scaled test (2007).

test field	centre-to-centre distance piles $s_x = s_y$ m	diameter pile caps d m	height fill H m	unit weight fill γ kN/m^3	friction angle fill φ deg	subgrade reaction k kN/m^3	stiffness GR $J_x = J_y$ kN/m	sur-charge load p kPa
5	0.95	0.15	2.70	18 [b]	35	236	235[a]	0
3	0.75	0.15	2.70	18 [b]	35	236	235 [a]	0
4	0.60	0.15	2.70	18 [b]	35	236	235 [a]	0

[a] Oh and Shin (2007) simulated their tests with 2D plane strain FLAC calculations using $J = 800$ kN/m, despite their tensile test results.

[b] This unit weight was reduced by 60% to 7.2 kN/m^3 to take into account the arching that occurs towards the test box sides as indicated in Figure 5.12 and explained in Chapter 5.3.10.

The short-term stiffness at 2% GR strain was 205 kN/m in the machine direction and 330 kN/m in the transverse direction. A reduction of 12% in GR stiffness was applied to take into account the influence of the loading time. This reduction is confirmed by the measured development of the strain (Oh and Shin, their Figure 15). Apparently, the subsoil support is enough to prevent continuous creep of the PP reinforcement. In the calculations, the average stiffness in both directions was used since the GR strains measured by Oh and Shin are probably the average of both directions. It should be noted that Oh and Shin simulated their tests with 2D plane strain FLAC calculations using $J = 800$ kN/m, despite their tensile test results.

5.3.11 *German laboratory scaled experiments*

Zaeske (2001) and Kempfert et al. (1999, 2004) reported a series of scaled laboratory tests. Figure 5.13 shows the set-up, a 1-g model. The scale is 1:3 to 1:6. Peat with a water content of 300% was used for the soft soil underneath the GR in between the four piles.

A 5 cm layer of sand was applied on top of the peat and the piles. On top of this, a stiff steel frame was placed to which the GR was attached. A fill of varying height was introduced. The surcharge load was applied by a stiff load plate with a 5 cm thick water cushion underneath to distribute the surcharge load uniformly over the fill. The total load $A+B$ in the piles was measured, along with soil pressures and GR deflections. Additionally, the GR strains were measured at the locations indicated in Figure 5.13 with strain gauges type 0.6/120LY1 (Hottinger Baldwin Messtechnik GmbH).
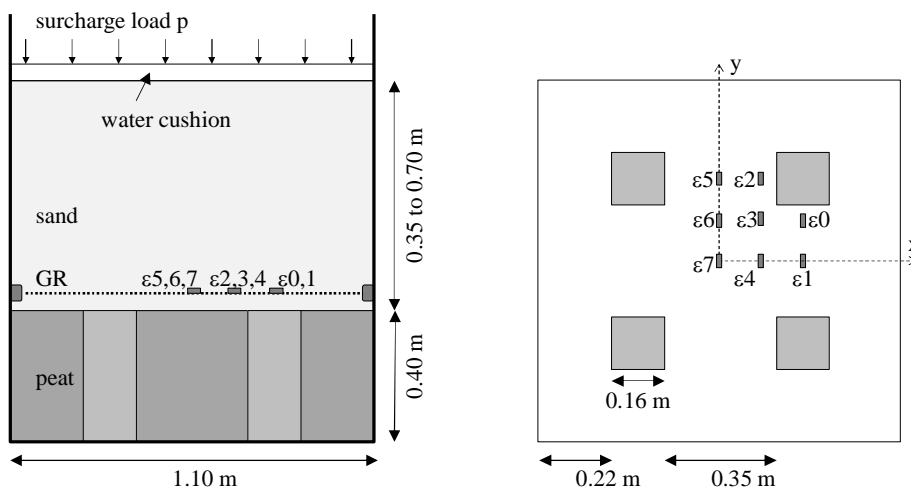
Figure 5.13 Cross-section and top view of the German laboratory tests reported in Zaeske (2001) and Kempfert et al. (1999 and 2004), Germany. Drawing modified after Zaeske (2001).

After the installation of the fill the surcharge load was increased in steps of 8.26 kPa until the maximum top load of 124 kPa was reached. The time between each step was long enough for the primary settlement.

This paper considers four similar tests: tests 5 to 8. The fill height was 0.35 m in tests 5 and 6 and 0.70 m in tests 7 and 8. The fill consisted of poorly graded sand with $d_{50} = 0.35$ mm. The GR was 'type A' in tests 5 and 7 and 'type B' in tests 6 and 8. Type A was a knitted PET Fortrac geogrid 60/60-20; type B was PET geogrid R 30/30-12. The failure strain of PET geogrids is around 10%.

Table 5.10 Parameters used in the calculations for Zaeske's laboratory tests (2001, also reported in Kempfert et al., 2004).

test	centre-to-centre distance piles s_x and s_y m	width square pile caps a m	height fill H m	unit weight fill γ kN/m³	friction angle fill φ deg	subgrade reaction k kN/m³	stiff-ness GR along $J_x = J_y$ kN/m	sur-charge load[a] p kPa
5	0.50	0.16	0.35	18.1	38	2125	1000	0-99
6	0.50	0.16	0.35	18.1	38	2125	500	0-91
7	0.50	0.16	0.70	18.1	38	2125	1000	0-102
8	0.50	0.16	0.70	18.1	38	2125	500	0-90

[a] 80% of the applied surcharge load to take into account the friction between the box walls and fill.

Determination of parameters

Short-term tensile tests according to EN 10319 showed, for GR type A, a short-term tensile stiffness $J = 1000$ kN/m for less than 1.5% strain. This was 500 kN/m for GR type B. It is not known how long each loading step was and, to stay on the 'safe side' of the prediction, the stiffness was not reduced to take the loading time into account. Reducing GR stiffness would have increased the predicted GR strain.

Fill properties were determined with triaxial testing on sand samples at 100% Proctor density (Zaeske, 2001, page 41). They are listed in Table 5.10.

In the calculations, the surcharge load p was reduced by 20% to take into account the friction between the box walls and the fill. Zaeske did not mention the influence of friction. Van Eekelen et al. (2012a, Chapter 2 of this thesis) measured the friction in similar tests with a fill of sand. They found an average friction of 21% of the applied surcharge load. In both test series, a similar effort was made to reduce the friction with rubber sheets and grease.

The calculation value for the subgrade reaction k was determined as follows: $k = E_{peat}/t_{peat}$, where $E_{peat} = 850$ kN/m² (Zaeske, 2001, page 40) is the stiffness of the peat underneath the GR; and $t_{peat} = 0.40$ m is the thickness of the peat layer. This results in $k = 850/0.4 = 2125$ kN/m³.

5.3.12 *Dutch laboratory scaled experiments*

Van Eekelen et al. (2012a, 2013, Chapters 2 and 4 of this thesis) reported a series of nineteen scaled laboratory experiments, which will be summarised here for the sake of clarity. Figure 5.14 gives the set-up, which is a 1-g model. The scale is 1:3 to 1:5. A foam cushion modelled the soft soil around the 4 piles. This cushion was a watertight wrapped soaked foam rubber cushion. A tap was installed to drain the cushion during the test, modelling the consolidation process of the soft soil.

A 1.5 to 2 cm layer of sand was applied on top of the foam cushion and the piles, followed by one or two stiff steel frames to which one or two GR layers were attached. A fill of varying height was placed. The top load was applied with a water cushion that applied stresses comparable with field stresses.
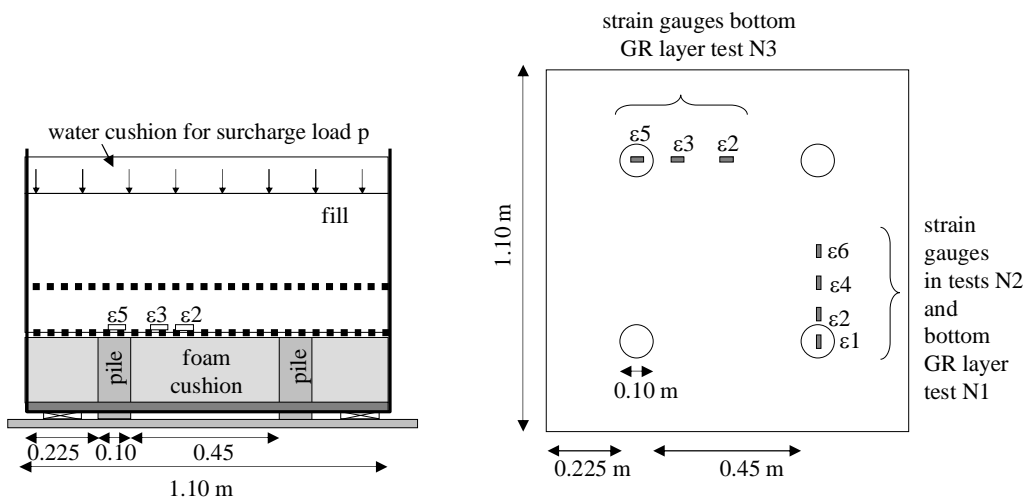
Figure 5.14 Cross-section and top view of the Dutch laboratory tests reported in Van Eekelen et al. (2012a, b, 2013, Chapters 2, 3 and 4 of this thesis), the Netherlands.

The test set-up was similar to Zaeske's test set-up (2001). In the series reported here, however, the fill consisted in most cases of granular material instead of sand, the subsoil support was not peat – it was controlled with the foam cushion instead – and the load distribution was measured differently so that load parts *A*, *B* and *C* could be measured separately.

Each test was carried out as follows: (1) 6 litres of water was drained from the foam cushion (modelling subsoil consolidation), (2) installation of the water cushion on top of the fill followed by a first top load increase, (3) one or more drainage steps of 6 litres until the subsoil support approached 0 kPa, (4) second top load increase, (5) one or more drainage steps followed by top load increases of 25 kPa each until the maximum top load (usually 100 kPa) was reached and the subsequent drainage steps and (6) draining the foam cushion under vacuum to

create a situation without subsoil support. There was a wait of at least two hours between each loading or drainage step to let the model stabilise.

Different GR types were installed. Only one of them, laid Secugrid PET 30/30 geogrid, was suitable for the gluing on of strain gauges. This paper presents the results of these three tests, N1, N2 and N3, which are listed in Table 5.11. The fill was a well-graded granular fill (crushed recycled construction material 1-16 mm). Den Boogert et al. (2012a,b) carried out displacement-controlled (2 mm/min) triaxial tests on three 300 mm · 600 mm samples (diameter · height) and found a peak friction angle φ_{peak} of 49.0° and a dilation angle ψ of 9°.

Table 5.11 Specification of the Dutch laboratory tests reported by Van Eekelen et al. (2012a, adopted in Chapter 2 of this thesis) and discussed in this paper.

test	GR	centre-to-centre distance $s_y = s_y$ m	diameter circular pile caps d m	height fill H m	height fill between 2 GR layers m	fill unit weight γ kN/m^3	fill friction angle φ deg
N1	2 laid PET biaxial geogrids each 30/30	0.55	0.10	0.42	0.050	15.74	49.0
N2	1 laid PET biaxial geogrid 30/30	0.55	0.10	0.42		17.24	49.0
N3	2 laid PET biaxial geogrids each 30/30	0.55	0.10	0.42	0.087	16.16	49.0

The failure strain of the applied PET biaxial geogrid is around 10%.

Determination of parameters and remarks on calculations
The test geometry and fill properties are given in Table 5.11.
Table 5.12 gives the values used in the calculations for the surcharge load p, subgrade reaction k, and the GR stiffness J for each point just before each loading step or drainage step. The calculation value for the surcharge load was determined as follows. First, the friction R along the box walls was determined: $R = (\gamma H + p) \cdot s_x \cdot s_y - (A + B + C)_{measured}$. Then the calculation value for the surcharge load $p_{calculation}$ was determined as $p_{calculation} = p_{supplied} - R$.

The calculation value for the subgrade reaction k was determined as follows: $k = C \cdot z_{average}$, where C is the pressure in the subsoil-foam cushion and $z_{average}$ is the average settlement of the GR determined using the total amount of water drained from the foam cushion. In the tests, however, the subsoil support was constant. Using constant subsoil support in the calculations for, for example, test N3 instead of subgrade reaction k results in a difference of less than 1% in the calculated GR strain.

Each loading situation in the experiments was maintained for 2 to 14 hours. The short-term GR stiffness, which is strain-dependent and determined with the standard quick tensile test (CEN ISO 10319) was reduced by 12% to take the loading time into account.

Table 5.12 Parameters used in the calculations for the laboratory experiments of Van Eekelen et al. (2012a, Chapter 2 of this report).

sur-charge load	sub-grade reaction	GR stiffness	sur-charge load	sub-grade reaction	GR stiffness	sur-charge load	sub-grade reaction	GR stiffness
N1-p	*N1-k*	*N1-J*	*N2-p*	*N2-k*	*N2-J*	*N3-p*	*N3-k*	*N3-J*
kPa	kN/m^3	kN/m	kPa	kN/m^3	kN/m	kPa	kN/m^3	kN/m
0.00	5824	3036	0.00	649	1518	0.08	411	3036
0.00	1285	3036	6.23	1742	1518	21.57	3138	3036
8.06	736	3036	6.22	364	1518	21.13	1029	3036
21.97	1677	3036	20.62	1222	1518	20.19	421	3036
22.46	641	3036	20.05	470	1518	43.76	1332	3036
22.36	214	3036	41.20	685	1518	42.63	662	3036
43.90	881	3036				41.80	312	2634
43.52	200	3036				41.42	131	2119
42.34	246	3019				64.36	573	1754
43.93	8	2211						

5.4 Comparison of measurements with analytical models

5.4.1 Analytical calculations

Table 5.13 gives an overview of the analytical models considered in this paper. Strip subsoil support is considered to be unrealistic (Lodder et al. (2012), Van Eekelen et al. (2012b, Chapter 3 of this thesis), Filz et al. (2012)) and is therefore considered only in a limited number of cases for the purposes of comparison.

Hewlett and Randolph's model (1988) is currently used in the French ASIRI (2012) and as a second option in the British Standard (BS8006, 2010), and therefore combined with a uniformly distributed load. Neither standard allows subsoil support to be taken into account in design. However, in the present study, Hewlett and Randolph's model have been combined with subsoil support so that the results match the measurements more closely. Without subsoil support, the predicted GR strains would be larger.

In this paper, all safety factors have been disregarded. Reduction factors have been applied only to reduce strain- and time-dependent GR stiffness. This reduction was specified in each case in Chapter 5.3.

Table 5.13 Analytical models considered.

code for model	arching model	load distribution	support from subsoil underneath[f]
Z-tri-str[g]	Zaeske[a]	triangular[a]	GR strip[a]
Z-inv-all		inverse triangular[c]	all GR between piles[e]
Z-uni-all		uniform	
HR-uni-str	Hewlett & Randolph[b]	uniform	GR strip
CA-inv-all	Concentric Arches (CA)[d]	inverse triangular[c]	all GR between piles
CA-uni-all		uniform	
CA-tri-all		triangular[a]	
CA-inv-str		inverse triangular[c]	GR strip
CA-uni-str		uniform	
CA-tri-str		triangular[a]	

[a] Zaeske (2001), Kempfert et al., (2004), [b] Hewlett and Randolph (1988), [c] Van Eekelen et al. (2012b, Chapter 3 of this thesis), [d] Van Eekelen et al. (2013, Chapter 4 of this thesis), [e] Lodder et al. (2012), [f] In some cases, calculations were carried out without subsoil support so that the difference between strip support and all support disappeared, [g] Z-tri-str is the combination of models that is currently adopted in EBGEO (2010) and CUR (2010).

5.4.2 Full-scale test in Rio de Janeiro

Table 5.14 lists the GR strains measured by Almeida et al. (2007, 2008). These measurements confirm the assumption that the highest GR strains occur lengthwise in the GR strips. The maximum GR strain is found at the edges of the pile caps. This has also been found with measurements in the model experiments of Zaeske (2001) and Van Eekelen et al. (2012a, Chapter 2 of this thesis) and numerical calculations such as those presented by Han and Gabr (2002).

The other GR strains ($\varepsilon 5$ and $\varepsilon 9$ on GR strips in the transverse direction; $\varepsilon 11$ and $\varepsilon 12$ and $\varepsilon 7$ in the centre of four piles) were much smaller, as expected. Only one exception was found: strain gauge $\varepsilon 7$ in between four piles is surprisingly large but still smaller than the GR strains measured in and along the GR strips. A more detailed analysis of these measurements can be found in Van Eekelen et al. (2014).

Table 5.14 Measured GR strains (%) in Rio de Janeiro, Brazil (Almeida et al., 2007, 2008).

edge of pile caps			on and parallel to GR strips		on GR strips, transverse direction		centre of 4 piles, parallel to pile array		centre of 4 piles, diagonal direction	
$\varepsilon 1$	$\varepsilon 2$	$\varepsilon 3$	$\varepsilon 6$	$\varepsilon 10$	$\varepsilon 5$	$\varepsilon 9$	$\varepsilon 7$	$\varepsilon 8$	$\varepsilon 11$	$\varepsilon 12$
2.05	1.73	1.50	1.50	1.36	0.51	0.32	1.14	0.97	0.25	0.63

The initial GR deflection or sag that occurs in this case results in relatively low GR strains (Bezuijen et al., 2010). In a comparable case without sag, more GR strain would have been measured. The cohesive fill and the initial GR sag make this case less suitable for validation. Chapter 5.5 therefore places less emphasis on the results of this case, and this was indicated with white-coloured dots in the figures in that chapter.

Figure 5.15 compares the calculated and measured strains in and along the GR strips. As explained in Chapter 5.3.2, a large range of values for φ have been given on the horizontal axis. Figure 5.15*a* shows the maximum strains at the edge of the pile caps.

Both the measured and the calculated strains are larger at the edges of the pile caps than in the centre of the GR strips. As expected, all calculation models indicate that an increase in φ gives a decrease in GR strain. However, this dependency seems too strong for Zaeske's arching model, resulting in very low strains for high values of φ.

Hewlett and Randolph (1988) already recommended not using their model for low embankments. Their model predicts a GR strain that is much too high. The *CA-inv* model matches the measurements best.
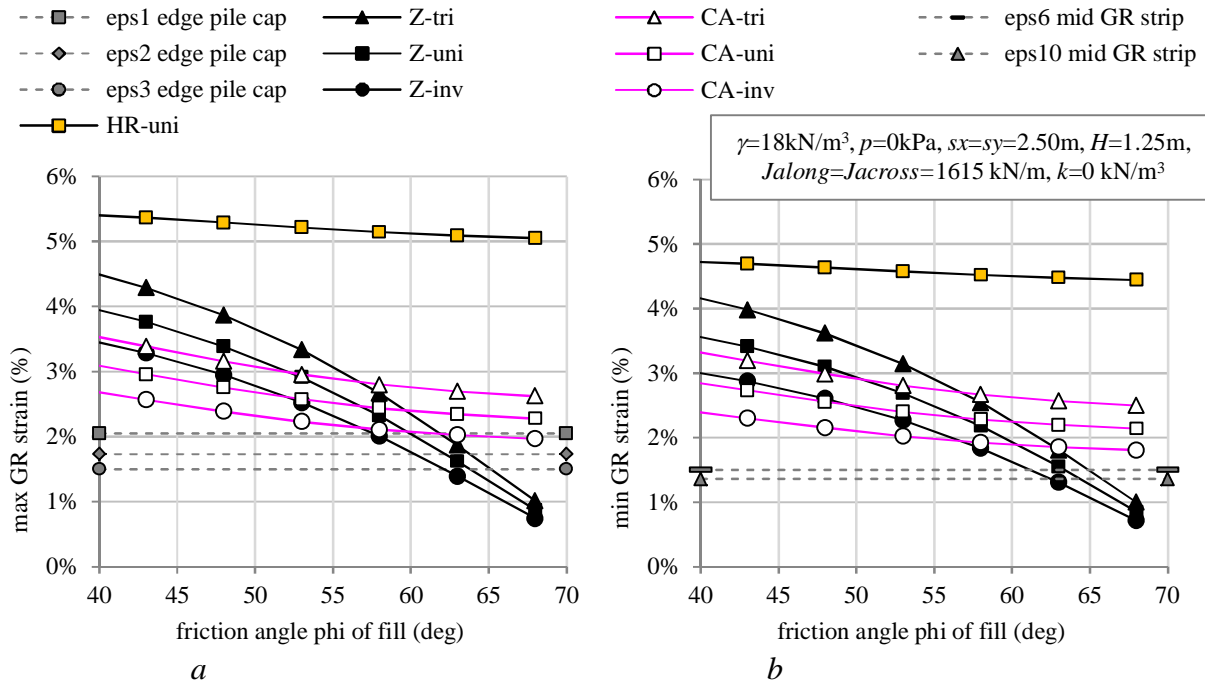
Figure 5.15 Comparison of measured and calculated GR strains for the full-scale test in Rio de Janeiro (Almeida et al, 2007, 2008) (*a*) GR strains at the pile cap edge and (*b*) GR strains in the centre of GR strips. Calculations with three step 1 models (Figure 5.2): Zaeske (2001), Hewlett and Randolph (1988) and the CA model (Van Eekelen et al. 2013, Chapter 4 of this thesis) and three step 2 load distributions (Figure 5.3): triangular, uniform and inverse triangular.

Generally, in design practice, it is advisable to disregard cohesion. Figure 5.15 also shows the consequences of doing this, and therefore of calculating with $\varphi = 42^{\circ}$. The *CA-inv* model would give a prediction that is not far from the measured value, but on the safe side. The other models give more GR strain, leading to a more conservative design.

5.4.3   Full-scale case in Woerden

As in the previous case, the subsoil support is negligible in this case. Figure 5.16*a* shows the comparison of the measured and the calculated arching. The figure shows that the prediction of both the CA and the Zaeske arching model match the measurements.
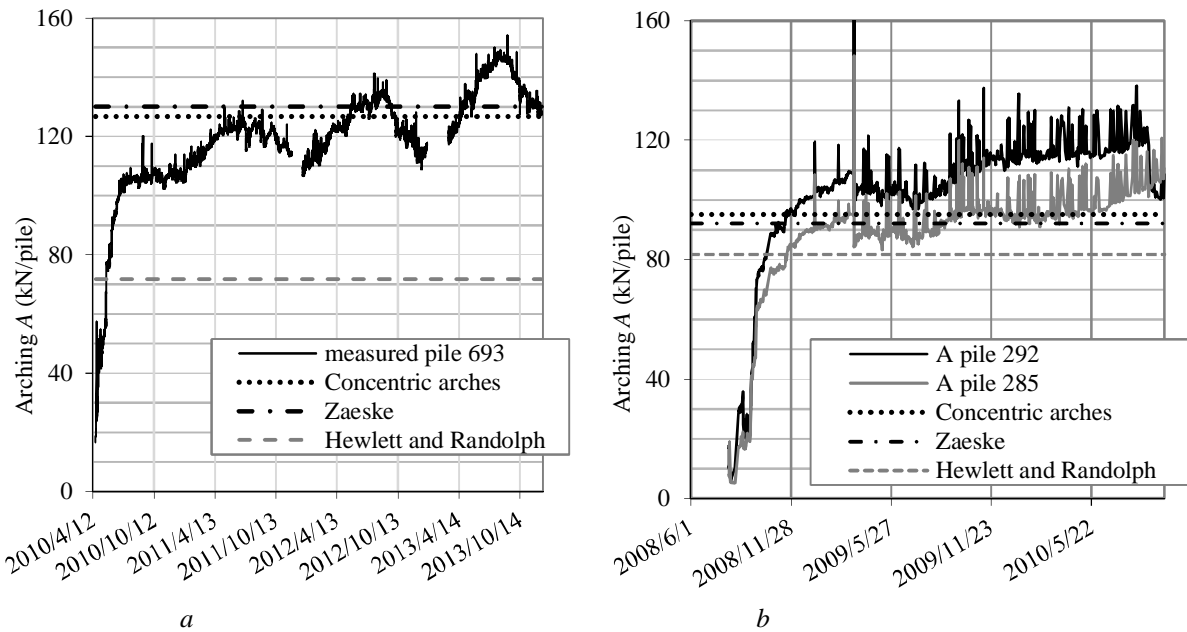
Figure 5.16 Calculation step 1. Measured and calculated arching *A* for (*a*) the Woerden case (Van Eekelen et al., 2012c) and (*b*) the Houten case (Van Duijnen et al., 2010).

The average GR strain measured between August and September 2013 was compared with the calculations in Table 5.15. The prediction of the inverse triangular load distributions matched the measurements well.

Table 5.15 Calculated maximum GR strain and measured GR strain (average values for the period 3 August 2013 – 14 September 2013), 38 months after the road was opened. Case Woerden (Van Eekelen et al., 2012c).

measured GR strain (%)						calculated GR strain (%)[b]						
	$\varepsilon 2$	$\varepsilon 16$	$\varepsilon 10$	$\varepsilon 9$	$\varepsilon 15$	$\varepsilon 6$						
optic fibre	0.54	0.61	0.32	0.55	0.4	0.40						
correction[a]	0.20	0.20	0.20	0.20	0.20	0.20	Z-tri	Z-uni	Z-inv	HR-uni	CA-tri	CA-uni	CA-inv
total strain	0.74	0.81	0.52	0.75	0.67	0.60	1.18	1.01	0.86	1.97	1.25	1.08	0.92

[a] Strain before zero measurement of 4 June 2010 determined with strain cables on 9 June 2010

[b] No subsoil support in this case, and therefore no difference between strip-subsoil and all-subsoil

Figure 5.17 shows measurements carried out in a tube that was installed directly upon the GR across piles 686, 687 and 688. The positions of these piles are indicated in Figure 5.5. Figure 5.17 also shows the second derivative of the measured shape of the GR (the tube), which is directly related to the load distribution on the GR between the piles. This second derivative shows clearly that an inverse triangular load distribution approximates the measurements better than any of the other load distributions considered.
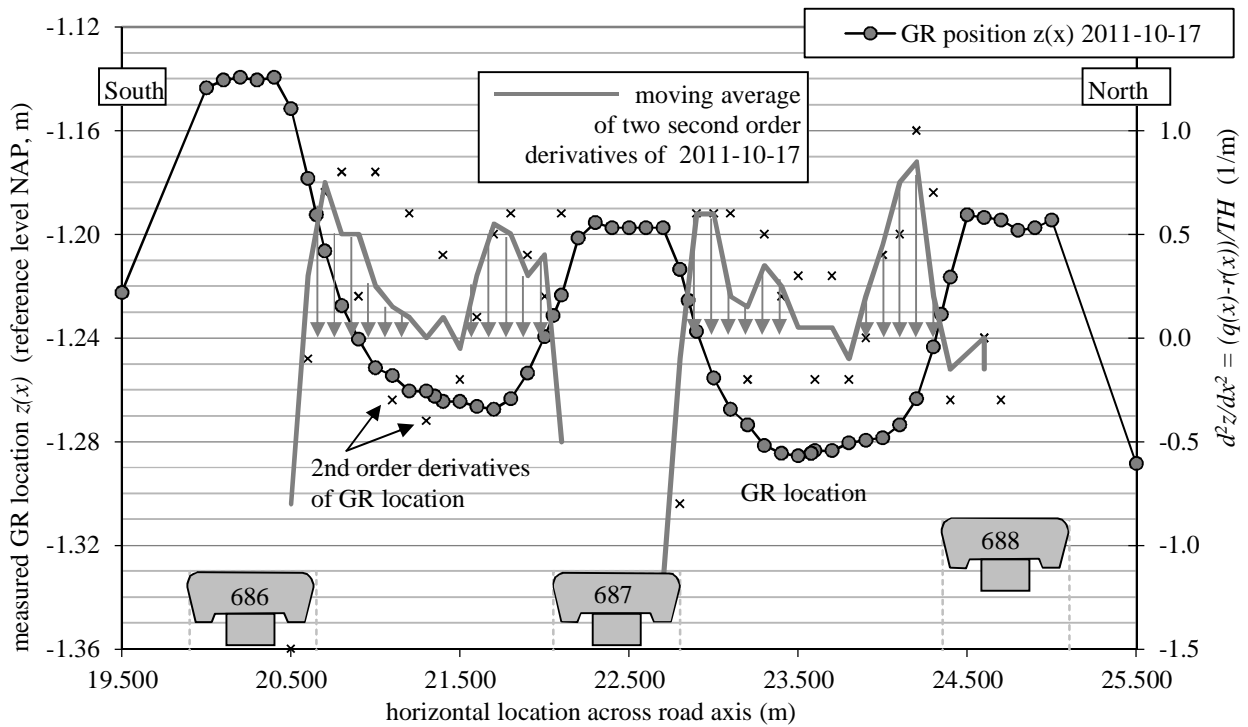
Figure 5.17 Measured settlement in a tube installed upon the GR across piles 686-689, as indicated in Figure 5.5, and its 2nd derivative, which is directly related to the load distribution on the GR between the piles (Case Woerden, Van Eekelen et al., 2012c).

5.4.4   Full-scale case in Houten

Figure 5.16*b* compares the measured and calculated arching. The predictions of both the CA and the Zaeske arching models match the measurements quite well. Further measurements have been reported by Van Duijnen et al. (2010).

Table 5.16 Average of the GR strains (%) measured in 2010 and calculated maximum GR strains (%). The railway was opened in November 2008. Case Houten (Van Duijnen et al., 2010).

measured		Z-tri-str[a]	Z-uni-str	Z-inv-str	Z-tri-all	Z-uni-all	Z-inv-all	HR-uni-str	CA-tri-str	CA-uni-str	CA-inv-str	CA-tri-all	CA-uni-all	CA-inv-all
transverse														
ε1 = 0.481	ε2 = 0.240	1.08	0.88	0.82	0.32	0.31	0.49	1.12	0.99	0.80	0.75	0.28	0.28	0.44
longitudinal														
ε3 = 0.054	ε4 = 0.024	1.00	0.81	0.87	0.33	0.35	0.57	1.07	0.89	0.73	0.80	0.28	0.31	0.52

[a] model in EBGEO (2010) and CUR226 (2010)

Table 5.16 compares the measured and calculated GR strains. As explained in Chapter 5.3.4, the measured GR strains are indeed relatively high across the track and relatively low in the direction of the track. The transverse GR strains are in the same range as predicted with *CA-inv-all*. The GR strains measured along the track are so small that they have not been taken into account in the discussion in Chapter 5.5 of this paper.

The current subsoil support is greater than assumed during design. Decreasing subsoil support due to consolidation would lead to more GR strain if the load on the GR were to remain the same, both in reality and in the calculations. However, in the calculations, the load on the GR would indeed remain the same because a limit equilibrium arching model is used. In reality, the load on the GR would decrease due to increasing arching. The GR strain would therefore fall less in reality than in the calculations. For decreasing subsoil support, the relationship between measured GR strain and design model would provide additional safety: the calculated GR strains are larger than the measured values.

The inverse triangular distribution gives more strain than the uniform load distribution and, in the case of 'all subsoil', also more than the triangular load distribution. This is explained in the next chapter relating to the French experiments.

5.4.5 Large-scale French experiments

As in the previous case, this case has a large amount of subsoil support. Arching is therefore less efficient since the differences in stiffness in the system are smaller. This results in less pressure on the piles and a more uniformly distributed pressure on the GR between the piles.
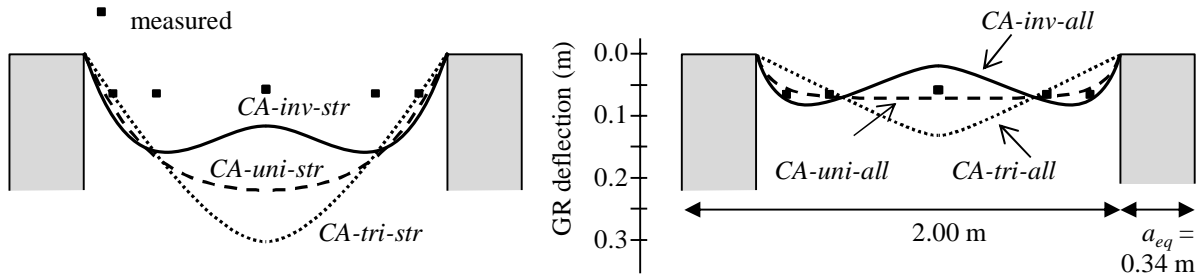
a. strip subsoil support in calculations   b. all subsoil support in calculations

Figure 5.18 Comparison of measured and calculated GR deflection in test field 3R of Briançon and Simon (2012) when $\varphi = 53^o$. The measured GR deflection is the measured settlement by comparison with the settlement measured on top of the piles. Calculations with the Zaeske arching model give comparable results, as shown in Figure 5.20. Measurements and calculations for test field 4R are also comparable.
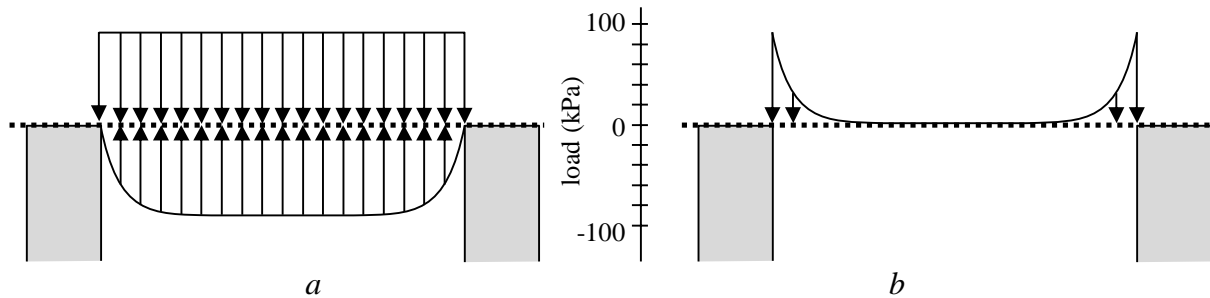
Figure 5.19 Result of analytical calculation *CA-uni-all* for Briançon and Simon (2012): *(a)* uniformly distributed load in combination with subsoil support gives *(b)* a net load distribution that matches the inverse triangular load distribution in Figure 5.3 better than the uniform or triangular load distribution.

Figure 5.18 compares calculated and measured GR deflection. The figure shows that taking all subsoil into account results, as expected, in a better match with the measurements. The measured GR deflection matches the *CA-uni-all* calculations best. This uniformly distributed load is combined with the counter-pressure, as shown in Figure 5.19. This results in a *net* load distribution that matches the inverse triangular load distribution better than the uniform or triangular load distribution.

The calculations with inverse triangular load distribution show most GR deflection close to the piles. The resulting shape of the deformed GR leads to a relatively high

GR strain. This is caused by the large counter-pressure in the centre of the GR strip, while the downwardly directed load midway between the piles is zero. This mechanism may occur in practice to a small extent, as shown by the measurements in Figure 5.18. However, a stiff subsoil leads to a more uniform load distribution on top of the GR and a net load distribution that is approximately inverse triangular.

Figure 5.20 compares the measured and calculated GR strains for a wide range of friction angles *φ*. *CA-inv-all* generally gives higher GR strains than measured, which is also the case for the other models for low friction angles.
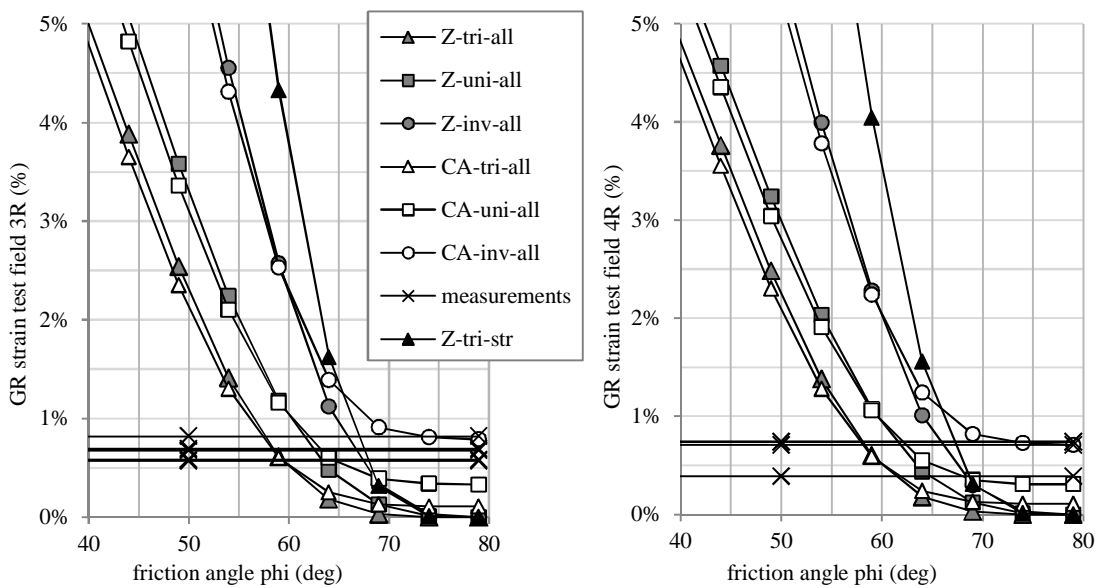
Figure 5.20 Comparison of measured and calculated maximum GR strains in Briançon and Simon's full-scale field test (2012).

5.4.6 Finnish full-scale test and 2D FDM calculations

Figure 5.21*a* compares the measured settlement at the base of the embankment with the 2D plane strain FDM calculations of Huang et al. (2009). There is a good match. The second derivative of these derived settlements is directly related to the load distribution on the GR. Between the second and third column the second derivative matches an inverse triangular load distribution better than any of the other considered load distributions. The second derivative between the first two columns is lower and flatter. This part of the settlement tube is located below the slope of the embankment.

Figure 5.21*b* compares the measured GR strains with the 2D plane strain FDM calculations and 3D analytical calculations. It was found that the 2D plane strain calculations with *CA-inv-all* gave nearly the same GR strain as its 3D equivalent and is therefore not shown in the figure. Note that the wall width in the 2D calculations is smaller than the column diameter in the 3D calculations, as indicated in Table 5.5. The 2D strains would have been smaller than the 3D strains for the same column/wall size. The figure shows a good match between measurements and several analytical calculations.
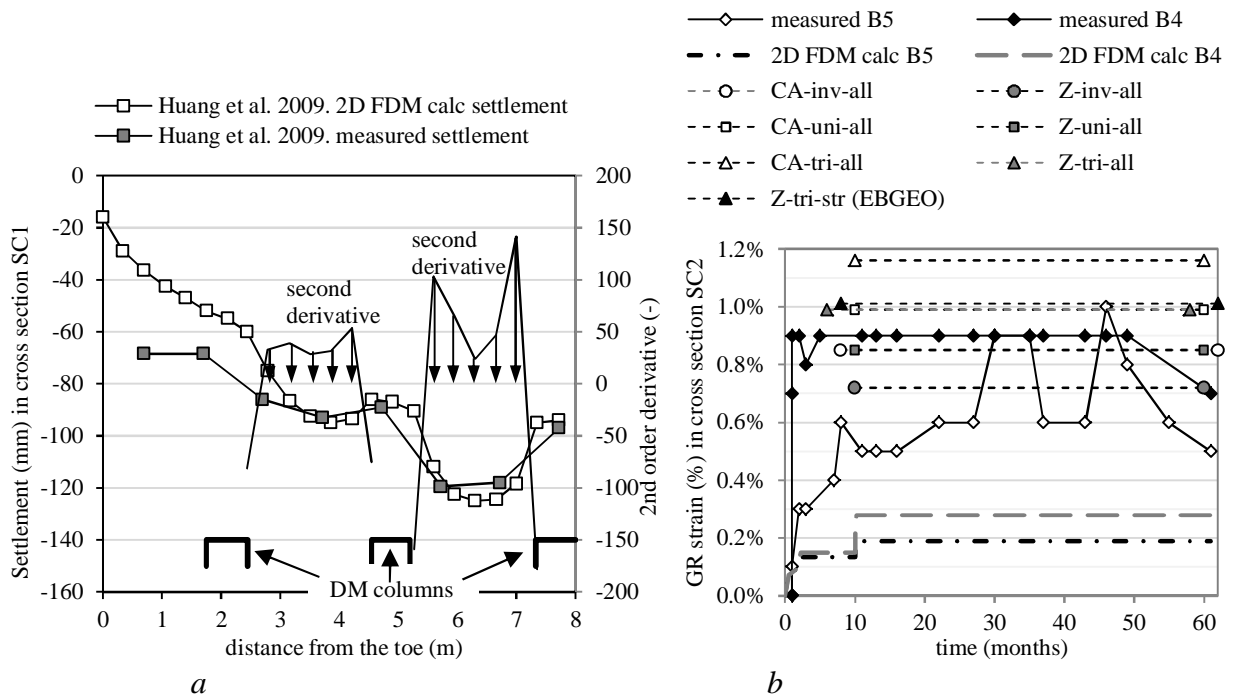
Figure 5.21 Finland. Measured and calculated (*a*) settlement at the base of the embankment in cross-section SC1 and (*b*) maximum GR strains. The left-hand picture also gives the second-order derivative of the FDM-calculated settlement; this is linearly related to the load distribution on the GR. Measurements and FDM calculations from Huang et al. (2009).

5.4.7 The Krimpenerwaard N210 piled embankment

Table 5.17 Average of the GR strains measured in 2010 and calculated GR strains in the N210 Krimpenerwaard road, the Netherlands (Haring et al., 2008; Van Duijnen, 2014).

average of measurements			calculations		Z-tri-str[b]	Z-tri-all	Z-uni-all	Z-inv-all	CA-tri-all	CA-uni-all	CA-inv-all
		%		sub-grade kN/m³	%	%	%	%	%	%	%
longitudinal[a]	pile cap	1.10	longitudinal[a]	0	1.43	1.43	1.23	1.06	1.30	1.13	0.96
	between piles	0.60		250	0.72	0.35	0.31	0.43	0.28	0.26	0.38
tranverse taking into account both GR layers	pile cap	1.00	tranverse taking into account both GR layers	0	1.32	1.32	1.14	0.98	1.21	1.04	0.89
	between piles	2.40		250	0.71	0.34	0.30	0.41	0.28	0.25	0.36
tranverse taking into account 1 GR layer[a]	pile cap	1.00	tranverse taking into account 1 GR layer[a]	0	2.03	2.03	1.76	1.51	1.85	1.60	1.38
	between piles	2.40		250	0.92	0.39	0.37	0.57	0.31	0.31	0.50

[a] These cases are included in Figure 5.27. [b] model in EBGEO (2010) and CUR226 (2010)

Table 5.17 shows that the measured GR strains exceed the calculated values. If the calculations are repeated with no subsoil ($k = 0$ kN/m³), the agreement between measurements and calculations improves. The GR installation was difficult for reasons explained in Chapter 5.3.7. Otherwise, no explanation for the discrepancy between measurements and calculations could be found.

5.4.8 Hamburg full-scale test

Figure 5.22 compares the measured and calculated GR strains. The figure shows that the stiff subsoil results in larger GR strains for the inverse triangular load distribution than the uniformly or triangular load distribution. An explanation is given in Chapter 5.4.5.
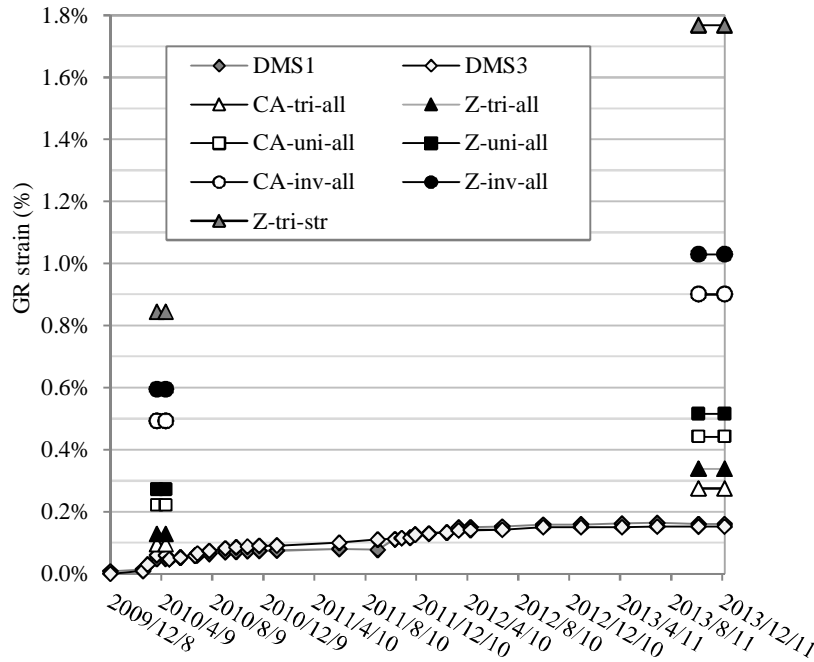
Figure 5.22 Comparison of measured and calculated maximum GR strains in the full-scale field test in Hamburg (Weihbrauch, 2010, 2013).

5.4.9   Sloan's large-scale experiments (2011)

Sloan et al. (2011) described five tests. The present paper considers the third and the fourth. In the second test, the same wire extensometers (ε) were applied as in the later tests to measure GR strains. In the second test, however, strains of up to 22% were measured. This must have been a wrong measurement because the GR would have ruptured at that GR strain. Sloan made some changes in the measurement system and believed that the strain measurements were reliable in the rest of the tests.

The tests used PP reinforcement. PP creeps. When PP reinforcement is loaded and not supported, as in these tests, it is expected that the reinforcement will creep. Figure 5.23 confirms this. Seven days after dissolving the EPS, just before the loading with the small truck, the reinforcement was still creeping by 0.15 to 0.35% per day. After loading on day 7, creep actually accelerated. The reinforcement did not stop creeping before the end of the test. The tests are therefore not very suitable for comparison with analytical calculations and will therefore not be included in the discussion in Chapter 5.5.

However, Figure 5.23 compares the measured GR strains with analytical calculations. The measured GR strains match *CA-tri* or *Z-uni* best in test CSE#3 and *CA-inv* in test CSE#4.

a. Test CSE#3 (H = 1.86 m)   *b. Test CSE#4 (H = 2.29 m)*
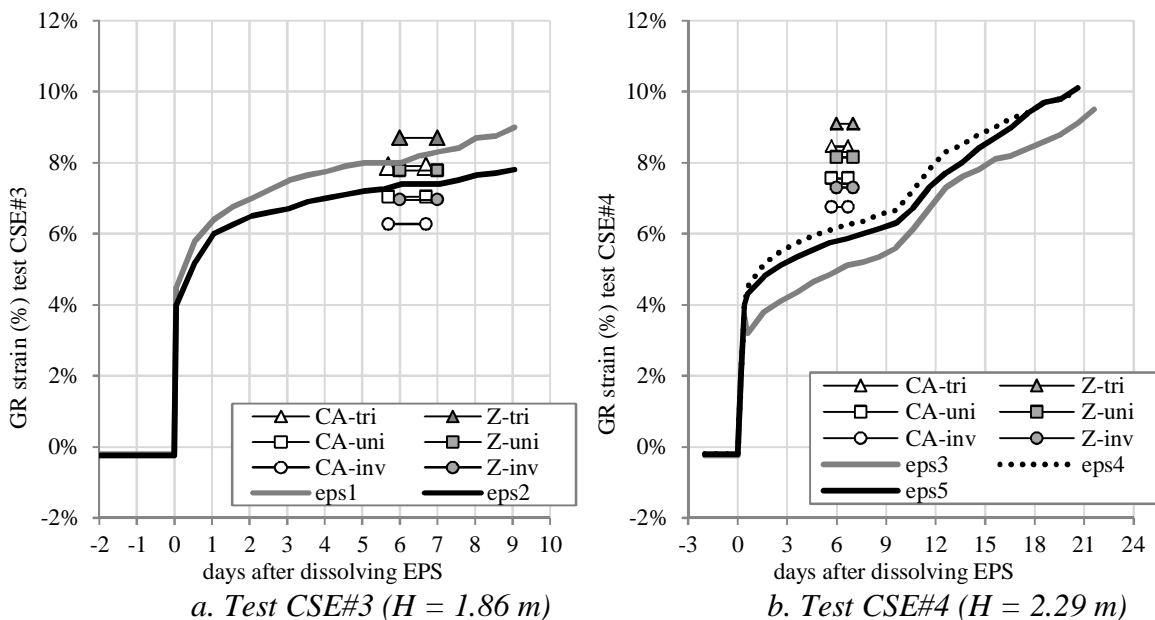
Figure 5.23 GR strains (%), comparison between measurements of Sloan (2011) and calculations.

5.4.10 Oh and Shin's scaled tests (2007)

Within 2 days after the installation of the last layer of the embankment, settlement attained the maximum values and remained constant. Table 5.18 and Figure 5.24 compare the measured and calculated GR strains. The 'maximum' strains were measured on top of the small pile caps. The 'minimum' strains were measured between adjacent piles. These results show that the predictions with 'all subsoil' are nearly the same for the CA and the Zaeske models. Consequently, the Zaeske predictions are not shown in Figure 5.24. The *inv* models follow the tendency of the measurements best. The strip subsoil models predict GR strains that are too high.

Table 5.18 Measured and calculated GR strains in Korea (Oh and Shin, 2007).

ctc distance s_x	GR strain	mea- sured	*Z-tri- str*	*Z-tri- all*	*Z-uni- all*	*Z-inv- all*	*HR- uni-str*	*CA- tri-all*	*CA- uni-all*	*CA- inv-all*
m		%	%	%	%	%	%	%	%	%
0.95	max	3.36	10.05	2.70	2.95	4.80	10.19	2.70	2.95	4.80
0.75	max	2.44	6.87	2.88	2.62	3.50	6.71	2.93	2.66	3.54
0.60	max	0.96	4.61	2.62	2.21	2.48	4.29	2.71	2.28	2.55
0.95	min	1.50	8.62	2.61	2.37	3.47	7.80	2.61	2.37	3.47
0.75	min	1.50	6.15	2.76	2.24	2.75	5.56	2.80	2.28	2.78
0.60	min	0.68	4.27	2.52	1.98	2.09	3.78	2.59	2.05	2.14
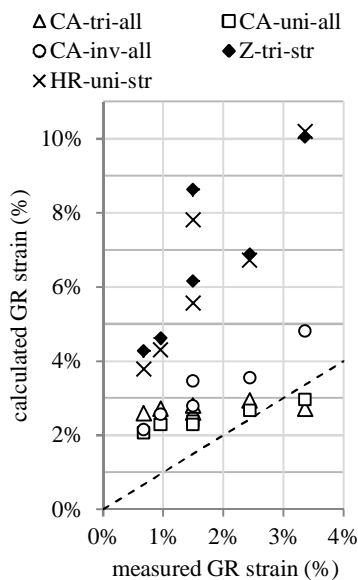
Figure 5.24 Comparison of measured and calculated GR strains (%) for Oh and Shin's scaled model experiments (2007).

5.4.11 German laboratory scaled experiments

Zaeske (2001) and Kempfert et al. (1999, 2004) showed that the largest GR strains were found in and along the GR strip. The maximum was found close to the pile cap, in other words with strain gauge $\varepsilon0$ (see Figure 5.13). Figure 5.25 therefore gives the measurements with $\varepsilon0$ for Zaeske's tests 5 and 7, as presented in his Figures 4.21 and 5.12 (2001). The results for tests 6 and 8 show a comparable match between measurements and calculations.

It should be noted that the measurements in Zaeske's Figures 4.21 and 5.12 do not match the measurements in Zaeske's Figure 6.19 and Figure 6 in Kempfert et al. (2004). The authors of the present paper are of the opinion that these last two figures contain some mistakes and that figures 4.21 and 5.12 give the correct measurements.
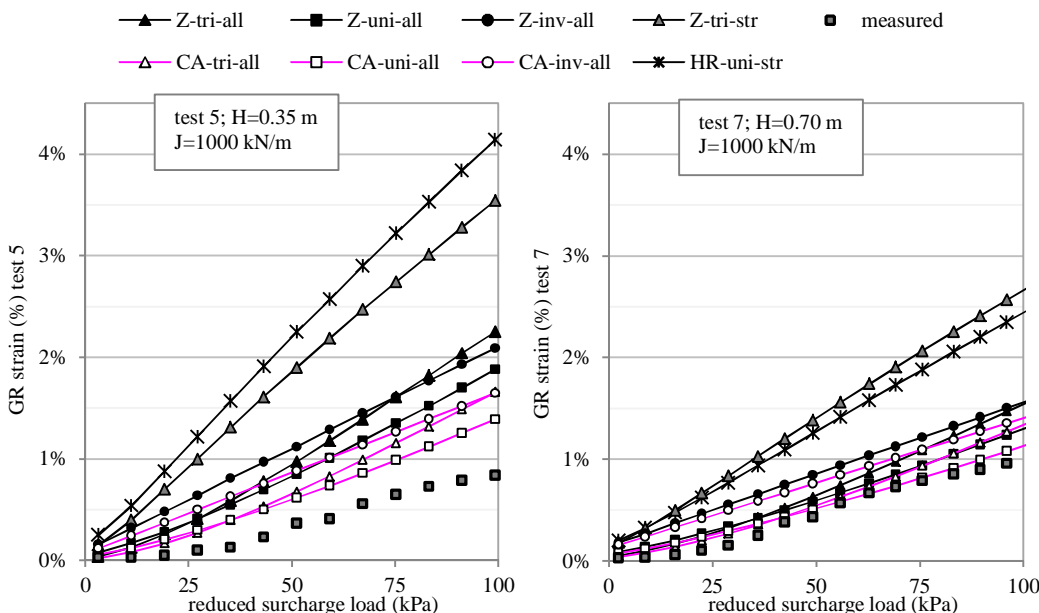
Figure 5.25 GR strains (%), comparison between calculations and measurements with strain gauge $\varepsilon0$ (see Figure 5.13) in Zaeske's laboratory experiments (2001). The surcharge load in the calculations was 80% of the applied surcharge load to compensate for the friction between the test box walls and the sand fill. This reduced load is also given on the horizontal axis.

The figure shows that *Z-tri-str* (adopted in EBGEO and CUR) and *HR-uni-str* give greater GR strains than measured. Extension of the subsoil support to 'all subsoil' improves the prediction considerably. The CA model results in a better match than the Zaeske model. These tests have a relatively stiff subsoil. As explained in Chapter 5.4.5, the uniformly distributed load distribution results in the best match with the measurement, and the inverse triangular load distribution gives larger strains.

5.4.12 Dutch laboratory scaled experiments

Van Eekelen et al. (2012a, b and 2013, Chapters 2, 3 and 4 of this thesis) considered step 1 and step 2 separately. Van Eekelen et al. (2012a, adopted in Chapter 2 of this thesis) showed that decreasing subsoil support gives an increase in arching. This has not been found by any limit-state arching model. However, Van Eekelen et al. (2013, Chapter 4 of this thesis) showed that the CA model matches the measured load distribution better than the Zaeske model.

Van Eekelen et al. (2012b, Chapter 3 of this thesis) considered step 2 and showed that the measured GR strain matches the GR strain calculated with the inverse triangular load distribution and taking all the subsoil into account better.
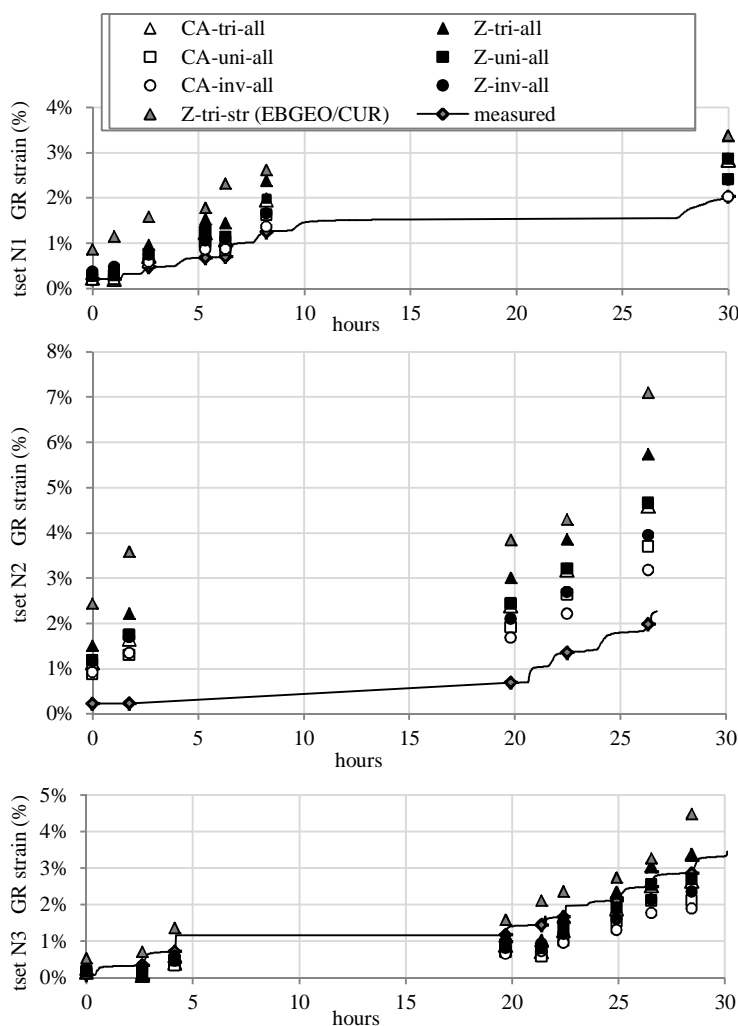
Figure 5.26 GR strains (%), comparison between calculations and measurements in the Dutch laboratory experiments of Van Eekelen et al. (2012a, Chapter 2 of this thesis).

Figure 5.26 compares the measured and calculated GR strains for three experiments in which strain gauges were used. The figure shows that *CA-inv-all* matches the first two tests best. This was not the case for the third test. No explanation was found.

5.5   Discussion

Figure 5.27 and Figure 5.28 compare the measurements presented above with six combinations of calculation methods, explained in Table 5.13. The tests with a cohesive fill (Almeida et al., 2007 and Briançon and Simon, 2012) have been included, even though they are less comparable with the analytical models developed for non-cohesive fill.

Figure 5.27*e* and *f* show that *Z-tri-str* and *HR-uni-str* match the measurements least. These models overestimate the measurements with average 146% and 189%, as shown by the trendlines given in Figure 5.27. Figure 5.27 also shows that the Concentric Arches model (figures *a* and *b)* matches the measurements better than the Zaeske arching model (figures *c* and *d).* The average overestimation of the CA model is 16-34%, the average overestimation of the Zaeske model is 24-42%. At low friction angles, the Zaeske model generally gives higher GR strains than measured. At high friction angles, the Zaeske model gives lower GR strains than measured. This is in accordance with the findings of Van der Peet (2014) and Van der Peet and Van Eekelen (2014). They showed that the increase of arching with increasing friction angle in 3D finite-element calculations matches the CA model, while the arching in the Zaeske model increases much more strongly with increasing friction angle.

The cases with no or nearly no subsoil support are most critical as the highest GR strains will occur in relative terms. Figure 5.28 therefore shows only these cases. From this figure, it can be concluded that *CA-inv-all* matches the measurements best. Thus, the inverse triangular load distribution gives the best prediction of the GR strain. This is explained as follows. If the GR sags, the deflection is larger midway between the piles than close to the piles. The load is always attracted to stiffer elements. This is arching. A large part of the load is therefore attracted to the pile directly. However, a relatively large part is also attracted to the parts of the GR close to the piles, which sags less and therefore seems to be stiffer.
Figure 5.27 shows that the uniformly distributed load matches the measurements for the cases with subsoil support best. This is explained as follows. The differences in deflection between the different parts of the GR are smaller if the GR is partly supported by the subsoil. Less arching therefore occurs, and this is also true for the area between the piles, resulting in a more evenly distributed load.

The combination of this uniformly distributed load and counter-pressure from below results in a net load that matches the inverse triangular load distribution best, as shown in Figure 5.19. In the cases where the subsoil is very stiff, the inverse triangular load distribution results in less GR deflection in the centre between piles than it is close to the pile cap edges, as can be seen in Figure 5.18.
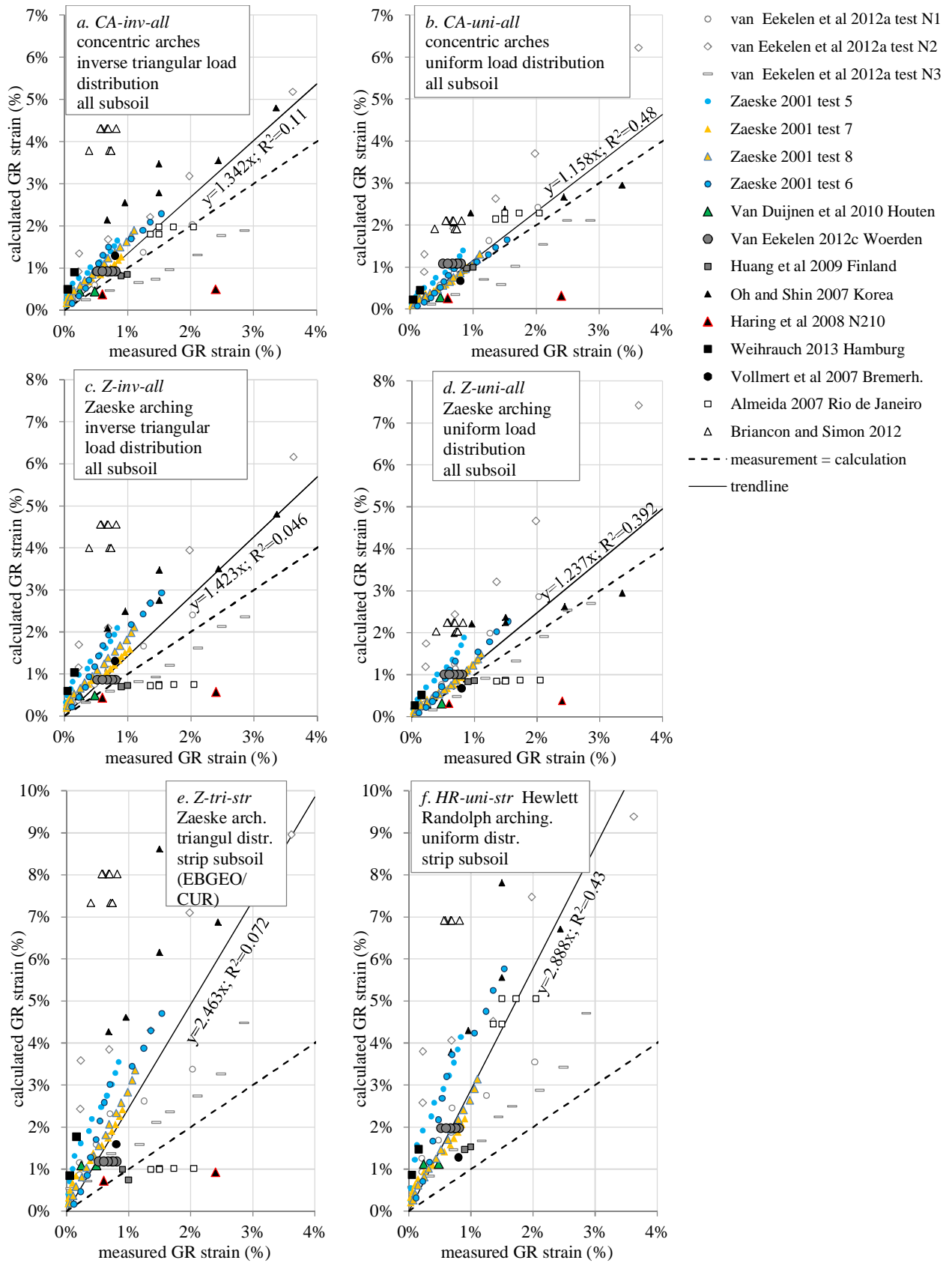
Figure 5.27 Comparison of measured GR strains with results of analytical calculations, including trend line through all data.
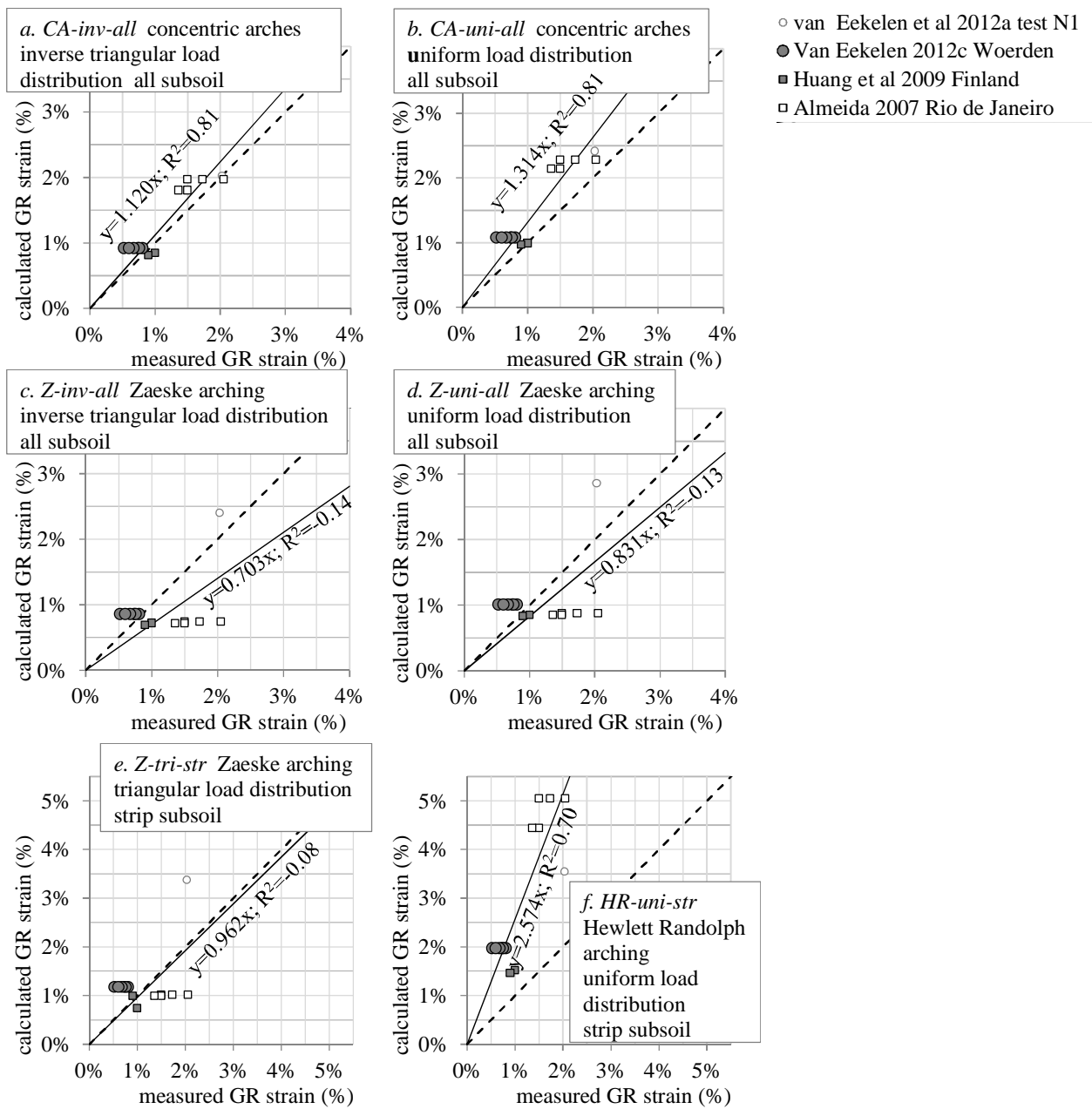
Figure 5.28 Comparison of measured GR strains with results of analytical calculations; only the cases without or nearly without subsoil support have been included.

This results in relatively large GR strains and therefore a relatively conservative design.

It is concluded that it is best to use an inverse triangular load distribution for the cases without, or with limited, subsoil support and a uniformly distributed load for the cases with substantial subsoil support. This can be elaborated by using the load distribution that gives the lowest value for the GR strain. In this way, a smooth transition is obtained from the situation with no subsoil support to the situation with a limited amount of subsoil support. And this gives the best match with the

measurements. Figure 5.29 shows that this choice results in an average overestimation of the measured values of 6%.
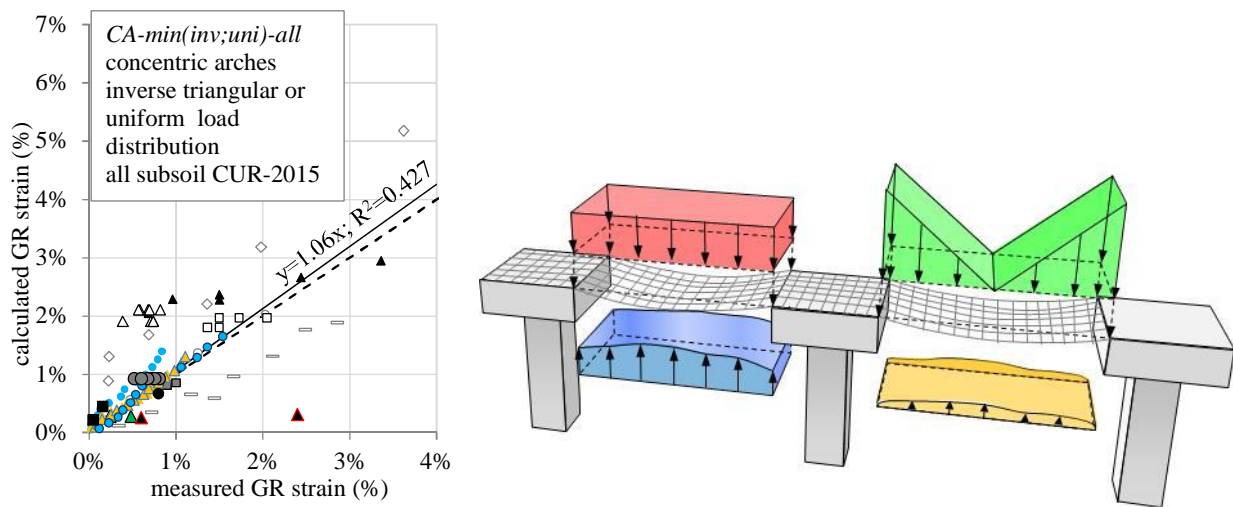
Figure 5.29 Comparison of measured GR strains with results of analytical calculations; Calculation model: the minimum of the values of *CA-inv-all* and *CA-uni-all*. This model has been adopted in CUR226 (2015). The legend of Figure 5.27also applies to this figure.

5.6   Dutch design guideline CUR226 (2015)

The Dutch CUR committee decided to amend the Dutch CUR 226 (2010) to produce CUR 226 (2015) using the Concentric Arches model in combination with all subsoil support and the load distribution that gives the lowest GR strain. In this way, the inverse triangular distribution is applicable for the cases without, or with limited, subsoil support and a uniformly distributed load in the cases with subsoil support. A probabilistic analysis is currently being carried out, leading to a model factor with a value between 1.10 and 1.25[18].

Van Eekelen et al. (2013, Chapter 4 of this thesis) give the equations of the Concentric Arches model; appendix 5.A gives the other equations.

5.7   Conclusions

This paper compares several analytical models for the design of basal reinforcement in a piled embankment with case studies from literature. Three parts of the analytical models have been varied: (1) the arching model (2) the load distribution on the GR strip between adjacent piles and (3) the subsoil support. The

---

[18] The probabilistic study has been reported in Van Duijnen et al., 2015. See also Chapter 6.4.4.

models considered were variations on and/or extensions to the models of Hewlett and Randolph (1988) and Zaeske (2001, also reported in Kempfert et al., 2004). Seven full-scale cases and four series of experiments have been summarised. Special attention was paid to the realistic determination of the soil parameters for the analytical calculations. Their values should be the best guess values (mean values), not the characteristic as in design practice. The current combination of analytical models in EBGEO and CUR226 is the arching model of Zaeske, a triangular load distribution and subsoil support below the GR strip only. BS8006 gives the option to use the combination of Hewlett and Randolph and a uniform load distribution as an alternative to the modified Marston and Anderson (1913) approach. These two combinations match the measurements least. They overestimate the measured strains respectively with average 146% and 189%.

The Concentric Arches model of Van Eekelen et al. (2013, Chapter 4 of this thesis) gives an average overestimation of the measured GR strains of 16 to 34%. For Zaeske's multi-scale arching model (2001) this is 24 to 42%. From this it can be concluded that the Concentric Arches model gives GR strains that match the measurements better than Zaeske's model (2001). This conclusion holds for any load distribution. At low fill-friction angles, Zaeske's arching model generally gives low arching, leading to higher GR strains than measured. At high friction angles, Zaeske's model gives relatively high arching levels, and therefore lower GR strains than measured. Van der Peet (2014) and Van der Peet and Van Eekelen (2014) also show that Zaeske's model gives low arching for low friction angles and relatively high arching for high friction angles by comparison with their 3D numerical analyses.

In conditions without subsoil support, the inverse triangular load distribution gives the best prediction of the GR strain. When subsoil support is considerable, the load on the GR strip is approximately uniformly distributed. This uniform load is combined with the counter-pressure that is directed upwards. This combination results in a *net* load distribution that matches an inverse triangular load distribution more than a uniform or triangular load distribution, as shown in Figure 5.19.

In the model presented by Zaeske (2001), only the subsoil underneath the GR strip between adjacent piles is taken into account. The authors have found it advisable to take all subsoil support into account. This is theoretically better, and it is also confirmed by the comparison between calculations and measurements described in the present paper.

The Dutch CUR committee decided to adapt the Dutch CUR 226 (2010) into CUR 226 (2015), using the Concentric Arches model in combination with all subsoil support and the load distribution that gives the lowest GR strain; either the inverse triangular load distribution or the uniformly distributed load.

Appendix 5.A Step 2 equations[19] for uniform and inverse-triangular load distribution

Uniform load distribution[20]
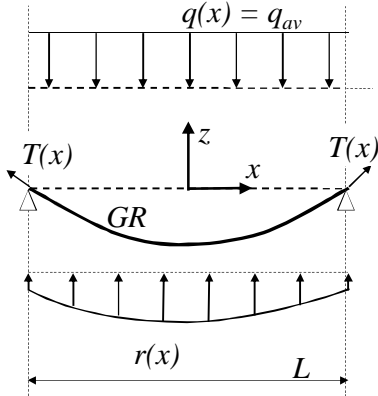
$$q_{uni}(x) = -q_{av}$$

$$z_{uni}(x) = -\frac{q_{av}}{K}\left(\frac{e^{\alpha x} + e^{-\alpha x}}{e^{\frac{1}{2}\alpha L} + e^{-\frac{1}{2}\alpha L}} - 1\right)$$

$$z_{uni}'(x) = -\frac{q_{av}\alpha}{K}\left(\frac{e^{\alpha x} - e^{-\alpha x}}{e^{\frac{1}{2}\alpha L} + e^{-\frac{1}{2}\alpha L}}\right)$$

(5.4)

Inverse triangle load distribution
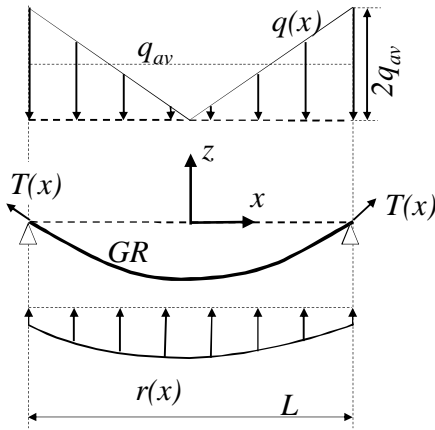
$$q_{inv}(x) = \frac{-4q_{av}}{L} \cdot x$$

$$z_{inv}(x) =$$
$$-\frac{2q_{av}}{KL\alpha}\left(Me^{\alpha x} + (M - 2)e^{-\alpha x} - 2\alpha x\right)$$

$$z_{inv}'(x) = -\frac{2q_{av}}{KL}\left(Me^{\alpha x} - (M - 2)e^{-\alpha x} - 2\right)$$

$$\text{where } M = \frac{L\alpha + 2e^{-\frac{1}{2}\alpha L}}{e^{\frac{1}{2}\alpha L} + e^{-\frac{1}{2}\alpha L}}$$

(5.5)

Without subsoil support ($K = 0$ kN/m^3):

$$z_{inv}(x) = -\frac{q_{av}L^2}{12T_H}\left(8\left(\frac{x}{L}\right)^3 - 1\right)$$

$$z_{inv}'(x) = -\frac{2q_{av}L}{T_H} \cdot \left(\frac{x}{L}\right)^2$$

---

[19] Appendix B of this thesis gives design graphs which can be used instead of these equations.
[20] The load distribution that gives the smallest GR strain should be used: this will be either the inverse triangular or the uniformly distributed load distribution.

Where $z(x)$ (m) is the GR deflection, $z'(x)$ its derivative, L (m) is the clear distance between adjacent pile caps ($L_x = s_x - a_{eq}$ and $L_y = s_y - a_{eq}$), T_H is the horizontal component of the tensile force $T(x)$ in the GR strip and α^2 (m^{-2}) is given by:

$$\alpha^2 = \frac{K}{T_H} \tag{5.6}$$

Where the subgrade reaction coefficient k (kN/m^3) is changed as follows into K (kN/m^3) to take into account all subsoil support (following Lodder et al., 2012 and Van Eekelen et al., 2012b, adopted in Chapter 2 of this thesis):

$$K = \frac{A_{L_{x,y}} \cdot k}{L_{x,y} \cdot a_{eq}} \tag{5.7}$$

Where $a_{eq} = B_{ers}$ (m) is the width of the square pile cap or the equivalent width of the circular pile cap and $A_{Lx,y}$ (m^2) is the GR area belonging to a GR strip in x- or y direction:

$$A_{Lx} = \tfrac{1}{2} \cdot \left(s_x \cdot s_y \right) - \frac{d^2}{2} \cdot \arctan\left(\frac{s_y}{s_x} \right)$$

$$A_{Ly} = \tfrac{1}{2} \cdot \left(s_x \cdot s_y \right) - \frac{d^2}{2} \cdot \arctan\left(\frac{s_x}{s_y} \right) \tag{5.8}$$

with arctan in radials, d (m) is the pile cap diameter, $q(x)$ (kPa) is the distribution load on the GR strips between adjacent piles and q_{av} (kPa) is the average load on the GR strips:

$$q_{av} = \frac{B + C}{A_{GRstrip\ transversal} + A_{GRstrip\ longitudinal}} \tag{5.9}$$

Where $B+C$ (kN/pile) is the total vertical load on the geosynthetic reinforcement. This value can be calculated with the equations given in Van Eekelen et al., 2013. The tensile force $T(x)$ in the geosynthetic reinforcement (kN/m) can be calculated as:

$$T(x) = T_H \sqrt{1 + \left(z'(x) \right)^2}$$

$$\varepsilon(x) = \frac{T(x)}{J} \tag{5.10}$$

The maximum tensile force T_{max} occurs at the edge of the pile cap. The value of T_H can be solved by equalising the average geometric and constitutive strain:

$$\varepsilon_{geometric,average} = \frac{\int\limits_{x=0}^{x=\frac{1}{2}L} \sqrt{1 + \left(\frac{dz}{dx}\right)^2}\, dx - \frac{1}{2}L}{\frac{1}{2}L} =$$

$$\varepsilon_{constitutive,average} = \frac{\frac{1}{J}\int\limits_{x=0}^{x=\frac{1}{2}L} T(x)\, dx}{\frac{1}{2}L}$$

(5.11)

6 Discussion

6.1 Introduction

Several design methods for basal reinforced piled embankments were already available before the start of the research described here. They produce results that vary widely. Measurements that were published later – for example in Van Duijnen et al. (2010) and Van Eekelen et al. (2015a) – showed that the models in use in the European design guidelines overpredict GR strain and therefore there was room for improvement.

Chapter 1.2 showed that GR design includes two calculation steps: the arching behaviour in the fill (step 1) and the load-deflection behaviour of the GR (step 2). On the basis of scaled model experiments (Chapter 2, Van Eekelen et al., 2012a) suggestions were made for a new model for calculation step 2: an inverse triangular net load distribution on the GR strips and an extension of the subsoil support to 'all subsoil' (Chapter 3). An explanation was found for this inverse-triangular load distribution and the strong load concentration on the GR strips with the development of the new Concentric Arches (CA) Model (Chapter 4).

Chapter 5 compared the results of the new analytical model, and several existing models, with GR strains measured in eleven field monitoring projects or experiment series from the literature. These projects included the experiments reported in Chapter 2 and two field monitoring projects carried out as part of this research. The conclusion was that the CA model matches the measurements better than any of the other step 1 models. In conditions without subsoil support, the inverse triangular load distribution gives the best prediction of the GR strain. When subsoil support is considerable, the load on the GR strip is approximately uniformly distributed.

This discussion chapter answers the three research questions (Chapter 1.3) and discusses the research results.

6.2 How is the vertical load distributed on the basal reinforcement of a piled embankment?

6.2.1 Load distribution dependent on stiffness behaviour

In a uniform earth structure, the vertical pressure at a given depth is uniformly distributed. In a basal reinforced piled embankment, the vertical pressure at the GR level depends on the stiffness behaviour of the separate elements. The stiffer the element, or the less the element moves, the more load it attracts. This is arching.

Most of the conclusions in this chapter are based on observations in scaled model tests. Chapter 6.2.2 looks at whether scaled model tests can be sufficiently reliable to draw such conclusions about load distribution and arching.

The piles and pile caps are the stiffest elements and they therefore attract most load. This load part, which is transferred to the pile caps directly, is called 'load part *A*' or 'arching *A*' in this thesis and depends on several features, as described in Chapter 4. The scaled experiments showed that one major factor that has an influence is subsoil support (Chapter 2.4.1): decreasing subsoil support results in more GR deflection, less load on the GR and more arching *A*. This is in line with the idea that less stiff behaviour attracts less load.
The experiments also showed that the load is attracted to stiffer elements more efficiently if the fill is stronger; the arching is more efficient for higher friction angles φ (Chapter 2.5.1) and embankments with a larger fill height H (Chapter 4.3.3).

The GR strips between adjacent piles behave relatively stiffly because the span between adjacent piles is relatively small. Additionally, some GR types are biaxial or uniaxial and are stiffer along the GR strips than, for example, diagonally. Consequently, the GR strips behave more stiffly than the surrounding GR and the GR strips therefore attract much more load than the surrounding GR. This load concentration on the GR strips was measured by Zaeske (2001, see Figure 4.6) and proven with 3D numerical calculations (Figure 6.2). This effect is clearest in the cases with little or no subsoil support.

The load distribution on the GR strips depends on the GR deflection. The areas with the least GR deflection attract most load. The GR close to the pile caps is deflected least, because the deflection is limited by the unmoving pile cap. This location therefore attracts more load than the locations further away from the pile cap and so the highest pressures are found alongside the pile cap, with the lowest pressures on the GR strip being found at the central point between the pile caps. If there is no subsoil support, the GR at the central point between the pile caps sags

most and therefore attracts the least load. However, if there is subsoil support, the GR at the central point will sag less, and the GR sags more evenly, and the load will be distributed more uniformly. The uniform load is combined with the counter-pressure that is directed upwards, resulting in a *net* load distribution that matches a parabola-like load distribution as shown in Figure 5.19.

The load distribution can be studied by directly measuring the load at several places, as shown in Figure 4.7, or by calculating it with numerical methods, as in Han et al. (2012), Den Boogert et al. (2012a, b) and Van der Peet and Van Eekelen (2014). They indeed found inverse-triangular-like distributions on the GR strips. However, it is often more practical to use the measured shape of the deformed GR, as this is easier to measure and there is a linear relationship between the net load distribution on the GR strips and the second derivative of the measured shape of the deformed GR strip (equation (3.27)). This second derivative can be determined from the measured GR deflection in field tests, numerical calculations and experiments.

Figure 5.21 compares the field measurements and FDM results of Huang et al. (2009). The figure shows that the calculated GR deflection matches the measured values well. The second derivative of their calculated GR shape, and therefore the corresponding load distribution, matches the inverse triangle quite well.

Figure 5.17 shows the second derivative of the measured GR shape in the Woerden field test and it is approximately inverse triangular.

Figure 6.1 shows the measured GR deflection during our test T2 (see Table 2.1 for the test specifications), or more precisely, the difference between the scanned positions of the sand layer below the GR before and after the test. Figure 6.1*c* shows the GR deflection in the cross-section lines in Figure 6.1*b*. Figure 6.1*c* gives the second derivative of the GR positions in these cross-sections.

The figure shows that the net load distribution for cross-sections a-a, d-d and e-e matches an inverse triangular load distribution more than a uniform or triangular load distribution. The load distribution, however, is even more parabola-like and the load is concentrated more near the pile caps than the inverse triangle indicates. Section 0 discusses the difference between parabola-like and inverse triangular shapes and concludes that the difference for the GR strain is negligible.

Figure 6.1 also shows that the load distribution is approximately uniformly zero in cross-sections b-b and c-c.
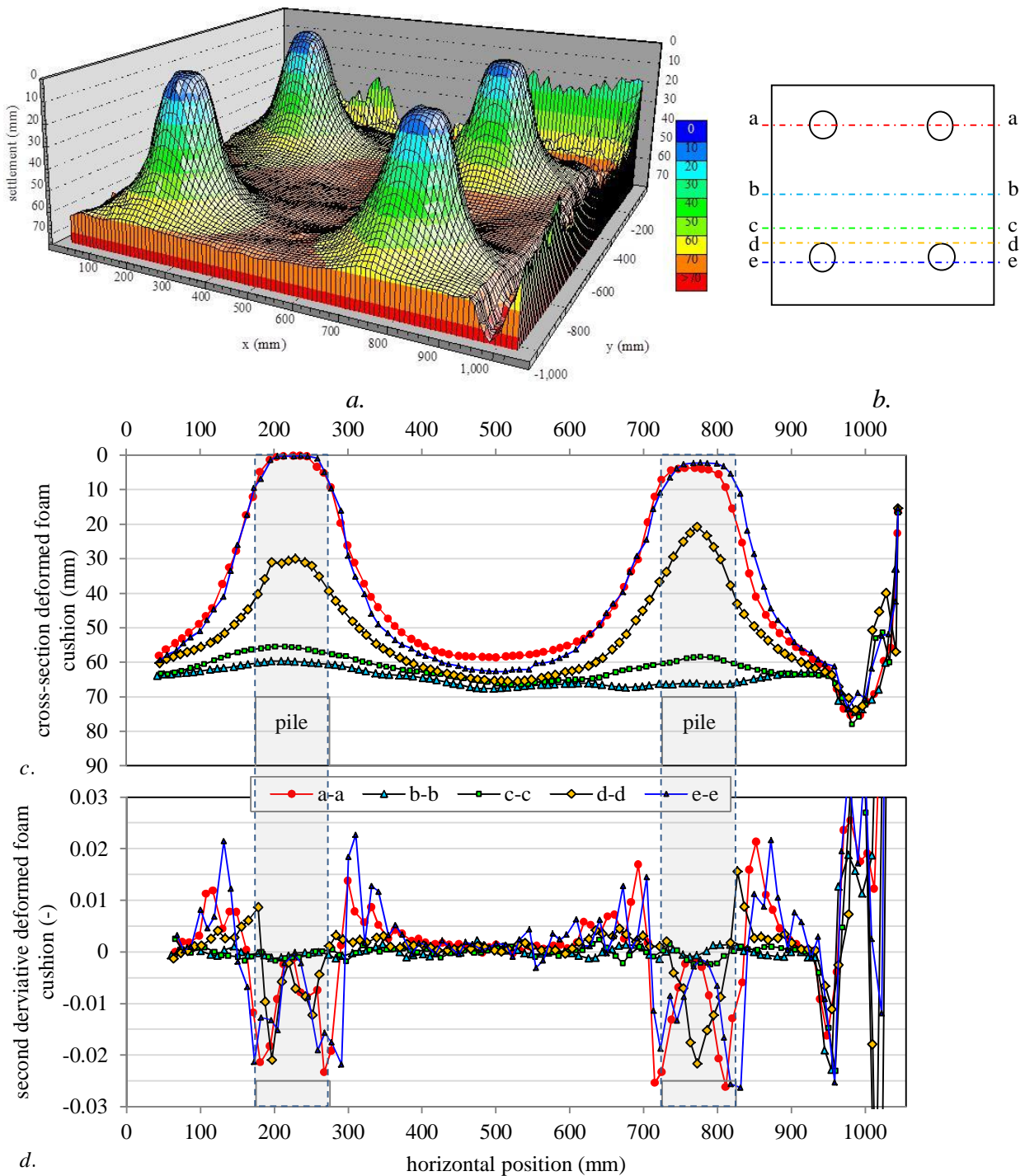
Figure 6.1 Measured GR deflection test T2, 3D scan results, change in the sand layer below the GR layer. (*a*) 3D scan result of GR position, (*b*) position of cross-sections, (*c*) cross-sections with GR positions, (*d*) second derivative of GR positions in cross-sections.

The load distribution described in this chapter is confirmed by the 3D numerical calculations of Van der Peet and Van Eekelen (2014) (see Figure 6.2). This figure shows the situation without subsoil support. The figure shows that most load is exerted on the pile, and most of the rest of the load is exerted on the GR strips, on which more load is exerted close to the piles than in the centre.
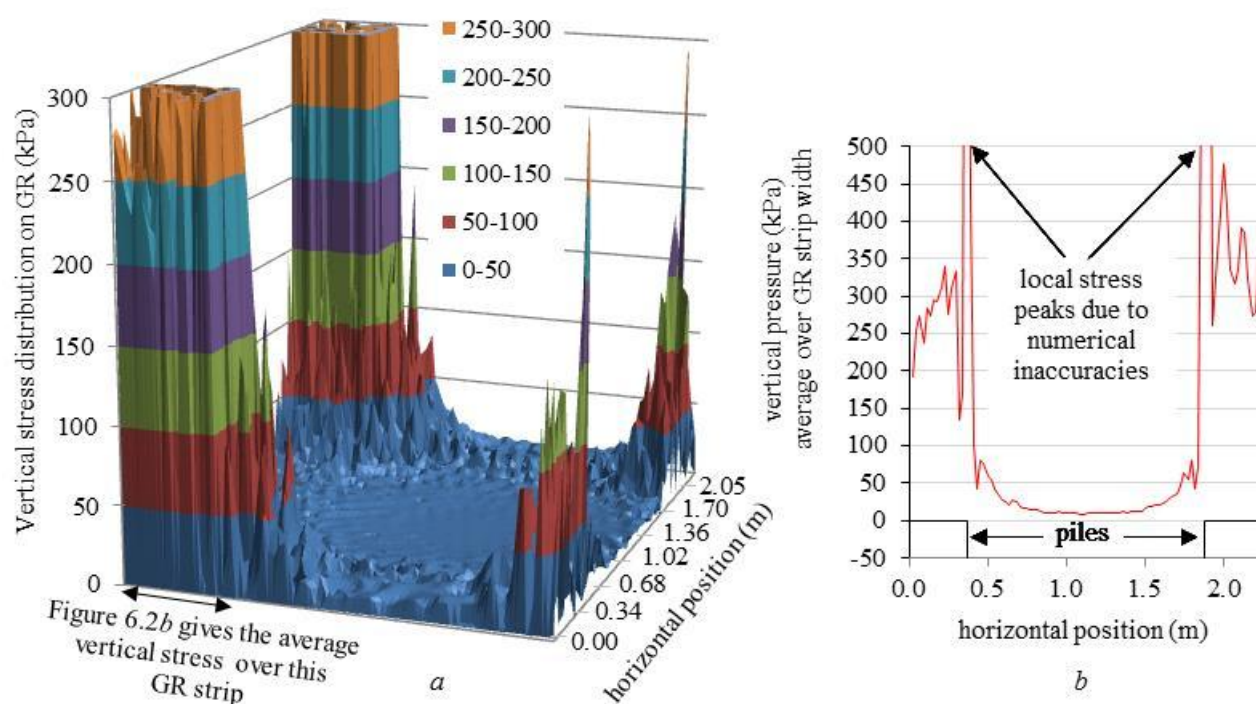
Figure 6.2 Results of the 3D numerical analysis (*a*) vertical stress distribution on the basal reinforcement (GR), (*b*) average vertical stress over the width of the GR strip indicated in (*a*). The figure shows a concentration of load on the GR strips between adjacent piles and more load closer to the piles. Source: Van der Peet and Van Eekelen (2014). The GR strips to the left, rear and front are shown; the GR strip to the right is not[21]

The load distribution is different if the subsoil support plays a role permanently: the load transferred directly to the pile cap (*A*) will be lower and the load distribution on the GR strips will be more uniform. If the GR is relatively stiff compared to the subsoil, the load will still be localised on the GR strips. If the GR is relatively flexible compared to the subsoil – a situation that is comparable with a piled embankment without GR – the load on the subsoil will be distributed more or less uniformly on the entire area between the four piles (Figure 4.6) and *A* will be much lower. The analytical model proposed in this thesis is applicable only to basal reinforced piled embankments.

---

[21] Note that the value of the vertical stresses in Figure 6.2 is limited to 300 kPa to give a clear picture, although FEM calculations of basal reinforced piled embankments give numerical inaccuracies resulting in stress peaks along the edges of the pile caps, as shown in Figure 6.2*b*. The stress peaks can be reduced considerably by reducing the element size in the calculations or accepted error. Van der Peet (2014) chose a mesh that balanced sufficient accuracy with an acceptable calculation time. Moreover, the visualisation in Figure 6.2 uses values in a square grid that have been interpolated from the tetrahedron-element stress points. This interpolation process means that the numerical inaccuracies play a grater role in the visualisation. Van der Peet and Van Eekelen (2014) included the stress peaks in the relevant stress points in their quantitative analysis and they argue that their results are sufficiently reliable.

6.2.2 Are scaled experiments sufficiently accurate to analyse basal reinforced piled embankments?

The scaled experiments presented in Chapters 2 and 4.2 were carried out without scaling the stresses. The shear modulus G of the fill was therefore not scaled in the tests, and so the model and the prototype behaved in the same way, and complications due to stress-dependent behaviour were avoided. This was possible because the fill weight is negligible by comparison with the applied surcharge load. The GR stiffness therefore scales with the length, and not with the length squared, contrary to suggestions made by, for example, Demerdash (1996).

The centre-to-centre pile distances applied in Dutch practice are currently between 0.90 and 2.50 m. The centre-to-centre distance for the piles in the experiments was 0.55 m and so the test set-up was scaled by a factor 1.6 to 4.5 by comparison with field applications (the prototype).

Table 6.1 gives the scaling rules between the tests and the prototype. The strength and tensile modulus are scaled down by a factor of $1 : x$, while the mesh size of each geogrid was kept constant. This may have affected the load transfer on top of the piles.

Table 6.1 Scaling rules.

			test/prototype scale 1:x
length		m	$1 : x$
area	length · length	m^2	$1 : x^2$
stress	force / area	kPa	$1 : 1$
force[a]	stress x area	kN	$1 : x^2$
tensile stiffness[b]	force / length	kN/m	$1 : x$
tensile strength[b]	force / length	kN/m	$1 : x$
deflection/distance between the piles	length / length	m/m	$1 : 1$

[a] 'Force' refers to the force on the pile head.

[b] Tensile strain and strength refer to the geosynthetic.

Table 6.2 Example scale 1:3.

		Test	Prototype
model box		1.1 x 1.1 m^2	3.3 x 3.3 m^2
diameter piles	d	0.1 m	0.3 m
centre-to-centre distance piles	s_x, s_y	0.55 m	1.65 m
embankment height	H	0.42 m	1.26 m
maximal top load	P	50 - 100 kPa	50 - 100 kPa
GR strength (in test K2)		135 kN/m	405 kN/m
GR stiffness ($J_{2\%}$ in test K2)	$J_{2\%}$	2269 kN/m	6807 kN/m

Table 6.3 Scaling surcharge load and determination prototype static traffic load.

	Test	Prototype
surcharge load	100 kPa	100 kPa
weight fill $\gamma \cdot H$	20·0.42 = 8.4 kPa	20·1.26 = 25.2 kPa
traffic load[a] p		100 – 25.2 + 8.4 = 83.2 kPa

[a] If full arching is reached, the prototype can also be a larger embankment with less traffic load.

Table 6.2 shows the dimensions of a test set-up with a scale of 1:3. It is not necessary to use these scaling rules for calculations when analysing the test series. If the calculation model is correct, it should work for both prototype and model dimensions.

The surcharge load p in the tests was increased to 50, 75 or 100 kPa.
Table 6.3 compares a maximum surcharge load of 100 kPa with the prototype surcharge load. The stresses at the GR level should be the same, and it is assumed that the transient traffic load can be modelled with a static load. Heitz (2006) indicates that the situation may be different for cyclic loading.

On this basis, it can be concluded that the experiments were indeed carried out with a realistic average stress at the GR level, which makes the experiments sufficiently accurate for use in piled embankment analysis. Van Eekelen and Bezuijen (2012b) discuss this issue further.

6.2.3 Pile spacing limitations

When the distance between the pile caps becomes too large, the arching is less efficient, as shown by Hong et al. (2014) with field measurements on a 2D piled embankment without GR. They showed that a 'stand-alone' pile attracts less load than a pile in a pile group and explain this by distinguishing between arching for pile groups and "punching" for stand-alone piles.

Their results show that the applicability of the CA model should be limited to situations where the distance between the piles is comparable with those applied in the cases considered in this study[22].

---

[22] Up to 2.50 m.

6.3 How can the load distribution be explained and how can it be described with an analytical arching model?

6.3.1 Arching in a basal reinforced piled embankment

This chapter explains the observed inverse-triangular load distribution on the GR strips and the concentration of load on the GR strips. Furthermore, it describes how the CA model follows this explanation.

Arching occurs around an area that settles more than the adjacent area. The load on the area that settles most decreases and the load on the adjacent area, which settles less, increases at the same time. The principal stress directions around the area that settles most follow approximately circular or elliptical shapes as shown in Figure 6.3 and Figure 6.4.

a   *b*

Figure 6.3 Comparison of principal stress directions above a GR strip between adjacent piles *(a)* Concentric Arches model and *(b)* 3D numerical analysis. Source of figure *(a)*: Van Eekelen et al. (2013) and Figure 4.9. Source of figure *(b)*: Van der Peet and Van Eekelen (2014).

GR usually deforms in smooth curves, with the maximum deflection in the centre between piles. Each GR part that settles more than its neighbour receives less load than its neighbour. The CA model describes this behaviour with a set of concentric arches. The larger the arch around a settling area, the more load it exerts on its subsurface. The arches give the directions of the principal stresses. 3D numerical analyses confirm the idea of principal stresses that follow concentric arches and exert an increasing load on the GR with increasing arch size (Figure 6.3). Chapter 4.4.2 describes how the concentric arches develop as a result of ongoing GR deflection.

The load exerted on the GR between the piles concentrates on the GR strips. This can be explained by imagining hemispherical stress paths between each group of four piles. The loads are transported along these hemispheres outwards, towards the stiffer piles, the stiffer GR strips and the stiffer intersection planes between the hemispheres of adjacent pile units. Above the GR strips the hemispheres intersect, and the loads are forced to follow a new path, along 2D arches, towards the piles. These 2D arches are loaded relatively heavily and exert part of their load on their ground surface: the GR strips.

This mechanism of transport of load along hemispheres and 2D arches in the hemisphere intersection plane is modelled with the CA model, which combines 3D hemispheres and 2D arches. The CA model is explained and shown in Figure 4.10 and Figure 4.11. Its combination of 2D and 3D concentric Arches results in a load distribution comparable to the one described in the previous chapter, as shown in Figure 4.19.

The Concentric Arches model is an improvement on the existing arching models listed in Chapter 4.1, because none of these existing analytical models describe the load and strain localisation on and in the GR strips. Furthermore, the CA model provides us with an explanation for the approximately inverse triangular load distribution on the GR strips. And, finally, the existing arching models tend to under-predict measured values of arching *A* in many cases, while the Concentric Arching model matches these measurements well. This has been shown in Chapters 4.3 and 5.5.

6.3.2 Partial arching

Partial arching occurs when an embankment is thin by comparison with the pile spacing, see Figure A.5 in the appendix. In that case, the arching cannot develop fully and a relatively large part of the surcharge load will be transferred to the GR and its subsoil directly.

If the embankment is very thin by comparison with the pile spacing, it is expected that the pile is 'not felt' in the centre between the four piles. This would result in a pressure on the GR at that location that approaches the undisturbed pressure $\gamma H + p$. The piles themselves attract a load higher than $\gamma H + p$. This means that the pressure must decrease somewhere between the centre point between the four piles and the piles. This theory is not confirmed by the 3D numerical analysis of Van der Peet (2014) as shown in Figure 6.4; she found that the pressure close to the piles and (not shown in Figure 6.4) close to the GR strips is larger than the pressure in the centre point between the four piles.
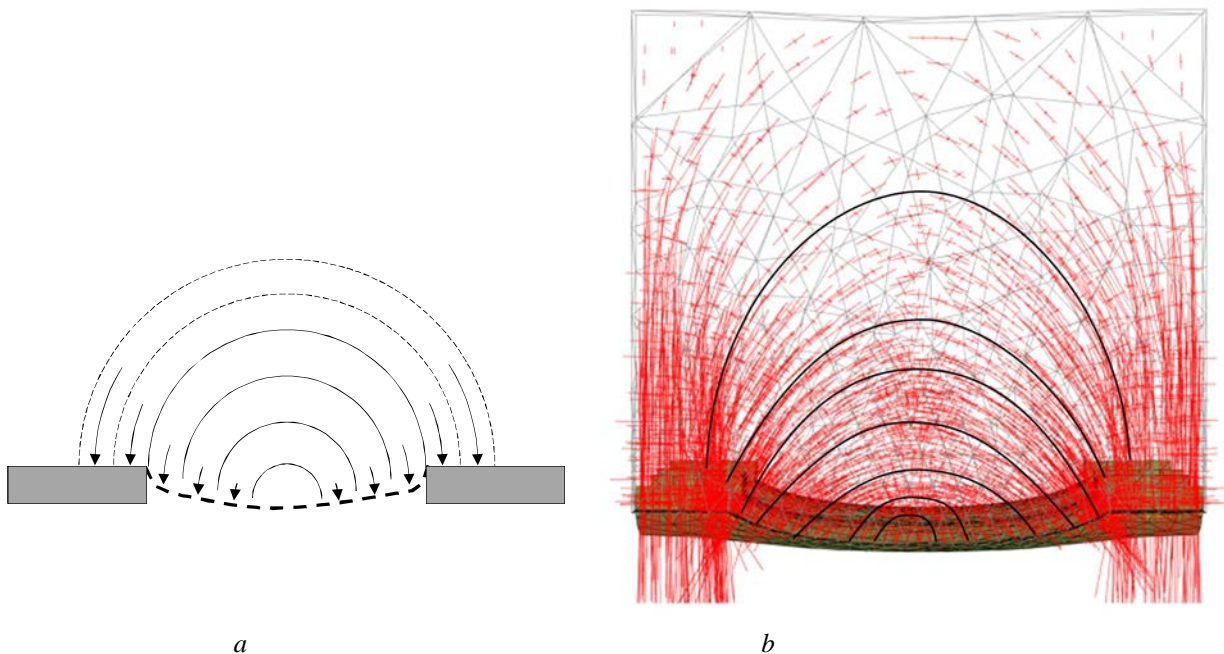
a   *b*
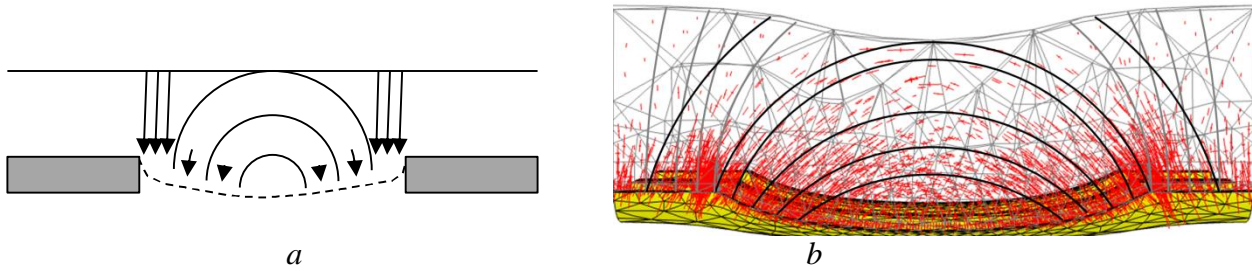
Figure 6.4 Partial arching. Comparison of principal stress directions above a GR strip between adjacent piles (*a*) Concentric Arches model and (*b*) 3D numerical analysis. Source of figure (*b*): Figure 4.28 of Van der Peet (2014).

The Concentric Arches model gives a solution for partial arching that follows the findings of Van der Peet (2014): stress release occurs on the centre part of the GR square, $L_{x3D} \cdot L_{x3D}$ in Figure 4.22, which is the area of the 3D hemispheres. The area between this square and the GR strips is loaded with the full load: $\gamma H + p$. This fully loaded area is indicated by $F_{GRsquare3}$ in Figure 4.22 and this area is also heavily loaded in the numerical calculations of Van der Peet. No field measurements are available yet to support the analytical model or the numerical calculations. However, the arching *A* calculated with this approach matches measured arching quite well (Figure 4.17 and Figure 4.18).

6.3.3   Arch shapes

Van der Peet (2014) and Van der Peet and Van Eekelen (2014) showed numerically that the principal stresses do not always follow circular arches (see Figure 6.3 and Figure 6.4). The arch in Figure 6.3 resting on the corners of the piles is semi-circular: it has the same radius in the vertical and horizontal directions. The larger arches, which rest on top of the piles, are higher than they are wide, making them more elliptical than circular. The smaller arches, and also the arches in the thin embankment shown in Figure 6.4, are consistently wider than they are high. This is similar to the Zaeske model, in which the arches are wedges that are thicker in the middle than at the sides, as shown in Figure 4.3. Another feature of these results, however, resembles the concentric arches model: the smaller arches rest on the GR instead of the piles.

Van der Peet and Van Eekelen (2014) also show that similar arch shapes can be observed in a section between two piles that are linked by a diagonal rather than directly. In a section that overlaps the GR square, from the centre of a strip to the centre of another strip, the arches are less visible. This is partly because the stresses are lower and partly because the arches on the strips affect the arches on the GR square. This resembles the assumptions of the Concentric Arches model.

The CA model uses circular arches only, rather than wider arches for low arches and narrower arches for higher arches. The effect of this simplification of arch shapes is not known. However, Chapters 4.5 and 5 show that the CA model match measurements well for varying conditions.

6.3.4   Combination of 3D hemispheres and 2D arches

The CA model consists of a set of 3D hemispheres that intersect above the centre line of the GR strips. In this intersection plane, the hemispheres meet and support each other, resulting in an area with relatively large pressures. The hemispheres intersect in circular arches.

The load travels first along the 3D hemispheres and then continues along the 2D arches towards the pile caps. The 2D arches exert part of the load on their subsurface: the GR strips. The CA model assumes that the width of intersection plane with 2D arches is the same as the width of the GR strips. The 3D hemispheres are therefore 'cut' along the edges of the GR strips, as shown in Figure 6.5. Figure 6.5*a* shows the theoretical load transfer along the largest hemispheres and arches. Figure 6.5*b* shows the load transfer along smaller hemispheres and arches.

<center>*a*   *b*</center>
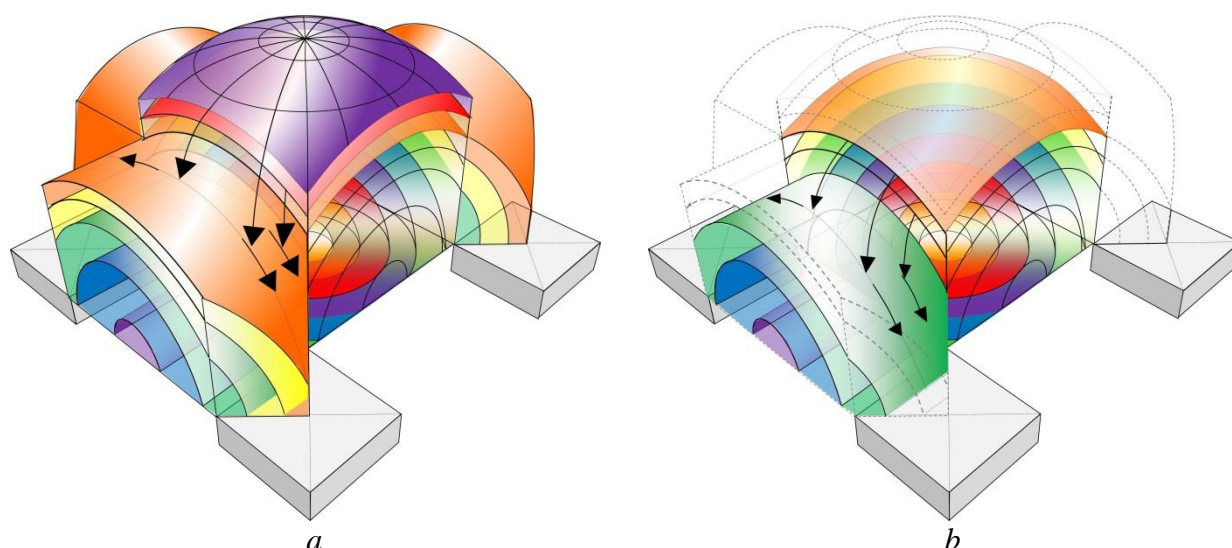
Figure 6.5 Connection between 3D hemispheres and 2D arches in the CA model. *a*. theoretical load transfer along the largest hemisphere. *b*. theoretical load transfer along a smaller hemisphere.

In the equations of the CA model, however, all load that is transferred from the 3D hemispheres to the 2D arches is applied on top of the largest 2D arch (with height H_{xg2D} or H_{yg2D}, see Figure 4.10), as given by equations (4.10) and (4.11). This schematisation means that the relatively large load coming from the largest

hemispheres is applied uniformly and relatively low down on the largest 2D arch. This leads to a larger load on the GR strip than suggested by reality. The part of the load that travels along the smaller hemispheres towards the 2D arches is also applied on top of the same, largest, 2D arch, which is higher than indicated by Figure 6.5*b*. This results in a smaller impact on the GR strip than suggested by reality. The exact consequence of transferring the load to the top of the 2D arches is not known, but it is expected that the effect will be limited. This is confirmed by the comparisons of the model results with measurements in Chapter 5.

6.4 Which design method fits best with observations and measurements of arching A and GR strains in field monitoring projects and experiments?

6.4.1 Combining the CA model and the inverse triangular and uniformly distributed load distribution

This thesis proposes analytical models for basal reinforced piled embankments. The conclusions and the newly developed analytical model are based on experiments and field tests with fills that are mainly dry. Wet fills, horizontal loads like spreading forces and horizontal traffic loads and cyclic loads are outside the scope of this thesis.

Three model elements have been changed or extended with respect to the design method in EBGEO (2010) and CUR (2010): the arching model for calculation step 1, the load on the GR strips, and subsoil support for the GR in calculation step 2. This chapter discusses these three elements.

Firstly, Chapter 4 considered several families of arching models and narrowed down the study to equilibrium models for several reasons, such as the need for dependency on soil properties and because a radical departure from existing European design models was felt to be undesirable. The CA model is therefore a modification and extension of the equilibrium models of Zaeske (2001) and Hewlett and Randolph (1988).

Chapter 5.5 shows that the CA model gives GR strains that match measurements in seven field tests and four experiment series better than any of the other equilibrium models. This conclusion holds for any load distribution. Van der Peet (2014) and Van der Peet and Van Eekelen (2014) also show that the Concentric Arches model gives the best match with their results of 3D numerical analyses. Furthermore, the model gives an explanation for the observed load distribution, including the concentration of the load on the GR strips between adjacent piles.

Secondly, two issues are important with respect to load on the GR strips: the distribution of the total *B+C* between the GR strips in the longitudinal and transverse directions, further discussed in Chapter 6.4.2, and the distribution of the load on each strip. In Chapter 2.4.3, it was concluded that the net load distribution on the GR strips is approximately inverse triangular. However, this is an approximation of the real load distribution, which is probably non-zero in the centre, resembling a parabola more than an inverse triangle. Chapter 6.4.3 compares alternative load distributions of this kind with the triangular, uniform and inverse triangular load distributions and concludes that the difference between these parabolic load distributions and the inverse triangular load distribution is negligible.

In Chapter 5.5, it was concluded that, when there is no subsoil support, the inverse triangular load distribution gives the best prediction of the GR strain. When subsoil support is considerable, the load on the GR strip is approximately uniformly distributed. This uniform load is combined with the counter-pressure that is directed upwards. This combination results in a *net* load distribution that matches an inverse triangular load distribution more than a uniform or triangular load distribution, as shown in Figure 5.19. For the inverse triangular and uniform load distributions, as well as parabolic load distributions, the resulting GR strain is considerably less than assumed previously with the triangular load distribution adopted in the German and Dutch guidelines (EBGEO, 2010 and CUR226, 2010), as shown in Chapters 3.4.4 and 6.4.3.

Thirdly, the original model of Zaeske considers only the subsoil support underneath the GR strips. This is considered to be unrealistic since there is no reason why only part of the subsoil should contribute to the support (Lodder et al., 2012, Chapter 3.4.1; Filz et al., 2012). Subsoil support was therefore extended to 'all subsoil' between the pile caps.

6.4.2   *Nonsquare rectangular pile arrangements*

Once the load on the area between the piles has been calculated, this load has to be divided between the GR strips in the *x*- and *y*-directions: the *x*-strip and *y*-strip in Figure 6.6. The approach adopted in the Zaeske model in EBGEO and CUR226 (2010) is different from the approach in the CA model in CUR226 (2015) adopted in CUR226 (2015). If $s_x = s_y$, there is no difference between the two methods. If $s_x \neq s_y$, however, the two methods give different results.

The two methods are as follows. In the case of the CA model proposed in this thesis, the load *B+C* in kN/pile on the GR is calculated with equation (4.16).

The CA model works with the average load on the GR strips, which is calculated with equation (5.9):

$$q_{av} = \frac{B + C}{A_{x-GRstrip} + A_{y-GRstrip}} \tag{6.1}$$

where $A_{x-strip}$ and $A_{y-strip}$ are the areas of the *x*-GRstrip and *y*-GRstrip respectively. This gives the force $F_{x,CA}$ and $F_{y,CA}$ for the CA model on respectively the *x*-GR strips and the *y*-GR strips:

$$F_{x,CA} = q_{av} \cdot L_x \cdot B_{ers} \qquad F_{y,CA} = q_{av} \cdot L_y \cdot B_{ers} \tag{6.2}$$

where L_x, L_y and B_{ers} (m) are indicated in Figure 6.6.
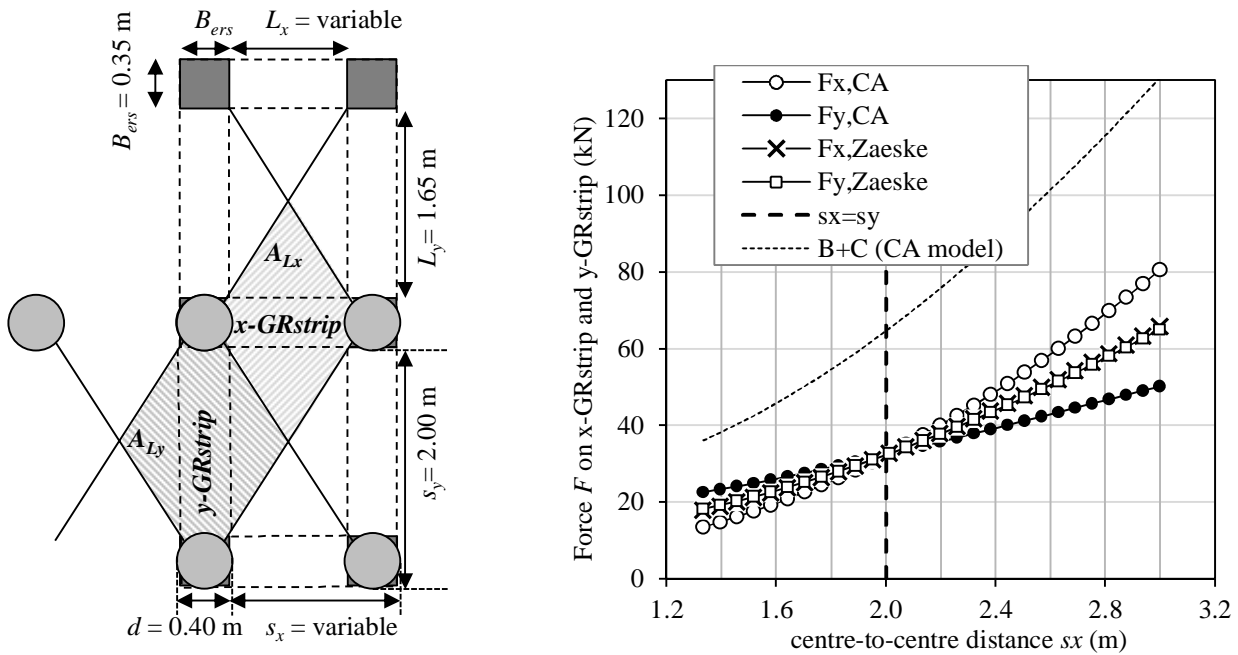
Figure 6.6 Distribution of load between *x*- and *y*-GR strips, $\gamma = 18.3$ kN/m³, $\varphi = 51°$, $p = 0$ kPa, $H = 2.6$ m. The value of the total load on the strips *(B+C)* is calculated with the CA model. *B+C* is distributed over the GR strips according to respectively the CA model and the Zaeske model.

In the case of the Zaeske (2001) model, the average pressure $\sigma_{v;r}$ on the GR area between the piles ($A_{Ly} + A_{Lx}$) is calculated with equation (3.2). Zaeske uses the diamond areas indicated in Figure 6.6 to calculate the force $F_{x,Zaeske}$ and $F_{y,Zaeske}$ on the *x*-GR strips and the *y*-GR strips:

$$F_{x,Zaeske} = \sigma_{v;r} \cdot A_{Lx} \qquad F_{y,Zaeske} = \sigma_{v;r} \cdot A_{Ly} \tag{6.3}$$

Figure 6.6 shows the resulting force on the GR strips for these two methods. In the figure, the centre-to-centre distance s_y is kept constant and s_x is varied. The load distribution between the GR strips is the same in both models for $s_x = s_y$. In the Zaeske model, the total load on the *x*- and *y*-strips is approximately the same, independent of the difference between s_x and s_y. The implication for the situation with subsoil is shown in Figure 6.7: if $s_x > s_y$, Zaeske gives $\varepsilon_x < \varepsilon_y$ and the CA model gives $\varepsilon_x > \varepsilon_y$, which seems more realistic. According to Zaeske, less GR is necessary in the direction with the larger pile spacing.
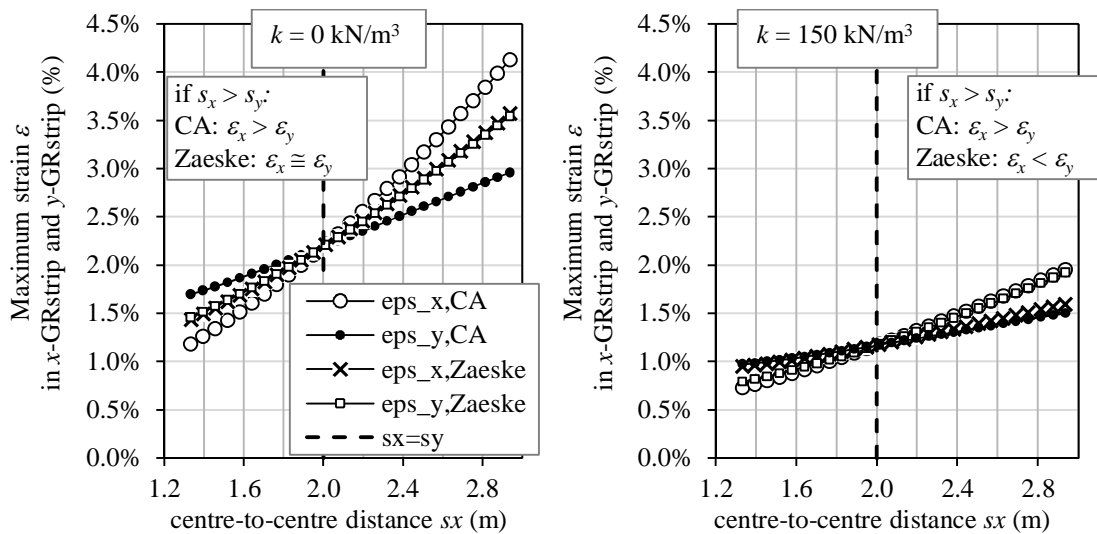
Figure 6.7 Maximum strain in *x*- and *y*-GR strips based on the GR strip forces in Figure 6.6. Additional parameters: $J = 5000$ kN/m, left: $k = 0$ kN/m³, right: $k = 300$ kN/m³. The strains were calculated with the inverse triangular load distribution. The same tendencies were found for the uniform load distribution.

Parabola
$q(x) = |a \cdot x^2|$ where
$a = 4 \cdot (3 \cdot q_{av} + 2 \cdot q_{min})/L^2$

Parabola no-zero center
$q(x) = |a \cdot x^2 + b|$ where
$a = -4(q_{min} - 3 \cdot q_{av} - 2 \cdot q_{min})/L^2$ and
$b = q_{min} = 0.12 \cdot q_{av}$

Inverse triangle
$q(x) = |4q_{av} \cdot x/L|$

Inverse triangle non-zero centre
$q(x) = |2(q_{max} - q_{min}) \cdot x/L + q_{min}|$ where
$q_{min} = 0.12 \cdot q_{av}$ and $q_{max} = 2 \cdot q_{av} - q_{min}$

Uniform
$q(x) = q_{av}$

Triangle
$q(x) = |4q_{av} \cdot x/L|^{*}$
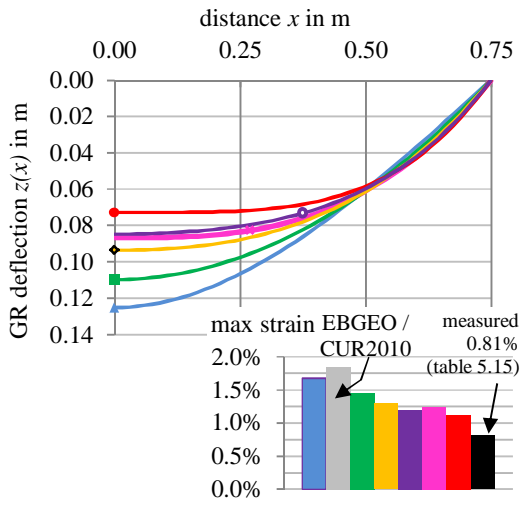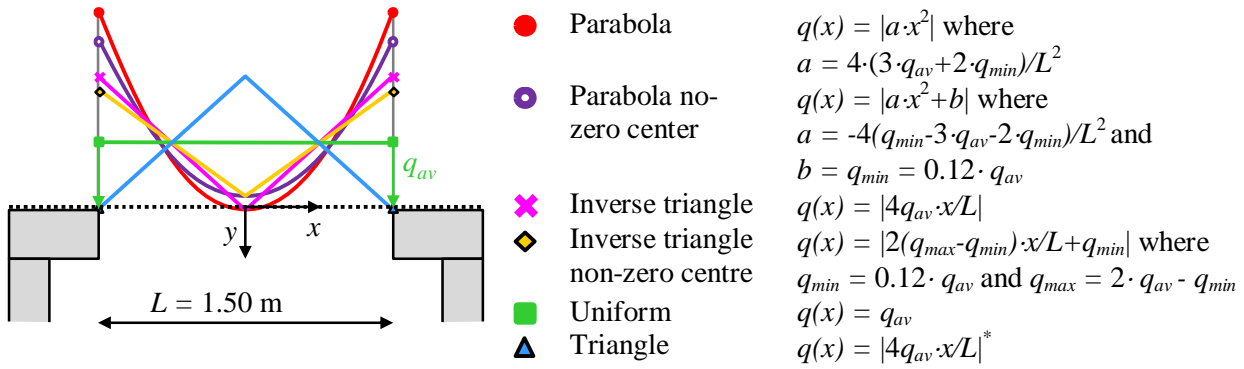
a. Subgrade reaction $k = 0$ kN/m³
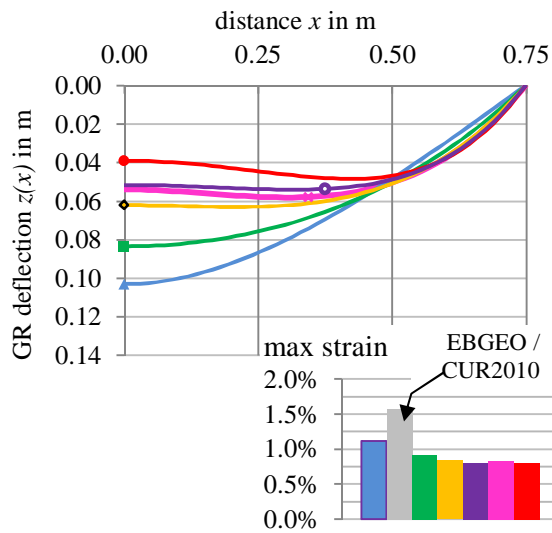
b. Subgrade reaction $k = 100$ kN/m³
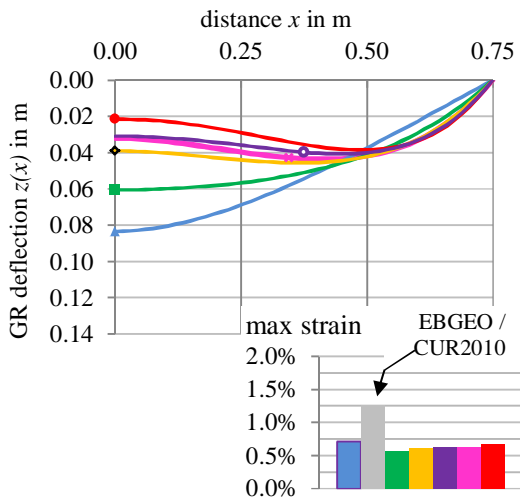
c. Subgrade reaction $k = 200$ kN/m³
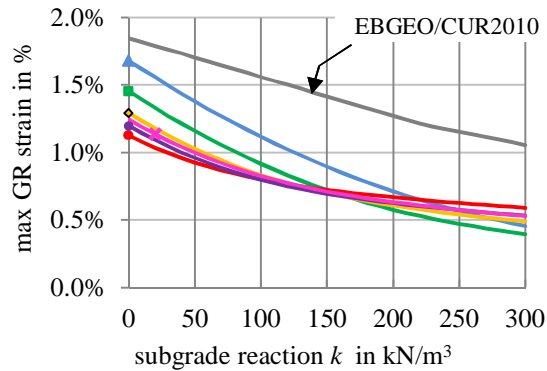
d. influence subgrade reaction on maximum GR strain

Figure 6.8 Influence of load distribution on GR deflection and GR strain for calculation example 1 from appendix 4.B (page 123). Calculation models: Concentric Arching model ($q_{av} = 27.32$ kPa, see appendix 4.B), all subsoil. The GR strain calculated with EBGEO (2010) and CUR226 (2010) is also given (Zaeske (2001): arching, triangular load distribution, strip subsoil).

*first half of span, with *y*-axis along pile cap edge

6.4.3 Alternative load distributions on the GR strips

Figure 6.8 compares the influence of several load distribution schematisations on the GR deflection and the maximum GR strain. This thesis proposes using the inverse triangular load distribution for the situation without subsoil support. This is a schematisation that represents reality: in reality, the load distribution will be more like the purple curves in Figure 6.8: a cup-parabola with a value larger than zero in the centre.

Alternatively, the load distribution may approach the inverse triangular load distribution, but without a zero midpoint. Figure 6.8 shows that all these three load distributions (in yellow, pink and purple) give nearly the same GR deflection and maximum GR strain. It can therefore be concluded that the relatively simple inverse triangular load distribution is adequate.

Figure 6.8*b* and *c*, with a subgrade reaction $k = 100$ and 200 kN/m^3, show that the calculations with the inverse triangular or parabolic load distributions give most GR deflection close to the piles. The resulting shape of the deformed GR leads to a relatively high GR strain, as was also explained in Chapter 5.4.5 of this thesis. This is caused by the large counter-pressure in the centre of the GR strip, while the downward load midway between the piles is zero. This mechanism may occur in practice to a small extent, as shown by the measurements in Figure 5.18. However, stiffer subsoil leads to a more uniform load distribution (green in Figure 6.8).

The pragmatic approach proposed in this thesis and adopted in the CUR226 (2015) guideline uses the Concentric Arches model in combination with all subsoil support and the load distribution that gives the lowest GR strain. In this way, the inverse triangular distribution is applicable to the cases without, or with limited, subsoil support; a uniformly distributed load is applicable to the cases with substantial subsoil support.

6.4.4 Safety analysis

Chapter 5.5 showed that the new model, with the CA model and the combination of inverse triangular and uniform load distribution, calculates GR strains that are on average 1.06 times the measured values, while the Zaeske (2001) model used in CUR226 (2010) calculates GR strains that are on average 2.46 times the measured values. The standard deviation was also smaller with the new model, even though a considerable standard deviation remained.

One can debate whether a design guideline should adopt a model that nearly always gives a design on the safe side, as with the Zaeske model, or whether a

design guideline should adopt a model that describes reality as well as possible and consider safety separately. The Dutch CUR226 committee decided to adopt the new model presented in this thesis and to combine this with the inclusion of a model factor to cope with the uncertainty in the model. The value of the model factor was determined using the data points resulting from the comparison between measurements and calculations presented in Chapter 5.

Van Duijnen et al. (2015) reported on the safety analysis used to determine the model factor and the associated load and material factors. Following the suggestions made in EC 1990 (2011, Eurocode 0), they conducted a statistical assessment of the differences between the measured and calculated GR strains and then carried out Monte Carlo (MC) simulations for several reference cases in order to obtain the model factor. Multiplying this model factor by the GR strain calculated with characteristic values gives a value that is higher than the real GR strain in 95% of the cases. In other words, if the model factor is used, reality is worse than the calculation in 5% of the cases.

Subsequently, Van Duijnen et al. (2015) determined three sets of partial material and load factors associated with the model factor for a level 1 design approach (the method with partial factors). They showed that using these factor sets satisfy the reliability indices required for the three reliability classes of EC 1990 (2011, Eurocode 0). The resulting model and partial factors were adopted in CUR226 (2015).

7 Conclusions

7.1 Introduction

This thesis about basal reinforced piled embankments analysed the mechanisms that determine the GR strain resulting from the dead weight of the embankment and traffic weight. The study improved our understanding of the load distribution in a basal reinforced piled embankment, and a new design model for the geosynthetic reinforcement was developed and validated.

Nineteen 3D scaled model experiments and three field monitoring projects were carried out. The measured vertical deformations in a number of these scaled model experiments guided the development of ideas underlying the newly developed analytical design model. The field tests added full-scale observations and measurements. The models were validated using the measurements of load distribution and GR strain from these field studies and three tests in the model test series, and from five field studies and three model test series and some numerical results from the literature. Furthermore, two Master's students conducting research as part of this doctorate study validated the newly developed analytical model using 3D numerical analysis with Plaxis 3D Tunnel and Plaxis 3D.

7.2 GR design in two steps

Several countries have issued design guidelines for basal reinforced piled embankments, and researchers are still working on improvements to analytical design methods. Analytical models for the GR design in piled embankments calculate the GR strain. When multiplied by the GR stiffness this gives the tensile force (kN/m), which determines the required GR strength. The calculation of the GR strain includes two calculation steps, as shown in Figure 1.3.

Calculation step 1 divides the total vertical load into two parts: load part A (kN/pile) and the 'residual load' ($B+C$ in Figure 1.3a, in kN/pile). Load part A, which is also referred to as 'arching A' in this thesis, is the part of the load that is transferred to the piles directly. This load part is relatively large due to arching, which is the mechanism in which load is inclined to be attracted towards stiffer elements, in this case the pile caps. The thesis also considers the ratio $A\% = A/(A+B+C)$.

Calculation step 2 then calculates the GR strain in the GR strip between each pair of adjacent piles by loading the GR strip with the residual load *B+C* and, if possible, supporting the GR strip by the subsoil.

The purpose of the second calculation step is to calculate the GR strain but it also results in a further division of the vertical load: load part *B* (kN/pile), which passes through the GR to the piles, and load part *C* (kN/pile), which is the subsoil support, as indicated in Figure 1.3*a*.

7.3   Measuring technique in piled embankments

Arching *A* needs to be measured to validate calculation steps 1 and 2 separately. The fact that this was done in this research represented a major step forward. Both arching *A* and load part *B* were measured separately in all three field monitoring projects and in the experiments. This was done with total pressure cells - with the same diameter as the circular pile caps - that measured the pressure on the pile caps above the GR (*A*) and underneath the GR (*A+B*). In the experiments, load part *C* was also measured separately. The combination with GR-strain measurements made the full analysis of the two calculation steps possible.

Several problems frequently occur when measuring GR strains. Traditional strain gauges cannot be glued to the fabric of most GR types. In other cases, the failure strain of the strain gauges may be smaller than the failure strain of the GR and the strain gauge may then fail too soon. However, this latter problem was not observed in piled embankments in this study. Finally, it is possible that the strain gauges may affect GR stiffness behaviour.

In the Woerden test, good results were obtained by applying optic fibres. They responded very clearly to truck passages, as shown by Van Eekelen et al. (2012c, 2015b and d). In the model experiments, promising results were obtained with a specially developed measurement system using bicycle gear cables (Chapter 2, Van Eekelen et al., 2012a). A larger version of this system was tried out in this field test alongside the optic fibres (Van Eekelen et al., 2012c). The system is very simple and it is still in the trial phase, but the results are promising.

The positions of the settlement tubes were measured repeatedly with a liquid levelling system. These measurements were usually taken at intervals of 0.50 m. It would be better to reduce this distance, for example to 0.10 m. Doing so makes it possible to study the shape of the deformed GR and therefore the load distribution on the GR, as discussed in Chapter 4.2.

7.4   Observations in experiments, field tests and numerical analysis

7.4.1   Arching

The measured arching *A,* and load part *B* and its corresponding GR strain and GR vertical deflection, follow a smoothly ascending curve when plotted against the net load. This was concluded from the model experiments and confirmed with the finite element calculations of Den Boogert et al. (2012a,b) and Van der Peet and Van Eekelen (2014).

Consolidation of the subsoil is necessary for the development of arching. It causes more GR deflection and it increases the net load, which in turn results in an increase in arching (load part *A* and *A%*) and an increased load through the GR (load part *B*) respectively.

To allow GR deflection to occur, the reinforcement should not be too stiff. This is generally not a problem with geosynthetic reinforcement. Furthermore, it is necessary to force sufficient GR deflection before the road is asphalted or the railway built. In practice, the development of arching and GR deflection is encouraged by sending construction cranes and trucks over the embankment under construction. Measurements show that this results in the development of arching over a period of approximately 1 to 3 months, as shown in Figure 5.16. After that point in time, GR deflection more or less stops.

The dependency of arching *A* or *A%* on several factors is discussed further in Chapter 7.4.3.

7.4.2   Load and strain distribution

A major part of the load is attracted to the piles directly. This load part is arching *A*. The residual part of the load is (*B+C*).

There is a major difference between piled embankments with or without GR. If no GR is applied, (*B+C*) between the piles is distributed more or less evenly on the subsoil. With GR, a major part of (*B+C*) is concentrated on the GR strips between adjacent piles. Van der Peet and Van Eekelen (2014) showed this concentration of load on the GR strips with numerical calculations. Zaeske's experiments (2001, see Figure 4.6 of this thesis) showed the difference between piled embankments with or without GR. Using GR makes arching much more efficient. The difference between piled embankments with or without GR requires a distinction between models describing each situation.

All experiments reported in Chapters 2 and 4 show that the GR strains occur mainly in the GR strips on top of and between adjacent piles (Figure 2.7 and Figure 2.8). In the laboratory tests, the largest GR strains were actually found on top of the piles. These tests used smooth, small-scale piles. This is different from the situation in practice, where large concrete caps are generally used. The size of these pile caps and the friction between the GR and the pile cap causes the GR to be clamped in place, so that GR strains above the centre of the pile cap are much smaller. It is therefore assumed that the GR strain prediction will be sufficiently accurate if it is assumed that GR strain occurs only in the GR strips between adjacent piles. This concurs with the assumptions of the calculation models in BS8006 (2010), EBGEO (2010) and CUR226 (2010, 2015) and is confirmed by numerical calculations (Den Boogert, 2011).

The smallest load on the GR strips occurs in the centre of the strip midway between the piles and the largest load close to the pile cap edges. The load distribution on the GR strips is therefore approximately inverse triangular. This was concluded from the measured shape of the deformed GR strips in the experiments (Chapter 2.4.3) and in the field (Chapter 5.4.3), the measured load distribution in the experiments (Chapter 4.3.4) and from the load distribution or the GR strip shape in numerical calculations (Den Boogert et al., 2011; Han et al., 2012; Van der Peet and Van Eekelen, 2014).

7.4.3   Factors of influence

It was possible to analyse several determinant factors using the results of the experiment series reported in Chapters 2 and 4.2. Most conclusions were confirmed by numerical calculations.

Chapter 7.4.1 described the considerable influence that consolidation has on arching.

Arching $A\%$ increases with embankment height H and seems to stabilise in higher embankments (Chapter 4.5.3). This was confirmed numerically by, for example, Le Hello and Villard (2009) and Van der Peet and Van Eekelen (2014).

A higher fill friction angle φ gives more arching, especially during consolidation. This results in load part B on the GR being some 39% larger for sand than for granular fill at the end of tests T2 (sand fill, $\varphi = 40.9^{o}$) and T3 (granular fill, $\varphi = 49.0^{o}$). The influence of the fill friction angle on the arching was also shown numerically by, for example, Van der Peet (2014), Van der Peet and Van Eekelen (2014) and Le Hello and Villard (2009).

The GR stiffness *J* does not affect the measured arching *A,* as long as the stiffness complies with a good-quality design model (nevertheless, the exact limiting values of the GR stiffness between which this conclusion is true have not been investigated). However, the GR stiffness is related to the measured GR deflection and therefore the GR strain, as shown in Chapter 2.5.4. Van der Peet and Van Eekelen (2014) also found no influence of the GR stiffness *J* on arching.

An increase in surcharge load *p* or net load leads to both an increase in arching *A* and load part *B* because the total load increases, as shown in Figure 2.5 and Figure 2.11. If subsoil is available to bear the load, the percentage of the load going directly to the piles, *A*%, decreases with increasing surcharge load *p*.
Values for *A*% measured at the end of each consolidation phase are more or less constant after the initial phase. This shows that the arching stabilises quickly in the situation with little or no subsoil support: it already has developed fully for a relatively small net load.

The difference in performance between a geotextile and a geogrid, given the same mechanical characteristics, was negligible in the model experiments that we conducted. The difference between, for example, applying a sand or granular fill was much larger.

If two GR layers are considered, one consisting of a single biaxial grid layer and the other one consisting of two uniaxial layers installed directly on top of one another, the same load distribution and deformations are measured as shown in Chapter 2.5.3. The stiffness of one biaxial GR layer is therefore equal to the total stiffness of the two uniaxial layers installed directly on top of one another. In other words, $1 + 1 = 2$.

Systems with two GR layers with or without a fill layer between them also behave similarly. In both systems, arching depends linearly on the net load on the fill. However, the dependence is slightly stronger in systems with a fill layer. This means that, in the system with a fill layer between the GR layers, arching is slightly less in the first phase of the tests and slightly more in the last phase of the tests than in the system without that fill layer. The deformation pattern is similar in all cases (both with and without a fill layer between the GR layers), at least for the geometry considered in the experiments presented in Chapter 2. For design purposes it is sufficient to consider the systems with and without a fill layer between the GR layers as the same. In other words, once again, $1 + 1 = 2$. This was demonstrated and explained in Chapter 2.5.5, and in Van Eekelen and Bezuijen (2014).

7.5   New analytical model for calculating the maximum GR strain

This thesis presents a new model that is a modification and extension of the existing models of Zaeske (2001) and Hewlett and Randolph (1988). The model consists of two steps: step 1, arching, and step 2, load-deflection behaviour. These two steps are explained here.

7.5.1   Calculation step 1: analytical model for arching

This thesis presents a new equilibrium model: the Concentric Arches (CA) model. It is a variation on the Hewlett and Randolph (1988) and EBGEO (Zaeske, 2001) equilibrium models. Other model types were excluded from this study because they do not include material behaviour or because a radical departure from existing European design models was felt to be undesirable. The model consists of concentric hemispheres and arches that develop as a result of ongoing GR deflection. Larger hemispheres or arches exert more pressure on their subsurface.

The CA model consists of concentric 3D hemispheres and 2D arches. The load is transported along the 3D hemispheres outwards, towards the stiffer piles, the stiffer GR strips and the stiffer intersection planes between the hemispheres of adjacent pile units. Above the GR strips, the hemispheres intersect, and the load turns and follows the 2D arches towards the piles. A set of analytical equations was established that describes the combination of 3D hemispheres and 2D arches.

The vertical effective stress in the fill between the piles decreases with depth. This pattern was measured by Zaeske (2001) and the CA model finds a comparable tendency. The hemispheres and 2D arches exert part of their load on their ground surface. As the 2D arches are loaded relatively heavily they exert a relatively large part of the load on their ground surface: the GR strips.

The Concentric Arches model describes both full and partial arching, the latter for embankments thinner than the height of full hemispheres. In that case, the stress in the centre between four piles is reduced by arching and the area close to the GR strips is loaded fully with $\gamma H + p$. This rather pragmatic solution concurs with the stress release in the centre between four piles found numerically by Van der Peet (2014). The partial arching model of the CA model is different from the earlier equilibrium models considered: Hewlett and Randolph (1988) did not provide a real solution for partial arching, while Zaeske (2001) removes the upper part of his model, leaving only the lower scales of his model. The CA partial arching model matches the measurements in the experiments and numerical calculations much better than the other equilibrium models considered, as shown in Chapter 4.5.3,

where the calculation results were compared with measurements in experiments and numerical results of Le Hello and Villard (2009) and Van der Peet and Van Eekelen (2014).

The CA model results in a load distribution on the GR that resembles the load distribution observed in experiments, field measurements and numerical analysis; a load concentration on the piles and the GR strips with an approximately inverse triangular load distribution on the GR strips. The CA model therefore provides a physical explanation for the observed load distribution. The concentric stress arches have also been found by several authors presenting numerical studies on arching such as Vermeer et al. (2001), Nadukuru and Michalowski (2012), Han et al. (2012) and Van der Peet and Van Eekelen (2014).

The Concentric Arches model explains how arching increases with subsoil consolidation (GR deflection): new arches are formed in succession as GR deflection progresses.

However, in the limit-state version of the model presented in this paper, the model behaves in a rigid-plastic way and no longer describes the influence of subsoil consolidation or deformation but describes fully developed arching. The influence of deformation cannot be incorporated in rigid-plastic models such as the equilibrium models or frictional models. A new class of models would be needed to account for this. However, establishing those models would conflict with the initial thinking that a radical departure from existing design models was undesirable, and this area is outside the scope of this thesis.

Using numerical techniques would make it possible to make calculations that include subsoil consolidation. However, as indicated in the introduction (Chapter 1.2), these methods are generally not permissible in GR design since the methods tend to underpredict GR strain, as shown by for example Farag (2008). This seems to be specifically the case for situations with subsoil support as shown by Van der Peet and Van Eekelen (2014). This thesis therefore narrowed its focus to analytical GR design.

The equations for the Concentric Arches model are given in Chapter 4.4.5.

7.5.2   Calculation step 2: load-deflection behaviour

This thesis proposes modifications to the Zaeske (2001) approach for calculation step 2. The model still considers only the GR strip between adjacent piles. The width of the strip is equal to the width of the square pile caps or the equivalent width of circular pile caps.

The strips are loaded by *B+C*, as determined in calculation step 1. The distribution of this load is inverse triangular or uniform, depending on which gives the least GR strain. In this way, the inverse triangular distribution applies in cases with little or no subsoil support and the uniformly distributed load in the cases with significant subsoil support.

In the model presented by Zaeske (2001), only the subsoil underneath the GR strip between adjacent piles is taken into account. Measurements in the experiments showed that it is better to take all subsoil support into account (Chapter 3.4.4): this is a theoretical improvement and it is also confirmed by the comparison between calculations and measurements described in Chapter 5. The subgrade reaction k is therefore increased to take into account all subsoil underneath the GR instead of the subsoil support beneath the strip only.

It has been shown in this thesis that the inverse triangular load distribution is a good approach, even though the load may be more parabola-like and may have a non-zero pressure in the centre of the GR strip, and even though the load may be more concentrated near the pile caps than the inverse triangle indicates. However, such minor changes in the load distribution do not have a significant effect on the resulting calculated GR strain. The change from a triangular load distribution to a uniform or inverse-triangular one is much larger, leading to a GR strain reduction in the range of 40 to 60%.

The proposed calculation model does not take GR strains on the pile caps into account, as in the original models. These GR strains can be the largest GR strains under specific conditions, such as for the smooth, small-diameter pile caps in the test set-up. As this will generally not be the case in the field, it was decided not to modify the step 2 calculations to take the GR strains on the pile caps into account.

The equations for step 2, including 'all subsoil' and the inverse triangular and the uniformly distributed load distribution are given in appendix 5.A. Additionally, appendix B of this thesis gives design graphs that can be used instead of the equations.

7.5.3 Factors of influence

Consolidation of the subsoil results in an increase in arching *A*. Chapter 7.5.1 explained that the rigid-plastic CA model does not describe this.

The Concentric Arches model is dependent on the embankment height *H* in a way similar to that found in experiments and in the numerical calculations of Le Hello

and Villard (2009) and Van der Peet and Van Eekelen (2014). For other models, the match is less satisfactory.

For fills with low friction angles, Zaeske's arching model generally gives low arching, leading to higher GR strains than measured. At high friction angles, Zaeske's model gives relatively high arching levels, and therefore lower GR strains than measured. Van der Peet (2014) and Van der Peet and Van Eekelen (2014) confirm this tendency of Zaeske's model by comparing Zaeske's results with 3D numerical analyses. The dependency of the CA model on the fill friction angle gives a much better match with these 3D numerical analyses.

The influence of the GR stiffness J in the step 2 calculations with the new model is comparable with that in the measurements.

The surcharge load p, like GR stiffness, does not affect the relative amount of arching in the equilibrium models considered. However, the numerical analyses show that higher surcharge loads give higher values for $A\%$. One explanation may be that the surcharge load is added at the top of the embankment, where the load is easily transferred horizontally to the piles. This would be less obvious if the load was added lower down the embankment. Secondly, the surcharge load leads to a higher confining pressure in the embankment, enhancing the strength of the fill and consequently the arching.

7.6   Validation of analytical models

The CA model calculates values for arching A that match measurements well, and generally better than values calculated with EBGEO/CUR (2010), especially in the case of relatively thin embankments. This finding is important for design calculations for the construction phase.

Several analytical models were validated with a lot of field and model tests. Variations on three parts of the analytical models were considered: (1) the arching model (2) the load distribution on the GR strip between adjacent piles and (3) the subsoil support. The models considered were variations on and/or extensions to the models of Hewlett and Randolph (1988) and Zaeske (2001, also reported in Kempfert et al., 2004).

Particular attention was paid to the realistic determination of the soil parameters for the analytical simulations of the lab and field tests. The values in these simulations should be the best-guess values (mean values) rather than the characteristic values, as in design practice.

The current combination of analytical models in EBGEO (2010) and CUR226 (2010) is Zaeske's arching model (2001): triangular load distribution and subsoil support below the GR strip only. BS8006 gives the option of using the combination of Hewlett and Randolph and a uniform load distribution as an alternative to the modified Marston and Anderson (1913) approach. These two combinations match the measurements least; they calculate strains that are on average 2.46 and 2.89 times the measured strains respectively.

When applying the inverse triangular load distribution, the CA model gives on average 1.34 times the measured GR strains and Zaeske's multi-scale arching model (2001) does the same by a factor of 1.42. For the uniform load distribution, this figure is 1.16 for the Concentric Arches model and 1.24 for Zaeske's model. It can therefore be concluded that the Concentric Arches model gives GR strains that match the measurements better than Zaeske's model (2001). This conclusion holds for any load distribution.

If the load distribution that gives the smallest GR strain is chosen – in other words, the inverse triangular distribution for the cases without, or with limited, subsoil support and a uniformly distributed load in the cases with subsoil support – the Concentric Arches model gives on average 1.06 times the measured GR strains, in other words, an average overestimation of the measured strains of only 6%, as shown in Figure 5.29.

In conditions without subsoil support, the inverse triangular load distribution predicts the GR strain best: the calculated GR strains were on average 12% larger than measured, by comparison with 31% in the case of the Zaeske (2001) model. When subsoil support is considerable, the load on the GR strip is distributed in an approximately uniform way. This uniform load is combined with the counter-pressure that is directed upwards, leading to a *net* load distribution that matches an inverse triangular load distribution more than a uniform or triangular load distribution, as shown in Figure 5.19.

The Dutch CUR committee decided to replace the Dutch CUR 226 (2010) with CUR 226 (2015), using the Concentric Arches model in combination with all subsoil support and the load distribution that gives the lowest GR strain: either the inverse triangular load distribution or the uniformly distributed load.

7.7 Recommendations for future research

7.7.1 Horizontal load on the GR

The 3D numerical calculations presented by Van der Peet and Van Eekelen (2014) show that the direction of the major principal stresses just above the GR is not vertical everywhere, even though this is one of the assumptions underlying the Concentric Arches model. The implications of this finding should be investigated.

Furthermore, the effect of lateral loads caused by, for example, spreading forces or lateral traffic forces, should be considered more carefully. The experiments and finite element calculations of Farag (2008) should be taken into consideration.

7.7.2 Subsoil support

The experiments presented in this thesis showed that subsoil consolidation has a major impact on arching and on the GR strain. The CA model proposed in this thesis explains increasing arching with subsoil consolidation and GR deflection. The explanation is that new arches are formed in succession as GR deflection progresses. However, in the limit-state version of the model presented in this thesis, the model behaves in a rigid-plastic way and it no longer describes the influence of subsoil consolidation or deformation.

This suggests that it could be better not to separate the first and second calculation steps as is done in this thesis. This has been suggested by, for example, Deb et al. (2010).

Furthermore, the subsoil support in calculation step 2 was modelled using springs. Optimisation through the introduction of a consolidation model in step 2 would be a useful extension. This would also reduce the difficulties affecting the determination of a correct value for the subgrade reaction. In this case, negative skin friction along the pile shafts should be taken into account, as in the French ASIRI (2012).

7.7.3 Traffic load

All design methods use a uniform distributed surcharge load to take traffic load into account. There are several methods for converting a normative truck load into a uniformly distributed surcharge load. Van Eekelen et al. (2015b,d) present measurements during truck passages showing that the calculation methods may overestimate the influence of the truck passages. It is possible that the load may be spread more than has been assumed. Further research is needed.

The influence of cyclic loading by traffic can either enhance or disrupt the arching mechanism. Improvement occurs as a result of compaction due to vibration or traffic. This improves the soil strength and therefore arching. Arching may be adversely affected by fractures or slip planes generated by the passage of heavy trucks. Heitz (2006) and Van Eekelen et al. (2007) have shown, on the basis of model experiments and field measurements respectively, that the arching tends to be restored after damage has occurred: they found an increase in arching during a period of rest.

Heitz (2006) studied the influence of cyclic loading on piled embankments with and without GR. He concluded that the introduction of GR reduced the influence of the vibrations on arching considerably. He calibrated a calculation rule to reduce arching in cases with a relatively large cyclic loading, the "κ model". Heitz based his calibration purely on his unreinforced experiments: it was not possible to use his reinforced tests because he had not been able to measure A separately. Heitz also concluded that arching can recover between periods of cyclic loading. This, and the fact that the κ model was based on the unreinforced tests, makes it likely that the current κ model is more conservative than necessary. Further research is recommended.

7.7.4   Water

In natural peat swamps, water tables may be as high as 0.10 to 0.20 m below the surface. In urbanised delta areas with soft soil, this figure is often around 0.50 to 0.70 m. In these areas, road surfaces often have to be built at relatively low levels. This leaves limited space for the construction of dry embankments on pile foundations. However, most piled embankments are designed in such a way that the embankment can be kept dry. This means reducing the pile spacing or installing the road surface at a higher level than in the original design.

As a result, there is considerable pressure to locate embankments below the level of the water table. Furthermore, floods, heavy showers or artesian water can affect the arching behaviour due to changes in the fill behaviour, the reduction of effective stresses, and the weight or swell of the subsoil. Van Eekelen et al., (2012c), Briançon and Simon (2012) and Sloan (2011) all presented measurements showing that moisture affects arching behaviour. However, the mechanism is not yet understood and further research is required.

7.7.5   Other fill types

The analytical models considered have been developed for cohesionless frictional fills, and it has been assumed that frictional fills such as crushed rock, sand or

crushed recycled construction material such as concrete and masonry will be used. In practice, however, these fills often have some level of cohesion. In those cases, it is generally advisable to disregard this cohesion and therefore to introduce an additional safety.

Furthermore, in some countries, such as Brazil and Indonesia, the fill materials consist of laterite, a tropical residual soil. Although the properties of laterite can vary greatly, its behaviour is usually cohesive. Research looking at the long-term arching behaviour of these tropical soils in piled embankment applications is recommended. Model experiments with laterite of the kind described in Chapter 2 and Van Eekelen et al., 2012a should be conducted.

Appendices

A. Analysis and Modification of the British Standard BS8006 for the Design of Piled Embankments

Abstract

The piled embankment is an increasingly popular construction method. The Dutch Design Guideline for piled embankments (CUR 226) was published in the first half of 2010. Several existing models were analysed before it was decided to adopt the calculation rules in the Dutch Guideline. The British Standard BS8006 sometimes calculates tensile forces in the geosynthetic reinforcement that differ considerably from the tensile forces calculated with other models. For quite thin embankments in particular, BS8006 designs a relatively strong and therefore expensive geosynthetic reinforcement by comparison with other design models. These differences are not always fully understood, leading to uncertainty. This paper analyses BS8006 and demonstrates why it behaves differently from other models. It also examines why this behaviour is different than would be expected. For example, it is shown that calculations using BS8006 are based on a load which is higher than the actual load.

A modification to BS8006 is proposed, which is shown to give results comparable to the results of the German Standard EBGEO for situations where there is no subsoil support. The results of BS8006, Modified BS8006, and the German/Dutch guideline are compared with finite element calculations and field measurements. It is concluded that the results derived with the Modified BS8006 are more accurate than those obtained using BS8006.

A. 1   Introduction

The piled embankment is an increasingly popular construction method. In the Netherlands for example, more than 20 piled embankments have been constructed during the last 10 years. Many more piled embankments have been reported in countries such as Germany, England, Scandinavia, the United States, Brazil, India, and Poland. The Dutch Design Guideline (CUR 226) was published in the first half of 2010. This Guideline adopts major parts of the German Guideline EBGEO (2010).

Several existing models have been analysed to determine the calculation rules used in the Dutch Guideline. The British Standard BS8006 sometimes calculates tensile forces in the geosynthetic basal reinforcement (GR) that differ considerably from other models. In the case of quite thin embankments in particular, BS8006 designs a relatively strong and thus expensive GR in comparison with other design models. These differences are not always fully understood leading to uncertainty. This paper analyses BS8006 and demonstrates why it behaves differently from other models. It also shows why this behaviour is different than would be expected. A modification for BS8006 is proposed, referred to as the Modified BS8006.

220

The tensile force in the GR must first be calculated to design the GR in a piled embankment. The tensile force is caused by vertical load (traffic, soil weight) and by lateral load (active ground pressure due to outward horizontal thrust of the embankment). This paper only considers the tensile force calculations caused by the vertical loads in the system.

Chapter A. 2 of this paper thoroughly analyses BS8006 for reinforcement in piled embankments, and identifies its limitations. The resultant proposal for the Modified BS8006 is given in Chapter A. 3.
The final two chapters compare the results of BS8006, the Modified BS8006, and the German/Dutch guidelines with finite element calculations and field measurements.

Safety philosophy is beyond the scope of this paper, and all safety factors in the calculation methods are therefore ignored. The paper focuses on the tensile force calculations caused by vertical loads in the piled embankment. Throughout the paper, pile spacing is assumed to be identical in both directions, except in Chapter A.3.4. Here, equations for the Modified BS8006 are elaborated for the situation that $s_x \neq s_y$. Differences in GR stiffness J in both directions do not influence the equations.

A. 2 British Standard BS8006 for the design of reinforcement in piled embankments

A.2.1 Introduction

British Standard BS8006 calculates the tensile force in the GR caused by the vertical load in the following four steps[23]:

1. The vertical load is divided into three parts
2. The load on the reinforcement is concentrated on the strips of reinforcement between adjacent pile caps.
3. Full arching is assumed
4. The tensile force in the GR is calculated, from the vertical load part *B*.

Each of these four steps will be analysed in Chapters A.2.2 to A.2.5.

---

[23] The rest of this thesis distinguishes between two calculation steps. Step 1 (arching) is the division of the load into two parts, which corresponds with this first step (for $C = 0$). Step 2 in the rest of the thesis corresponds to the other three steps listed here. Step 2 mentioned here, about the load concentration on the GR strips between adjacent pile caps, is discussed in this appendix for BS8006 and in Chapter 6.4.2 for Zaeske (2001) and the new CA model.

A.2.2 Step 1: dividing the vertical load into load parts

A.2.2.1. Load division based on the principle of arching

The load in the soil is attracted to stiff elements, in this case the piles. This results in a tendency for the vertical load to bend off laterally, resulting in an 'arch' in the embankment fill. This phenomenon is called arching.

This paper defines the division of the vertical load into parts (due to arching) as follows (Figure A.1): Load part '*A*' is the load part that is transferred directly to the piles. The weight of the soil wedge below the arch is carried by both the GR and the soft subsoil. Part of the soil wedge weight is transferred through the GR to the piles, and is referred to as load part '*B*'. The load part that is carried by the subsoil between the piles is referred to as '*C*'. In this paper, *A, B* and *C* are expressed in kN/pile (per pile area, or per $s_x \cdot s_y$, with $s_{x,y}$ the centre-to-centre distance between two piles). The next chapter explains how *A*, *B* and *C* are determined in BS8006.
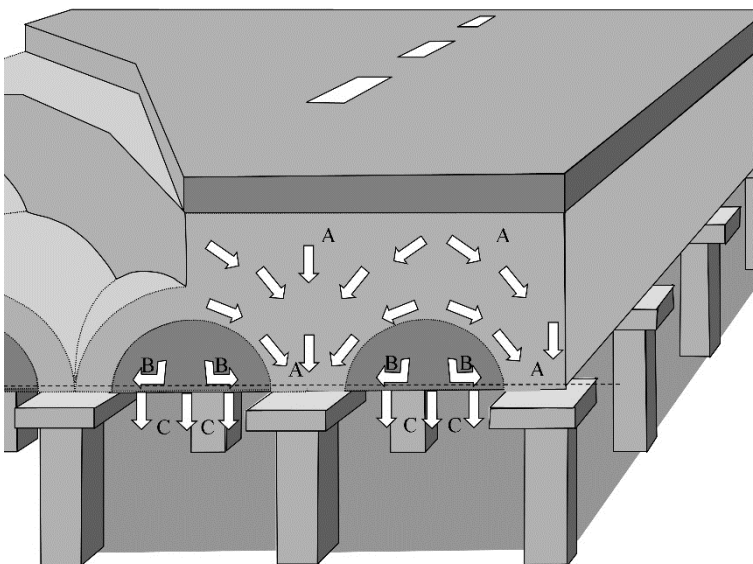
Figure A.1 Dividing the load into three parts: *A* - directly to the piles, *B* - via the GR to the piles, *C* - to the soft subsoil in between the piles (*C* = 0 in BS8006).

A.2.2.2. Determining load part A in BS8006

BS8006 bases its calculation of *A* on the work of Marston and Anderson (1913)[24]. Marston and Anderson carried out numerous experiments to determine the arching above a pipe in soil (Figure A.2). The following equation was found for the load on an infinitely long pipe:

---

[24] BS8006-1:2010 gives the model of Hewlett and Randolph (1988) as an alternative. This is outside the scope of this paper.

$$\frac{p'_{c,pipe}}{\sigma'_v} = \frac{C_{c,pipe} a_{pipe}}{H}$$

<div align="right">(A.1)</div>

where:

$p'_{c,\,pipe}$	kPa	Load part that is transferred to the pipe directly
σ'_v	kPa	Average vertical load directly above the pipe
$C_{c,\,pipe}$	-	Arching coefficient. Marston and Anderson determined the arching coefficient for several types of soft soil below and adjacent to the pipe. For softer clay, Marston and Anderson found a lower C_c. This means that the pipe will sink further into the softer clay, and the pipe will attract a relatively small part of the load. There is therefore less arching.
a_{pipe}	m	Diameter of the pipe
H	m	Height of fill above pipe (Figure A.2) or height of fill above reinforcement in a piled embankment

Figure A.2 BS8006 bases its calculation of load part *A* on the experimental research of Marston and Anderson (1913).

Jones et al. (1990) adapted this equation for the 3-dimensional (3D) situation of a pile by squaring the right term:

$$\frac{p'_c}{\sigma'_v} = \left(\frac{C_c a}{H}\right)^2 \quad \text{or} \quad p'_c = \left(\frac{C_c a}{H}\right)^2 \sigma'_v$$

<div align="right">(A.2)</div>

And thus load part *A* is:

$$A = p'_c a^2 = \left(\frac{C_c a}{H}\right)^2 a^2 \sigma'_v$$

<div align="right">(A.3)</div>

Equation (A.2) has been adopted in BS8006 on page 185 (BS8006-1: 2010). Jones et al. (1990) and BS8006 also adapted how the arching coefficient C_c for the 3D geometry of a piled embankment should be determined as follows:

End-bearing piles:

$$C_c = 1.95\frac{H}{a} - 0.18 \qquad \text{(A.4)}$$

Friction and other piles:

$$C_c = 1.5\frac{H}{a} - 0.07 \qquad \text{(A.5)}$$

Where:

p'_c	kPa	Load part in kPa that is transferred directly to the pile. $p'_c = A/A_p$ where A (kN) is the load part directly on the pile as shown in Figure A.1and A_p (m^2) is the area of the pile; $A_p = a^2$.
σ'_v	kPa	Average vertical effective stress directly above the pile cap
C_c	-	Arching coefficient adapted by Jones et al. (1990) for the piled embankment
a	m	Size of pile cap, or the equivalent size side in the case of circular piles
H	m	Height of fill above reinforcement

A.2.2.3. Determining load parts B and C in BS8006

Load part *A* has been determined in the previous chapter. This result can be used to determine load parts *B* and *C*. BS8006 assumes that the subsoil will not support the embankment over time. Therefore, $C = 0$ kN/pile in any design calculation with BS8006.

This is a conservative (i.e. safe) assumption. Assumptions using $C > 0$ kN/pile can lead to unsafe situations unless it can be proven that this case will exist in the field. For example, a future groundwater level decrease can result in sufficient settlement to loosen any subsoil support, or a working platform placed on the subsoil before pile installation may cause settlements below the mattress.

In other cases where it can be proven that minimal settlements are expected, calculations can reasonably include some subsoil support, as in the German EBGEO. To validate design calculation methods with field tests, it is in any case necessary that calculations include subsoil support. This is because a considerable degree of subsoil support has been measured in the available field studies (in the Netherlands for example, in the N210 project (Haring et al. (2008), a rail road project in Houten (Van Duijnen et al., 2010), and in the Kyoto Road project (Van Eekelen et al., 2010a)). Although this support was measured during monitoring, it may disappear in future years.

Chapter A.2.2.2 explains how *A* is determined and also that BS8006 assumes $C = 0$ kN/pile. This makes it possible to calculate *B* from the vertical equilibrium. The total load (kN/pile) on one square *s·s* is:

$$\left(\gamma H + p\right)s^2 \tag{A.6}$$

Where $s\ (= s_{x,y})$is the pile spacing in m, as shown in Figure A.3.
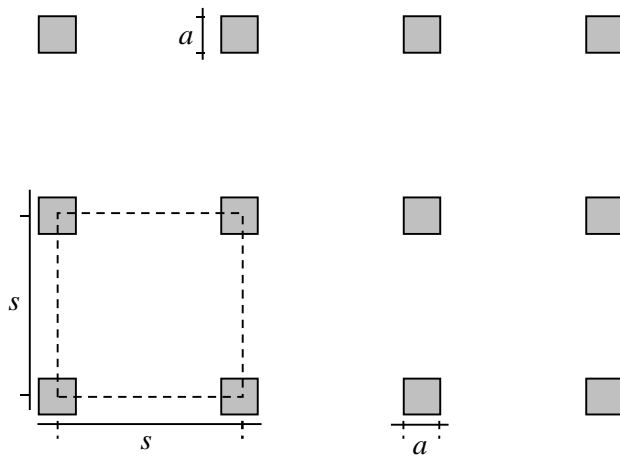
Figure A.3 Definition of *s* and *a*.

Load part *A* (kN/pile) transferred directly to the piles is:

$$A = p'_c\, a^2 \tag{A.7}$$

where p'_c is calculated from equation (A.2). Load part *B* (in kN/pile) on the geosynthetic reinforcement is:

$$B = p'_r\left(s^2 - a^2\right) \tag{A.8}$$

where

p'_r	kPa	Pressure on GR. $p'_r = (B+C)/(s^2\text{-}a^2)$ with $B+C$ (kN) shown in Figure A.1 and $(s^2\text{-}a^2)$ (m^2) is the area of the GR. In BS8006, $C = 0$, so $p'_r = B/A_r$
B	kN/pile	Load part that is transferred through the geosynthetic reinforcement to the pile

225

When the subsoil support is zero, vertical equilibrium gives B_t = total load - A:

$$p'_r \left(s^2 - a^2 \right) = \left(\gamma H + p \right) s^2 - p'_c \, a^2 \tag{A.9}$$

and thus,

$$p'_r = \frac{\left(\gamma H + p \right) s^2 - p'_c \, a^2}{s^2 - a^2} = \left(\gamma H + p \right) X \tag{A.10}$$

where X is a grouped variable [-]:

$$X = \frac{\left(s^2 - a^2 \dfrac{p'_c}{\gamma H + p} \right)}{s^2 - a^2} \tag{A.11}$$

It should be noted that the equations given so far all use a fully 3-dimensional configuration (an embankment on piles has a 3D configuration, in contrast to an embankment on walls that has a 2D configuration, as shown in Figure A.4).

a. *Jones/BS8006: 2D*   b. *BS8006: 3D*

Figure A.4 (*a*) The equations for the line load W_T in BS8006 are determined using the 2D configuration, (*b*) For safety reasons, BS8006 applies these equations (with the total load on the GR) for each strip in both directions while changing the analysis to the 3D configuration.

A.2.3 Step 2: concentration of load part B on the reinforcement strips between the pile caps

A.2.3.1 Calculation of the line load WT for a 2D configuration
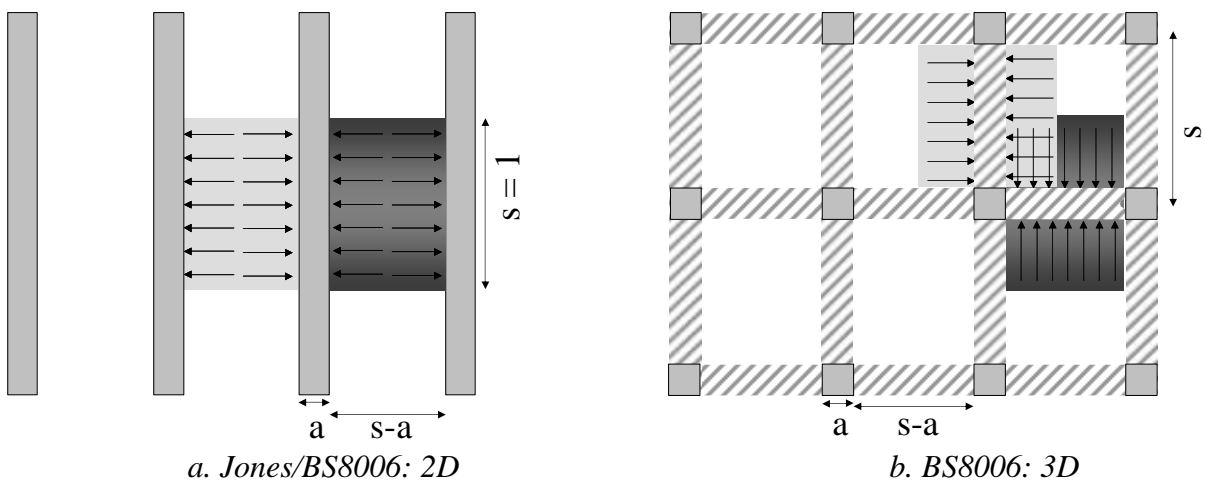BS8006 assumes that the vertical load on the GR is carried only by the GR strips between two adjacent pile caps. These 'strips' are shown shaded in Figure A.4*b*. It is assumed that only very limited strain and tensile stress occur in the reinforcement between these strips.

Jones et al. (1990) determined this line load W_T for the 2D configuration, as shown in Figure A.4a. The strip with width *s* is intended to carry the entire load that rests on a square *(s-a) s*. Here, *s* is unity (1 m). This only becomes relevant in the 3D case. Thus Jones et al. find:

$$p'_r(s-a)s = W_T(s-a) \quad \rightarrow \quad p'_r = \frac{W_T}{s} \quad or \quad W_T = s\,p'_r \tag{A.12}$$

Where: W_T (kN/m): In the 3D case (Figure A.4*b*): Line load resting on the reinforcement strip in between two piles. For the 2D case (Figure A.4*a*): evenly distributed load acting on the reinforcement across its span between two supporting walls per unit length of wall, with unity width *s* = 1m. This is in agreement with, for example, Le Hello (2007).

Although the width of the GR strip *s* in the 2D case is unity 1 m, the line load is first calculated for a strip without width. BS8006 then reintroduces this width in the equations, see equation (A.23).

Combining equation (A.12) with the vertical equilibrium in equation (A.10) gives:

$$W_T = s(\gamma H + p)X \tag{A.13}$$

with the grouped variable *X* given in equation (A.11). Note that equation (A.13) is a mixture of the 3D-equilibrium equation (A.10) and the 2D (plane strain) line load equation (A.12).

Equations (A.13) and (A.11) agree with equation (2) of Jones et al. (1990). BS8006-1:2010 adopts these equations to express the line load in the second equation on page 186 (Chapter 8.3.3.7.1). This expression for the line load is for the case *H ≤ 1.4 (s-a)*, which is referred to as 'partial arching' throughout this paper. Chapter A.2.4 explains the concepts of 'partial arching' and 'full arching'.

A.2.3.2. Double application of the line load W_T for a 3D configuration

Jones et al. (1990) derived the equation for the line load W_T equation (A.13). BS8006 adopts this nearly-plane strain equation. However, BS8006 uses the recommendation of Jones et al. that this line load should be calculated both to the GR strips perpendicular to the load axis, and to the GR strips along the road axis, as shown in Figure A.4*b*. This means that the analysis has now changed to the 3D case by calculating the load resting on the GR twice. Jones et al. made this choice to guarantee sufficient safety, an understandable decision for a first design standard in the nineties.

Figure A.4*a*. shows the plane strain situation where the vertical equilibrium is satisfied. However, BS8006 uses Figure A.4*b*, where the vertical equilibrium is not satisfied. Equation (A.13) from BS8006 for line load can be used to calculate the average load on the GR, load part *B*, and the pile efficiency E_p.

This paper defines load part *B* as the load transferred through the GR to the piles, in kN per pile. Two GR strips lie in one *s·s* square, so that *B* can be determined using equation (A.13) of BS8006:

$$B = 2W_T(s-a) = 2s(\gamma H + p)(s-a)X \tag{A.14}$$

Note that this equation for *B* does not agree with (A.8). Vertical equilibrium no longer exists. The average stress on the reinforcement resulting from the BS8006 equations is:

$$p'_r = \frac{B}{s^2 - a^2} = \frac{2W_T}{s+a} = \frac{2s(\gamma H + p)}{s+a}X \tag{A.15}$$

This gives a pile efficiency E_p ($^{kN/pile}/_{kN/pile}$):

$$E_p = 1 - \frac{B}{w_{tot}} = 1 - \frac{2s(\gamma H + p)(s-a)X}{s^2(\gamma H + p)} = 1 - \frac{2(s-a)}{s}X \tag{A.16}$$

A.2.4 Step 3: assuming the existence of full arching.

BS8006 assumes the existence of full arching, analogous to McKelvey (1994) who assumes the existence of a 'plane of equal settlement'. The assumption is as follows: when the embankment is sufficiently high for the arch to develop fully, then the entire load from above the arch will be transferred directly to the piles. Reinforcement in the bottom of the embankment will thus not 'feel' the traffic load or an increasing embankment height.

BS8006 assumes that full arching occurs as soon as the height of the embankment is greater than the arch height. The arch height is estimated to be equal to the diagonal distance between the pile caps, thus 1.4*(s-a)*, see Figure A.5.
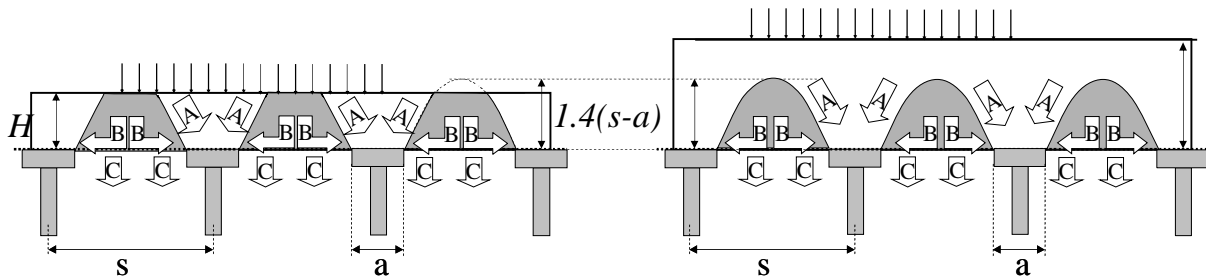

Figure A.5 left: partial arching, right: full arching.

BS8006 assumes, with the assumption of full arching, that the load on the GR reaches a maximum when the height of the fill is increased. Several field measurements are available to validate the partial-arching situation ($H < 1.4(s-a)$), as shown in Chapter A. 6 and, for example, in Van Duijnen et al, 2010 and Haring et al., 2008). Jenck et al. (2005) compare BS8006 with 2D tests and concludes that *A* is strongly overestimated when H increases beyond full arching. In any case, insufficient data are available to satisfactorily prove the existence of full arching for a thick embankment with a basal GR.

The finite element calculations in Chapter A. 5 do not show the existence of full arching. The assumption of full arching may lead to relatively low calculated tensile forces. BS8006-1:2010 solves this by requiring that the GR should be designed to carry at least a practical minimum proportion of the embankment loading equivalent to 15% (see page 188 of BS8006-1:2010).

BS8006 elaborates full arching as follows: as soon as *H > 1.4(s-a),* the traffic load is no longer calculated to the reinforcement but is simply set to zero (*p = 0*) in the original partial-arching equation (A.13). Furthermore, the weight of the embankment above *1.4(s-a)* is no longer calculated for, so that *H* in equation (A.13) is replaced by its maximum, namely *1.4(s-a).* In this way, the equation for the line load W_T for full arching (for *H > 1.4(s-a)*) of BS8006 can be found (see BS8006-1:2010 page 186):

$$W_T = 1.4s\gamma\left(s-a\right)X \tag{A.17}$$

where *X* is given in equation (A.11).

Equation (A.17) from BS8006 for the full-arching line load can be used to derive the average load p'_r on the GR, load part *B,* and the pile efficiency E_p. This can be

used to derive the average load on the GR p'_{rt}, for the 2D configuration given in Figure A.4*a* and equation (A.12):

$$p'_{rt} = \frac{W_T}{s} = 1.4\gamma (s - a) X \tag{A.18}$$

However, W_T is calculated twice, in the same way as for partial arching, as shown in Figure A.*4b*. This therefore results in

$$p'_r = \frac{2W_T}{s+a} = \frac{2.8 s \gamma (s - a)}{s+a} X \tag{A.19}$$

and *B* (in kN/pile) for full arching, see equation (A.14):

$$B = 2W_T (s - a) = 2.8 s \gamma (s - a)^2 X \tag{A.20}$$

This gives a pile efficiency E_p ($^{kN/pile}/_{kN/pile}$):

$$E_p = 1 - \frac{B}{w_{tot}} = 1 - \frac{2.8 s \gamma (s - a)^2 X}{s^2 (\gamma H + p)} = 1 - \frac{2.8 \gamma (s - a)^2}{s (\gamma H + p)} X \tag{A.21}$$

A.2.5 Step 4: from line load to tensile force

The equally-distributed load W_T on the GR strip without width is determined in steps 2 and 3 (equations (A.13) and (A.17)). The tensile force *T* in the GR strip can be derived from this W_T. For this purpose, the GR strip is modelled as a tension membrane and the following assumptions are made:

- there is no subsoil support
- the line load W_T is equally distributed
- the GR strip fixed at the sides of the pile caps
- the tensile force is calculated at the side of the pile cap and is therefore a maximum (not an average, as in the German EBGEO).

The first two assumptions result in a parabola-shaped deformed tension membrane, as shown in Appendix A.A. It is noted that several researchers (for example Van Eekelen et al, 2011b) found that the greatest load is concentrated around the edges of the pile caps. This means that the assumption of equal load distribution is closer to reality than some other commonly-used models, such as the triangular shaped load in EBGEO (2010).

Appendix A.A shows how a differential equation for the tension membrane is derived and solved, resulting in the tensile force T in kN in the GR strip (the strip has a zero width):

$$T = \frac{W_T(s-a)}{2}\sqrt{1+\frac{1}{6\varepsilon}} \qquad (A.22)$$

Dividing this by the width a of the GR strip then gives the tensile force T_{rp} in the strip with width a in kN/m:

$$T_{rp} = \frac{W_T(s-a)}{2a}\sqrt{1+\frac{1}{6\varepsilon}} \qquad (A.23)$$

Here, the (estimated) strain ε is an input parameter to calculate the tensile force T_{rp}. The apparent stiffness of the geosynthetic reinforcement can therefore be calculated as:

$$J = \frac{T_{rp}}{\varepsilon} \qquad (A.24)$$

A.2.6 Different interpretations of BS8006 from literature

Chapter A.2.3 showed that the BS8006 equations are based on 3D equilibrium equations as well as 2D equations, to concentrate the load in line loads on the GR strips. Furthermore, the load on the GR is calculated twice. Several authors have interpreted BS8006 in order to compare it with other models.

For example, Abusharar et al. (2009) and Le Hello (2007) assumed that the equations were developed for a fully 2D configuration. Love and Milligan (2003), Stewart (2005), and Russell and Pierpoint (1997) on the other hand assumed that the equations were developed for a 3D configuration. These interpretations are elaborated and compared in appendix A.B.

A. 3   Proposal for improving the BS8006

A.3.1 Combining a 3D configuration and 3D determination of the line load

For quite thin embankments in particular, BS8006 designs a relatively strong and thus expensive geosynthetic (basal) reinforcement in comparison with other design models. These differences are not always fully understood, leading to uncertainty. The previous chapter has demonstrated that one of the main reasons is that calculations using BS8006 are based on a higher load than the existing load.

This chapter proposes a modification of the British Standard BS8006. In this Modified BS8006, the calculation for the load on the GR is only incorporated once. Also, the line load is calculated according to the 3D configuration given in Figure A.6.
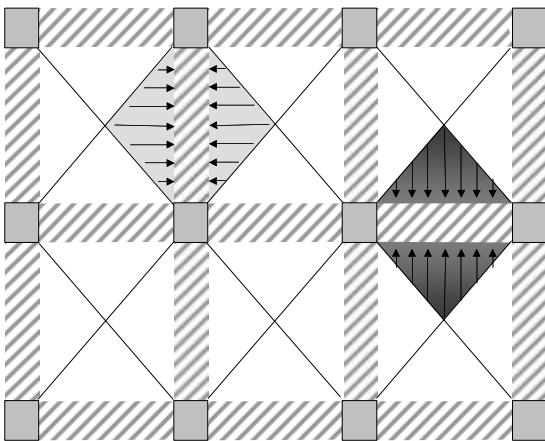
Figure A.6 Calculation of the load to the GR strips in Modified BS8006.

In this case, a GR strip carries half of the load on one square $s \cdot s$, which gives:

$$p'_r\left(s^2 - a^2\right) = 2W_T(s - a) \tag{A.25}$$

The difference between BS8006 and Modified BS8006 is the assumed unsupported area that transfers the tensile loads onto the reinforcement strip between adjacent pile caps. BS8006 calculates this as $s(s-a)$, see Figure A.4*b*. Figure A.6 calculates this as $\dfrac{s^2 - a^2}{2} = \left(\dfrac{s+a}{2}\right)(s-a)$. The area ratio of BS8006 (Figure A.4*b*)/BS8006 modified (Figure A.7) is: $\left(\dfrac{2s}{s+a}\right)$.

If we take as an example $s = 4$ m and $a = 1$ m, then the previous ratio = 1.6. In this example, BS8006:1995 therefore utilises a total unsupported area 60% greater than the modified BS8006 proposal, and thus will calculate a reinforcement tension some 60% greater for this particular pile cap size and spacing geometry. This is the main basis for the difference between BS8006:1995 and the proposed BS8006 modified method.

A.3.2 Partial arching

Calculating vertical equilibrium for Figure A.6 gives (see equation (A.10)):

$$p'_r = (\gamma H + p) X \tag{A.26}$$

The line load W_T should be calculated according to equation (A.25):

$$W_T = \tfrac{1}{2} p'_r (s + a) \tag{A.27}$$

Combining these equations gives the basic equation for the line load W_T for the Modified BS8006 model:

$$W_T = \tfrac{1}{2} (\gamma H + p)(s + a) X \tag{A.28}$$

The average load p'_r on the GR, load part *B*, and the pile efficiency E_p can be derived using this basic Modified BS8006 equation. The following p'_r (kN/pile) is found:

$$p'_r = \frac{2W_T}{(s + a)} = (\gamma H + p) X \tag{A.29}$$

This gives the following *B* (kN/pile):

$$B = p'_r * A_r = \frac{2W_T}{(s + a)}(s^2 - a^2) = 2W_T (s - a) = (\gamma H + p)(s^2 - a^2) X \tag{A.30}$$

This in turn gives a pile efficiency E_p ($^{kN/pile}/_{kN/pile}$):

$$E_p = 1 - \frac{B}{w_{tot}} = 1 - \frac{(\gamma H + p)(s^2 - a^2) X}{s^2 (\gamma H + p)} = 1 - \frac{(s^2 - a^2)}{s^2} X \tag{A.31}$$

A.3.3 Full arching

The assumption of full arching can be applied to the Modified BS8006. However, it has already been argued in Chapter A.2.4 that the assumption of full arching may lead to relatively low calculated tensile forces, which is solved in BS8006 as shown in Chapter A.2.4. If the Modified BS8006 applies full arching, the tensile forces may even decrease. These equations should therefore only be applied with great care. Further validation of the full-arching theory is recommended. If full arching is assumed in the Modified BS8006, $p = 0$ kPa and $H = 1.4(s-a)$ are used in equation (A.28):

$$W_T = 0.7\, \gamma \left(s^2 - a^2 \right) X \tag{A.32}$$

The average load p'_r on the GR, load part B, and the pile efficiency E_p can be derived using this basic Modified BS8006 equation. The following p'_r (kN/pile) is found:

$$p'_r = \frac{2W_T}{(s+a)} = 1.4\gamma (s-a) X \tag{A.33}$$

This gives the following B (kN/pile):

$$B = p'_r * A_r = \frac{2W_T}{(s+a)}\left(s^2 - a^2\right) = 2W_T (s - a) = 1.4\gamma (s-a)\left(s^2 - a^2\right) X \tag{A.34}$$

This in turn gives a pile efficiency E_p ($^{\text{kN/pile}}/_{\text{kN/pile}}$):

$$E_p = 1 - \frac{B}{w_{tot}} = 1 - \frac{1.4\gamma (s-a)\left(s^2 - a^2\right) X}{s^2 (\gamma H + p)} = 1 - \frac{\left(s^2 - a^2\right)}{s^2} X \tag{A.35}$$

Table A.1 summarises the assumptions and starting points of Jones' equations, BS8006, and the Modified BS8006. The proposed modification gives a fully 3D elaboration and a correct vertical equilibrium.

A.3.4 Different pile spacing along and perpendicular to road axis

This chapter gives the equations for the Modified BS8006 if the pile spacings along and perpendicular to the road axis are not equal; $s_x \neq s_y$. The grouped variable X in equation (A.11) changes in:

$$X \quad = \quad \frac{\left(s_x s_y - a^2 \dfrac{p'_c}{\gamma H + p} \right)}{s_x s_y - a^2} \qquad\qquad (A.36)$$

Table A.1 Summary of the assumptions and starting points of Jones' equations, the original BS8006, and the Modified BS8006.

	Jones[a] Plane strain	BS8006	Modified BS8006
1. calculate load part A that passes directly to the piles (based on Marston and Anderson, equation (A.2)).	Marston (equation (A.2))	Marston (equation (A.2))	Marston (equation (A.2))
2. support of subsoil?	no	no	no
3. calculate load part B_t on the reinforcement	3D equilibrium	3D equilibrium	3D equilibrium
4. concentrate load part B on the reinforcement in between the pile caps	2D geometry	2D geometry	3D geometry
5. double the load on the reinforcement, by applying line load to both directions along and perpendicular to the road axis	only 2D, thus only one direction considered	yes	no
6. for comparison between the models: calculate back the load on the reinforcement from the line load	2D geometry	differs per author[b]	3D geometry
7. vertical equilibrium? For partial arching	Yes	No	Yes
8. vertical equilibrium? for full arching	No	No[c]	No

[a] Jones et al. concentrated on a 2D method because the finite element studies developed for the paper could only model in plane strain, i.e. 2D. This does not mean that Jones et al were proposing a 2D design approach, as explained in Chapter A.2.3.2.

[b] see appendix A.B, for example Abusharar et al. (2009) and Le Hello (2007) use a 2D geometry, whereas Love and Milligan (2003), Stewart (2005) and Russell and Pierpoint (1997) use a 3D geometry, Chen et al. (2008a).use an alternative 2D approach.

[c] as recognized by Cornet and Horgan, 2010, in the paper in which they present the differences between BS8006:1995 and BS8006:2010.
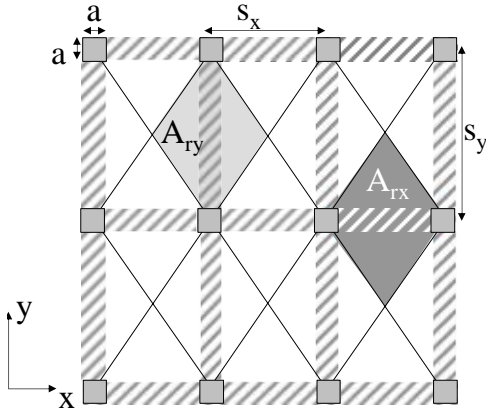
Figure A.7 Pile spacing $s_x \neq s_y$

The GR areas A_{rx} and A_{ry}, with $s_y > s_x$, of Figure A.7 are:

$$A_{rx} = \tfrac{1}{2}\left(s_x s_y - a^2\left(2 - \frac{s_x}{s_y} \right) \right)$$

$$A_{ry} = \tfrac{1}{2}\left(s_x s_y - a^2 \frac{s_x}{s_y} \right)$$

(A.37)

The strips in the *x*- and *y*-directions carry the load p'_r on areas A_{rx} and A_{ry} respectively.

$$p'_r A_{rx} = W_{Tx}\left(s_x - a \right)$$

$$p'_r A_{ry} = W_{Ty}\left(s_y - a \right)$$

(A.38)

Using equation (A.10) it follows:

$$W_{Tx} = \frac{\left(\gamma H + p \right) X A_{rx}}{s_x - a}$$

$$W_{Ty} = \frac{\left(\gamma H + p \right) X A_{ry}}{s_y - a}$$

(A.39)

with A_{rx} and A_{ry} and X given in equations (A.36) and (A.37).
For full arching, the height of the arch should equal the diagonal pile spacing, giving the full-arching equation (for $H > \sqrt{s_x^2 + s_y^2}$):

$$W_{Tx} = \frac{\gamma \sqrt{s_x^2 + s_y^2}\, X A_{rx}}{s_x - a}$$

$$W_{Ty} = \frac{\gamma \sqrt{s_x^2 + s_y^2}\, X A_{ry}}{sy - a}$$

(A.40)

A. 4 Summary plane strain, BS8006 and Modified BS8006

Table A.2 and Table A.3 summarise the plane strain equations, BS8006 and the Modified BS8006. For BS8006, the vertical equilibrium is not correct. In the case of the Modified BS8006, the vertical equilibrium is correct for partial arching but not for full arching.

Table A.2 Partial arching.

		plane strain	BS8006 (Jones et al.)	Modified BS8006
total load w_{tot} per pile area	kN/pile	$s^2(\gamma H + p)$	$s^2(\gamma H + p)$	$s^2(\gamma H + p)$
line load on reinforcement strip W_T	kN/m	$s(\gamma H + p)X$	$s(\gamma H + p)X$	$0.5(\gamma H + p)(s+a)X$ [a]
average pressure p'_r on geosynthetic reinforcement	kPa	$\dfrac{W_T}{s} = (\gamma H + p)X$	$\dfrac{2W_T}{s+a} = \dfrac{2s(\gamma H + p)}{s+a}X$	$\dfrac{2W_T}{s+a} = (\gamma H + p)X$
load part B on geosynthetic reinforcement	kN/pile	$(s-a)(\gamma H + p)X$	$2s(s-a)(\gamma H + p)X$	$(s^2 - a^2)(\gamma H + p)X$
pile efficiency $E_p = 1 - B/w_{tot}$	kN/kN	$1 - \dfrac{(s-a)}{s^2}X$	$1 - \dfrac{2(s-a)}{s}X$	$1 - \dfrac{(s^2 - a^2)}{s^2}X$

[a] if $s_x \neq s_y$, see equations (A.39) and (A.36).

With: $X = \dfrac{\left(s^2 - a^2 \dfrac{p'_c}{\gamma H + p}\right)}{s^2 - a^2}$

Table A.3 Full arching.

		Plane strain	BS8006 (Jones et al)	Modified BS8006
total load w_{tot} per pile area	kN/pile	$s^2(\gamma H + p)$	$s^2(\gamma H + p)$	$s^2(\gamma H + p)$
line load on reinforcement strip W_T	kN/m	$1.4s\gamma(s-a)X$	$1.4s\gamma(s-a)X$	$0.7\gamma\left(s^2 - a^2\right)X$
average pressure p'_r on geosynthetic reinforcement	kPa	$\dfrac{W_T}{s} = 1.4\gamma(s-a)X$	$\dfrac{2W_T}{s+a} = \dfrac{2.8s\gamma(s-a)}{s+a}X$	$1.4\gamma(s-a)X$
load part B on geosynthetic reinforcement	kN/pile	$1.4\gamma(s-a)^2 X$	$2.8s\gamma(s-a)^2 X$	$1.4\gamma(s-a)\left(s^2 - a^2\right)X$
pile efficiency $E_p = 1 - B/w_{tot}$	kN/kN	$1 - \dfrac{1.4\gamma(s-a)^2}{s^2(\gamma H + p)}X$	$\dfrac{2.8\gamma(s-a)^2}{s(\gamma H + p)}X$	$1 - \dfrac{1.4\gamma(s-a)\left(s^2 - a^2\right)}{s^2(\gamma H + p)}$

A. 5   Comparison with finite element calculations.

A.5.1 Geometry and properties

This chapter compares the results of finite element calculations (Plaxis) and the Modified BS8006, BS8006, and EBGEO. Moreover, parameter variation demonstrates the influence exerted by the properties of these models. Table A.4 shows the properties of the piled embankment's basic geometry (also see Van Eekelen and Jansen, 2008). Comparison calculations in this paper only consider the tensile forces due to the vertical load. Spreading forces are ignored.

Table A.4 Properties of basic geometry example calculation.

end-bearing or friction piles			end bearing
does the subsoil provide support? modulus of subgrade reaction	k	kN/m^3	no support: $k = 0$ kN/m^3
height embankment (between top pile cap and road surface)	H	m	1.25
centre-to-centre distance piles (along and perpendicular to road axis)	$s_x=s_y$	m	1.75
diagonal centre-to-centre distance	s_d	m	2.47
(equivalent) diameter pile caps	d	m	0.50 m
(equivalent) width pile cap	a	m	0.44 m
area pile caps		m^2	0.20 m^2
material fill			granular material
material fill volume weight	γ	kN/m^3	20
material fill internal friction angle	φ	deg	37.5
permanent weight asphalt and foundation layer		kPa	6
traffic load	p	kPa	30
long-term tensile stiffness geosynthetic reinforcement, along road axis[a].	J	kN/m	1500

[a] In the BS8006 calculations, the input strain is adapted until the calculated tensile stiffness of the reinforcement is equal to $J = 1500$ kN/m (calculated using equation (A.61)).

Table A.5 Parameters of finite element calculations.

	γ	E'_{50}[a]	E_{ur}	φ	C	ψ	OCR	λ	κ	μ
	kN/m^3	MPa	MPa	deg	kPa	deg	-	-	-	-
model 1: simple model										
granular material	20	20	80	37.5	1	7.5	-		-	-	-
model 2: more sophisticated model										
granular material	20	150	600	37.5	1	7.5	-		-	-	-
soft clay	13	-	-	-	-	-	1.1 1.2	0.067	0.009	0.0033
stiff sand layer	20	50	200	35	1	5	-		-	-	-

[a] $E'_{50} = E'_{oed}$

For the geometry of this pile field (s = 1.75 m and d = 0.5 m), the transition between partial and full arching according to BS8006 is where
H = 1.4(s-a) = 1.4(1.75-0.44) = 1.89 m, and the minimum embankment height according to the BS8006 is H = 0.7(s-a) = 0.7(1.75-0.44) = 0.92 m. In practice, the geometry of many piled embankments falls within the 'partial arching' area.

A.5.2 Finite element calculations

Two types of axial symmetric calculations were carried out using finite element analysis. The first is a relatively simple model (1). The second (2) is more sophisticated and was carried out to validate the first calculation (Van Eekelen and Jansen, 2008).

1. The soft subsoil was ignored (switched off). A one-metre-long pile was modelled.
2. The soft subsoil was modelled using the Softsoil-creep model. The support provided by the (drained) subsoil creeps away below the reinforcement. In the final situation, the subsoil is no longer carrying any load.

In both models, the Hardening Soil model was applied to model the granular fill. Table A.5 shows the calculation parameters.

The geosynthetic reinforcement is modelled without interface elements, resulting in maximal friction between granular material and the GR.
The calculations show that models 1 and 2 give very similar results (less than 10% difference in the total forces on the pile caps and the tensile forces in the GR). The figures therefore only give the results of the simple FE analysis (1).

A.5.3 Results of calculation comparison

Table A.6 shows the calculated tensile forces for the properties given in Table A.4. The Modified BS8006 and EBGEO correlate quite closely, agreeing more with the FE analysis than with BS8006. It is noted that the 3D calculations of BS8006, Modified BS8006 and EBGEO are different from the axial symmetric FE analysis. A 3D FE analysis will calculate locally higher tensile loads than an axial symmetric analysis. It is expected that 3D FE analysis will lead to reinforcement loads similar to the EBGEO and modified BS8006 results.

Table A.6 Calculated tensile forces for the properties given in Table A.4.

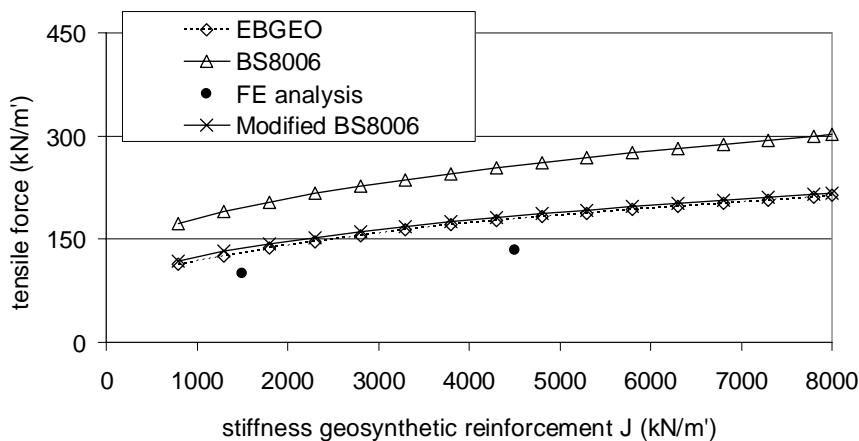|	Tensile force (kN/m)
BS8006	196
Modified BS8006	137
EBGEO	130
FE analysis axial symmetric	101

Figure A.8 Tensile force with varied stiffness geosynthetic reinforcement J. Comparison of FE analysis, EBGEO, BS8006 and Modified BS8006 (only partial arching occurs here due to the geometry).

Figure A.8 to Figure A.11 present several variation studies. In Figure A.8 and Figure A.9, the geosynthetic reinforcement and the internal friction angle of the fill are varied respectively. The geometry shown in Table A.4 means that only partial arching occurs, as $H = 1.25 < 1.4(s\text{-}a) = 1.89$. In Figure A.8, the tensile force predicted by the Modified BS8006 and EBGEO is virtually identical. These predictions are also comparable for Figure A.9, although EBGEO is dependent on the internal friction angle of the fill and BS8006 is not. The influence of the internal friction angle on the EBGEO results is obviously limited. In both figures, the Modified BS8006 and EBGEO predict a higher tensile force than the

FE analysis. The prediction given by BS8006 is much higher as the load on the GR is included twice, as explained in Chapter A.2.3.2.
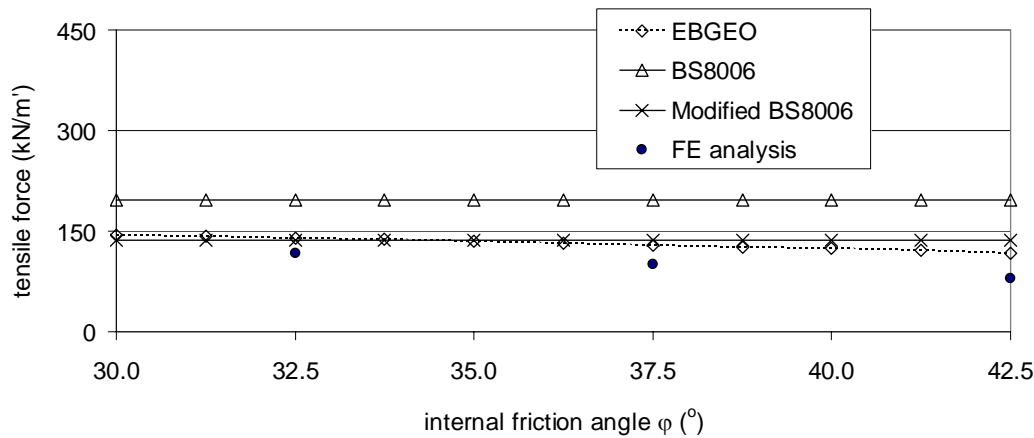
Figure A.9 Tensile force with varied internal friction angle φ of fill.

Figure A.10 varies the embankment height H. The characteristic dip in the BS8006 calculations shows the transition between partial and full arching (for full arching, the top load p is suddenly set to zero, as explained in Chapter A.2.4). Lawson (1995) provides a solution to 'smooth' this dip, so that the transition between partial and full arching is more gradual. For partial arching (left of the dip), the BS8006 prediction is much higher than the Modified BS8006, EBGEO, or the FE analysis. This is again due to the fact that the load on the GR is calculated twice.
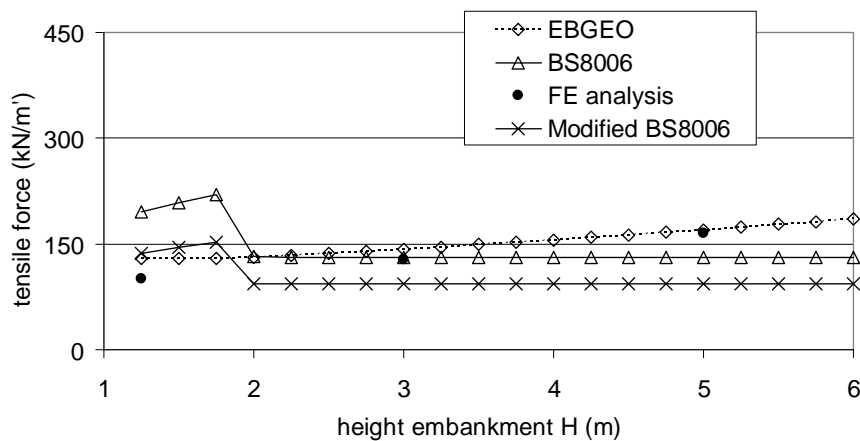
Figure A.10 Tensile force with varied embankment height. Comparison of FE analysis, EBGEO, BS8006, and Modified BS8006 (the transition from full to partial arching is at $H = 1.4(s\text{-}a) = 1.89$ m).

For full arching (right of the dip), the tensile forces of both BS8006 and the Modified BS8006 suddenly decrease as traffic load is no longer 'felt' on the GR. The tensile forces remain constant with increasing embankment height, while the difference with the FE analysis and EBGEO increases. These axial symmetric FE

analysis does not take into account the 'absolute full arching' mechanism as in BS8006. As a result, the FE analysis does not find an embankment height where the tensile force in the GR no longer increases if the height is raised. The full-arching assumption is therefore not included in Figure A.11. This figure is identical to Figure A.10, but full arching is not assumed. The equations of partial arching ($H < 1.4(s-a)$) are therefore applied for the whole figure. The Modified BS8006 now agrees more closely with the FE analysis than BS8006, but EBGEO still agrees most closely for the higher embankments. This shows the need to further validate the calculation rules for high embankments, and to assume full arching.
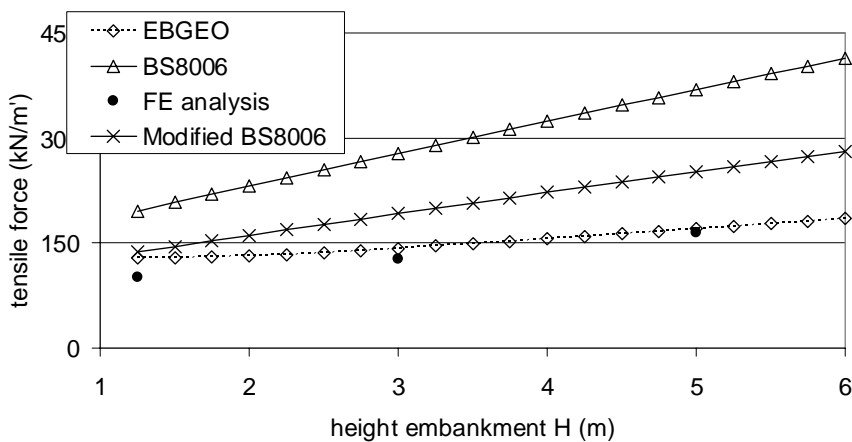
Figure A.11 Identical to Figure A.10, but without 'full arching'. Variation in embankment height *H*.

A. 6   Comparison with field test measurements

A.6.1 The Kyoto Road

A.6.1.1.Geometry
The 'Kyoto Road' in Giessenburg, the Netherlands is a large-scale field test. Figure A.12 shows the geometry. The system consists of 13-m-long timber piles positioned centre-to-centre 1.27x1.27 m^2, concrete pile caps (measuring 0.3 m in diameter), geogrid reinforcement, and 1.15 m of compacted fill (silty sand mixture).

Two geogrid layers were constructed: Fortrac® 350/30-30 M along the road axis (bottom) and Fortrac® 400/30-30 M across. Figure A.13 shows their isochrones, which can be used to determine the time-dependent tensile stiffness *J* (Table A.7, with a strain of 2%).
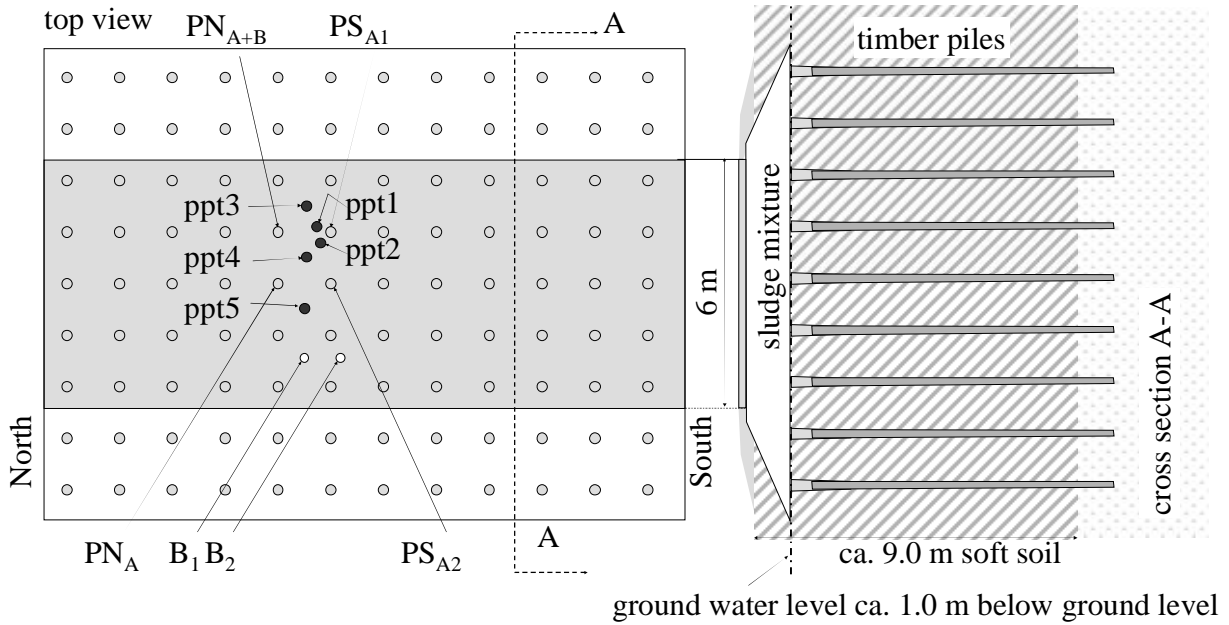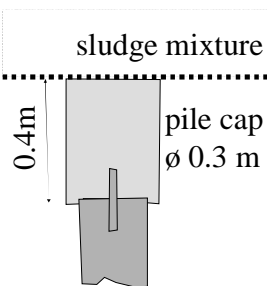
Figure A.12 Layout of the Kyoto Road.

Figure A.13 Isochrones of the applied geogrids, source: Huesker Synthetic GmbH.

Table A.7 Tensile stiffness of the Kyoto Road geogrid reinforcement.

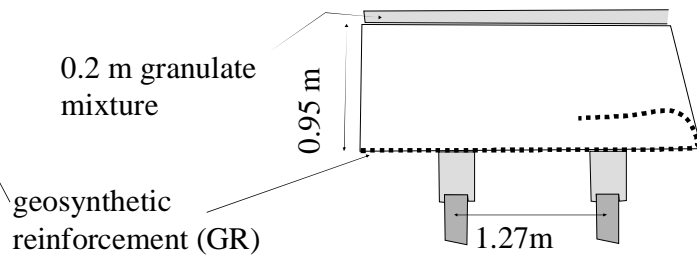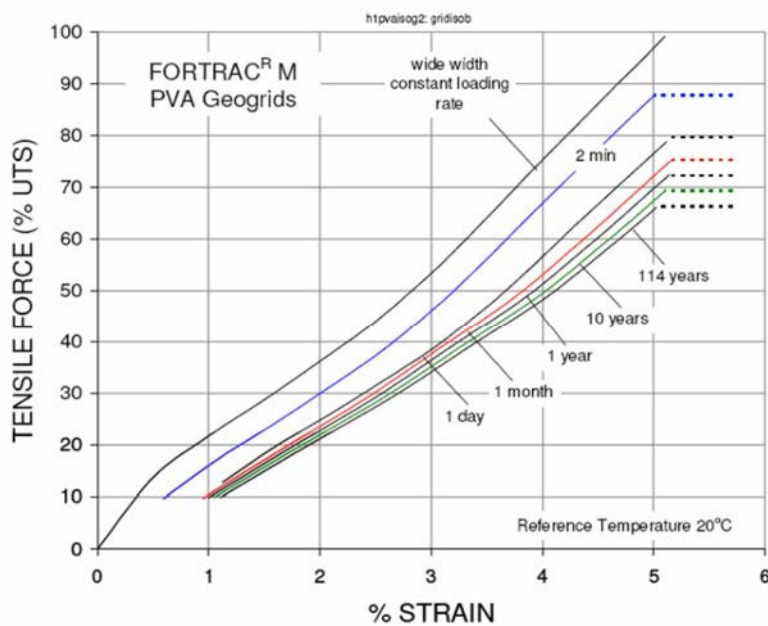| along road axis / perpendicular to road axis	time under load	ultimate tensile strength UTS (kN/m)	tensile stiffness J^a (kN/m)
along	1 day	350	(25.0/2) 350 = 4375
perpendicular	1 day	400	(25.0/2) 400 = 5000
along	1 year	350	(22.8/2)·350 = 3990
perpendicular	1 year	400	(22.8/2) 400 = 4560
along	10 years	350	(22.1/2) 350 = 3868
perpendicular	10 years	400	(22.1/2) 400 = 4420

[a] $J = $ (% of UTS / strain) · UTS, values at 2% strain

Table A.8 Young's moduli of subsoil.

		thickness	E
		m	kPa
top layer	peat	$d1 = 1.45$ m	1077
second layer	clay	$d2 = 1.50$ m	2000

A.6.1.2. Subsoil

The local soil was excavated up to a depth of 1.15 m to remove broken rubble. The Kyoto Road was constructed immediately afterwards in less than four days. Therefore, the subsoil was not able to swell before the piles and embankment were in place. Table A.8 shows Young's moduli E as determined from the drained compression tests carried out before construction (values below pre-consolidation stress). From this, the modulus of subgrade reaction k can be calculated:

$$k = \frac{E_1 E_2}{E_1 d_2 + E_2 d_1} = \frac{1077 \cdot 2000}{1077 \cdot 1.5 + 2000 \cdot 1.45} = 477 \; kN \, / \, m^3$$

This value is probably lower than in practice, because the subsoil did not swell fully between excavation and construction. Furthermore, the effective stress will be lower at the end of construction than the initial stress, so the subsoil should behave more stiffly.

A.6.1.3 Properties of fill

The fill consists of a dredged silty sand containing some additives (mainly clay and cement). This fill type was used because the re-use of waste material is environmental-friendly. Non-cohesive granular material is normally used for embankment fills. Table A.9 shows the fill properties.

Table A.9 Properties of fill. (γ unit weight, W water content, K_v the vertical permeability, φ internal friction angle and c cohesion)

γ_{wet}	γ_{dry}	$\gamma_{average}$	W	K_v	φ	c
kN/m^3	kN/m^3	kN/m^3	%	m/s	deg	kPa
22.2	17.0	18.6	18.1	2.1 E-9	33.8	11.5

A.6.2 Monitoring and prediction

A.6.2.1 Monitoring

The monitoring results are reported in Van Eekelen et al. (2010a). Monitoring from November 2005 to May 2009 included the total forces on top of piles – both above the reinforcement (PS_A and PN_A in Figure A.12) and below the reinforcement (PN_{A+B}), – the groundwater level, and the pore pressures below the embankment (locations of the piezometers (ppt) in Figure A.12). This paper focuses on comparing measured load distribution with predictions from BS8006, the Modified BS8006, and EBGEO.

A.6.2.2. Comparison of measurements and predictions

Figure A.14 and Table A.10 compare the measured and predicted values for *A, B* and *C*. The tensile forces were not measured. The five predictions in Table A.10 are:

- BS8006
- Modified BS8006
- EBGEO without subsoil support (k=0)
- EBGEO with subsoil support, with modulus of subsoil reaction $k = 477$ and $k = 1000$ kN/m^3.

For all BS8006 calculations, the input strain has been adapted to correspond to the tensile modulus of the geogrids $J = 3990$ kN/m for 1 year loaded GR (Table A.7). Finally, Table A.11 compares the predicted tensile forces for several tensile moduli of the geogrids: $J = 4375/3990/3868$ kN/m (Table A.7) for 1 day/1year/10 years of loading.
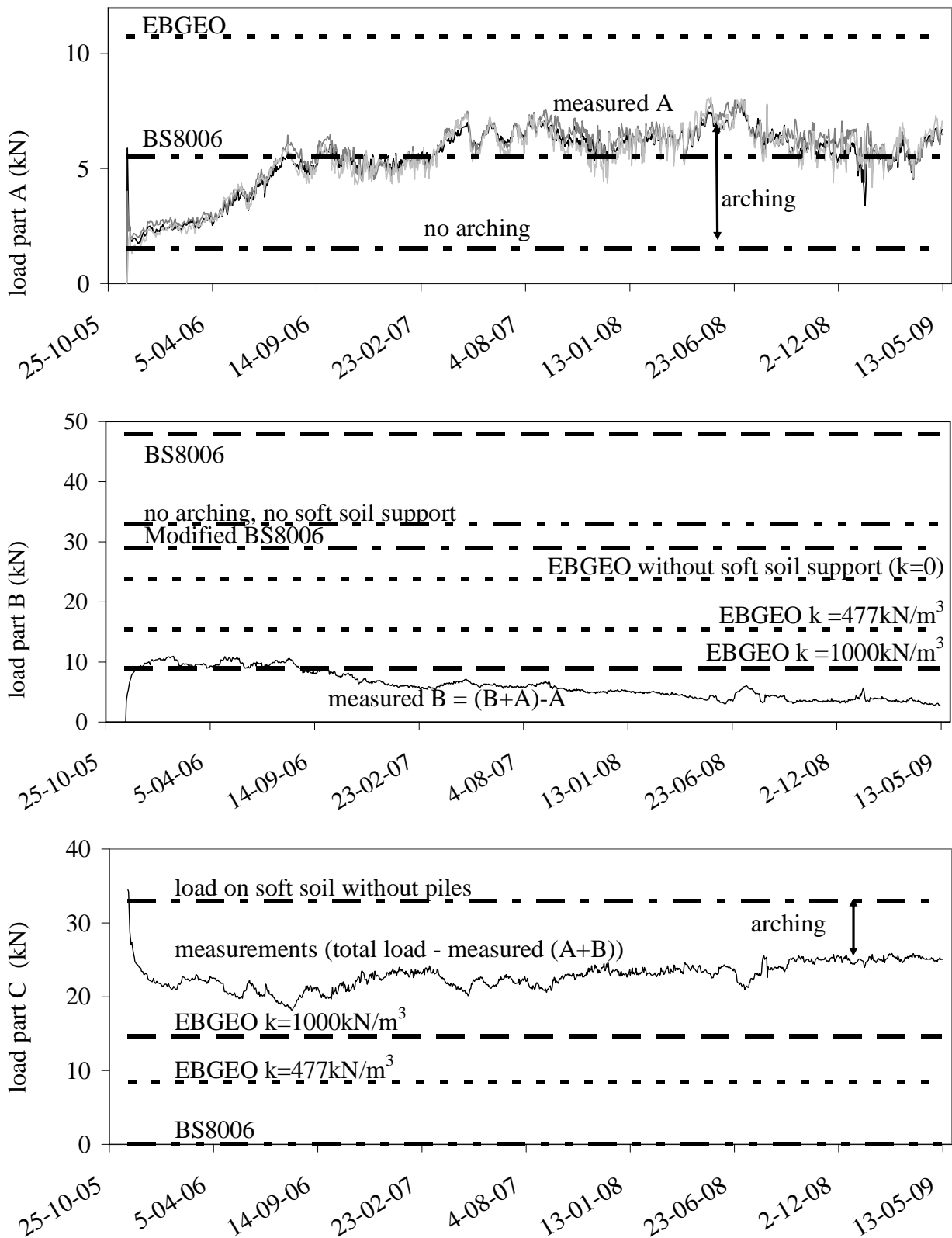
Figure A.14 Comparison measured and predicted *A, B* and *C*.

Table A.10 Predictions of *A, B, C* and tensile force (kN/m) in GR, stiffness of GR is $J_{2\%,\ 1\ year}$ = 3990 kN/m, Kyoto Road construction took place in November 2005.

	BS8006 $k=0^a$	Mod. BS8006 $k=0^a$	EBGEO $k=0^a$	$k=477$		Kyoto Road measurements $k=0^a$	$k=0^a$
	kN/m^3	kN/m^3	kN/m^3	kN/m^3		kN/m^3	kN/m^3
load part *A*	5.5	5.5	10.7	10.7	Load part *A*	5.5	5.5
load part *B*	48	29	24	15	Load part *B*	48	29
load part *C*	0	0	0	8.5	Load part *C*	0	0
tensile force *T*	117	82	82	53	Tensile force *T*	117	82
pile efficiency E_p	-0.39 [b]	0.16	0.31	0.31	Pile efficiency E_p	-0.39 [b]	0.16

[a] no support of subsoil

[b] negative due to double calculation of load on GR

Table A.11 Predictions of tensile force (kN/m) in GR, variation of GR stiffness.

time under load	*J* (kN/m)	BS8006	Modified BS8006	EBGEO without subsoil	EBGEO with $k = 477$ kN/m^3
1 day	4375	120	85	85	55
1 year	3990	117	82	82	53
10 years	3868	116	81	81	52

The prediction differences for short- and long-term tensile stiffness of the geogrids are minimal due to their low creep (Figure A.13 &Table A.7). However, the long-term measurements show that there is a constant slight increase in *C*, indicating that some creep (GR deflection) takes place as expected.

The differences in the predictions for different sub-grade reaction modules *k* ($k = 0$, $k = 477$ kN/m³ and $k = 1000$ kN/m³) are considerable. There is close agreement between the predicted and measured *B* for EBGEO with $k = 1000$ kN/m³. In this case, the *k* of the subsoil in fact seems to be higher than the determined value of 477 kN/m³. As discussed in Chapter A.6.1.2, the value of *k* determined from compression tests is probably too low. Measurements in road N210 (Van Eekelen et al, 2010b) also tend to show that the subsoil contributes more than EBGEO predicts with the *k* value assumed for N210.

The determination of *B* is seen as very important, as this is the load part that directly determines the tensile force in the GR. Predicting *B* using the EBGEO

agrees most closely with the measurements. Table A.11 shows that for this geometry, the EBGEO without subsoil support predicts the same tensile force as the Modified BS8006. The tensile forces of the Modified BS8006 and EBGEO can be identical, although B is not the same. This is because the load distribution over the GR strip is considered differently.

Design should of course be carried out using safety margins: subsoil support may decrease due to settlement, for example by more than 30% due to groundwater variations (Figure A.14 & Van Eekelen and Bezuijen 2008).

A. 7   Conclusions

A.7.1 Thin embankments

BS8006
- BS8006 calculates the distributed vertical line load W_T on the GR using an equation that combines the 3D-equilibrium equation and the 2D-calculation to concentrate the load into a line load. BS8006 therefore incorporates both 2D and 3D.
- BS8006 calculates the vertical load on the GR twice to convert to a fully 3D case. The vertical equilibrium is therefore not correct.

Modified BS8006
- Changing the BS8006 equations so that they use a 3D geometry approach (and thus no double load calculation) resulted in the Modified BS8006.
- The Modified BS8006 approaches FE analysis-axial-symmetry more closely than BS8006.
- For thin embankments (partial arching), EBGEO and the Modified BS8006 give nearly the same tensile forces, providing that subsoil support is ignored.
- For the geometry and properties of the Kyoto Road, EBGEO with no subsoil support and the Modified BS8006 predict the same tensile force in the geogrids. EBGEO measurements and predictions agree closely. If the aspect of subsoil support is incorporated in the Modified BS8006, both EBGEO and the Modified BS8006 would give good agreement with the Kyoto Road measurements.
- It is recommended that subsoil support is incorporated in the (Modified) BS8006, at least so that the model can be validated with field tests where subsoil support usually occurs.

A.7.2 High embankments (full-arching theory)

- For thick embankments ($H > 1.4(s\text{-}a)$), BS8006 assumes that full arching occurs. The full-arching theory assumes that traffic load or extra soil weight due to increased embankment height is not carried by the reinforcement. This extra load is simply 'cut off'. This assumption is not confirmed by finite element calculations. Further validation of the full-arching theory is recommended, for example using field measurements on thick embankments.
- Due to the elaboration of the full-arching assumptions, an increasing embankment height gives a dip in the predicted tensile force in the reinforcement if a calculation using a non-zero surcharge load is carried out.
- It is recommended that the behaviour of high embankments is further validated before applying the Modified BS8006 for full arching ($H > 1.4(s\text{-}a)$ or $H > \sqrt{s_x^2 + s_y^2}$), as the Modified BS8006 with full arching gives lower predicted tensile forces in the GR than BS8006.
- Elaboration of the full-arching assumption is too black-and-white to ensure a sound prediction. The transition should be implemented more smoothly, as described by Lawson (1995).

Appendix A.A Differential equation for step 4: from line load to tensile force

The tensile force is calculated from the line load W_T.

A tension membrane is considered with a tensile force T, components T_V and T_H, and a load $q(x)$ in kN/m. The equilibrium of a small particle is first considered with a length ds (projection on x-axis dx) given in Figure A.15.

From the horizontal equilibrium it follows:

$$T_H - T_H - dT_H = 0 \qquad \rightarrow \qquad dT_H = 0 \tag{A.41}$$

From the vertical equilibrium it follows:

$$-T_V + qdx - pdx + T_V + dT_V = 0 \qquad \rightarrow \qquad q - p = -\frac{dT_V}{dx} \tag{A.42}$$

As the subsoil support is ignored in BS8006:

$$q = -\frac{dT_V}{dx} \tag{A.43}$$
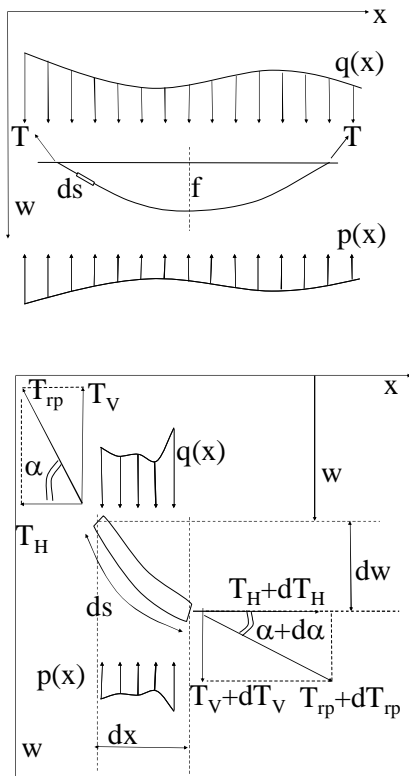
Figure A.15 Equilibrium tension membrane.

The relationship between the components T_H and T_V of the tensile force, *dw* and *dx*, and the angle α is:

$$\tan \alpha = \frac{T_V}{T_H} = \frac{dw}{dx} \qquad \rightarrow \qquad T_V = T_H \frac{dw}{dx} \tag{A.44}$$

This gives:

$$\frac{dT_V}{dx} = \frac{dT_H}{dx}\frac{dw}{dx} + T_H \frac{d^2w}{dx^2} \tag{A.45}$$

Using equation (3.22) and thus $\frac{dT_H}{dx} = 0$ it follows:

$$\frac{dT_V}{dx} = T_H \frac{d^2w}{dx^2} \tag{A.46}$$

Using equation (3.23), this gives the differential equation for reinforcement strips:

$$\frac{d^2 w}{dx^2} = -\frac{q}{T_H} + \frac{p}{T_H} \tag{A.47}$$

For BS8006, with $p = 0$ it follows:

$$\frac{d^2 w}{dx^2} = -\frac{q}{T_H} \tag{A.48}$$

BS8006 assumes that $q(x)$ is the equally-distributed load W_T. Integrating equation (A.43) gives:

$$T_V = -W_T x + c_1 \tag{A.49}$$

And integration of equation (A.48) gives:

$$T_H w = -\tfrac{1}{2} W_T x^2 + c_1 x + c_2 \tag{A.50}$$

where c_1 and c_2 integration are constants. Two constraints give expressions for c_1 and c_2:

$$\begin{aligned} x = 0 &\rightarrow w = 0 \rightarrow c_2 = 0 \\ x = (s - a) &\rightarrow w = 0 \rightarrow c_1 = \tfrac{1}{2} W_T (s - a)^2 \end{aligned} \tag{A.51}$$

Thus, using equations (A.49) and (A.50):

$$\begin{aligned} T_V &= -W_T x + \tfrac{1}{2} W_T (s - a) \\ w &= -\frac{\tfrac{1}{2} W_T x (s - a - x)}{T_H} \end{aligned} \tag{A.52}$$

The extremes are:

$$\begin{aligned} x = 0 &\rightarrow T_V = \tfrac{1}{2} W_T (s - a) \\ x = s - a &\rightarrow T_V = -\tfrac{1}{2} W_T (s - a) \\ x = \tfrac{1}{2}(s - a) &\rightarrow w_{extreme} = f = \frac{W_T (s - a)^2}{8 T_H} \end{aligned} \tag{A.53}$$

or, the inverse of the last equation:

$$T_H = \frac{W_T(s-a)^2}{8f} \tag{A.54}$$

Bouma (1989) shows the relationship between the length of the undeformed and the deformed GR strip:

$$\Delta l = \tfrac{8}{3}\frac{f^2}{s-a} \quad or \quad f^2 = \tfrac{3}{8}(s-a)\Delta l \tag{A.55}$$

where:

f m   Maximal deflection of the GR strip in between two pile caps
Δl m   Difference of GR strip length between the original length *(s-a)* and the deformed length

The relationship between the (average) strain ε and Δl is given by:

$$\Delta l = \varepsilon(s-a) \tag{A.56}$$

This gives: $f = (s-a)\sqrt{\dfrac{3\varepsilon}{8}}$ \hfill (A.57)

When incorporated into equation (A.54) this gives:

$$T_H = \frac{W_T(s-a)}{\sqrt{24\varepsilon}} \tag{A.58}$$

The tensile force *T* in the GR strip can now be calculated:

$$T_{x=0} = \sqrt{T_{Vx=0}^2 + T_{Hx=0}^2} = \frac{W_T(s-a)}{2}\sqrt{1+\frac{1}{6\varepsilon}} \tag{A.59}$$

where $T_{x=0}$ is the total tensile force (in kN) in the geosynthetic reinforcement strip with zero width. Dividing this by the width *a* of the GR strip finally gives the tensile force $T_{rp,x=0}$ in the GR strip with width *a* kN/m:

$$T_{rp} = \frac{W_T(s-a)}{2a}\sqrt{1+\frac{1}{6\varepsilon}} \tag{A.60}$$

To summarise, this calculation is based on the following assumptions:

- there is no subsoil support
- the line load W_T is equally distributed
- deformation is parabolic in shape
- the GR strip is fixed at the corners of the pile caps
- the tensile force is calculated at $x = 0$ and is therefore a maximum (and not an average, as in the German Standard EBGEO).

In practice, equation (A.60) must be repeated. Here, the strain ε has the function of an input parameter for calculating the tensile force T_{rp}. This means that the apparent stiffness of the geosynthetic reinforcement can be calculated as:

$$J \;=\; \frac{T_{rp}}{\varepsilon} \tag{A.61}$$

Appendix A.B. Different interpretations of BS8006 from literature

Introduction

Chapter A.2.3 showed that the BS8006 equations are based on 3D-equilibrium equations as well as 2D equations to concentrate the load on the GR strips. BS8006 calculates the load on the GR twice. Several authors have interpreted BS8006 so that it can be compared with other models. This appendix presents their views and compares their work.
The authors begin with the line load equations (A.13) and (A.17) and calculate back to p'_r, B or the pile efficiency $E_p = 1\text{-}B/w_{tot}$. The authors usually follow either a 2D or a 3D interpretation of the 2D/3D-BS8006.
These interpretations do not influence the final calculated tensile force, as the tensile force is calculated from the line load equations (A.13) or (A.17) and the tensile force equation (A.60). When comparing BS8006 with other models, however, it is important to realise that BS8006 is a 2D-3D combination, doubling the load on the reinforcement and assuming full arching.

Assuming a 2D configuration
For example, Le Hello (2007) assumed a 2D configuration. Starting from equation (A.12) and assuming the configuration of Figure A.4*a* the author finds:

$$p'_r = \frac{W_T}{s} \tag{A.62}$$

Partial arching
For partial arching, the equation for the line load is given by equation (A.13). Combining this with equation (A.62) gives:

$$p'_r = \frac{W_T}{s} = (\gamma H + p)X \tag{A.63}$$

Continuing the assumption of a 2D configuration gives:

$$B = (s-a)p'_r = (s-a)(\gamma H + p)X \tag{A.64}$$

and thus a pile efficiency E_p:

$$E_p = 1 - \frac{B}{w_{tot}} = 1 - \frac{(s-a)(\gamma H + p)X}{s^2(\gamma H + p)} = 1 - \frac{(s-a)X}{s^2} \tag{A.65}$$

Full arching
For full arching, the equation for the line load is given by equation (A.17). Combining this with equation (A.62) gives:

$$p'_r = \frac{W_T}{s} = 1.4\gamma(s-a)X \tag{A.66}$$

Continuing the assumption of a 2D configuration gives:

$$B = (s-a)p'_r = 1.4\gamma(s-a)^2 X \tag{A.67}$$

and thus a pile efficiency E_p:

$$E_p = 1 - \frac{B}{w_{tot}} = 1 - \frac{1.4\gamma(s-a)^2 X}{s^2(\gamma H + p)} \tag{A.68}$$

Abusharar et al (2009) also calculate the total load for determining the pile efficiency on the basis of 2D. This means that they use a total load $s(\gamma H + p)$, thus s instead of s^2. Throughout this paper, the pile efficiency is calculated using the calculated B and the total load on one grid $s \cdot s$, thus $s^2(\gamma H + p)$.
Chen et al. (2008a) compared the results of 2D experiments with – among others – BS8006. However, Chen did not fully use BS8006, but instead used the original 2D equation of Marston (equation (A.1))) when applying the arching coefficients C_c of BS8006 (equation (A.4)).

Assuming a 3D configuration
Other authors assume that BS8006 has determined its line load (equation (A.12) to (A.11)) using the 3D configuration shown in Figure A.6 (for example, see Love and Milligan, 2003, Russell and Pierpoint, 1997, Stewart and Filz, 2005). The German Standard EBGEO applies nearly the same configuration, except that the pile caps are circular. The authors assume that this tensile strip carries half the load on one square $s \cdot s$, giving:

$$3D: \quad p'_r\left(s^2 - a^2\right) = 2W_T(s-a) \qquad \rightarrow \qquad p'_r = \frac{2W_T}{s+a} \tag{A.69}$$

Authors such as Love and Milligan (2003), Stewart (2005), and Russell and Pierpoint (1997) arrive at this equation.

Partial arching
For partial arching, the equation for the line load is given by equation (A.13). Combining this with equation (A.69) gives:

$$p'_r = \frac{2W_T}{s+a} = \frac{2s(\gamma H + p)}{s+a}X \tag{A.70}$$

This gives the following B (kN/pile):

$$B = p'_r \cdot A_r = \frac{2W_T}{(s+a)}\left(s^2 - a^2\right) = 2W_T(s-a) = 2s(\gamma H + p)(s-a)X \tag{A.71}$$

This in turn gives a pile efficiency E_p ($^{\text{kN/pile}}/_{\text{kN/pile}}$):

$$E_p = 1 - \frac{B}{w_{tot}} = 1 - \frac{2s(\gamma H + p)(s-a)X}{s^2(\gamma H + p)} = 1 - \frac{2(s-a)}{s}X \tag{A.72}$$

Full arching

For full arching, the equation for the line load is given by equation (A.17). Combining this with equation (A.69) gives:

$$3D: \quad p'_r = \frac{2W_T}{s+a} \quad = \quad \frac{2.8s\gamma(s-a)}{s+a}X \tag{A.73}$$

Authors such as Love and Milligan (2003), Stewart (2005), and Russell and Pierpoint (1997) also arrived at this last equation. This gives the following B (kN/pile):

$$B = p'_r \cdot A_r = \frac{2W_T}{(s+a)}(s^2 - a^2) = 2W_T(s-a) = 2.8s\gamma(s-a)^2 X \tag{A.74}$$

This in turn gives a pile efficiency E_p ($^{\text{kN/pile}}/_{\text{kN/pile}}$):

$$E_p = 1 - \frac{B}{w_{tot}} = 1 - \frac{2.8s\gamma(s-a)^2 X}{s^2(\gamma H + p)} = 1 - \frac{2.8\gamma(s-a)^2}{s(\gamma H + p)}X \tag{A.75}$$

Different interpretations from literature: a conclusion

Jones et al. (1990) developed the equations partly for a 3D configuration (equilibrium), and partly for a 2D configuration (line load determination).

Some authors assume that the equations were developed on the basis of a fully 2D configuration. Others assume that the equations were developed for a 3D configuration. The 2D case results in different values for p'_r, B and E, the 3D case results in the same values for p'_r, B and E as found in the elaboration of BS8006 (Chapter A. 2).

B. Design Graphs for Calculation Step 2

inverse triangular load distribution

$$(k_s \cdot A_L \cdot L) / (J \cdot a_{eq}) =$$
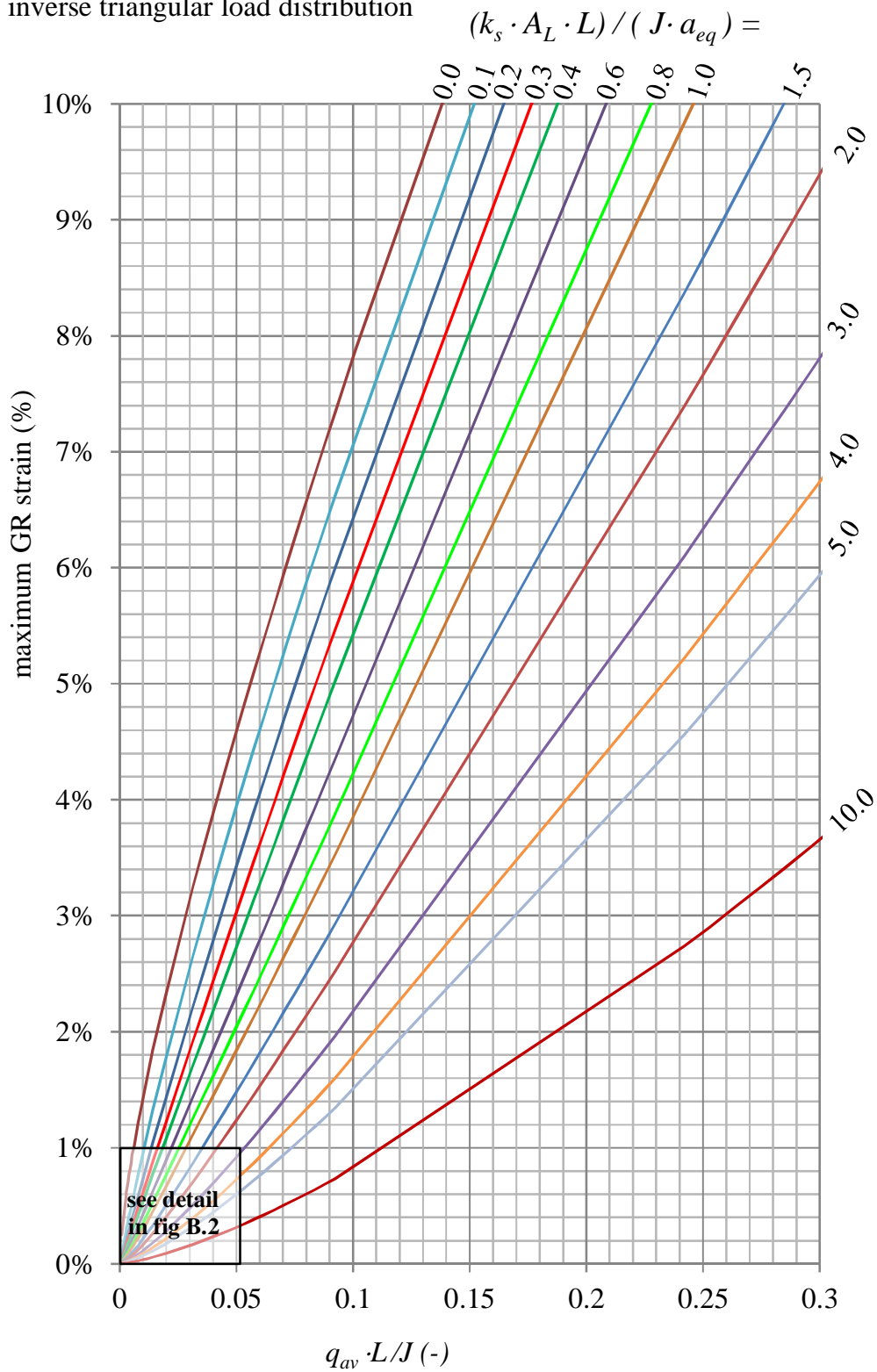
Figure B.1 Design graph, maximum GR strain for the inverse triangular load distribution

detail inverse triangular load distribution

$(k \cdot A_L \cdot L) / (J \cdot a_{eq}) =$

maximum GR strain (%)

$q_{av} \cdot L / J \ (\text{-})$
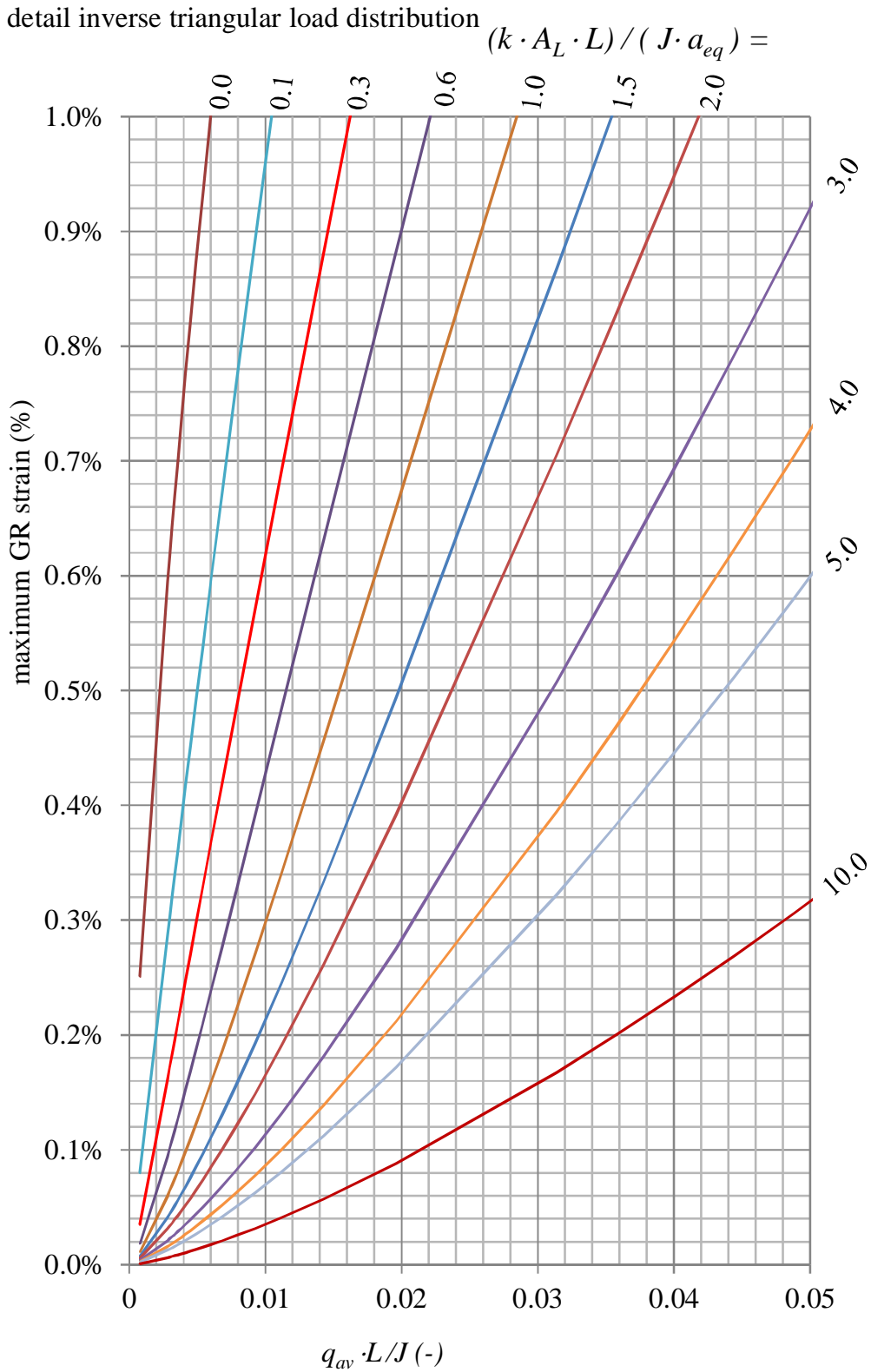
Figure B.2 Design graph, maximum GR strain for the inverse triangular load distribution. Detail of Figure B.1.

uniform load distribution

$(k \cdot A_L \cdot L) / (J \cdot a_{eq}) =$

Figure B.3 Design graph, maximum GR strain for the uniform load distribution.

detail uniform load distribution

$(k \cdot A_L \cdot L) / (J \cdot a_{eq}) =$

maximum GR strain (%)

$q_{av} \cdot L / J (-)$

Figure B.4 Design graph, maximum GR strain for the uniform load distribution. Detail of Figure B.3.

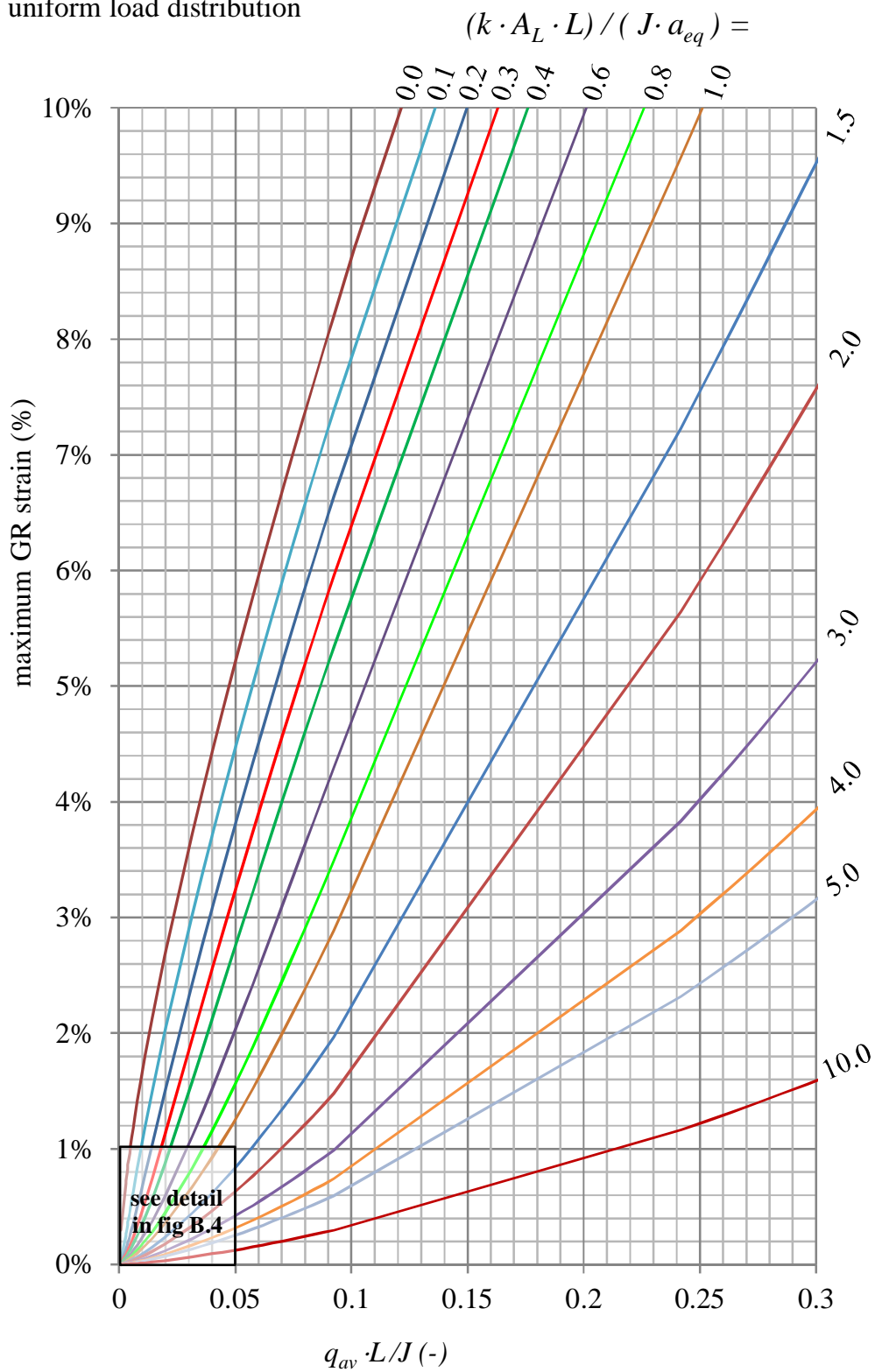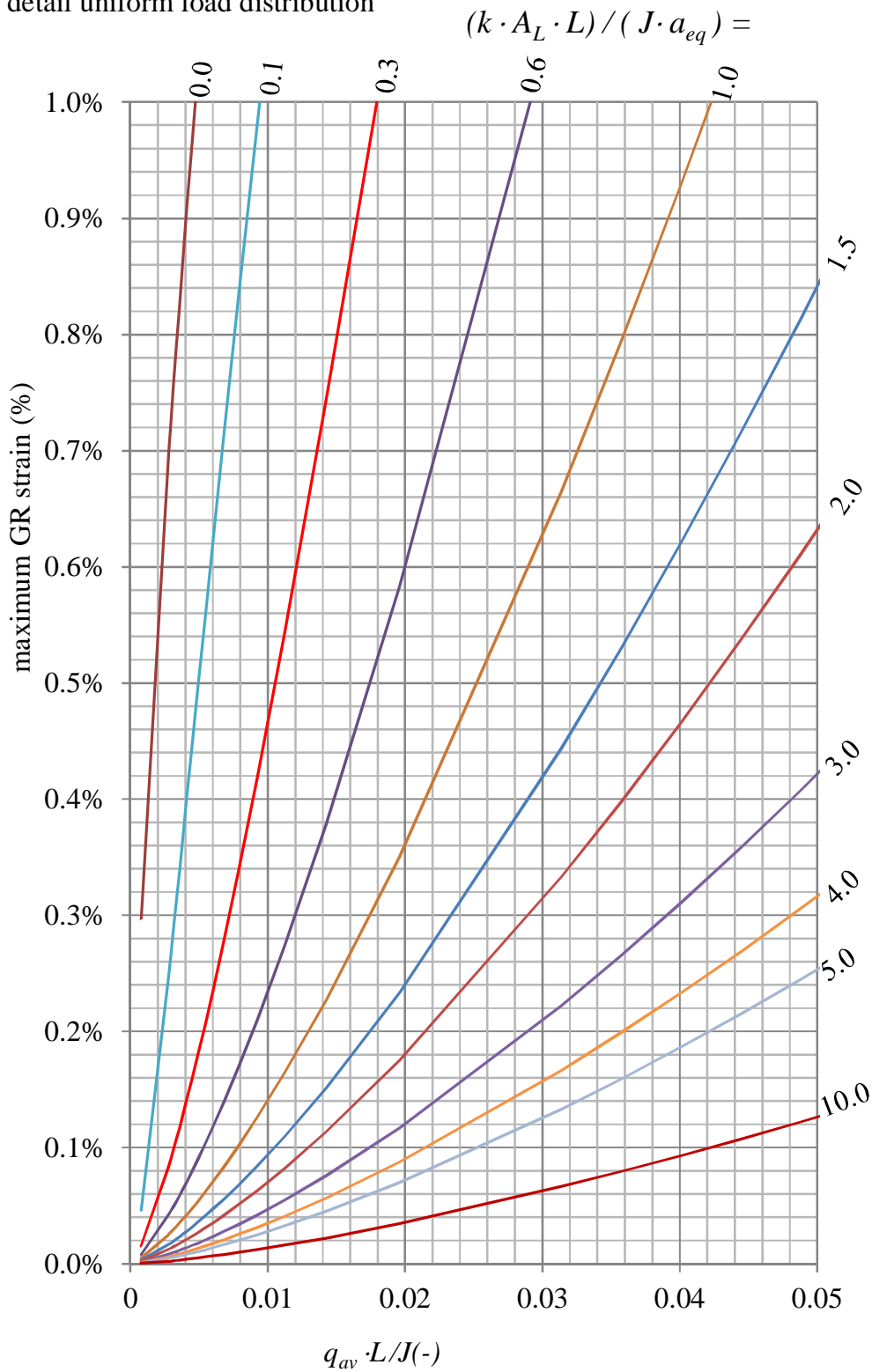# Publications

An overview of publications written within or along the research carried out for this study:

Peer reviewed journal papers

2015	Chapter 5 of this thesis	Van Eekelen, S.J.M., Bezuijen, A., van Tol, A.F., 2015a. Validation of analytical models for the design of basal reinforced piled embankments. Geotextiles and Geomembranes Volume 43, Issue 1, 56 – 81.
2013	Chapter 4 of this thesis	Van Eekelen, S.J.M., Bezuijen, A., van Tol, A.F., 2013. An analytical model for arching in piled embankments. Geotextiles and Geomembranes 39: 78 – 102.
2012	Chapter 2 of this thesis	Van Eekelen, S.J.M., Bezuijen, A., Lodder, H.J., van Tol, A.F., 2012a. Model experiments on piled embankments Part I. Geotextiles and Geomembranes 32: 69 - 81.
2012	Chapter 3 of this thesis	Van Eekelen, S.J.M., Bezuijen, A., Lodder, H.J., van Tol, A.F., 2012b. Model experiments on piled embankments. Part II. Geotextiles and Geomembranes 32: 82 - 94 including its corrigendum: Van Eekelen, S.J.M., Bezuijen, A., Lodder, H.J., van Tol, A.F., 2012b2. Corrigendum to 'Model experiments on piled embankments. Part II' [Geotextiles and Geomembranes volume 32: 82 - 94]. Geotextiles and Geomembranes 35: 119.
2011	Appendix A of this thesis	Eekelen, S.J.M., van, Bezuijen, A., and van Tol, A.F., 2011a, Analysis and modification of the British Standard BS8006 for the design of piled embankments, Geotextiles and Geomembranes 29: 345-359.

Extended/peer-reviewed conference proceedings (>= 4 pages)

2015	Van Eekelen, S.J.M., Bezuijen, A., van Tol, A.F., 2015b. Axial pile forces in piled embankments, field measurements. In: Proceedings of ECSMGE 2015, Edinburgh.
2014	Van Eekelen, S.J.M., Bezuijen, A., 2014. Is 1+1=2? Results of 3D model experiments on piled embankments. In: Proceedings of 10ICG, Berlin, Germany, paper number 128.
2014	Bezuijen, A., van Eekelen, S.J.M., 2014. Basal reinforced piled embankments; Validation of inverse triangular load distribution with an extended Terzaghi equation. In: Proceedings of 10ICG, Berlin, Germany, paper number 201.
2014	Van Eekelen, S.J.M., Almeida, M.S.S, Bezuijen, A., 2014. European analytical calculations compared with a full-scale Brazilian piled embankment. In: Proceedings of 10ICG, Berlin, Germany, paper number 127.
2014	Van der Peet, T.C., van Eekelen, S.J.M., 2014. 3D numerical analysis of basal reinforced piled embankments. In: Proceedings of 10ICG, Berlin, Germany, paper number 112.
2013	Van Eekelen, S.J.M. and Bezuijen, A. 2013a. Equilibrium models for arching in basal reinforced piled embankments. In: Proceedings of 18th ICSMGE, Paris. 1267 – 1270.
2013	Van Eekelen, S.J.M. and Bezuijen, A., 2013b. Dutch research on piled embankments, In: Proceedings of Geo-Congress, California, March 2013.

2012   Van Eekelen, S.J.M., Bezuijen, A., van Duijnen, P.G., 2012c. Does a piled embankment 'feel' the passage of a heavy truck? High frequency field measurements. In: Proceedings of the 5th European Geosynthetics Congress EuroGeo 5. Valencia. Digital version volume 5: 162-166.

2012   Van Eekelen, S.J.M., Bezuijen, A., 2012a. Inversed triangular load distribution in a piled embankment, 3D model experiments, field tests, numerical analysis and consequences. In: Proceedings of EuroGeo5, Valencia, Spain.

2012   Van Eekelen, S.J.M., Nancey, A., Bezuijen, A., 2012. Influence of fill material and type of geosynthetic reinforcement in a piled embankment, model experiments. In: Proceedings of EuroGeo5, Valencia, Spain.

2012   Lodder, H.J., van Eekelen, S.J.M., Bezuijen, A. 2012. The influence of subsoil reaction in a basal reinforced piled embankment. In: Proceedings of EuroGeo5, Valencia, Spain.

2012   Van Eekelen, S.J.M., Bezuijen, A., 2012b. Model experiments on geosynthetic reinforced piled embankments, 3D test series. In: Proceedings of Eurofuge, Delft.

2012   Van Eekelen, S.J.M., Bezuijen, A. 2012c. Basal reinforced piled embankments in the Netherlands, Field studies and laboratory tests, In: Proceedings ISSMGE - TC 211 International Symposium on Ground Improvement IS-GI Brussels.

2011   Van Eekelen, S.J.M., Lodder, H.J., Bezuijen, A., 2011b. Load distribution on the geosynthetic reinforcement within a piled embankment. In: Proceedings of ICSMGE 2011, Athens, 1137-1142.

2010   Van Eekelen, S.J.M., Jansen, H.L., van Duijnen, P.G., de Kant, M., van Dalen, J.H., Brugman, M.H.A., van der Stoel, A.E.C., Peters, M.G.J.M., 2010. The Dutch design guideline for piled embankments. In: Proceedings of 9ICG, Brazil 1911-1916.

2010   Van Duijnen, P.G., van Eekelen, S.J.M., van der Stoel, A.E.C., 2010. Monitoring of a Railway Piled Embankment. In: Proceedings of 9ICG, Brazil, 1461-1464.

2010   Bezuijen, A., van Eekelen, S.J.M., van Duijnen, P.G., 2010. Piled embankments, influence of installation and type of loading. In: Proceedings of 9ICG, Brazil, 1921-1924.

2010   Van Eekelen, S.J.M. and Bezuijen, A., Alexiew, D., 2010. The Kyoto road piled embankment: 31/2 years of measurements. In: Proceedings of 9ICG, Brazil, 1941-1944.

2010   Van Eekelen, S.J.M. and Venmans, A.A.M., Piled embankments in the Netherlands; how to decide, how to design?, New Techniques on Soft Soils, ed. Márcio Almeida, ISBN 978-85-7975-002-1, 157-166,

2009   Van Eekelen, S.J.M., Bezuijen, A., van Duijnen, P.G. and Jansen, P.G., 2009. Piled embankments using geosynthetic reinforcement in the Netherlands: design, monitoring & evaluation. In: Proceedings of the 17th ICSMGE in Alexandria, Egypt, M. Hamza et al. (Eds.), © 2009 IOS Press., 1690-1693.

Other publications

Dutch language journals
2015   Van Eekelen, S.J.M., Bezuijen, A., van Tol, A.F., 2015. Paalmatrasonderzoek, boog- en membraanwerking. GeoKunst, GeoTechniek, January 2015, 48-53.
2012   Den Boogert, Th., van Duijnen, P.G., Peters, M., van Eekelen, S.J.M., 2012. Paalmatrasproeven III, Eindige elementenberekeningen, GeoKunst, GeoTechniek, January 2012, 48-53.
2012   Van Eekelen, S.J.M., Bezuijen, A., van Duijnen, P.G., 2012. Wat voelt een paalmatras van een vrachtwagen? Veldmetingen te Woerden. Land + Water, June – July 2012.
2012   Van Eekelen, S.J.M., 2012. Nederlandse ontwerprichtlijn paalmatrassen geeft betrouwbaar ontwerp, CT Civiele Techniek, no. 7, 34-36.
2011   Eekelen, S.J.M., van, Lodder, H.J., Bezuijen, A., 2011. Paalmatrasproeven I, Vervormingen van geokunststoffen in een paalmatras, en de daaruit volgende belastingsverdeling, Geokunst, GeoTechniek, April 2011, 78-80.
2011   Van Eekelen, S.J.M., van der Vegt, J.W.G., Lodder, H.J., Bezuijen, A., 2011. Paalmatrasproeven II, belangrijkste conclusies, GeoKunst, GeoTechniek, July 2011, 46-50.
2011   Van Eekelen, S.J.M., 2011. Paalmatrasproeven IIa. Eén laag biaxiaal of twee lagen uniaxiale wapening in een paalmatras, GeoKunst, GeoTechniek, juli 2011, 51-52.
2011   Van Eekelen, S.J.M., 2011. Nederlandse ontwerpichtlijn paalmatrassen geeft betrouwbaar ontwerp, 2011, CT Civiele Techniek, nummer 7, 34-36.
2010   Van Eekelen, S.J.M., 2010. Snel en onderhoudsarm bouwen met paalmatrassen, GWW-Totaal, juni 2010.
2009   Van Eekelen, S.J.M., 2009. De Nederlandse CUR Ontwerprichtlijn voor Paalmatrassystemen, GeoTechniek, Thema-uitgave Geotechniekdag 2009, 14-18.
2009   Van Duijnen, P.G., van Eekelen, S.J.M., 2009. Eerste paalmatras onder spoorbaan in Nederland, overgangsconstructie zonder onderhoud? Geokunst, GeoTechniek, October 2009, 58-63.

English-language journals (not peer-reviewed)
2014   Van Eekelen, S.J.M., Bezuijen, A., van Tol, A.F., 2014, Research on Basal Reinforced Piled Embankments, Arching and Load-Deflection Behaviour, IGS News, Vol. 30, No. 3, 14-18.
2014   Van der Peet, T.C., van Duijnen, P.G., van Eekelen, S.J.M., 2014. Validating a new design method for piled embankments with Plaxis 2D and 3D. Published in Plaxis Bulletin, Autumn issue 2014, 6 – 9.
2013   Van Eekelen, S.J.M., Bezuijen, A., 2013. A new equilibrium model for arching in basal reinforced piled embankments, Geotechniek Special ICSMGE, September 2013, 7-9.
2012   Van Eekelen, S.J.M., Bezuijen, A., 2012. Dutch Research on basal reinforced piled embankments, Geotechniek Special Ground Improvement, May/June 2012, 12-17.
2012   (Den Boogert, Th., van Duijnen, P., van Eekelen, S.J.M., Numerical analysis of geosynthetic reinforced piled embankment scale model tests, Plaxis Bulletin, 31, spring issue 2012, 12-16).

2009   Van Eekelen, Suzanne, The Dutch Design Guideline for Piled Embankments, IGS News, Vol. 25, No. 2, July 2009, page 23.

Syllabi

2013   Van Eekelen, S.J.M., syllabus on basal reinforced piled embankments. Part of the syllabus 'Foundation engineering' of the university of Ghent and the syllabus "CIE4376 Embankments and Geosynthetics" of the Delft University of Technology, 30 pages.

2013   Van Eekelen, S.J.M., syllabus on basal reinforced piled embankments, 15 pages, part of the syllabus of the Post-Academic PAO course "Realisatie bouw en infrastructuur op slappe bodem" ("Realisation of constructions and infrastructure on soft soil").

References

Abusharar, S.W., Zeng, J.J., Chen, B.G., Yin, J.H., 2009. A simplified method for analysis of a piled embankment reinforced with geosynthetics. Geotextiles and Geomembranes 27, 39-52.

Almeida, M.S.S., Ehrlich, M., Spotti, A.P., Marques, M.E.S., 2007. Embankment supported on piles with biaxial geogrids. Geotech. Eng., 160(4), 185-192.

Almeida, M.S.S., Marques, M.E.S., Almeida, M.C.F., Mendonca, M.B., 2008. Performance on two low piled embankments with geogrids at Rio de Janeiro. In: Proceedings of the First Pan American Geosynthetics Conference and Exhibition, Cancun, Mexico, 1285-1295.

ASIRI, 2012. Recommandations pour la conception, le dimensionnement, l'exécution et le contrôle de l'amélioration des sols de fondation par inclusions rigides, ISBN: 978-2-85978-462-1.

Bezuijen, A., van Eekelen, S.J.M., van Duijnen, P.G., 2010. Piled embankments, influence of installation and type of loading. In: Proceedings of the 9th International Conference on Geosynthetics, Brazil, 2010; 1921-1924.

Blanc, M., Rault, G., Thorel, L., Almeida, M., 2013. Centrifuge investigation of load transfer mechanisms in a granular mattress above a rigid inclusions network. Geotextiles and Geomembranes 36: 92 - 105.

Blanc, M., Thorel, L., Girout, R., Almeida, M., 2014. Geosynthetic reinforcement of a granular load transfer platform above rigid inclusions; comparison between centrifuge testing and analytical modelling. Geosynthetics International, Volume 21, Issue 1: 37-52.

Bouma, A.L., 1989. Mechanica van constructies, elasto-statica van slanke structuren, First ed. Delftse Uitgevers Maatschappij b.v. ISBN 90 6562 11.

BS1377, part 8: 1990. British Standard Methods of tests for Soils for civil engineering purposes, Part 8. Shear strength tests (effective stress). British Standards Institution, London

BS8006-1: 2010. Code of practice for strengthened/reinforced soils and other fills. British Standards Institution, ISBN 978-0-580-53842-1.

Briançon, L., Simon, B., 2012. Performance of Pile-Supported Embankment over Soft Soil: Full-Scale Experiment, J. Geotechn. Geoenviron. Eng. 2012.138:551-561.

Britton, E.J., Naughton, P.J., 2008. An experimental investigation of arching in piled embankments. In: Proceedings of the 4th European Geosynthetics Congress EuroGeo 4. Edinburgh. Paper number 106.

Britton, E.J., Naughton, P.J., 2010. An experimental study to determine the location of the critical height in piled embankments. In: Proceedings of the 9th Conference on Geosynthetics, Brazil, 1961-1964.

Cain, W., 1916. Earth Pressure, Retaining Walls and Bins, New York, John Wiley and Sons. Inc.

Carlsson, B., 1987. Reinforced soil, principles for calculation, Terratema AB, Linköping (in Swedish).

Casarin, C., 2011. private communication, São Paulo, Brazil.

CEN EN ISO 10319:2008 Geosynthetics - Wide-width tensile test. NEN, Delft, Netherlands.

Chen, Y.M., Cao, W.P., Chen, R.P., 2008a. An experimental investigation of soil arching within basal reinforced and unreinforced piled embankments. Geotextiles and Geomembranes 26, 164-174.

Chen, R.P., Chen, Y.M., Han, J., Xu, Z.Z., 2008b. A theoretical solution for pile-supported embankments on soft soils under one-dimensional compression. Can. Geotech. J. 45, 611-623.

Collin, J.G., 2004. Column supported embankment design considerations. 52nd Annual Geotechnical Engineering Conference- University of Minnesota.

Corbet, S.P., Horgan, G., 2010, Introduction to international codes for reinforced soil design. In: Proceedings of 9ICG, Brazil, pp. 225-231.

CUR 226, 2010. Ontwerprichtlijn paalmatrassystemen (Design Guideline Piled Embankments), ISBN 978-90-376-0518-1 (in Dutch).

CUR 226, 2015. Ontwerprichtlijn paalmatrassystemen (Design Guideline Piled Embankments), updated version (in Dutch).

Deb, K., 2010. A mathematical model to study the soil arching effect in stone column-supported embankment resting on soft foundation soil. Applied Mathematical Modelling 34 (2010), 3871-3883.

Deb, K. Mohapatra, S.R., 2013. Analysis of stone column-supported geosynthetic-reinforced embankments, Applied Mathematical Modelling, Volume 37, Issue 5, 1 March 2013, 2943-2960.

Demerdash, M.A., 1996. An experimental study of piled embankments incorporating geosynthetic basal reinforcement. PhD Thesis, University of Newcastle upon Tyne, UK.

Den Boogert, T.J.M., 2011. Piled Embankments with Geosynthetic Reinforcement, Numerical Analysis of Scale Model Tests. Master of Science thesis, Delft University of Technology.

Den Boogert, Th., van Duijnen, P.G., van Eekelen, S.J.M., 2012a. Numerical analysis of geosynthetic reinforced piled embankment scale model tests. Plaxis Bulletin 31, 12-17.

Den Boogert, Th., van Duijnen, P.G., Peters, M., van Eekelen, S.J.M., 2012b. Paalmatrasproeven III, Eindige elementenberekeningen, GeoKunst, GeoTechniek, January 2012, 48-53.

EBGEO, 2010 (in German). Empfehlungen für den Entwurf und die Berechnung von Erdkörpern mit Bewehrungen aus Geokunststoffen e EBGEO, vol. 2. German Geotechnical Society, Auflage, ISBN 978-3-433-02950-3. Also available in English: Recommendations for Design and Analysis of Earth Structures using Geosynthetic Reinforcements EBGEO, 2011. ISBN 978-3-433-02983-1 and digital in English ISBN 978-3-433-60093-1.

EC1990: NEN-EN 1990+A1+A1/C2 (nl), 2011. Basis of structural design, ICS 91.010.30; 91.080.01, December 2011 (Eurocode 0).

Ellis, E., Aslam, R., 2009a. Arching in piled embankments. Comparison of centrifuge tests and predictive methods, part 1 of 2. Ground Engineering, June 2009, 34-38.

Ellis, E., Aslam, R., 2009b. Arching in piled embankments. Comparison of centrifuge tests and predictive methods, part 2 of 2. Ground Engineering, July 2009, 28-31.

Eskişar, T., Otani, J. and Hironaka, J., 2012. Visualization of soil arching on reinforced embankment with rigid pile foundation using X-ray CT. Geotextiles and Geomembranes 32: 44-54.

Farag, G.S.F., 2008. Lateral spreading in basal reinforced embankments supported by pile-like elements. Schiftenreihe Getechnik, Heft 20, Universität Kassel, März 2008.

Filz, G.M. and Smith, M.E., 2008. Net Vertical Loads on Geosynthetic Reinforcement in Column-Supported Embankments. Soil Improvement (GSP 172). Part of Geo-Denver 2007: New Peaks in Geotechnics. In: Proceedings of Sessions of Geo-Denver 2007.

Filz, G., Sloan, J., McGuire, M., Collin, J., Smith, M., 2012. Column-Supported Embankments: Settlement and Load Transfer. Geotechnical Engineering State of the Art and Practice: 54-77. doi: 10.1061/9780784412138.0003.

Filz, G., Sloan, J., 2013. Load Distribution on Geosynthetic Reinforcement in Column-Supported Embankments. In: Proceedings of Geo-Congress, California, 1829-1837.

Fischer, L. 1960. Theory and Practice of Shell Structures, Berlin: Wilhelm Ernst and Sohn. 541 pages.

Forsman, J., Honkala, A., Smura, M., 1999. Hertsby case: a column stabilized and geotextile reinforced road embankment on soft subsoil. Dry mix method for deep soil stabilization, H. Bredenberg, G. Holm, and B. B. Broms, eds., Balkema, Rotterdam, The Netherlands, 263–268.

Forsman, J. 2001. Geovahvistetutkimus, koerakenteiden loppuraportti 1996–2001 Georeinforcement-projcet, final report of test structures 1996–2001, Tiehallinto, Helsinki, Finland (in Finnish).

Guido, V.A., Kneuppel, Sweeney, M.A., 1987. Plate loading test on geogrid reinforced earth slabs. In: Proceedings Geosynthetics'87 Conference, New Orleans, 216–225.

Halvordson, K.A., Plaut, R.H., Filz, G.M., 2010. Analysis of geosynthetic reinforcement in pile-supported embankments. Part II: 3D cable-net model. Geosynthetics International 17 (2), 68 - 76. ISSN: 1072-6349, E-ISSN: 1751-7613.

Han, J., Gabr, M.A., 2002. Numerical Analysis of Geosynthetic-Reinforced and Pile-Supported Earth Platforms over Soft Soil, Journal of geotechnical and geoenvironmental engineering, January 2002; 44-53.

Han, J., Bhandari, A., Wang, F., 2012. DEM Analysis of Stresses and Deformations of Geogrid-Reinforced Embankments over Piles. Int. J. Geomech. 2012.12:340-350.

Handy, R. L., 1973. The Igloo and the Natural Bridge as Ultimate Structures, Arctic, Vol. 26, No. 4, 276-281.

Handy, R.L., 1985, The Arch in Soil Arching, Journal of Geotechnical Engineering, Vol. Ill, No. 3, March, 1985. ©ASCE, ISSN 0733-9410/85/0003-0302/$01.00. Paper No. 19547.

Haring, W., Profittlich, M., Hangen, H., 2008. Reconstruction of the national road N210 Bergambacht to Krimpen a.d. IJssel, NL: design approach, construction experiences and measurement results. In: Proceedings 4th European Geosynthetics Conference, September 2008, Edinburgh, UK.

Heitz, C., 2006. Bodengewölbe unter ruhender und nichtruhender Belastung bei Berücksichtigung von Bewehrungseinlagen aus Geogittern. Schriftenreihe Geotechnik, Uni Kassel, Heft 19, November 2006 (in German).

Hewlett, W.J., Randolph, M.F., 1988. Analysis of piled embankments. Ground Engineering, April 1988, Volume 22, Number 3, 12-18.

Hong, W.P., Lee, J.H., Lee, K.W., 2007. Load transfer by soil arching in pile-supported embankments. Soils and Foundations Vol. 47, No. 5, 833-843.

Hong, W.P., Lee, J., Hong, S., 2014. Full-scale Tests on embankments founded on piled beams. J. Geotech. Geoenviron. Eng. http://dx.doi.org/10.1061/(ASCE)GT.1943-5606.0001145.

Horgan, G.J., and Sarsby, R.W., 2002. The arching effect of soils over voids and piles incorporating geosynthetic reinforcement. Geosynthetics, 7th ICG, Delmas, Gourc & Girard (eds) © Swets & Zeitlinger, Lisse ISBN 90 5809 523 1, 373-378.

Huang, J., Han, j., Oztoprak, S., 2009. Coupled Mechanical and Hydraulic Modeling of Geosynthetic-Reinforced Column-Supported Embankments. J. Geotech. Geoenviron. Eng. 2009.135:1011-1021.

Jenck, O., Dias, D., Kastner, R., 2005, Soft ground improvement by vertical rigid piles two-dimensional physical modelling and comparison with current design models, Soils and Foundations, Vol. 45, No. 6, 15-30.

Jenck, O., Dias, D., and Kastner, R., 2009. Discrete element modelling of a granular platform supported by piles in soft soil – Validation on a small scale model test and comparison to a numerical analysis in a continuum. Computers and Geotechnics 36: 917–927.

Jones, B.M., Plaut, R.H., Filz, G.M., 2010. Analysis of geosynthetic reinforcement in pile-supported embankments. Part I: 3D plate model. Geosynthetics International 17 (2), 59e67. ISSN: 1072-6349, E-ISSN: 1751-7613.

Jones, C.J.F.P., Lawson, C.R., Ayres, D.J., 1990. Geotextile reinforced piled embankments, in: Geotextiles, Geomembranes and Related Products, Den Hoedt (ed.), 1990, Balkema, Rotterdam, ISBN 90 6191 119 2, 155-160.

Kempfert, H.G., Zaeske, D., Alexiew, D., 1999. Interactions in reinforced bearing layers over partial supported underground. In: Geotechnical Engineering for Transportation Infrastructure, Barends et al. (eds) © 1999 Balkema, Rotterdam, ISBN 90 5809 047 7.

Kempfert, H.G., Göbel, C., Alexiew, D., Heitz, C., 2004. German recommendations for reinforced embankments on pile-similar elements. In: Proceedings of EuroGeo 3, Munich, 279-284.

Lally, D. and Naughton, P.J., 2012. An investigation of the arching mechanism in a geotechnical centrifuge. In: Proceedings 5th European Geosynthetics Congress. Valencia. Vol 5. 363-367.

Lawson, C.R., 1995. Basal reinforced embankment practice in the United Kingdom, The practice of soil reinforcing in Europe. Thomas Telford. London. 173-194.

Le Hello, B., 2007. Renforcement par geosynthetiques des remblais sur inclusions rigides, étude expérimentale en vraie grandeur et analyse numérique. PhD thèses, l'université Grenoble I, (in French).

Le Hello, B., Villard, P., 2009. Embankments reinforced by piles and geosynthetics – Numerical and experimental studies with the transfer of load on the soil embankment. Engineering Geology 106 (2009) 78 – 91.

Liikennevirasto, 2012. Geolujitetut maarakenteet, Tiegeotekniikan käsikirja, Liikenneviraston oppaita 2/2012, ISBN 978-952-255-104-7. Finnish design guideline for geosynthetic reinforcement (in Finnish).

Lodder, H.J., 2010. piled and reinforced embankments, Comparing scale model tests and theory. Master of Science thesis, Delft University of Technology.

Lodder, H.J., van Eekelen, S.J.M., Bezuijen, A., 2012. The influence of subsoil reaction in a basal reinforced piled embankment. In: Proceedings of Eurogeo5, Valencia. Volume 5.

Love, J. and Milligan, G., 2003. Design methods for basally reinforced pile-supported embankments over soft ground, Ground Engineering., March 2003, 39-43.

Low, B.K., Tang, S.K., and Chao, V., 1994. Arching in piled embankments. J. of Geo. Eng., ASCE, 120(11), 1917-1938.

Marston, A., Anderson, A.O., 1913. The Theory of Loads on Pipes in Ditches and Tests of Cement and Clay Drain Tile and Sewer Pipe, Bulletin No. 31, Engineering Experiment Station.

McGuire, M.P., Filz, G.M., Almeida, M.S.S., 2009. Load-Displacement Compatibility Analysis of a Low-Height Column-Supported Embankment. In: Proceedings of IFCEE09, Florida, 225-232.

McGuire, M., Sloan, J., Collin, J., Filz, G., 2012. Critical Height of Column-Supported Embankments from Bench-Scale and Field-Scale Tests, ISSMGE - TC 211 International Symposium on Ground Improvement IS-GI Brussels.

McKelvey, J.A., 1994, the Anatomy of Soil Arching, Geotextiles and Geomembranes 13 (1994) 317-329.

Nadukuru, S.S., Michalowski, R.L., 2012. Arching in Distribution of active Load on Retaining Walls. J. Geotechn. Geoenviron. Eng., May 2012. 575-584.

Naughton, P., 2007. The Significance of Critical Height in the Design of Piled Embankments. Soil Improvement: 1-10. doi: 10.1061/40916(235)3.

Nordic guidelines for reinforced soils and fills (NGI), 2003. Revision A was published in February 2004, and can be downloaded at www.sgf.net.

Nunez, M.A., Briançon, L., Dias, D., 2013. Analyses of a pile-supported embankment over soft clay: Full-scale experiment, analytical and numerical approaches, Engineering Geology 153 (2013) 53-67.

Oh, Y.I., Shin, E.C., 2007. Reinforced and arching effect of geogrid-reinforced and pile-supported embankment on marine soft ground. Marine Georesources and Geotechnology, 25, 97-118.

Plaut, R.H., Filz, G.M., 2010. Analysis of geosynthetic reinforcement in pilesupported embankments. Part III: axisymmetric model. Geosynthetics International 17 (2), 77-85. ISSN: 1072-6349, E-ISSN: 1751-7613.

Public Work Research Center, 2000. Manual on Design and Execution of Reinforced Soil Method with Use of Geotextiles, second ed. Public Work Research Center, 248-256 (in Japanese).

Rogbeck, Y., Gustavsson, S., Södergren, I. Lindquist, D., 1998. Reinforced Piled Embankments in Sweden - Design Aspects. In: Proceedings of the Sixth International Conference on Geosynthetics, 755-762.

Russell, D., Pierpoint, N., 1997. An assessment of design methods for piled embankments, Ground Engineering, November 1997, 39-44.

SINTEF, 2002. A computer program for designing reinforced embankments. In: Proceedings of the 7 ICG, Nice 2002, France, vol. 1, 201–204.

Sloan, J.A., 2011. Column-supported embankments: full-scale tests and design recommendations. PhD thesis, Virginia Polytechnic Institute and State University, Blacksburg, VA.

Spotti, A.P., 2006. Monitoring results of a piled embankment with geogrids (in Portuguese). ScD Thesis. COPPE/UFRJ, Rio de Janeiro, Brazil.

Stewart, M.E. and Filz, G., 2005. Influence of Clay Compressibility on Geosynthetic Loads in Bridging Layers for Column-Supported Embankments. In: Proceedings of Geo-Frontiers 2005, USA, GSP 131 Contemporary Issues in Foundation Engineering.

Svanø, G., Ilstad, T., Eiksund, G., Want, A., 2000. Alternative calculation principle for design of piled embankments with base reinforcement. In: Proceedings of the 4th GIGS in Helsinki.

Terzaghi, K., 1943. Theoretical Soil Mechanics. John Wiley and Sons, New York.

Van der Peet, T.C., 2014. Arching in basal reinforced piled embankments, numerical validation of the Concentric Arches model, MSc thesis, Delft University of Technology, Delft, the Netherlands.

Van der Peet, T.C., van Eekelen, S.J.M., 2014. 3D numerical analysis of basal reinforced piled embankments. In: Proceedings of IGS10, September 2014, Berlin, Germany. Paper no. 112.

Van der Stoel, A.E.C., Brok, C., De Lange, A.P., van Duijnen, P.G., 2010. Construction of the first railroad widening in the Netherlands on a Load Transfer Platform (LTP). In: Proceedings of 9 ICG, Brazil, 1969-1972.

Van Duijnen, P.G., van Eekelen, S.J.M., van der Stoel, A.E.C., 2010. Monitoring of a Railway Piled Embankment. In: Proceedings of 9 ICG, Brazil, 1461-1464.

Van Duijnen, P.G., 2014. Personal communication.

Van Duijnen, P.G., Schweckendiek, T., Calle, E.O.F., van Eekelen, S.J.M., 2015. Calibration of partial factors for basal reinforced piled embankments. In: Proceedings of ISGSR2015 Risks, Rotterdam.

Van Eekelen, S.J.M., Bezuijen, A. Oung, O., 2003. Arching in piled embankments; experiments and design calculations. In: Proceedings of Foundations: Innovations, observations, design and practice, 885-894.

Van Eekelen, S.J.M., Van, M.A., Bezuijen, A., 2007. The Kyotoroad, a full-scale test. Measurements and calculations. In: Proceedings of ECSMGE 2007, Madrid, Spain, 1533-1538.

Van Eekelen, S.J.M. en Bezuijen, A., 2008. Considering the basic starting points of the design of piled embankments in the British Standard BS8006. In: Proceedings of EuroGeo4, paper number 315, September 2008, Edinburgh, Scotland.

Van Eekelen, S.J.M., Jansen, H., 2008. Op weg naar een Nederlandse ontwerprichtlijn voor paalmatrassen 1, Verslag van een casestudie, GeoKunst nr. 3, 2008 (in Dutch).

Van Eekelen, S.J.M., Bezuijen, A., Alexiew, D., 2010a. The Kyoto Road Piled Embankment: 31/2 Years of Measurements. In: Proceedings of 9 ICG, Brazil, 1941-1944.

Van Eekelen, S.J.M., Jansen, H.L., van Duijnen, P.G., De Kant, M., van Dalen, J.H., Brugman, M.H.A., van der Stoel, A.E.C., Peters, M.G.J.M., 2010b. The Dutch design guideline for piled embankments. In: Proceedings of 9 ICG, Brazil, 1911-1916.

Van Eekelen, S.J.M.; Bezuijen, A., van Tol, A.F., 2011a. Analysis and modification of the British Standard BS8006 for the design of piled embankments. Geotextiles and Geomembranes 29: 345-359. Adopted in appendix A of this thesis.

Van Eekelen, S.J.M., Lodder, H.J., Bezuijen, A., 2011b. Load distribution on the geosynthetic reinforcement within a piled embankment, In: Proceedings of ICSMGE 2011, Athens, 1137-1142.

Van Eekelen, S.J.M., Bezuijen, A., Lodder, H.J., van Tol, A.F., 2012a. Model experiments on piled embankments Part I. Geotextiles and Geomembranes 32: 69-81. Adopted in Chapter 2 of this thesis.

Van Eekelen, S.J.M., Bezuijen, A., Lodder, H.J., van Tol, A.F., 2012b. Model experiments on piled embankments. Part II. Geotextiles and Geomembranes 32: 82-94 including its corrigendum: Van Eekelen, S.J.M., Bezuijen, A., Lodder, H.J., van Tol, A.F., 2012b2. Corrigendum to 'Model experiments on piled embankments. Part II' [Geotextiles and Geomembranes volume 32: 82-94]. Geotextiles and Geomembranes 35: 119. Adopted in Chapter 3 of this thesis.

Van Eekelen, S.J.M., Bezuijen, A., van Duijnen, P.G., 2012c. Does a piled embankment 'feel' the passage of a heavy truck? High frequency field measurements. In: Proceedings of the 5th European Geosynthetics Congress EuroGeo 5. Valencia. Digital version volume 5: 162-166.

Van Eekelen, S.J.M., Bezuijen, A., 2012a. Inversed triangular load distribution in a piled embankment, 3D model experiments, field tests, numerical analysis and consequences. EuroGeo5, Valencia, Spain.

Van Eekelen, S.J.M., Bezuijen, A. 2012b. Model experiments on geosynthetic reinforced piled embankments, 3D test series. In: Proceedings of Eurofuge, Delft.

Van Eekelen, S.J.M., Bezuijen, A. 2012c. Basal reinforced piled embankments in the Netherlands, Field studies and laboratory tests, ISSMGE - TC 211 International Symposium on Ground Improvement IS-GI Brussels.

Van Eekelen, S.J.M., Bezuijen, A. van Tol, A.F., 2013. An analytical model for arching in piled embankments. Geotextiles and Geomembranes 39: 78-102. Adopted in Chapter 4 of this thesis.

Van Eekelen, S.J.M. and Bezuijen, A. 2013a. Equilibrium models for arching in basal reinforced piled embankments. In: Proceedings of 18th ICSMGE, Paris. 1267 – 1270.

Van Eekelen, S.J.M., Bezuijen, A., 2013b, Dutch research on piled embankments. In: Proceedings of Geo-Congress, California, March 2013, 1838-1847.

Van Eekelen, S.J.M., Almeida, M.S.S., Bezuijen, A., 2014. European analytical calculations compared with a full-scale Brazilian piled embankment. In: Proceedings of 10ICG, Berlin, Germany. Paper no. 127.

Van Eekelen, S.J.M., Bezuijen, A., 2014. Is 1 + 1 = 2? Results of 3D model experiments on piled embankments. In: Proceedings of 10ICG, Berlin, Germany. Paper no. 128.

Van Eekelen, S.J.M., Bezuijen, A. van Tol, A.F., 2015a. Validation of analytical models for the design of basal reinforced piled embankments. Geotextiles and Geomembranes. Volume 43, Issue 1, 56 - 81. Adopted in Chapter 5 of this thesis.

Van Eekelen, S.J.M., Bezuijen, A., van Tol, A.F., 2015b. Axial pile forces in piled embankments, field measurements. In: Proceedings of XVI ECSMGE, Edinburgh.

Van Niekerk, A.A., Molenaar, A.A.A., Houben, L.J.M., 2002. Effect of Material Quality and Compaction on the Mechanical Behaviour of Base Course Materials and Pavement Performance. In: Proceedings of the 6th international conference on the bearing capacity of roads and airfields, Lisbon, Portugal, June 2002: 1071-179. Swets and Zeitlinger BV.

Vermeer, P.A., Punlor, A., Ruse, N., 2001. Arching effects behind a soldier pile wall. Computers and Geotechnics 28 (2001) 379–396.

Vollmert, L., Kahl, M., Giegerich, G., Meyer, N., 2007. In-situ verification of an extended calculation method for geogrid reinforced load distribution platforms on piled foundations. In: Proceedings of ECSGE 2007, Madrid, Volume 3, 1573 - 1578.

Vollmert, L., 2014. Personal communication.

Völlmy, A., 1937. Eingebettete Rohre, Mitt. Inst. Baustatik, Eidgen. Tech. Hochschule, Zürich, Mitt. no. 9.

Weihrauch, S., Oehrlein, S., Vollmert, L., 2010. Baugrundverbesserungsmassnahmen in der HafenCity Hamburg am Beispiel des Stellvertreterprojektes Hongkongstrasse. Bautechnik. Volume 87, issue 10: 655-659 (in German).

Weihrauch, S., Oehrlein, S., Vollmert, L., 2013. Subgrade improvement measures fort the main rescue roads in the urban redevelopment area HafenCity in Hamburg. In: Proceedings of 18th ICSMGE, Paris.

Zaeske, D., 2001. Zur Wirkungsweise von unbewehrten und bewehrten mineralischen Tragschichten über pfahlartigen Gründungselementen. Schriftenreihe Geotechnik, Uni Kassel, Heft 10, February 2001 (in German).

Zhang, L., Zhao, M., Hu, Y., Zhao, H., Chen, B., 2012. Semi-analytical solutions for geosynthetic-reinforced and pile-supported embankment, Computers and Geotechnics, Volume 44, June 2012, 167-175, ISSN 0266-352X, 10.1016/j.compgeo.2012.04.001.

Zhuang, Y., Wang, K.Y., Liu, H.L., 2014. A simplified model to analyze the reinforced piled embankments, Geotextiles and Geomembranes, Volume 42, Issue 2, April 2014, 154-165.

Curriculum Vitae

Suzanne van Eekelen was born on 28 April 1966 in Nottingham, Great Britain, to Dutch parents, before moving to the Netherlands at the age of one. She obtained her secondary education diploma from the Lodewijk Makeblijde College in Rijswijk, South Holland, in 1984. In 1991, she completed her Master's degree at the Civil Engineering Department of Delft University of Technology with her thesis entitled *Numerical modelling of soil sampling*. She then embarked on her professional career with Delft Geotechnics, which later changed its name to GeoDelft before becoming part of Deltares. Suzanne completed this doctorate at Deltares and Delft University of Technology.

Suzanne van Eekelen is now a researcher in geotechnical engineering and an expert in the field of geosynthetic reinforcement, in particular piled embankments. She has reviewed or advised many piled embankment projects and she specialises in laboratory experiments and field monitoring. She has developed an analytical model for the design of basal reinforced piled embankments. This model, which is presented in this thesis, was adopted in the 2015 update of the Dutch CUR226 guideline for basal reinforced piled embankments.

In the past, Suzanne has engaged in research on constitutive modelling, developed the Delft Egg model for clay behaviour and later included creep behaviour in the Delft Soft Soil model. She has conducted numerical analyses of large deformations in soil, sample disturbance, granular flow under gravity, and shield tunnelling. She has led research on upgrading dikes with short sheet piling and been involved in a multi-disciplinary project on the IJssel Lake in the Netherlands.

Suzanne is the author or co-author of 10 international journal papers and approximately 100 proceedings papers and other publications. She has taught and lectured on several courses and multiple conferences, including courses at Delft University of Technology, Ghent University, PAO Netherlands and conferences such as the Dutch and Belgium Geotechnics Day (2009, 2012), the Brazilian Workshop Geosintéticos (2011), the Finnish Soil reinforcement workshop (2011) and several national and international conferences and courses of the IGS and ISSMGE.

Suzanne chairs several committees: since 2005, the Dutch CUR226 Committee for the Dutch Guideline for piled embankments; since 2013, the Dutch CUR198 Committee that updates the design guideline for retaining structures of reinforced soil and, since 2011, the Committee for Innovation and Knowledge transfer of the Dutch Chapter of the International Geosynthetics Society.

Suzanne has received several awards for her doctorate study:
- the IGS award 2014 for her research on piled embankments described in the journal papers included in this thesis (Van Eekelen et al., 2011, 2012a, 2012b, 2013, 2015a);
- the award for the best paper in Geotextiles and Geomembranes in 2012 for Van Eekelen et al., 2012a (Chapter 2 of this thesis);
- an Honourable Mention as one of the four best papers in Geotextiles and Geomembranes in 2011 for Van Eekelen et al., 2011a (included in the appendix to this thesis);
- for the same paper: the 2011 Keverling Buisman Award.

Suzanne is married to Maarten Vos. They have two sons and a daughter: Gerrit (1995), Roel (1997) and Ida (1999).

Linkedin: nl.linkedin.com/in/suzannevaneekelen
Publications on Google Scholar:
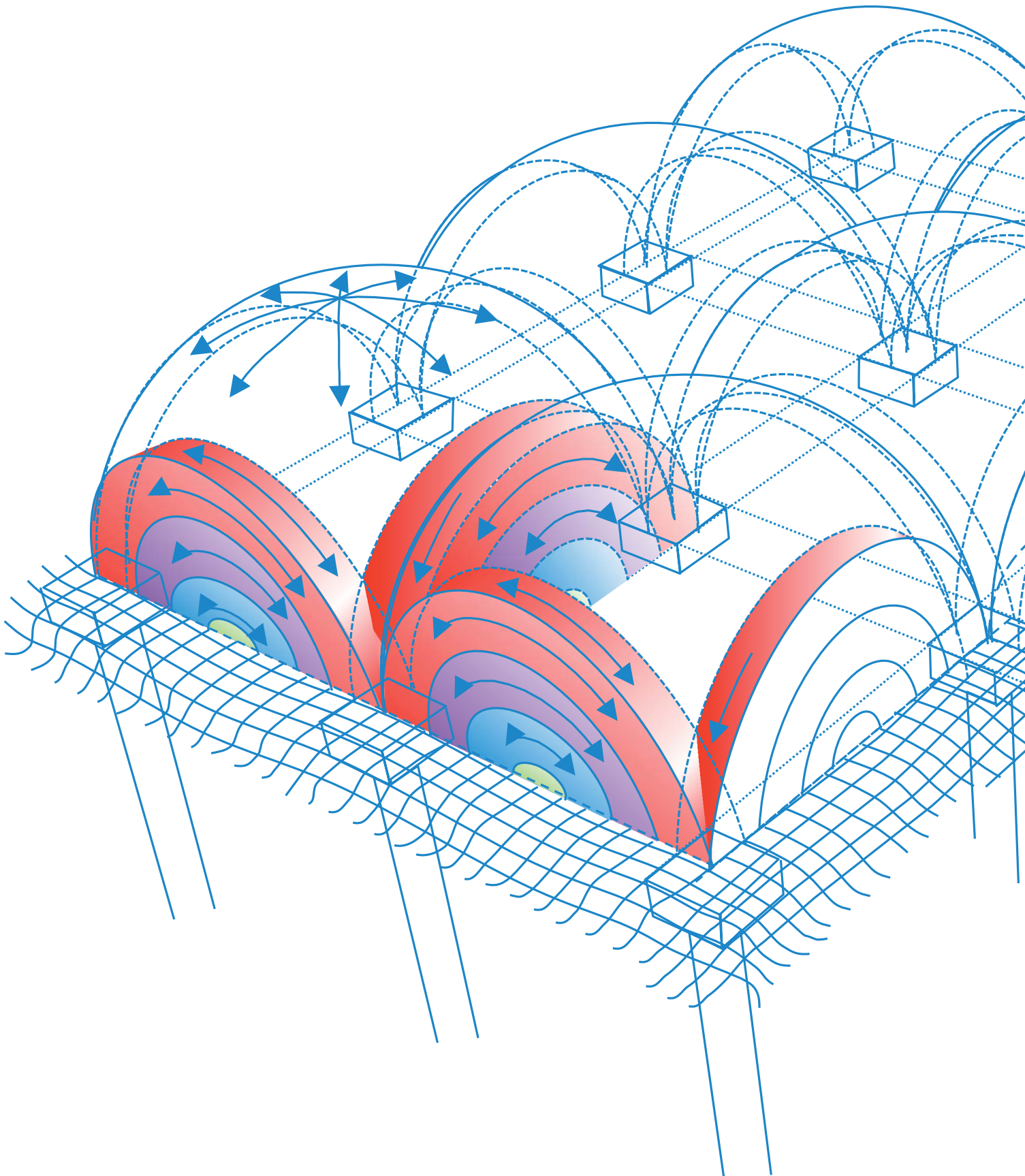http://scholar.google.nl/citations?user=lrmZe_EAAAAJ&hl=nl
Publications on Scopus:
http://www.scopus.com/authid/detail.url?authorId=6507209956

www.paalmatrassen.nl
www.piledembankments.com
Suzanne.vanEekelen@deltares.nl

Basal Reinforced Piled Embankments

Experiments, field studies and the development and validation
of a new analytical design model